

**Medical application and biological occurrence of  
inorganic nanoparticles and nanostructures**

**Dissertation**

to obtain the academic degree of

Doctor of Natural Sciences (Dr. rer. nat.)

prepared and submitted by

**M.Sc. Nataniel Białas**

born in Rzeszów, Poland

*Inorganic Chemistry*

*University of Duisburg-Essen, Essen, Germany*

November 2021

# DuEPublico

Duisburg-Essen Publications online

UNIVERSITÄT  
DUISBURG  
ESSEN

*Offen im Denken*

ub | universitäts  
bibliothek

Diese Dissertation wird via DuEPublico, dem Dokumenten- und Publikationsserver der Universität Duisburg-Essen, zur Verfügung gestellt und liegt auch als Print-Version vor.

**DOI:** 10.17185/duepublico/76112

**URN:** urn:nbn:de:hbz:465-20220705-084131-6

Alle Rechte vorbehalten.

*“Ce que je sais pour demain, c'est que la Providence se lèvera avant le soleil.”*

*“What I know for tomorrow is that Providence will rise before the sun.”*

*– Henri-Dominique Lacordaire OP (1802-1861)*



Research work, presented in this doctoral thesis, was performed in the time from July 2017 to March 2021 in the group of Prof. Dr. Matthias Epple at the Inorganic Chemistry of the University of Duisburg-Essen.

Supervisor and first reviewer: **Prof. Dr. Matthias Epple**

Second reviewer: **Prof. Dr. Bettina Siebers**

Chairman of the doctoral commission: **Prof. Dr. Maik Walpuski**

Place and date of the Ph.D. defense: **Essen, 12<sup>th</sup> January 2022**



---

**Table of contents**

List of abbreviations and units .....	XI
1. Introduction and motivation .....	1
2. Review of literature .....	3
2.1. Project I – Bioactive calcium phosphate nanoparticles for NF- $\kappa$ B silencing.....	3
2.1.1. Calcium phosphate as biomineral .....	3
2.1.2. Calcium phosphate nanoparticles: properties and uptake by eukaryotic cells.....	5
2.1.3. The potential of calcium phosphate nanoparticles in biomedical applications.....	7
2.1.4. The family of RNA .....	10
2.1.5. RNA interference as defence mechanism against genomic parasites .....	13
2.1.6. Host immune response and the role of NF- $\kappa$ B in inflammation .....	15
2.2. Project II – Chemistry of fossilized proboscidean enamel.....	18
2.2.1. Teeth in the life of vertebrates .....	18
2.2.2. Elephant taxonomy and the evolution of <i>Proboscidea</i> .....	20
2.2.3. The elephant dentition system .....	24
2.2.4. Proboscidean enamel microstructure .....	25
2.2.5. Evolution of proboscidean enamel and dentition system.....	27
2.3. Project III – Interactions between ultrasmall gold nanoparticles and bacteria.....	28
2.3.1. Ultrasmall gold nanoparticles: synthesis and properties.....	28
2.3.2. Structure of the bacterial cell envelope.....	30
2.3.3. Mechanisms and examples of particle uptake in bacteria.....	32
2.3.4. Metal resistance mechanisms in bacteria .....	34
2.3.5. Nanomaterials as antibacterial agents .....	36
3. Materials and devices .....	39
3.1. Reagents, fluorophores, media and kits .....	39
3.2. Biomolecules.....	41
3.3. Laboratory materials .....	42
3.4. Glass materials for fluorescence microscopy.....	43

3.5. Bacterial strains, growth media and cultivation conditions .....	43
3.6. Laboratory devices .....	44
3.7. Software .....	47
4. Methods, samples and experimental procedures .....	48
4.1. Project I – Bioactive calcium phosphate nanoparticles for NF- $\kappa$ B silencing.....	48
4.1.1. Syntheses of calcium phosphate nanoparticles .....	48
4.1.1.1. Fluorescent calcium phosphate nanoparticles for dissolution studies.....	48
4.1.1.2. Bioactive fluorescent calcium phosphate nanoparticles for gene silencing of NF- $\kappa$ B p65 .....	50
4.1.1.3. Bioactive fluorescent and ligand-decorated calcium phosphate nanoparticles for gene silencing of NF- $\kappa$ B p65 and cell targeting studies .....	52
4.1.1.4. Fluorescent calcium phosphate nanoparticles for tracking studies .....	54
4.1.2. Dissolution experiments of CaP nanoparticles .....	55
4.1.3. Preparation of Dy734-conjugated polyethyleneimine .....	56
4.1.4. Methods for nanoparticle characterization.....	57
4.1.5. Biological methods, cell lines and animals .....	58
4.1.5.1. <i>In vitro</i> methods .....	58
4.1.5.2. <i>In vivo</i> methods .....	59
4.2. Project II – Chemistry of fossilized proboscidean enamel.....	59
4.2.1. Proboscidean samples .....	59
4.2.2. Preparation of samples and enamel characterization methods.....	63
4.3. Project III – Interactions between ultrasmall gold nanoparticles and bacteria.....	65
4.3.1. Ultrasmall fluorescent gold nanoparticles for studies with bacteria .....	65
4.3.2. Preparation of electrocompetent <i>E. coli</i> cells.....	67
4.3.3. Electrotransformation of <i>E. coli</i> cells .....	67
4.3.4. Stimulation of eGFP expression in bacteria.....	68
4.3.5. Incubation of bacteria with ultrasmall gold nanoparticles for CLSM imaging .....	69
4.3.6. Studies on gold nanoparticle cytotoxicity in bacteria .....	70

4.3.7. Incubation of bacteria with ultrasmall gold nanoparticles for SIM imaging .....	70
4.3.8. Incubation of bacteria with ultrasmall gold nanoparticles for FACS studies .....	71
5. Results and discussion.....	72
5.1. Project I – Bioactive calcium phosphate (CaP) nanoparticles for NF-κB silencing .....	72
5.1.1. Characterization of CaP nanoparticles for dissolution studies.....	72
5.1.2. Characterization of CaP nanoparticles for gene silencing of NF-κB p65.....	74
5.1.3. Characterization of CaP nanoparticles for tracking studies .....	80
5.1.4. Characterization of ligand-decorated CaP nanoparticles for gene silencing of NF-κB p65 and cell targeting studies .....	83
5.1.5. Review of the biological results for CaP nanoparticles described in this thesis.....	95
5.2. Project II – Chemistry of fossilized proboscidean enamel.....	101
5.2.1. Chemical characterization of fossilized proboscidean enamel .....	101
5.2.1.1. Elemental analyses .....	101
5.2.1.2. TG and IR analyses .....	106
5.2.1.3. XRD analyses .....	109
5.2.1.4. Stable oxygen isotope ( $\delta^{18}\text{O}$ ) studies .....	111
5.2.2. Microstructure of fossilized proboscidean enamel .....	112
5.2.3. Supplementary information .....	119
5.3. Project III – Interactions between ultrasmall gold nanoparticles and bacteria.....	122
5.3.1. Characterization of bacterial strains and the ultrasmall gold nanoparticles.....	122
5.3.2. CLSM results on the uptake of gold nanoparticles by bacterial cells.....	124
5.3.3. CLSM results on nanoparticle cytotoxicity in bacteria.....	127
5.3.4. CLSM results of the control samples and possible channel cross-talk.....	129
5.3.5. SIM results on the uptake of gold nanoparticles by bacterial cells.....	130
5.3.6. FACS results on the uptake of gold nanoparticles by bacterial cells.....	135
6. Conclusions .....	137
7. Summary .....	140
8. Zusammenfassung .....	142

*Table of contents*

---

9. Podsumowanie .....	145
10. References .....	148
11. List of publications .....	174
12. List of conference presentations .....	175
13. <i>Curriculum Vitae</i> .....	178
14. Acknowledgements .....	181
15. Eidesstattliche Erklärung.....	183

## **List of abbreviations and units**

- % – percentage
- °C – degree Celsius
- 2D – two-dimensional
- 3D – three-dimensional
- 3DE – 3D enamel
- A – ampere
- AAS – atomic absorption spectroscopy
- Ab – antibody
- AF – Alexa Fluor<sup>®</sup>
- AF488 – Alexa Fluor<sup>®</sup> 488 (fluorophore)
- AF647 – Alexa Fluor<sup>®</sup> 647 (fluorophore)
- a.u. – arbitrary unit
- AuNPs – gold nanoparticles
- CaP – calcium phosphate
- CD69 – Cluster of Differentiation 69
- CFU – colony forming units
- CLSM – confocal laser scanning microscopy
- cm – centimeter
- conc. – concentration
- CTRL – control
- CuAAC – copper-catalyzed azide-alkyne cycloaddition
- Cy3 – sulfo-cyanine 3-alkyne (fluorophore)
- Cy5 – cyanine 5 (fluorophore)
- DLS – dynamic light scattering
- DMSO – dimethyl sulfoxide
- DNA – deoxyribonucleic acid
- DPBS – Dulbecco's phosphate buffered saline
- Dy734 – Dyomics 734 (fluorophore)
- ECJ – enamel-cement junction
- EDJ – enamel-dentin junction
- EDTA – ethylenediaminetetraacetic acid
- EDX – energy-dispersive X-ray spectroscopy
- eGFP – enhanced green fluorescent protein

ELISA – enzyme-linked immunosorbent assay  
EU – endotoxin unit  
FACS – fluorescence-assisted cell sorting  
FAM – 5-fluorescein-alkyne (fluorophore)  
FCS – fetal calf serum  
FITC – fluorescein isothiocyanate (fluorophore)  
GSH – glutathione  
h – hour  
HRTEM – high resolution transmission electron microscopy  
HSB – Hunter-Schreger-Bands  
IgG – immunoglobulin G  
IPTG – isopropyl- $\beta$ -D-thiogalactopyranoside  
IR – infrared  
K – degree Kelvin  
kDa – kilodalton  
kV – kilovolt  
L – liter  
LB – lysogeny broth  
LPS – lipopolysaccharide  
mA – milliampere  
Ma – millions of years  
mbar – millibar  
MFI – mean fluorescence intensity  
mg – milligram  
MIC – minimal inhibitory concentration  
 $\mu$ F – microfarad  
 $\mu$ g – microgram  
 $\mu$ L – microliter  
 $\mu$ m – micrometer  
 $\mu$ M – micromole  
min – minute  
MIP – maximum intensity projection  
miRNA – microRNA  
mL – milliliter

mm – millimeter  
mM – millimole  
MPS – (3-Mercaptopropyl)trimethoxysilane  
mRNA – messenger RNA  
ms – millisecond  
mV – millivolt  
mW – milliwatt  
 $M_w$  – molecular weight  
n/a – not applicable  
NF- $\kappa$ B – nuclear factor-kappa B  
ng – nanogram  
NHS – *N*-hydroxysuccinimide  
NIR – near-infrared  
nm – nanometer  
ORTHO – orthogonal projection  
*p.a.* – *pro analysi*  
PDI – polydispersity index  
PEI – polyethyleneimine  
PLE – prismless enamel  
psi – pound per square inch  
RE – radial enamel  
RISC – RNA-induced silencing complex  
RNA – ribonucleic acid  
RNAi – RNA interference  
rpm – revolutions per minute  
rRNA – ribosomal RNA  
RT – room temperature  
s – second  
SEM – scanning electron microscopy  
SIM – structured illumination microscopy  
siRNA – small interfering RNA  
siRNAc – control siRNA  
siRNAf – functional siRNA  
sulfo-SMCC – sulfo-*N*-succinimidyl 4-(maleimidomethyl)cyclohexane-1-carboxylate

*List of abbreviations and units*

---

t – tonne

TAMRA – carboxytetramethylrhodamine

TAMRAp – TAMRA-conjugated peptide

TEOS – tetraethoxysilane

TG – thermogravimetry

TNF- $\alpha$  – tumor necrosis factor-alpha

tRNA – transfer RNA

UV – ultraviolet light

Vis – visible light

wt% – weight percentage

XRD – X-ray powder diffraction

## 1. Introduction and motivation

This doctoral thesis deals with the subject of three interdisciplinary research projects. They combine broadly-defined inorganic chemistry with several other scientific disciplines, such as molecular biology, immunology, medicine, geology, paleontology and microbiology, and provide answers to important questions related with (i) human health and improvement of life quality, (ii) evolution of the Earth and its inhabitants, and (iii) better understanding of the living cell phenomenon.

The first research project, undertaken in this thesis, concerns the application of calcium phosphate (CaP) nanoparticles in biomedicine. Bioactive nanoparticles (with and without surface decoration), carrying therapeutic small interfering RNA (siRNA) were used to silence the expression of genes encoding one of the functional protein subunits of the nuclear factor-kappa B (NF- $\kappa$ B) complex. It is an important transcription factor involved in the regulation of processes related with cell development and immunity. Moreover, NF- $\kappa$ B is involved in the course of inflammatory processes, and abnormalities in its regulation on the molecular level underlie many severe diseases. The project assumed development of new nanoparticle formulations, the chemical research part (presented in this thesis), and further biological studies on the properties of bioactive nanoparticles *in vitro* (on the cell level) and *in vivo* (on the body level). The aim of the project was to develop and propose a novel therapeutic strategy, based on siRNA-mediated gene silencing of NF- $\kappa$ B, for the treatment of inflammatory diseases, which are often characterized by uncontrolled expression of NF- $\kappa$ B. Once released from the nanoparticles, the therapeutic siRNA enters the cell cytoplasm and leads to gene silencing *via* ribonucleic acid (RNA) interference (RNAi).

The second research project, undertaken in this thesis, concerns the use of analytical methods of the inorganic chemistry for in-depth compositional analyses of fossilized tooth enamel of extinct *Proboscidea*. The enamel, which is the hardest known biological tissue, is an excellent material for chemical and paleontological studies because it provides information not only about the animal (anatomy, physiology, evolution, diet) but is also a treasury of knowledge about the paleoclimate and paleoenvironment. The enamel is characterized by extraordinary resistance to chemical alteration caused by diagenesis (environmental influence) and retains its advanced prismatic microstructure nearly unchanged over tens of millions of years. This project involved comprehensive chemical analyses, using various methods, of the enamel composition of different extinct proboscideans living in the time range from Eocene to Pleistocene, with a special focus on elephants inhabiting in the past the Indian subcontinent

in the region of Himalayan foothills. Chemical studies on the enamel were supported by detailed microscopic investigations of the enamel prismatic microstructure, as well as studies assessing the impact of diagenesis on the chemical composition of the enamel. This project provided not only data that are consistent with the current state of literature but also provided completely novel data on enamel composition and structure in extinct Indian proboscideans. Furthermore, some innovative approaches in studies on proboscidean enamel were presented and proposed, like precise localized mapping of the elements. Results obtained in this project gave new insights to the knowledge on the evolution of extinct elephants and adaptation of their enamel to dietary shifts caused by paleoclimate transformations.

The third and last research project, undertaken in this thesis, is focused on the nature of interactions between bacteria and ultrasmall nanoparticles. The use of autofluorescent *Escherichia coli* strains, together with fluorescent nanoparticles, enabled visualization of nanoparticle uptake by bacteria and tracking the intracellular localization of nanoparticles using advanced fluorescence microscopy techniques. To maximize the chance of nanoparticle uptake by bacterial cells, and knowing from literature that particle size is the key parameter for nanoparticle internalization and transport through the bacterial cell envelope, non-cytotoxic ultrasmall gold nanoparticles (AuNPs) were applied. Although literature provides information on the uptake of various types of nanoparticles by bacteria, most of the available reports are observations done during studies on the antibacterial properties of nanoparticles. This means that internalization into bacteria usually resulted from pathological changes in the cell structure (*e.g.*, membrane damage) which were caused by the influence of the tested nanomaterial, *e.g.*, release of toxic metal ions from the nanoparticles. Therefore, the reported uptake was rather stimulated than spontaneous (like in nature) and did not correspond to the situation observed in healthy cells. In order to study the interactions between bacteria and nanoparticles, particularly important was to apply nanocarriers which would not adversely affect the viability of bacterial cultures. The aim of the project was to provide new data on non-lethal uptake of nanoparticles by bacteria, a topic which is intensively discussed in literature, and to show the potential of ultrasmall AuNPs with covalently-attached fluorophores in microbiological and microscopic studies. Results of the project contribute to a better understanding of the living cell physiology and the dynamics of interactions between bacteria and the environment.

## 2. Review of literature

### 2.1. Project I – Bioactive calcium phosphate nanoparticles for NF- $\kappa$ B silencing

#### 2.1.1. Calcium phosphate as biomineral

CaP is a general name of a broad family of Earth minerals, in which calcium ions ( $\text{Ca}^{2+}$ ) are bound to various phosphate ( $\text{PO}_4^{3-}$ ,  $\text{PO}_3^-$ ,  $\text{P}_2\text{O}_7^{4-}$ ), hydrogen ( $\text{H}^+$ ) or hydroxide ( $\text{OH}^-$ ) ions.<sup>1</sup> The most common mineral form of CaP is hydroxyapatite, with a molecular formula  $\text{Ca}_5(\text{PO}_4)_3\text{OH}$ . However, in nature, CaP can be also found in other mineral forms, like tricalcium phosphate [ $\text{Ca}_3(\text{PO}_4)_2$ ], octacalcium phosphate [ $\text{Ca}_8(\text{HPO}_4)_2(\text{PO}_4)_4 \cdot 5 \text{H}_2\text{O}$ ], dicalcium phosphate dihydrate [ $\text{CaHPO}_4 \cdot 2 \text{H}_2\text{O}$ ] or monocalcium phosphate monohydrate [ $\text{Ca}(\text{H}_2\text{PO}_4)_2 \cdot \text{H}_2\text{O}$ ], as well as in various forms of structurally amorphous CaP, with a variable composition of the general formula [ $\text{Ca}_x(\text{PO}_4)_y \cdot z \text{H}_2\text{O}$ ].<sup>2</sup>

An important parameter of CaP, related with the biological response of cells, is the mass ratio between calcium and phosphorus (P). Typically, the Ca/P ratio in biological apatite (bioapatite) is lower or close to that found in pure hydroxyapatite (1.67).<sup>1,3</sup> Ca/P ratio in adult human bone varies in the range 1.3-2.2 and is similar to that of mature human breast milk.<sup>4-6</sup>

CaP belongs also to the fundamental biominerals. These are biogenic mineral phases characterized by complex and heterogenous microstructures (single crystals, composites, amorphous materials). Biominerals play a unique role in the life of all organisms, from unicellular prokaryotes (*Archaea*, bacteria) to multicellular vertebrates.<sup>2,7</sup> Biominerals are biomaterials which provide skeletal support, protect against predators, provide weapon and participate in magnetoreception.<sup>8</sup> They can be commonly found in various animal hard tissues (bones, teeth, shells, dermal armors), usually as mixture of inorganic minerals, mainly calcium carbonate ( $\text{CaCO}_3$ ) or CaP, and organic biomolecules, such as proteins (*e.g.*, collagen) or polysaccharides (*e.g.*, chitin).<sup>9</sup>

CaP, as the main inorganic compound of human hard tissues, constitutes about 60, 70 and over 90 weight percentage (wt%) of bone, tooth dentin and tooth enamel mass, respectively.<sup>1,10</sup> Bone CaP (called carbonated apatite or dahlite) is made of hydroxyapatite nanocrystals (usually nanoneedles or nanoplatelets) incorporated into the collagen fibril matrix and oriented with the *c*-axis parallel to the fibrils (**Figure 1**).<sup>1,11</sup>

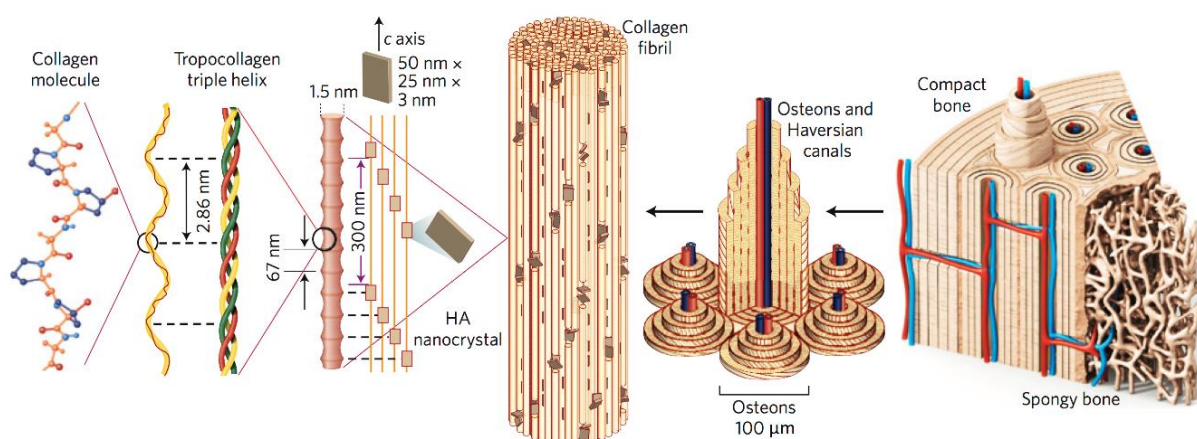


**Figure 1.** Microstructure of human bone. Image adapted and modified from Wegst et al.<sup>12</sup>

Due to the presence of nanometer-sized crystals and occurrence of residual stresses in the crystal lattice, bioapatite demonstrates a poorly crystalline microstructure, in contrast to hexagonally-organized geological apatite (**Figure 2**).

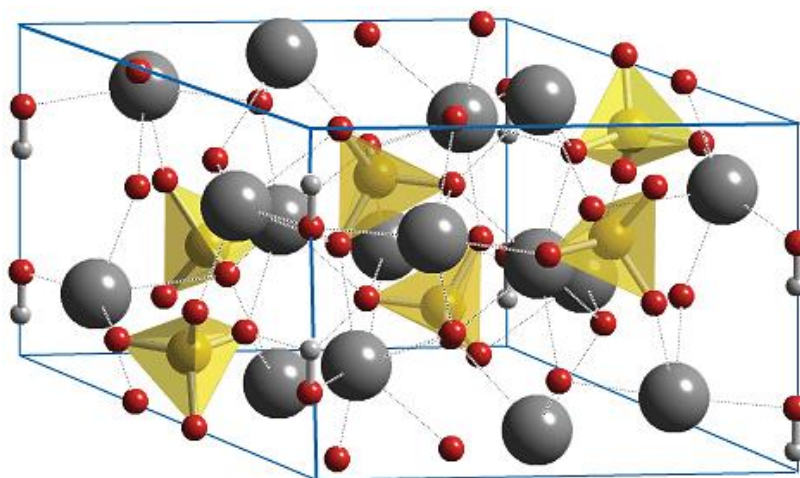


**Figure 2.** Unit cell of hydroxyapatite. Calcium (dark grey), phosphate (yellow), oxygen (red) and hydrogen (light grey) atoms are marked. Image adapted and modified from ChemTube3D ([www.chemtube3d.com/sshydroxyapatite](http://www.chemtube3d.com/sshydroxyapatite)).

Bone CaP can be also characterized by a broad range of possible ionic substitutions. For example, calcium ions in hydroxyapatite can be replaced by sodium ( $\text{Na}^+$ ), magnesium ( $\text{Mg}^{2+}$ ) or strontium ( $\text{Sr}^{2+}$ ) ions, whereas carbonate ( $\text{CO}_3^{2-}$ ) ions can substitute hydroxide or phosphate sites in A- or B-type substitution of hydroxyapatite, respectively.<sup>13</sup> The latter significantly enhances acid solubility of bioapatite.<sup>14</sup>

### 2.1.2. Calcium phosphate nanoparticles: properties and uptake by eukaryotic cells

Inorganic nanomaterials composed of CaP, gold (Au), iron oxide ( $\text{Fe}_3\text{O}_4$ ), silicon dioxide ( $\text{SiO}_2$ ), titanium dioxide ( $\text{TiO}_2$ ) and zinc oxide (ZnO) are of great interest of modern biomedicine, due to a broad range of possible applications, from diagnostic imaging, through overcoming microbial infections to controlled drug delivery into cells.<sup>15-18</sup> Among abovementioned nanomaterials, CaP nanoparticles are believed to be the most promising and can be characterized by distinctive adsorption abilities and biochemical stability. Moreover, they demonstrate excellent biocompatibility and biodegradability, as CaP is also the natural inorganic component of native bone and teeth, which makes them well-tolerated by the body and readily taken up by cells *via* endocytosis – the main particle uptake mechanism in eukaryotic cells (**Figure 3**).<sup>17,19</sup>

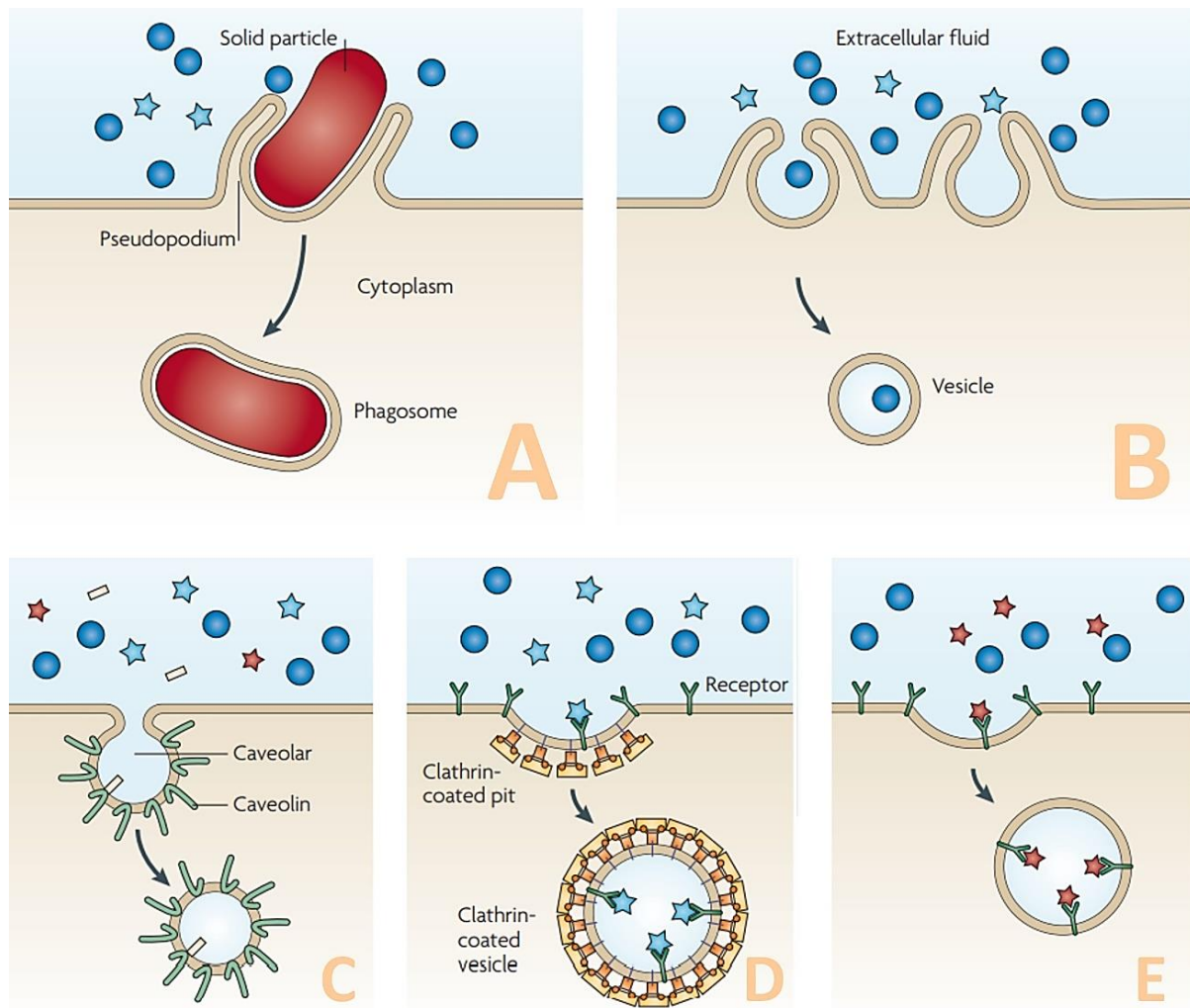


**Figure 3.** The general principle of endocytosis in eukaryotic cells. Internalization into cell is a vesicle-driven process, where vesicles are formed by invagination of the cell membrane.

*Phagocytosis (A; so-called “cell feeding”) is used by cells to ingest large particles (>1 μm) and other cells, e.g., bacteria or apoptotic cells; pinocytosis (B; so-called “cell drinking”) is a process in which, beside larger particles, significant amounts of the extracellular fluids are ingested by cells. For the uptake of molecules, viruses and smaller particles (<200 nm), caveolin-mediated endocytosis (C), clathrin-mediated endocytosis (D) and caveolin-independent/clathrin-independent endocytoses (E) are used, with a preferential particle uptake size of ~60 nm, ~120 nm and ~90 nm, respectively.<sup>20,21</sup> Image adapted and modified from Petros and DeSimone.<sup>21</sup>*

After internalization, in the cell cytoplasm, CaP nanoparticles are encapsulated in vesicles called endosomes (pH>7). Acid hydrolase-containing primary lysosomes (pH<5) get fused with the endosomes and form together hybrid organelles called endolysosomes. The decrease of pH inside the organelle results in the degradation of entrapped CaP nanoparticles and generation of high concentrations of calcium and hydrogenphosphate (HPO<sub>4</sub><sup>2-</sup>) ions. The osmotic pressure drives the influx of water from the cytosol (hypotonic environment) into the organelle and results in rupture of the secondary lysosome and release of its content into the cytoplasm. Inorganic products of nanoparticle degradation should not act immunostimulatory to the cells. Free biomolecules, if carried by the nanoparticles, can reach then their cellular targets. For instance, nucleic acids will either enter the cell nucleus and undergo transcription, in the case of deoxyribonucleic acid (DNA), or remain in the cytoplasm and induce gene silencing, in the case of RNA.<sup>17,22</sup>

Beside biochemical benefits, which are fundamental for biomedical applications of CaP nanoparticles, additional advantages of CaP nanoparticles are rapid and easy synthesis, and relatively low costs (at least for synthesis of “basic” unloaded CaP nanoparticles).<sup>17</sup> Structural flexibility of CaP materials enables to synthesize a range of CaP nanoparticles in different size and morphology, including spheres, rods and platelets.<sup>23</sup> Size and shape of CaP nanoparticles is a critical parameter in terms of the biological response and determines the application potential of nanoparticles in biomedicine. For example, CaP nanospheres and nanorods are recommended, as carriers, for the delivery of biomolecules into cells. Therapeutic cargos are usually loaded onto the nanoparticles during synthesis. The adsorption of biomolecules to nanoparticles may have a physical (physisorption) or chemical (chemisorption) nature. The main difference here is the specificity and strength of the cargo binding. In the first case, the adsorption is achieved *via* weak non-covalent interactions (hydrogen bonding, hydrophobic interactions, van der Waals forces, electrostatic attraction) between biomolecules and

nanoparticle surface. In the second case, the binding between biomolecules and nanoparticles has a strictly chemical nature, usually covalent, is strong and influences the release rate of the therapeutic.<sup>23</sup> Drugs used in nanoparticle-mediated therapies can be either attached to the nanoparticle surface or encapsulated in the nanoparticles.<sup>24</sup> The second option requires synthesis of core-shell nanocarriers. The nanoparticle core is the backbone to which drug molecules are bound. The shell (*e.g.*, made of silica) coats core-drug complexes and protects the bioactive cargo from enzymatic degradation, ensures colloidal stability of the nanoparticles and enables further surface modifications of the nanoparticles (*e.g.*, decoration with functional groups, peptides or proteins) for targeted drug delivery applications.<sup>25</sup>

Size and shape of CaP nanoparticles are strictly related with synthesis method and parameters. These are type and starting concentration of calcium and phosphate sources, type and concentration of inorganic and organic additives (*e.g.*, alkoxysilanes and polymers used for nanoparticle stabilization/capping), as well as direct synthesis parameters, like pH, temperature, stirring and time. While control over nanoparticle size seems to be well-established, the control over nanoparticle morphology still remains a challenge.<sup>26,27</sup>

It is believed that size up to 200 nm favors internalization of nanoparticles into eukaryotic cells. Moreover, due to a negative electrical charge of the cell surface, positively-charged nanoparticles are needed for occurrence of the electrostatic cell-particle attraction. Colloidal stability of CaP nanoparticles is a priority criterion in all kinds of biological applications. Stable nanoparticles do not tend to form microparticulate aggregates. Such micrometer-sized biologically inactive agglomerates cannot penetrate the cell membrane and thus will be rapidly phagocytized. Culture media (in *in vitro* experiments) and body fluids (in *in vivo* investigations) constitute a real challenge for maintaining colloidal stability of CaP nanoparticles.

Biological media are aqueous solutions containing a variety of active biomolecules, including carbohydrates, lipids, nucleic acids and proteins, as well as salts, which may significantly alter colloidal stability of the nanoparticles. After transferring into a biological medium, the surface of nanoparticles becomes immediately coated with a biomolecule layer composed mostly of proteins. The adsorbed “protein corona” has a dramatic influence on the functionality of nanoparticles, in particular on cell targeting.<sup>13,28,29</sup> This aspect needs to be kept in mind when designing therapeutic strategies with the usage of CaP nanoparticles.

### **2.1.3. The potential of calcium phosphate nanoparticles in biomedical applications**

CaP nanoparticles can serve as vectors for the delivery of nucleic acids (DNA, RNA) into cells and constitute an alternative to cell- and viral-based gene delivery systems (**Figure 4**). Nucleic

acids are promising agents in the treatment of cancer, and hereditary, chronic and inflammatory diseases, on the molecular level.<sup>17</sup>

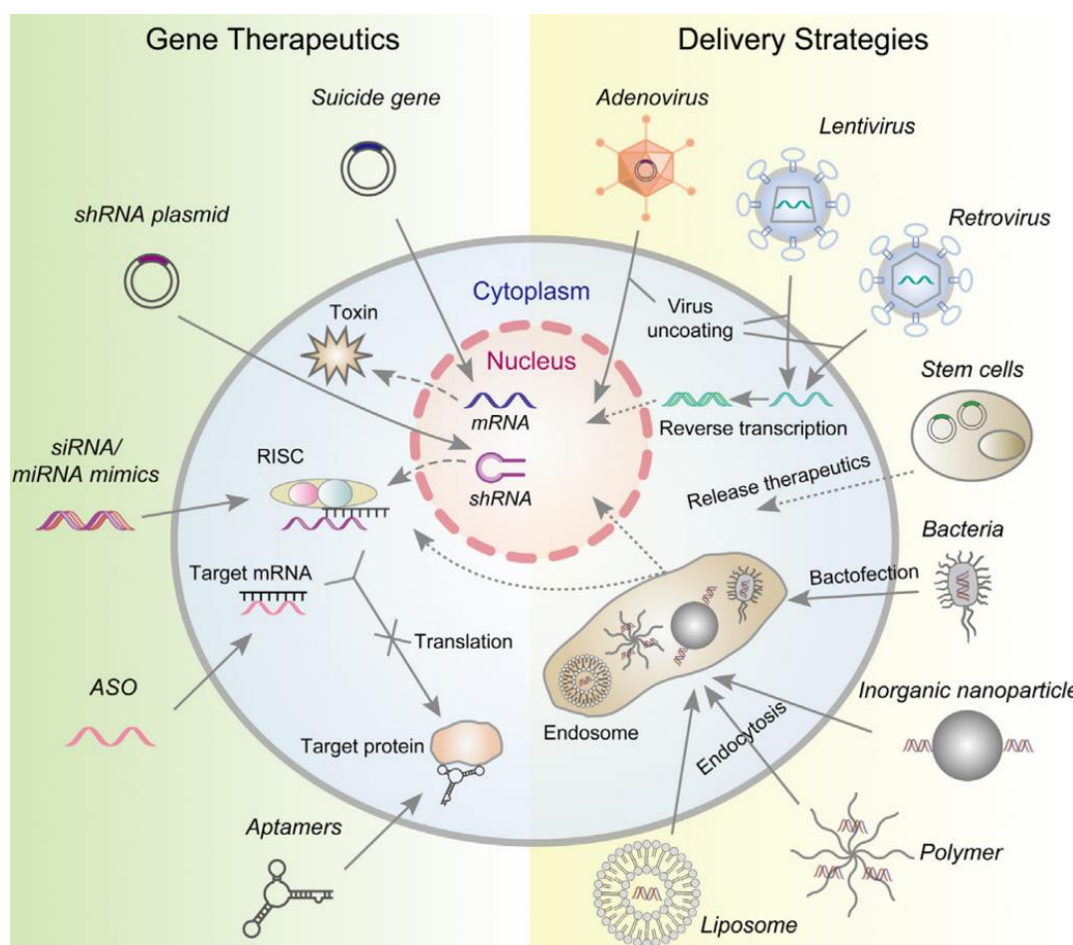


**Figure 4.** An overview of gene therapeutics (drugs) and systems for their delivery into eukaryotic cells. Therapeutic strategies can be based on (i) RNAi and, as a consequence, inhibition of protein synthesis by microRNA (miRNA), short hairpin RNA (shRNA), siRNA or antisense oligonucleotide (ASO), (ii) a direct interaction of specific aptamers (single-stranded DNA/RNA) with target proteins to regulate downstream signaling or (iii) introduction and expression of toxin encoding genes in cells (suicide genes). The delivery route of therapeutic cargos might have a viral (transduction) or non-viral (recombinant eukaryotic cells, bacteria, nanomaterials) nature.<sup>30,31</sup> mRNA – messenger RNA, RISC – RNA-induced silencing complex. Image adapted from Wang et al.<sup>30</sup>

This process is called transfection and constitutes the basis for gene therapy, one of the most modern strategies of disease treatment, in which the therapeutic effect is achieved by modifying expression of certain genes using therapeutic nucleic acids.

Negatively-charged nucleic acids (containing phosphate groups) cannot enter the cell in a free (unbound) form, due to charge similarity with the cell surface, and will be rapidly degraded in the extracellular environment.<sup>17</sup> Therefore, an oppositely-charged carrier is required. After adsorption onto positively-charged CaP nanoparticles (due to the presence of calcium ions and cationic polymers – commonly used as stabilizers), nucleic acids can penetrate the cell membrane, be released into the cell cytoplasm and influence the cell's protein synthesis machinery.<sup>32</sup> The positive charge of CaP nanoparticles is here double beneficial. It drives the loading of nanoparticles with biomolecules and promotes the uptake of nanoparticle-drug complexes by cells.<sup>17</sup> Based on this molecular strategy, two opposite effects of gene regulation can be obtained. Transfection with DNA will lead to upregulation of protein expression. Transfection with siRNA or miRNA, which are types of short non-coding RNA, will result in downregulation of protein expression by means of RNAi.<sup>13,33</sup> This regulatory process, called gene silencing, is used to control gene expression in cells.

Literature provides some examples of the application of CaP nanoparticles for gene silencing. Devarasu *et al.* used siRNA-CaP nanoparticles for silencing of the firefly luciferase (*luc*) gene in modified (*luc*-expressing) human lung adenocarcinoma cells (line: A549*luc*).<sup>34</sup> Frede *et al.* applied CaP nanoparticles loaded with siRNA against cytokines: tumor necrosis factor- $\alpha$  (TNF- $\alpha$ ), interferon gamma (INF- $\gamma$ )-induced protein 10 (IP-10) and keratinocyte-derived chemokine (KC), for gene silencing in murine intestinal epithelial cells (line: MODE-K).<sup>35</sup> Kara *et al.* loaded CaP nanoparticles with siRNA for the silencing of survivin (an apoptose inhibiting protein) and cyclin B1 (regulatory protein involved in mitosis) in human lung adenocarcinoma cells (line: A549).<sup>36</sup> Finally, Tenkumo *et al.* applied siRNA-loaded CaP nanoparticles for the silencing of TNF- $\alpha$  in murine monocyte macrophages (line: J774.2).<sup>37</sup>

Beside nucleic acids, CaP nanoparticles can be also used as delivery platforms for various low- and high-molecular weight therapeutics, and thus have even a broader range of possible applications in the field of biomedicine. Common examples are here antibiotics, anti-inflammatories, bisphosphonates and proteins, which can be loaded onto the nanoparticles either single or dual (in co-delivery systems) to enhance the therapeutic effect. For example, Zhao *et al.* used CaP nanoparticles for a combined delivery of anti-inflammatory ibuprofen and bovine serum albumin (BSA) into human gastric carcinoma cells (line: MGC-803). The application of BSA (a model protein drug) decreased the cytotoxicity of nanoparticles, as well as improved the efficiency of ibuprofen loading onto the CaP nanocarriers and extended the release rate of ibuprofen from the nanoparticles for a better therapeutic effect.<sup>38</sup> Another example of a dual delivery system was reported by Madhumathi *et al.* who synthesized CaP

nanoparticles loaded with an antibiotic (tetracycline) and ibuprofen, as a potential antibacterial and anti-inflammatory healing agent, for the treatment of bone infections requiring a multidrug therapy, like periodontitis. The nanoparticles were biocompatible with embryonic mouse fibroblasts (line: 3T3).<sup>39</sup> Combination of a bisphosphonate (alendronate) and model plasmid DNA encoding the enhanced green fluorescent protein (eGFP), entrapped in CaP nanoparticles, described by Bisso *et al.*, worked well in *in vitro* transfection of murine mammary carcinoma cells (line: 4T1), however, demonstrated already some limitations for a potential application in *in vivo* studies.<sup>40</sup> Mukherjee *et al.* demonstrated that tetracycline-loaded CaP nanoparticles acted antimicrobial against enterobacterial species known for the potential to develop multidrug resistance, like Gram-negative *E. coli*, *Salmonella kentucky* and *Shigella flexneri*. Interestingly, the minimal inhibitory concentration (MIC) values, which are defined as the lowest concentration of an antimicrobial substance which prevents visible growth of bacteria, for nanoparticle-carried tetracycline were several-fold lower than for the free-administered antibiotic. This effect is known as the synergistic activity.<sup>41</sup> Another example of an enhanced antibacterial effect observed for antibiotics incorporated onto inorganic nanoparticles was reported by Pan *et al.* who have shown that gentamycin loaded onto CaCO<sub>3</sub> nanoparticles demonstrated higher antibacterial activity against Gram-positive *Bacillus subtilis*, when compared to the unbound antibiotic. Moreover, the release time of nanoparticle-conjugated gentamycin was also significantly extended.<sup>42</sup> Although antibiotics are generally used for combating bacterial infections, Rivas *et al.* demonstrated that CaP nanoparticles loaded with broad-spectrum chloramphenicol were also efficient in killing human breast cancer cells (line: MCF-7) by inducing mitochondrial dysfunctions.<sup>43</sup>

#### 2.1.4. The family of RNA

RNA, beside proteins, lipids and carbohydrates, belongs to fundamental biomacromolecules and play an essential role in protein synthesis and regulation of gene expression in cells, as well as catalyzes biochemical reactions (activity of ribozymes).<sup>44</sup> Similarly as DNA, RNA is a linear polymer assembled of nucleotides and its major building “bricks” are aromatic nucleobases: adenine (A), guanine (G), cytosine (C) and uracil (U). In DNA, the latter is replaced by thymine (T). The nucleobase together with a 5-carbon sugar ribose and phosphate, all covalently bound, constitute a nucleotide.<sup>45</sup> Other differences between DNA and RNA are, that the first nucleic acid contains deoxyribose as sugar moiety and occurs in cells in form of a double-stranded helix, whereas the second nucleic acid is typically found in nature single-stranded, with

tendency to fold up into a variety of shapes. Double-stranded RNA is carried by some viruses.<sup>46,47</sup>

The three major types of RNA found in cells are mRNA, transfer RNA (tRNA) and ribosomal RNA (rRNA), and all of them are involved in protein synthesis. The first is a coding RNA, whereas the others are non-coding. In brief, in the process of transcription, which takes place in cell nucleus, based on a double-stranded DNA template, a single-stranded pre-mRNA transcript is synthesized by RNA polymerases. The pre-mRNA is composed of the coding (exons) and non-coding (introns) regions. The latter are removed from the pre-mRNA transcript in the process of splicing and the exons are assembled together to form mature mRNA. Before mRNA leaves the nucleus, it still has to be chemically-modified by addition of a guanyl cap (7-methylguanosine) to the 5'-end of the transcript and addition of a poly(A) tail (a sequence of adenine nucleotides) to the 3'-end of the transcript. These modifications ensure stability of mRNA and are necessary for a proper transport of the mRNA from the nucleus to the cell cytoplasm and recognition by ribosomes. Without post-transcriptional modifications, after translocation into the cytoplasm, the mRNA would be recognized as foreign RNA and potential danger to the cell (*e.g.*, of a viral origin) and rapidly degraded by exonucleases. Mature mRNA carries a complete genetic information, where base sequence in the nucleic acid encodes amino acid sequence in the protein and is complementary with base sequence in the sense (coding) strand of the DNA template. Next, in the process of translation, which takes place in the cell cytoplasm in ribosomes, the protein chain is synthesized according to the genetic information carried by mRNA in the direction 5'→3', where 1 codon (composed of three nucleobases) encodes 1 amino acid. The starting point of protein synthesis is marked with the initiator codon AUG (encodes methionine at the N-terminus of a protein chain) in the mRNA and the end of the protein synthesis is signaled by one of the three terminating codons of mRNA (UAA, UAG, UGA) which do not encode any amino acid and mark the C-terminus of the protein chain. tRNA is responsible for the delivery of appropriate amino acids from the cytoplasm into ribosomes (in form of aminoacyl-tRNA) and rRNA, together with proteins, builds the ribosomes and catalyzes the assembly of amino acids and elongation of the polypeptide chain (**Figure 5**).<sup>44,48</sup>

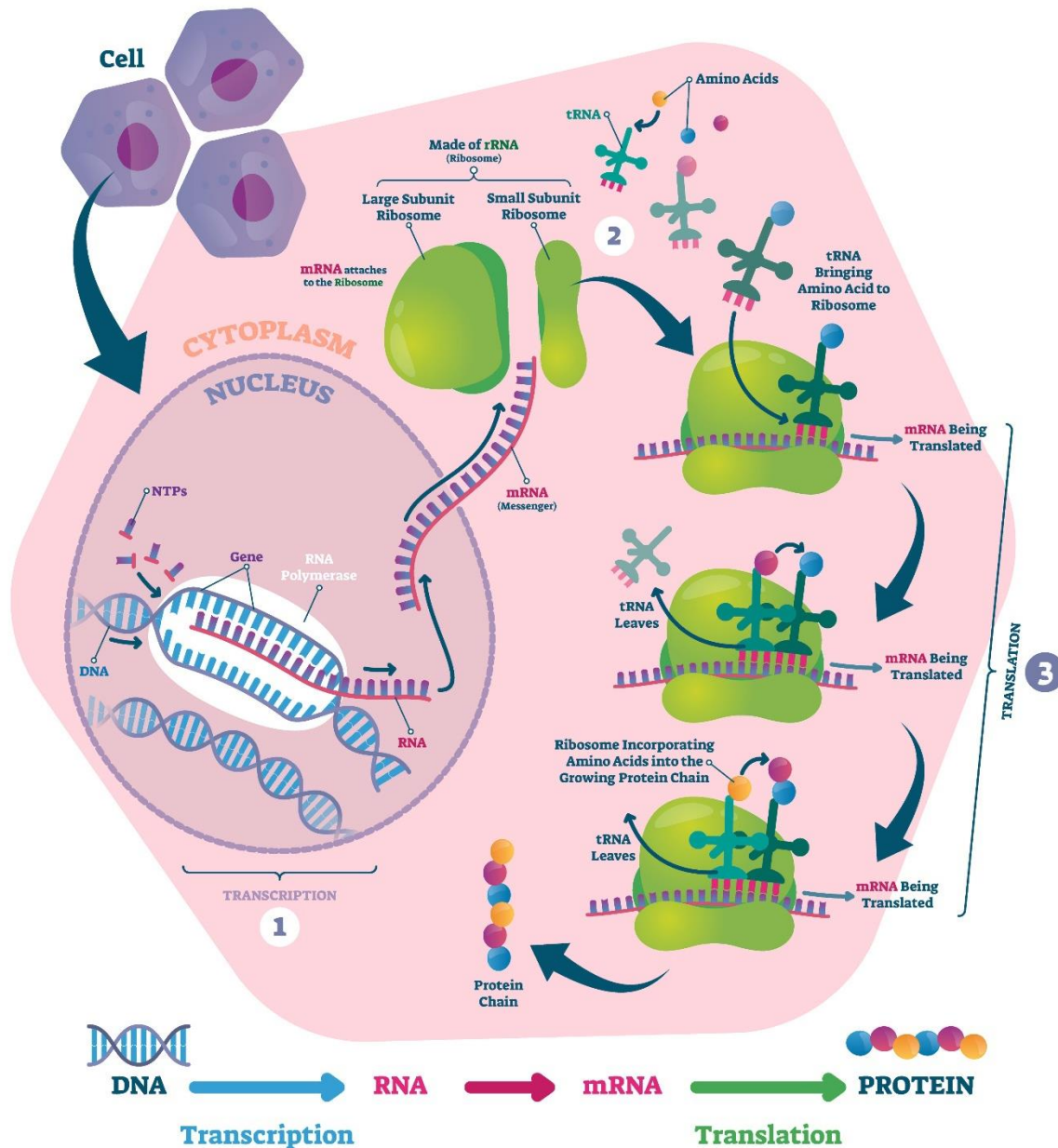


**Figure 5.** An overview of the process of protein synthesis in cells (description in text). NTPs – ribonucleoside triphosphates. Image adapted and modified from Nature Journals ([www.naturejournals.org/index.php/animalbio/ab-modules/technologies/protein-synthesis](http://www.naturejournals.org/index.php/animalbio/ab-modules/technologies/protein-synthesis)).

However, the RNA family consists not only of three major RNA types involved in protein synthesis but also of several other types of short and long non-coding RNA with very important functions in RNA editing and silencing, and regulation of gene expression in cells (**Figure 6**). In brief, small nuclear RNA (snRNA) is responsible for splicing of introns during posttranscriptional maturation of pre-mRNA and small nucleolar RNA (snoRNA) guides posttranscriptional modifications of rRNA and snRNA, whereas long HOTAIR RNA acts as an inducer of ubiquitin-mediated proteolysis. The latter plays an important role in a number of

cellular processes, including regulation of the cell cycle, modulation of the immune and inflammatory response, control of signal transduction pathways and cell development, by maintaining proteostasis.<sup>44,49-52</sup> Other short non-coding RNA molecules involved in the regulation of gene expression are PIWI-interacting RNA (piRNA) and tRNA-derived small RNA (tsRNA). The first is the genome guard in animal germ cells that silences transposons (so-called “jumping genes”) and protects the host genome from transposon-derived alterations. This is essential for a normal course of gametogenesis and reproduction.<sup>53,54</sup> The second is a specific tRNA cleavage product with a similar to miRNA molecular mode of action and with a still poorly understood role in the cell physiology. However, abnormalities in tsRNA expression in cells are related with pathological processes and seem to be associated with various diseases, like cancer, metabolic and neurodegenerative disorders and systemic lupus.<sup>55,56</sup>

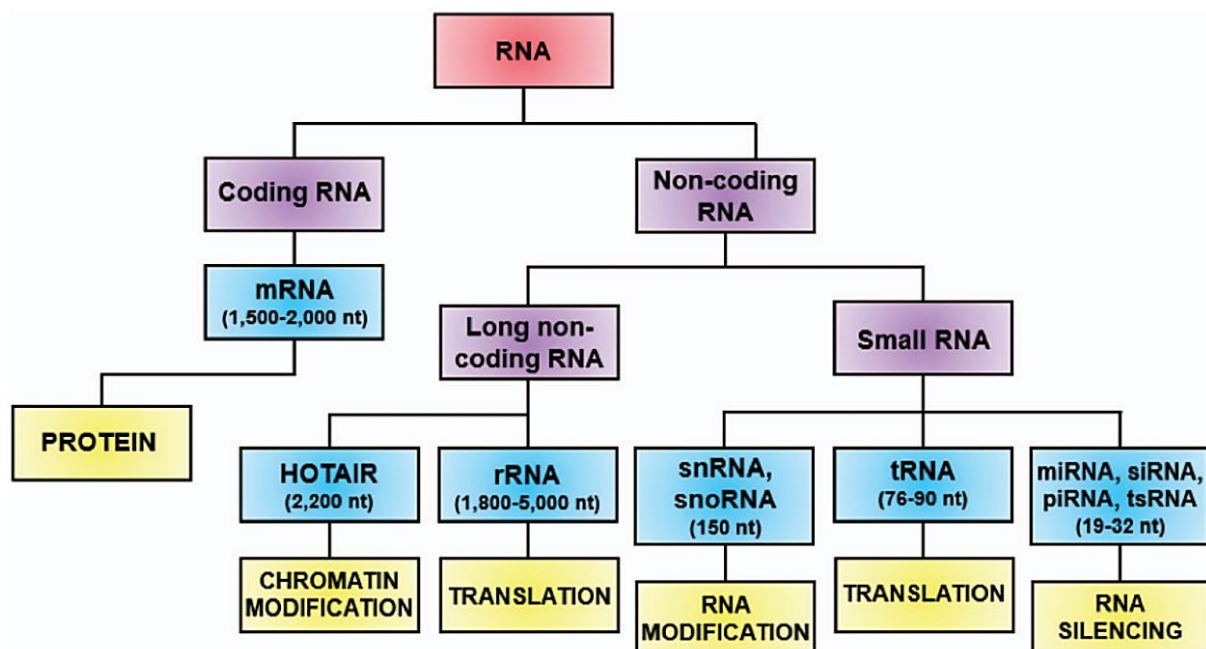


**Figure 6.** The RNA family consists of coding RNA (mRNA), as well as a variety of non-coding RNA with important roles in protein synthesis and regulation of gene expression (description in text). nt – nucleotide. Image adapted from Green et al.<sup>57</sup>

### 2.1.5. RNA interference as defence mechanism against genomic parasites

A very important role of short non-coding RNA is the inhibition of gene expression in cells by interaction with mRNA. This is the principle of RNAi discovered by Andrew Fire and Craig Mello in the 1990s and first reported in a nematode *Caenorhabditis elegans*.<sup>58</sup> RNAi is an evolutionary defense mechanism against invasion of exogenous genes (e.g., during viral

infections).<sup>33</sup> In this process, short RNA molecules, like single-stranded miRNA or double-stranded siRNA, interrupt the synthesis of proteins by knocking down the expression of target genes in a sequence-specific way. This can be achieved either *via* mRNA degradation by cleavage (miRNA, siRNA) or by repression of mRNA translation (miRNA). Therefore, siRNA is more efficient and specific in gene silencing, when compared to miRNA, whereas miRNA may influence expression of several target genes simultaneously (**Figure 7**).<sup>33</sup>

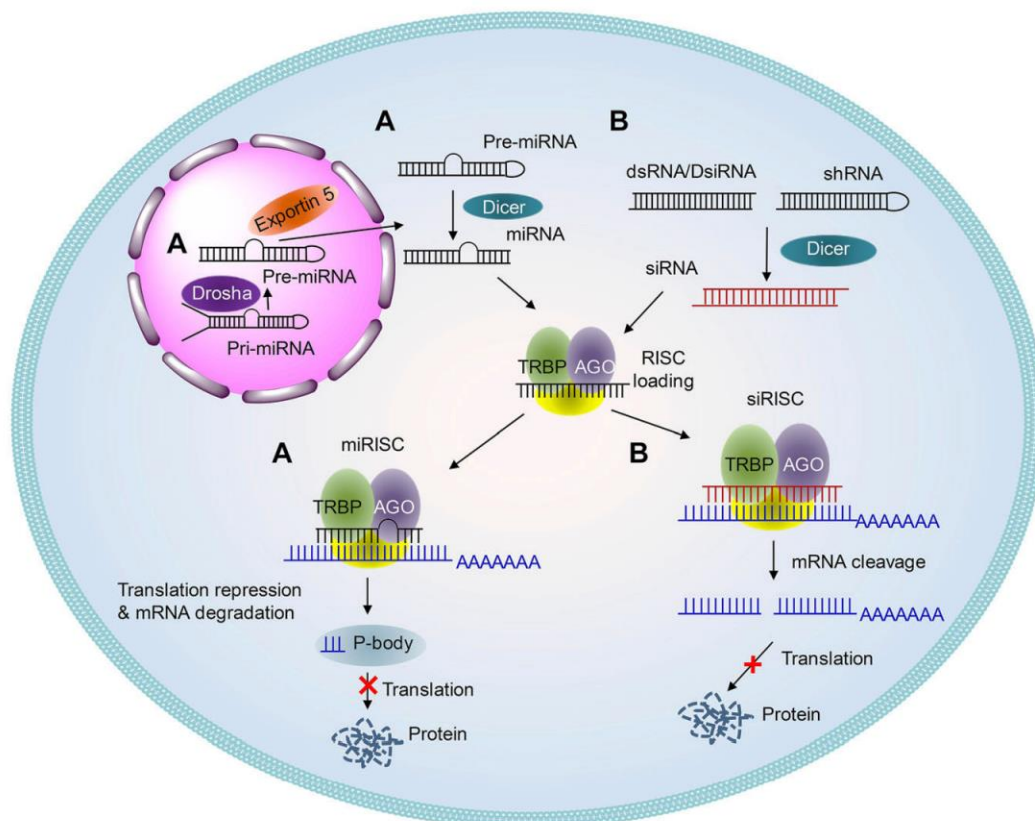


**Figure 7.** Pathways of miRNA- (A) and siRNA-mediated (B) RNAi (description in text). DsiRNA – Dicer-substrate siRNA, miRISC/siRISC – miRNA-/siRNA-incorporated RISC, P-body – processing body, shRNA – short hairpin RNA, TRBP – transactivating response RNA binding protein. Image adapted from Hu et al.<sup>33</sup>

In brief, RNA endonucleases (belonging to the RNase III-type family of proteins, like the Dicer) bind to long double-stranded RNA molecules and cleave them to short, typically 21-25 nucleotide long, RNA fragments called siRNA, in an adenosine triphosphate(ATP)-dependent process.<sup>59</sup> Next, siRNA joins the RISC, which is a ribonucleoprotein, and serves as template for recognition of homologous target mRNA and its enzymatic degradation by the RISC argonaute protein (AGO).<sup>33,60,61</sup> miRNA-mediated RNAi shares a common pathway with

siRNA-mediated RNAi, however, biogenesis of miRNA is slightly different than the one of siRNA. Mature miRNA derives from hairpin-containing primary miRNA (pri-miRNA) which is enzymatically processed (hairpin cleavage by the Drosha/DGCR8 complex) in the cell nucleus into precursor miRNA (pre-miRNA) and in that form exported (by the Exportin 5/RAN-GTP complex) into the cytoplasm for further processing by the Dicer/TARBP-2 complex (cleavage of pre-miRNA terminal loop), which results in the formation of approximately 22 nucleotide long mature miRNA duplexes which one strand interacts further with the RISC for RNAi.<sup>33,62,63</sup>

The therapeutic application of siRNA in the treatment of diseases is a dynamically developing branch of biomedicine. After two decades, since the discovery of RNAi by Fire and Mello, the US Food and Drug Administration and the European Commission approved the first commercial RNAi therapeutic (patisiran, ONPATRO™), based on siRNA encapsulated in lipid nanoparticles, for a targeted delivery into hepatocytes in gene therapy of polyneuropathy caused by hereditary transthyretin-mediated amyloidosis in adults. Another example of an already approved and commercially available therapeutic siRNA is GIVLAARI™ (givosiran) which is applied in gene therapy of adults with acute hepatic porphyria. This is a modified siRNA which does not require a nanocarrier for intracellular delivery, however, it requires conjugation with a ligand for a targeted delivery into hepatocytes. Further therapeutic siRNA already await final approval after completing clinical trials.<sup>33,64-67</sup>

### **2.1.6. Host immune response and the role of NF- $\kappa$ B in inflammation**

Innate and adaptive immunity are building units of the immune system. The first, referred as non-specific, is the body's frontline defense system which prevents pathogen widespread in tissues and reacts rapidly after threat recognition. Innate immunity is a general system without memory of previous responses, composed of body's anatomical barriers (skin and mucosa) and their secretion, immune cells (macrophages, dendritic cells, granulocytes), antimicrobial peptides, soluble mediators and cell receptors.<sup>68-70</sup> The second, referred as specific, is based on the activity of two main immune response mechanisms, *i.e.*, humoral and cellular.

Humoral immunity is antibody-mediated and B-cells (lymphocytes), activated by helper T-cells, play here the key role. After differentiation into plasma cells, B-cells produce antibodies in the bone marrow, in response to the presence of specific antigens. Antibodies bind to antigens and neutralize them, or lead to their lysis or phagocytosis. Humoral immunity targets antigens which are circulating in the extracellular space of infected cells.<sup>46,71,72</sup> Cellular immunity depends on the activity of T-cells (lymphocytes) and is a direct interaction between the immune

cells and the already infected host cells. The latter use class I major histocompatibility complex (MHC-I) proteins to display on their surface foreign antigens (*e.g.*, peptides of viral origin) from within the cell and thus mark themselves as infected. Circulating in the blood stream, cytotoxic T-cells bind to MHC-I molecules and after a positive receptor-mediated recognition of foreign antigens induce, by release of cytotoxic mediators, apoptosis (programmed cell death) of the infected cell and so prevent virus survival and spread.<sup>73,74</sup> In contrast to innate immunity, the adaptive immunity is pathogen-specific and typically provides a long-term protection based on the immune memory of B- and T-cells. After elimination of infection, for a long time, in the bloodstream remain antigen-specific memory B-cells and T-cells which, in case of re-exposure to the same antigen, can immediately start production of specific antibodies or be quickly converted into effector T-cells, respectively. This guarantees a rapid and sufficient secondary immune response.<sup>75</sup>

Inflammation is the biological reaction of the host immune system to infectious (viruses, microbial pathogens) and non-infectious (physical, chemical, biological, psychological) factors.<sup>76</sup> Plasma proteins and immune cells are rapidly recruited, in response to host infection or irritation, to remove the immunostimulus and initiate tissue healing. Inflammation may be acute (characterized by a quick reaction of immune cells at the site of injury, and quick healing and restoration of tissue homeostasis) or chronic (long-lasting inflammation characterized by prolonged expression of inflammatory mediators and constant stimulation of immune cells). Although inflammation is an evolutionary-conserved defense mechanism, abnormalities in its functioning and regulation lead to a systemic imbalance between secretion of pro- and anti-inflammatory cytokines and, especially if inflammation is chronic, is part of pathogenesis of various disorders, including cardiovascular and bowel diseases, diabetes, arthritis and cancer.<sup>69,76,77</sup>

Inflammatory pathways play an important role in the course of diseases. Stimuli, like cytokines: interleukin(IL)-1 $\beta$  (IL-1 $\beta$ ), IL-6, TNF- $\alpha$  and interferon gamma (INF- $\gamma$ ), and microbial virulence factors, like lipopolysaccharide (LPS, cell wall compound of Gram-negative bacteria) and teichoic/lipoteichoic/teichuronic acid (cell wall compounds of Gram-positive bacteria), interact with cell surface receptors, *e.g.*, Toll-like receptors, and receptors for IL-1 $\beta$ , IL-6 and TNF- $\alpha$  recognition. Interaction with the receptors triggers intracellular signaling cascades and leads to regulation of the inflammatory response. Examples of such signaling pathways are mitogen-activated protein kinase (MAPK), NF- $\kappa$ B, and Janus kinase and signal transducer and activator of transcription (JAK-STAT) system cascades.<sup>76,78,79</sup>

NF- $\kappa$ B is a family of transcription factors involved in various important biological processes, including lymphoid organogenesis, bone metabolism, and immune cell survival, activation and maturation. NF- $\kappa$ B is also involved in cellular response to environmental stressors. Furthermore, NF- $\kappa$ B regulates the innate and adaptive immunity, is the key mediator in inflammatory response and maintains immune homeostasis by controlling expression levels of pro- and anti-inflammatory agents. Abnormal regulation of NF- $\kappa$ B is connected with a variety of diseases, including autoimmune disorders, inflammatory diseases, septic shock and cancer.<sup>69,76,80,81</sup>

The NF- $\kappa$ B family is composed of five structurally similar proteins: NF- $\kappa$ B1 (p50/p105), NF- $\kappa$ B2 (p52/p100), RelA (p65), RelB and c-Rel (Rel). NF- $\kappa$ B can be activated either in a classical (canonical) or alternative (non-canonical) way (**Figure 8**). Under physiological conditions, the inhibitor  $\kappa$ B alpha (I $\kappa$ B $\alpha$ ) protein binds to NF- $\kappa$ B heterodimers p50-p65/c-Rel (in the canonical pathway) and p52-RelB (in the non-canonical pathway) and keep them inactive. In canonical signaling, after receiving a stimulus from general innate and adaptive immunoreceptors, like cytokine receptors (for interleukins), pattern-recognition receptors, TNF receptor (TNFR) superfamily members, T-cell receptor or B-cell receptor, growth factor- $\beta$ -activated kinase 1 (Tak1) activates the trimeric I $\kappa$ B kinase (IKK) complex. It consists of two catalytic subunits (IKK $\alpha$ , IKK $\beta$ ) and a regulatory subunit (IKK $\gamma$ ), and is responsible for site-specific IKK $\beta$ -phosphorylation of I $\kappa$ B $\alpha$  (at two N-terminal serines) which results in ubiquitin-dependent degradation of I $\kappa$ B $\alpha$  in the proteasome. Released NF- $\kappa$ B p50-p65/c-Rel heterodimers can be rapidly translocated from the cytoplasm to the cell nucleus where they bind specifically to DNA, and regulate gene transcription and expression of inflammatory cytokines. To prevent overexpression of NF- $\kappa$ B, the latter induces expression of its own silencer I $\kappa$ B $\alpha$  which terminates transcriptional activity of NF- $\kappa$ B. This control mechanism is based on the principle of a regulatory loop.<sup>69,80-84</sup> Non-canonical signaling is much more specific than canonical and can be activated by immunostimuli received from a subset of TNFR superfamily members, *i.e.*, lymphotoxin  $\beta$  receptor (LT $\beta$ R), B-cell activating factor receptor (BAFFR) and Cluster of Differentiation 40 receptor (CD40R), as well as receptor activator for NF- $\kappa$ B (RANK). The main activator of this pathway is NF- $\kappa$ B-inducing kinase (NIK) which, together with the IKK $\alpha$  homodimer, forms a complex responsible for phosphorylation-induced proteasomal processing (degradation of C-terminal I $\kappa$ B-like structure) of the p100 precursor protein into mature p52 protein. The latter forms RelB heterodimers (p52-RelB) which, after nuclear translocation, bind specifically to DNA and regulate gene transcription. Canonical NF- $\kappa$ B activation is involved in

most immune responses (innate and adaptive), whereas non-canonical NF- $\kappa$ B activation seems to support the canonical pathway in adaptive immune response.<sup>69,80-82</sup>

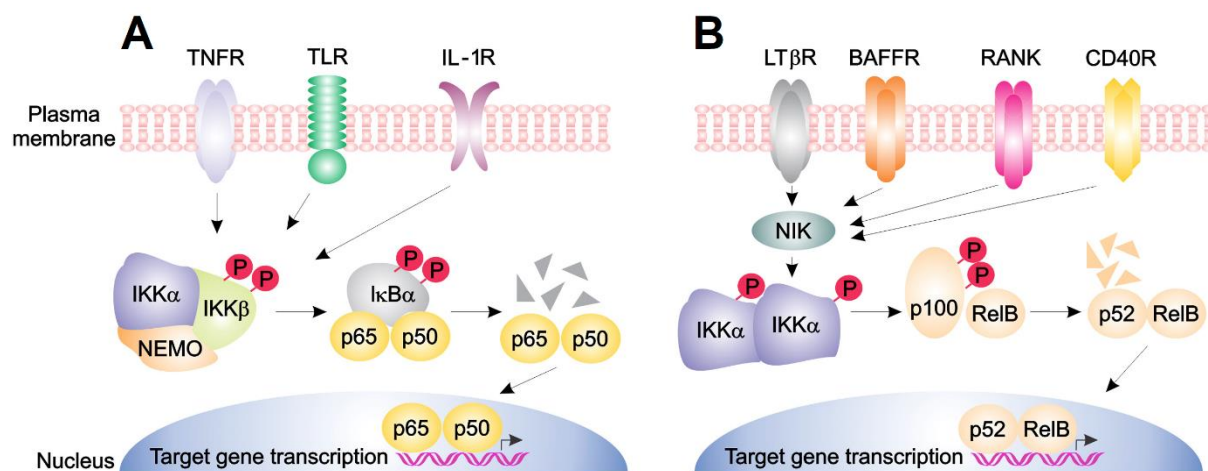


**Figure 8.** Canonical (A) and non-canonical (B) cascades of NF- $\kappa$ B activation (description in text). IL-1R – interleukin-1 receptor, NEMO – NF- $\kappa$ B essential modulator (or IKK $\gamma$  regulatory subunit), p – protein, P – phosphate, TLR – Toll-like receptor. p50, p100/p52, p65 and RelB are functional proteins of NF- $\kappa$ B, which form transcriptionally active heterodimers p50-p65 or p52-RelB. Image adapted and modified from Espín-Palazón and Traver.<sup>84</sup>

## 2.2. Project II – Chemistry of fossilized proboscidean enamel

### 2.2.1. Teeth in the life of vertebrates

Teeth play a fundamental role in the life of vertebrates, participating in trophic (related with food consumption) and non-trophic interactions with the environment. Beside their main role in cutting, shredding and mastication of food, as gates to the digestive system and its important part, teeth may play a role in animal movement, environmental modifications, and a variety of non-antagonistic and antagonistic interactions with other animals, as well as can be used for the sensing of the environment. Interestingly, the non-trophic, not trophic, functions of teeth shape their huge diversity observed in nature.<sup>85</sup> Anatomically, teeth are made of two main chemically and mechanically diverse parts. The first, called dentin, is a softer bone-like material in the tooth interior which coats the sensitive pulp filled with a network of nerves and blood vessels. The second, called enamel, is a hard and highly-mineralized material of the tooth exterior. Enamel is also known to be the hardest biological material found in nature. Among mineralized tooth tissues, cement can be also distinguished. It is softer than dentin and similar to bone, however, avascular and covers the roots of teeth (**Figure 9**).<sup>86,87</sup>

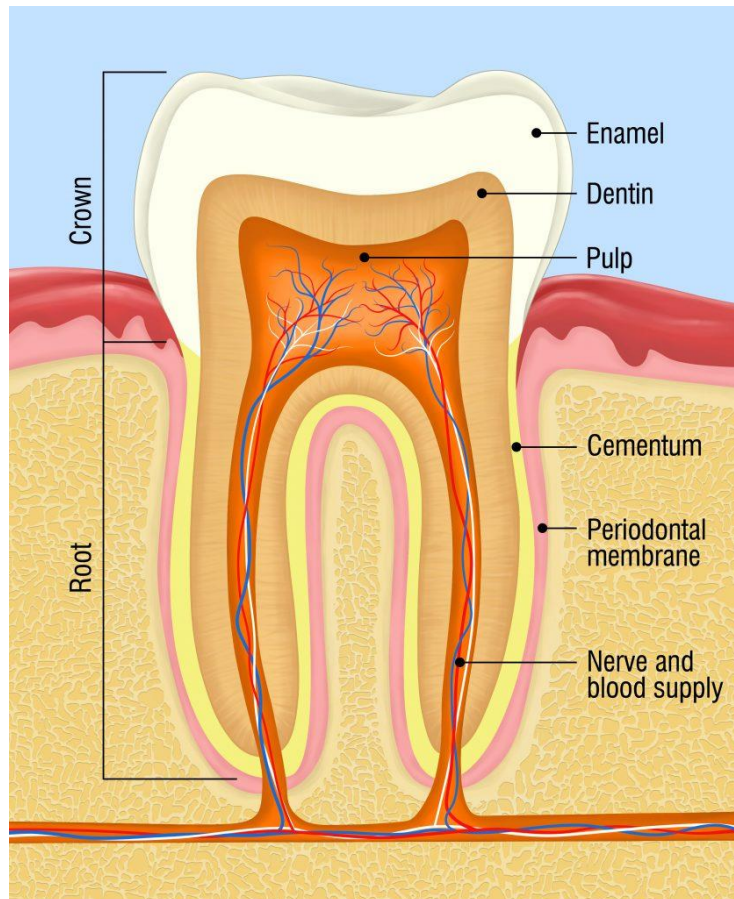


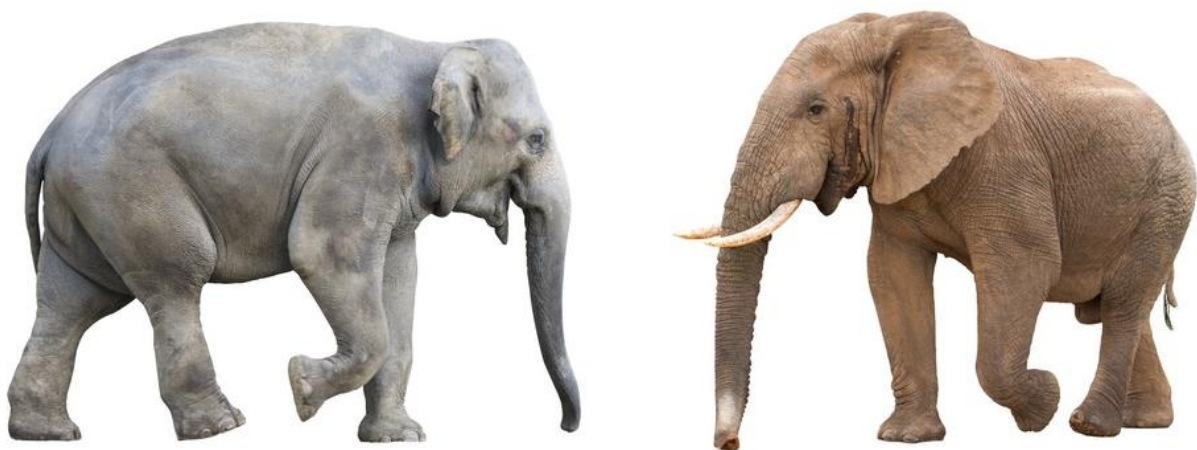
**Figure 9.** General structure of the tooth. Two main regions can be distinguished: the crown (upper part, above the gum) and the root (lower part, below the gum). The part of the tooth between the crown and the root is called the tooth neck. The tooth is anchored in the alveolar bone of the jaw with its root, surrounded by the periodontal membrane which is a soft connective tissue that stabilizes the tooth and relieves pressure generated during mastication. Furthermore, it constitutes a specific microenvironment for inflammatory reactions and is involved in mechanically-stimulated bone remodeling processes.<sup>88</sup> Figure adapted from [www.baysmile.com](http://www.baysmile.com).

The enamel consists mostly of CaP (~96 wt%), water (~3 wt%) and organic matter (~1 wt%). In comparison, dentin is made of ~70-75% CaP, ~5-10% water and ~20% of organic matter, whereas cement is composed of ~40-50% CaP, ~20-25% water and ~30-35% of organic matter.<sup>87,89,90</sup> A very high mineralization degree makes the enamel resistant to abrasive stress and 3-fold tougher than geological apatite.<sup>91</sup> Carbonated hydroxyapatite  $\text{Ca}_{10}(\text{PO}_4, \text{CO}_3)_6(\text{OH})_2$  is the main tooth mineral found in vertebrates, with some structural carbonate substitutions of the phosphate ions.<sup>92-94</sup> The crystallographic structure of bioapatite is based on the hydroxyapatite structure. Bone and teeth bioapatite typically contains ~3-7 wt% of carbonate.<sup>89</sup>

Interestingly, teeth of cartilaginous fish (*e.g.*, sharks and rays) consist of mineral fluorapatite  $\text{Ca}_{10}(\text{PO}_4)_6\text{F}_2$  instead of hydroxyapatite (found in teeth of other vertebrates).<sup>93,95-98</sup> Structurally, enamel can be characterized by tiny pore space, presence of elongated hydroxyapatite crystallites ( $>1 \mu\text{m}$ ), which comprise  $\sim 85\%$  of its volume, and a high level of organization, due to the prismatic microstructure. In contrast, dentin is porous, with short hydroxyapatite crystallites ( $<0.1 \mu\text{m}$ ), which comprise  $\sim 50\%$  of its volume, and lacks a prismatic organization. Dentin is less mineralized than enamel, has a larger surface area and demonstrates a higher carbonate content, which makes it more susceptible to dissolution under acidic conditions, when compared to the enamel.<sup>99,100</sup> Cement originates from uncalcified dense collagen fibril bundles which undergo, over the time, mineralization by hydroxyapatite crystals.<sup>101</sup> The very high level of mineralization preserves the prismatic microstructure of enamel which is resistant to geochemical alterations and remains almost unchanged during fossilization. This makes enamel an excellent research material for paleontological studies.<sup>102</sup>

### 2.2.2. Elephant taxonomy and the evolution of *Proboscidea*

Nowadays, *Proboscidea* are represented only by three elephant species, *i.e.*, the African bush elephant (*Loxodonta africana*), the African forest elephant (*L. cyclotis*) and the Asian elephant (*Elephas maximus*). The latter can be further divided into several subspecies, including *E. m. indicus*, *E. m. maximus*, *E. m. sumatranus* and *E. m. borneensis*. The nomenclature in elephant taxonomy is strictly related with the animal geographic distribution.<sup>103,104</sup> There are several main anatomic differences between recent elephants (**Figure 10**).



---

**Figure 10.** The Asian elephant (**left**) and the African elephant (**right**). The anatomic differences between recent elephants include, among others, body size, skull shape, and limb and trunk anatomy. Figure adapted from [www.assets.rbl.ms](http://www.assets.rbl.ms).

Typically, *Loxodonta* sp. has a more massive body, larger ears and a more flexible trunk with an additional second lower “finger”, when compared to *E. maximus*. Furthermore, representatives of these genera differ also in skull shape and the number of foot toenails.<sup>105-107</sup> Members of the family *Elephantidae* are the only remaining representatives of the large and well-developed past order *Proboscidea* which originated in Africa-Arabia in Early Paleocene (~65 Ma) and diversified since Eocene (~56-34 Ma).<sup>108</sup> However, the earliest ancestors of recent elephants were not much larger than a middle-sized dog and anatomically they did not resemble the recent elephants (**Figure 11**). Therefore, in Paleogene (~65-23 Ma) this group of animals did not play a prominent role in ecosystems of that time. Gigantism, development of a long and flexible trunk and differentiation of the dentition system (tusks, molars) were features which evolved over millions of years, as environmental adaptation, after elephant ancestors migrated to other continents and inhabited new territories.<sup>109</sup> Some of the early proboscideans from Africa include genera *Eritherium* from Paleocene and *Phosphatherium* from Early Eocene.<sup>110-112</sup> The Fayum Basin of Egypt has yielded other early *Proboscidea*, including *Moeritherium* sp. and *Palaeomastodon* sp.

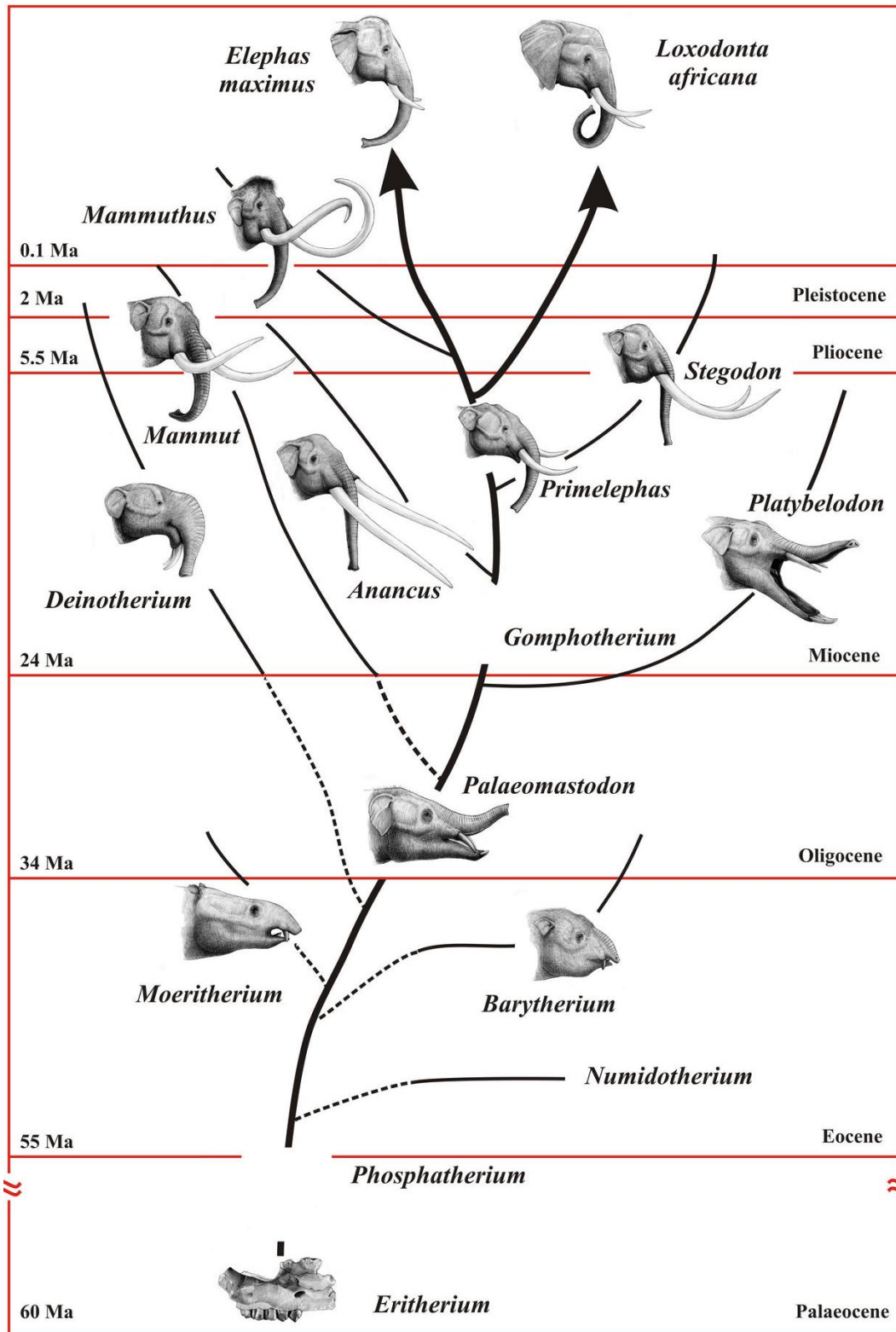


**Figure 11.** The cladogram of Proboscidea. Main evolutionary trends observed in proboscideans were related with an increase in body and tusk size, trunk elongation and decrease in tusk number from four (two upper and two lower) to only two (upper) tusks.<sup>113</sup> Drawings by Vladimir Nikolov based on Shoshani.<sup>113</sup> Figure adapted from [www.deviantart.com](http://www.deviantart.com).

*Proboscidea* are close relatives to aquatic *Sirenia* (dugongs and manatees) and terrestrial *Hyracoidea* (rock hyraxes). Taxonomic kinship between these orders has been proved by comparative anatomic analyses, genetic and immunologic studies, as well as by the fossil records.<sup>109,114,115</sup> Proboscideans were also key herbivores in Neogene ecosystems (~23-2.6 Ma) as several large-bodied elephant species occupied the landscape.<sup>116</sup> In Early Miocene (~23 Ma), due to plate tectonics, a terrestrial connection (known as “*Gomphotherium* Land Bridge”) between Africa-Arabia and Eurasia was formed and led to faunal exchange between previously isolated by the Tethys Sea continents.<sup>117</sup> As a consequence, the early proboscidean genera *Prodeinotherium* (~23 Ma) and *Gomphotherium* (~22 Ma) could enter Eurasia and reach the Indian subcontinent.<sup>115,118</sup> This was also the major mammal dispersion event in the Cenozoic Era and has been named as “Proboscidean Datum Event”.<sup>119</sup> The endemic evolution of gomphotheres in Asia likely led to the emergence of genera, such as *Anancus* and *Stegodon*.<sup>115</sup> Pliocene-Pleistocene (~5.3-0.01 Ma) waves of African immigrant elephants included genera *Elephas* and *Palaeoloxodon* (**Figure 12**).

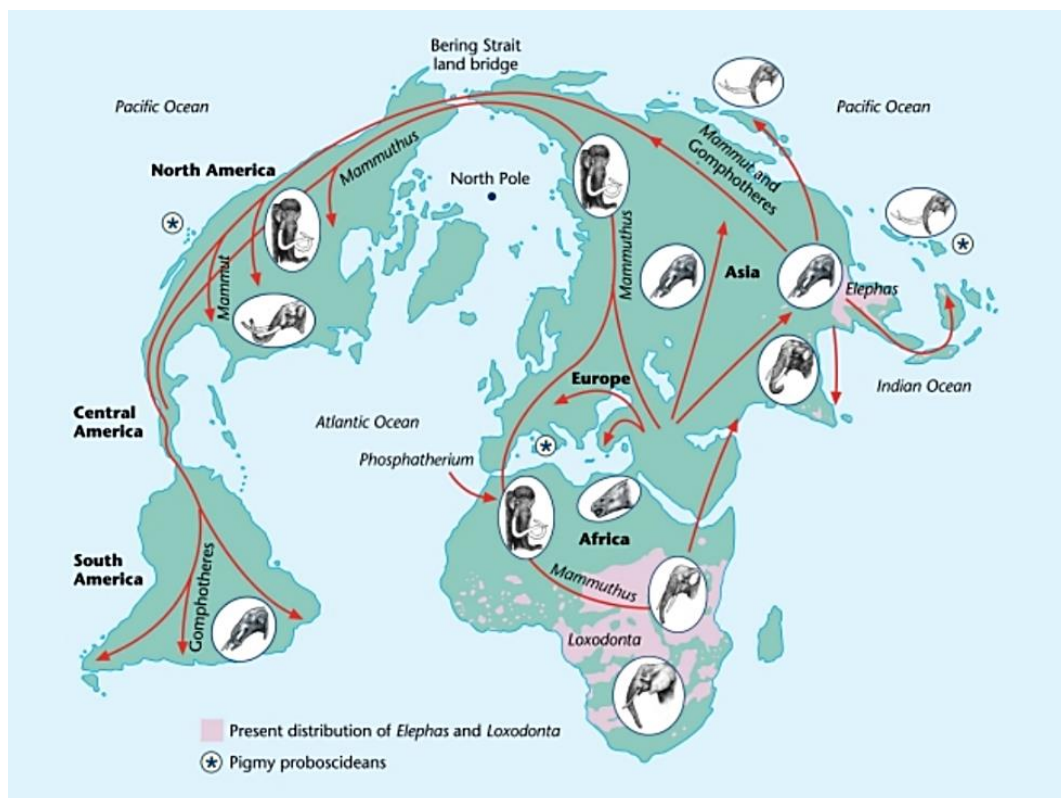


**Figure 12.** Dispersal patterns of Proboscidea. Their remains were found on all continents except Antarctica and Australia (thus not depicted on the map). Places where fossils of pigmy proboscideans were discovered are marked on the map with stars and the pink regions represent localization of the recent elephants *Loxodonta* sp. and *Elephas* sp.<sup>113</sup> Remains of

*pigmy elephants were found, so far, in the Mediterranean Basin and Indonesia, remains of pigmy mammoths on Californian Channel Islands, and the fossils of dwarfed Stegodon sp. were found in Southeast Asia.*<sup>120</sup> *Figure adapted from Shoshani.*<sup>113</sup>

### **2.2.3. The elephant dentition system**

Extinct and extant elephants share a specialized dentition system based on massive grinding teeth (molars) localized in cheeks on each side of the jaw. Typically, one or two of them are simultaneously exposed and used for chewing. When the molars, due to food mastication, are worn down they crumble into pieces and either fall out or are swallowed and excreted by the animal, and become replaced with new ones, which erupt from behind of the worn teeth. Each new molar is larger than the previous one. Elephant teeth develop not in a typical, in most animals, direction from the top to the bottom but in the back of the jaw and progressively move forward. This makes the elephant dentition system and the sequential way of molar replacement unique among mammals.<sup>106,121</sup> During the whole life an elephant typically develops 24 molar teeth, with 6 teeth in each jaw arcade. Usually, molar sets appear in several year time intervals with the last and also longest lasting 6<sup>th</sup> set of molars at the animal's age of ~30-40 years.<sup>121</sup> For mature elephants, which already lost their last molars, it becomes very difficult to chew and digest food and they typically die, if not from predators or poaching, of starvation and malnutrition. During food chewing by elephants a preferential jaw movement is forward-backward, not side-to-side. Beside massive molars, elephants possess also tusks which develop from elongated upper incisors and grow throughout the life of the elephant.<sup>122</sup> Elephants use tusks, among others, as weapon, to get food (*e.g.*, strip tree bark or dig up roots), dig holes for water and to lift objects. Males and females of the African elephant possess massive tusks similar in size, whereas in Asian elephants only males have massive tusks, and the females typically have either small vestigial tusks (called tushes) or no tusks at all.<sup>121</sup> Depending on the type of consumed food, elephant teeth evolved and adapted accordingly. Differences between the African and Asian elephants in the enamel profile of molar masticatory surface can be also observed. Molar teeth are made of enamel and dentin organized in lamellae, and cement (which fills up the space between them). Molars of the African elephants have up to 10 transverse lozenge-shaped enamel loops (on the tooth occlusal surface), which are thicker and broader than loops of the Asian elephant. In contrast, enamel loops of the Asian elephant are more numerous (up to 20 loops per molar) with a specific shape of flat parallel circles and occurrence of enamel folding (**Figure 13**).<sup>106,121</sup>

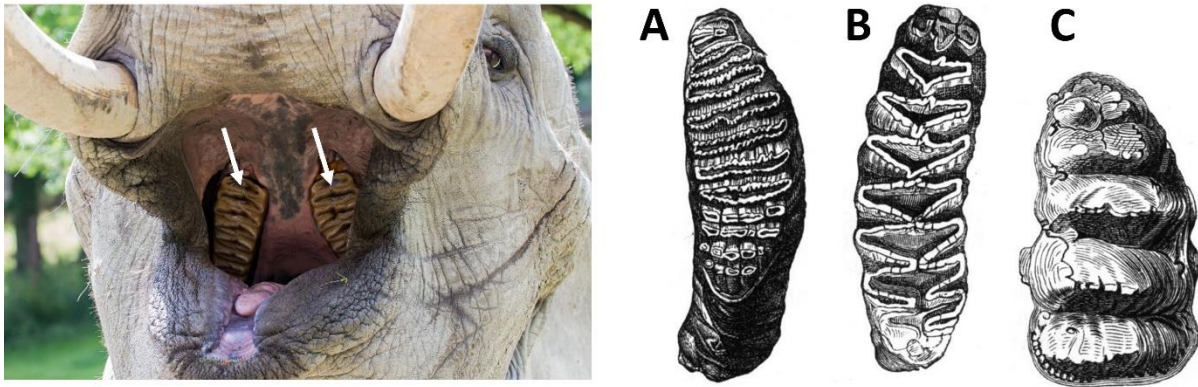


**Figure 13.** Localization of the upper molars in *Loxodonta* sp. (the teeth are indicated with arrows) (**left**). Comparison of the abrasive surface profiles of lower molars in extant *E. maximus* (**A**) and *L. africana* (**B**), and extinct *Mastodon giganteum* (**C**) (**right**). Genus-specific enamel loop patterns are clearly distinguishable on the surface of molars. The image of the elephant and drawings of elephant molars were adapted from [www.africafreak.com](http://www.africafreak.com) and [www.creationwiki.org](http://www.creationwiki.org), respectively.

The African forest elephants are mainly browsers and their diet is based on consumption of leaves, shoots and fruit from trees and bushes (“high-feeding” dietary profile). The Asian elephants are mainly grazers, which means that they typically eat grass, bark and shrubs (“low-feeding” dietary profile).<sup>123</sup> The African bush elephants combine these both dietary profiles, with varying proportions influenced by geographical, environmental and seasonal factors.<sup>124</sup> The diet of browsers can be characterized by higher nutrient and lower fiber concentrations, when compared to the diet of grazers. Additionally, grasses contain much silica ( $\text{SiO}_2$ ), which is abrasive and efficiently wears down the teeth of herbivores.<sup>125</sup> The wear type of the molar occlusal surface is a marker of the animal diet. Different types of food leave specific dental microwear “footprints” composed of abrasive damages, like scratches and pitches. Their proportion, as well as length and orientation of the first, and depth of the second, provide valuable information about the animal’s diet.<sup>126</sup>

#### 2.2.4. Proboscidean enamel microstructure

In all toothed animals the enamel is secreted by ameloblasts. These are cells which derive from the oral epithelium tissue of ectodermal origin and are present only during tooth development.<sup>127</sup> Enamel usually demonstrates a prismatic microstructure, which can be characterized by different organization patterns of the prisms (cylindrical bundles of crystallites), however, prismless enamel (PLE) can be also found in nature. PLE is also the

simplest and evolutionary the oldest type of enamel. It is present in teeth of fish, amphibians and reptiles, in which the physiological role of dentition system is limited to catching, piercing and holding prey (with no contact between the opposing jaws). In mammals, the enamel demonstrates already an advanced prismatic microstructure, as the dentition system is involved in food mastication which required enamel adaptation towards increased resistance to abrasive stress.<sup>128,129</sup>

In proboscideans, several types of enamel have been described, including prismatic and PLE enamel. Among prismatic enamel, three different microstructural types can be distinguished: 3D enamel (3DE), Hunter-Schreger-Bands (HSB) and radial enamel (RE). 3DE is irregular with no precise microstructural units. It is made of parallel prisms that come out of the enamel-dentin junction (EDJ) and tend to form bundles of various thickness (~15-20 prisms) which run in different directions. HSB is composed of parallel prisms which form layers of various thickness at an angle to prisms in adjacent layers. In RE, parallel prisms are radially directed from the EDJ. Proboscidean PLE consists of parallel apatite crystallites. HSB, RE and PLE are commonly found in placental mammals, whereas 3DE is typical for proboscideans.<sup>130</sup> The term “schmelzmuster” describes distribution of various enamel types within tooth.<sup>131</sup> There are three main categories of prism cross-section patterns based on prism shape and packing organization. Prism pattern 1 (PP1) refers to prisms with complete boundaries and arranged horizontally in relation to the tooth growth axis. Prism pattern 2 (PP2) shows arc-shaped prism cross-section with prisms arranged in vertical rows separated by inter row sheets. Prism pattern 3 (PP3) are arc-shaped prisms arranged in horizontal rows (**Figure 14**).<sup>132,133</sup> Most proboscideans show PP3, which in turn basically consists of three types of pattern motifs: keyhole, fan-shaped and ginkgo-leaf.

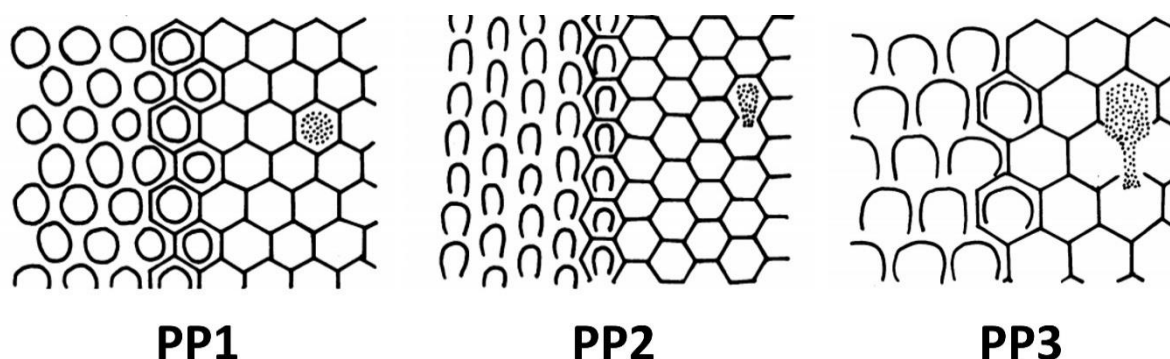


**Figure 14.** Schematic representation of prism patterns in mammalian enamel. Each diagram shows prism boundaries or sheaths, which represent planes of abrupt change in crystallite orientation within the enamel (*left*); secretory territories of ameloblasts (*right*); and

relationship of prism boundaries/sheaths to secretory territories (*middle*). The stippling represents areas which are defined as prisms in various patterns. **PP1** is predominant in the enamel of members of the infraorder Cetacea (Odontoceti) and the orders Insectivora, Chiroptera and Sirenia. **PP2** can be found in the enamel of representatives of the clade Ungulata, the infraclass Marsupialia and in primates. **PP3** typically occurs in the enamel of members of the orders Carnivora and Proboscidea, and in primates. Figure adapted and modified from Vrba and Grine.<sup>134</sup>

### 2.2.5. Evolution of proboscidean enamel and dentition system

Physiological function of the tooth determines biomechanical properties of the enamel and is the driving force for enamel adaptation and evolution.<sup>135-138</sup> For example, prism decussation in 3DE and HSB increases enamel resistance to breakage, whereas perpendicular orientation of prisms to the masticatory surface of the tooth in RE enhances enamel resistance to abrasive wear. In dental evolution of proboscidean molars, two main pathways can be distinguished. First, a general enamel thinning trend combined with tissue differentiation was observed.<sup>139</sup> Second, early *Proboscidea* had low-crowned molars (brachyodont) with enamel organized in a series of rounded cusps on the masticatory surface of the tooth. Over the time, the cusps fused into transverse enamel loops generating a lamellar structure of the molars (can be seen in **Figure 13**, in the profiles of molar abrasive surfaces of extinct *Mastodon* sp., and recent *Loxodonta* sp. and *Elephas* sp.).<sup>140</sup> The number of lamellae in molars increased with the time and led to the formation of high-crowned grinding teeth in late *Proboscidea*.<sup>123,141</sup> Hypsodonty evolution of molars from low-crowned (“mastodont-like”) to high-crowned (“elephant-like”) was an evolutionary-driven adaptation to the increasing role of abrasive food (particularly grass) in the diet of proboscideans.<sup>116</sup> This was due to climate change, which led to a shift in vegetation in Late Miocene from low- to high-abrasiveness and a constantly increasing role of silica-rich food in the diet of proboscideans.<sup>102,108,142-145</sup> On the Indian subcontinent such a dietary shift in proboscideans was observed around 8-7 Ma.<sup>146</sup>

It has to be mentioned, that not only molars but also tusks and tushes underwent different evolutionary changes and their variants differing in number, size, microstructure and composition could be found among extinct proboscideans.<sup>140,147</sup> It is believed that the negative (natural) selection, after a drastic decrease of global temperatures and humidity related with “Miocene Climatic Optimum Event” (~26-15 Ma), led to loss of the enamel (present only in juvenile animals in a small amount and for a short period of life) in the incisors and loss of their lower pair in *Elephantimorpha*. Among proboscideans, only deinotheres possessed lower

incisors and had no upper ones.<sup>148</sup> Tusks are composed mostly of dentin, demonstrating a very specific microstructure of the Schreger pattern, which is very important for paleontologists in taxonomic studies on extinct and extant proboscideans.<sup>149,150</sup> Remains of gomphothere *Cuvieronius* and *Rhynchotherium* found in the Americas demonstrate a kind of “recovery” of the lower tusches, however, it is believed to be a unique example of atavism (feature lost through evolutionary changes in previous generations) in proboscideans, as these animals lived on the Great Plains of North America in Late Miocene, where climate became locally warmer and more humid. Preservation of one pair of incisors was probably evolutionary beneficial to maintain body thermal energy, while living in a cold and dry environment.<sup>148</sup>

It has to be mentioned, that in extant elephants in Africa and Asia, a continuous trend of tusk reduction or even loss has been observed throughout the last years. However, this is not evolutionary-driven but in response to poaching pressure for ivory harvesting, which is an unnatural selection and driving mechanism of contemporary evolution.<sup>151</sup> Recent data for African elephants show a significant decrease of approximately 22% and 37% of mean tusk lengths in males and females, respectively, observed over the last 50 years.<sup>152</sup> Based on data published by National Geographic Society in 2018 on tusklessness among the African elephant females, poaching pressure reduced the occurrence of tusks in female elephants even 13-fold, when compared to animals living in unpoached elephant populations [www.nationalgeographic.com].

## **2.3. Project III – Interactions between ultrasmall gold nanoparticles and bacteria**

### **2.3.1. Ultrasmall gold nanoparticles: synthesis and properties**

AuNPs demonstrate a broad range of potential applications in biomedicine, due to their unique size- and shape-related optical properties (plasmon resonance, autofluorescence, photoluminescence), good biocompatibility and minor toxicity to cells.<sup>153-155</sup> A common method to synthesize AuNPs is reduction of chloroauric acid ( $\text{HAuCl}_4$ ), which is the gold precursor, in a liquid-phase method. In the presence of reducing agents, like sodium citrate ( $\text{Na}_3\text{C}_6\text{H}_5\text{O}_7$ ) or sodium borohydride ( $\text{NaBH}_4$ ), during reduction of the precursor, the concentration of gold atoms in solution increases continuously until the critical supersaturation level is exceeded. Next, the process of nucleation starts, where gold atoms gather and form crystal nuclei. This leads to a decrease of gold atom concentration in solution, below the critical supersaturation level, and stops production of new crystal nuclei. The already synthesized nuclei grow in size until saturation level in solution is reached and finally formation of nanometer-sized gold particles is completed (**Figure 15**). To prevent nanoparticle

agglomeration, the use of stabilizing (capping) agents is recommended.<sup>156-158</sup> The latter may influence also biological properties of nanoparticles. For example, Zhou *et al.* demonstrated that citrate-stabilized AuNPs (20-30 nm) were less inhibitory against Gram-negative *E. coli* and Gram-positive bacillus Calmette-Guérin (a mycobacterium) than similar in size nanoparticles stabilized with poly-allylamine hydrochloride (PAH). This is due to the fact that PAH is strongly bound to nanoparticles and better prevents their aggregation than weakly bound citrate.<sup>159</sup> Above described is an example of a “bottom-up” approach, based on the phenomenon of molecular self-assembly, where nanomaterials are final products of the assembly of atoms derived from reduction of precursor ions.<sup>160,161</sup>

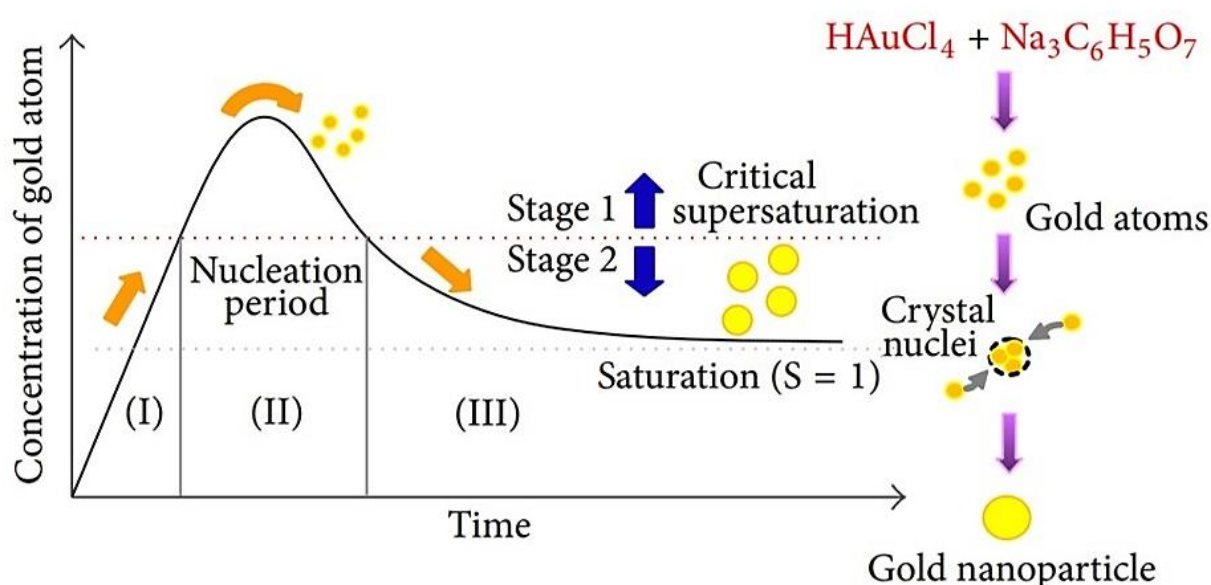


**Figure 15.** Schematic representation of the mechanism of AuNP formation by reduction in a liquid-phase synthesis. The method includes three major phases: (I) precipitation of gold atoms, (II) formation of gold nuclei and (III) growth of crystal nuclei until AuNPs are formed. Figure adapted and modified from Liu *et al.*<sup>157</sup>

The synthesis of AuNPs shows many advantages. It is relatively quick, allows to receive a high yield of good quality and stable nanoparticle product and gives the possibility to control size (1-50 nm) and shape (*e.g.*, rods, shells, spheres, stars, triangles) of the nanoparticles.<sup>153,157,158</sup> Furthermore, AuNPs may form stable chemical bonds with molecules containing N- (*e.g.*, amine;  $-\text{NH}_2$ ) and S- (*e.g.*, thiol;  $-\text{SH}$ ) functional groups.<sup>162</sup> This property taken together with a high surface area to volume ratio, enables decoration of AuNPs with a number of ligands.<sup>155,158</sup> Modifications of the surface chemistry of AuNPs make them applicable in sensing, image

enhancement, cell targeting, and controlled drug and gene delivery into cells.<sup>158,163,164</sup> Ultrasmall AuNPs (<2 nm in core diameter) demonstrate excellent cell penetration possibilities, even the ability to cross nuclear pores and enter the cell nucleus.<sup>158</sup> The ultrasmall size of gold nanoclusters determines a “molecule-like”, instead of typical for larger particles “size-dependent”, mode of action which influences their high biological reactivity in cells.<sup>165</sup> Size, shape and dispersion state are key parameters determining nanoparticle cytotoxicity. For instance, sphere- and rod-shaped AuNPs are usually reported as more harmful to cells than AuNPs with morphologies such as stars, flowers and prisms.<sup>166,167</sup> Nanoparticles with the size >10 nm are also less cytotoxic than the ultrasmall ones with excellent cell penetration abilities. Biological response to nanoparticle stress is cell-specific and can vary in different cell lines.<sup>158</sup>

### 2.3.2. Structure of the bacterial cell envelope

The cell is the most basic structural and functional unit of living organisms. Based on the organization of the cell structure, organisms can be divided into unicellular, called prokaryotes (*Archaea*, bacteria), and multicellular, called eukaryotes (protists, fungi, plants, animals). Bacterial cells differ in structure, when compared to eukaryotic cells (**Figure 16**).

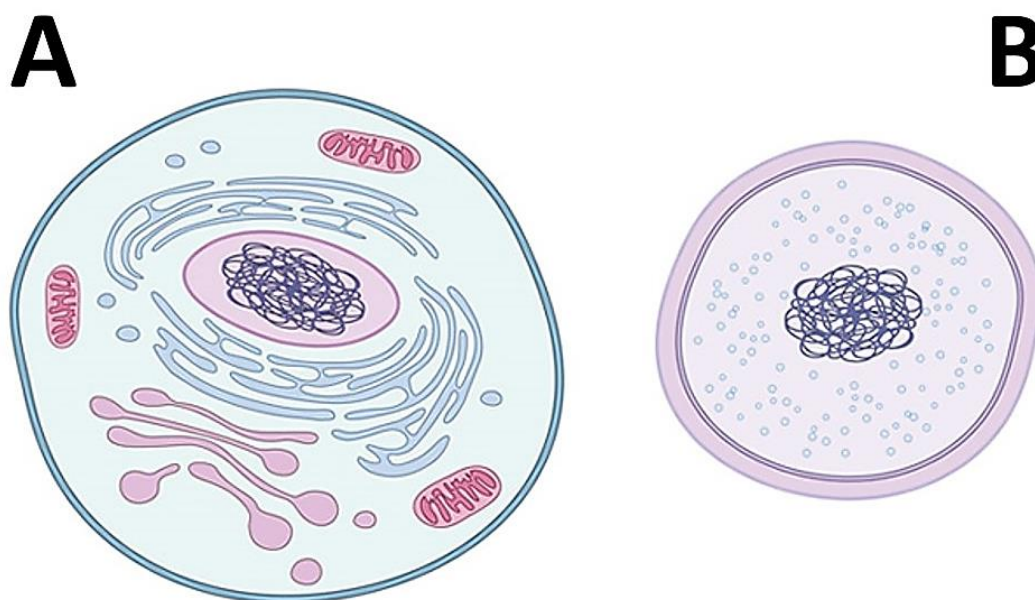


**Figure 16.** Simplified comparison of a representative eukaryotic (A) and prokaryotic (B) cell, with a main focus on differences in cell structure and complexity, related with the development of an advanced membrane network system within the cell and organization of the genome. Figure adapted and modified from Fuerst.<sup>168</sup>

For example, the latter possess a nucleus fully isolated from the cell cytoplasm (which contains the whole cell genome, despite mitochondrial DNA) and a complex endomembrane compartment system in the cell cytoplasm, which allows vital metabolic processes to run parallel, due to functional differentiation of the intracellular compartments.<sup>169</sup> Bacteria lack these structures, their genetic information is dispersed in the cytoplasm in form of a free circular nucleoid and their metabolic processes run in one general cell compartment containing all vital enzymes, however, they evolved a complex cell envelope, composed of the cell wall and the cell membrane. It regulates the interactions between bacteria and the environment, ensures survival of bacteria under unfavorable conditions, controls passage of nutrients into the cell and flow of excreted outside the cell, and participates in particle uptake.<sup>168,170,171</sup> Among *Eukaryota*, cell wall composed of chitin or cellulose can be found in fungi and plants, respectively.<sup>172,173</sup>

Based on the differences in the cell wall structure, Gram-positive and Gram-negative bacteria can be distinguished after performing differential cell staining using crystal violet-iodine complex (as primary stain) and fuchsin/safranin as counterstain. The staining method was developed in 1884 by the Danish physician Hans Christian Gram (1853-1938) for rapid and preliminary identification of bacteria.<sup>174</sup> After over a century, Gram-staining still remains a valid and useful method for pre-identification of bacteria, which is particularly important in the treatment of bacterial infections, where the application of broad spectrum antibiotics did not bring a desirable therapeutic effect and application of properly selected narrow spectrum antimicrobials, towards the disease causative agents, is already required.

The cell wall of Gram-positive bacteria (*e.g.*, *Bacillus* sp., *Staphylococcus* sp., *Streptococcus* sp.) is relatively simple in structure, when compared to the cell wall of Gram-negative bacteria, and consists mostly of a rigid and thick peptidoglycan network covering the phospholipid cell membrane (bilayer). It contains covalently bound teichoic, lipoteichoic and teichuronic acids, which are responsible for the negative charge of the cell surface and demonstrate immunomodulatory properties.<sup>175-178</sup> The cell wall of Gram-positive bacteria can demonstrate a thickness up to 80 nm. Although the cell wall of Gram-negative bacteria (*e.g.*, *Escherichia* sp., *Klebsiella* sp., *Pseudomonas* sp.) is much thinner (up to 10 nm), it is simultaneously more complex and flexible, as it is composed of two phospholipid bilayers (inner membrane and outer membrane) separated by the periplasmic space with only a few peptidoglycan layers (**Figure 17**).<sup>179-181</sup> The outer membrane of Gram-negative bacteria is decorated with glycolipids, *i.e.*, LPS and the enterobacterial common antigen (ECA, present only in enteric bacteria), which determine the negative charge of the cell surface and thus attract positively-charged ions and molecules.<sup>176,182,183</sup> Moreover, LPS and ECA are potent immunogens.<sup>184-186</sup>

Decoration of the outer membrane outer leaflet with amphiphilic LPS molecules may protect the bacterium from antibiotics.<sup>187,188</sup>

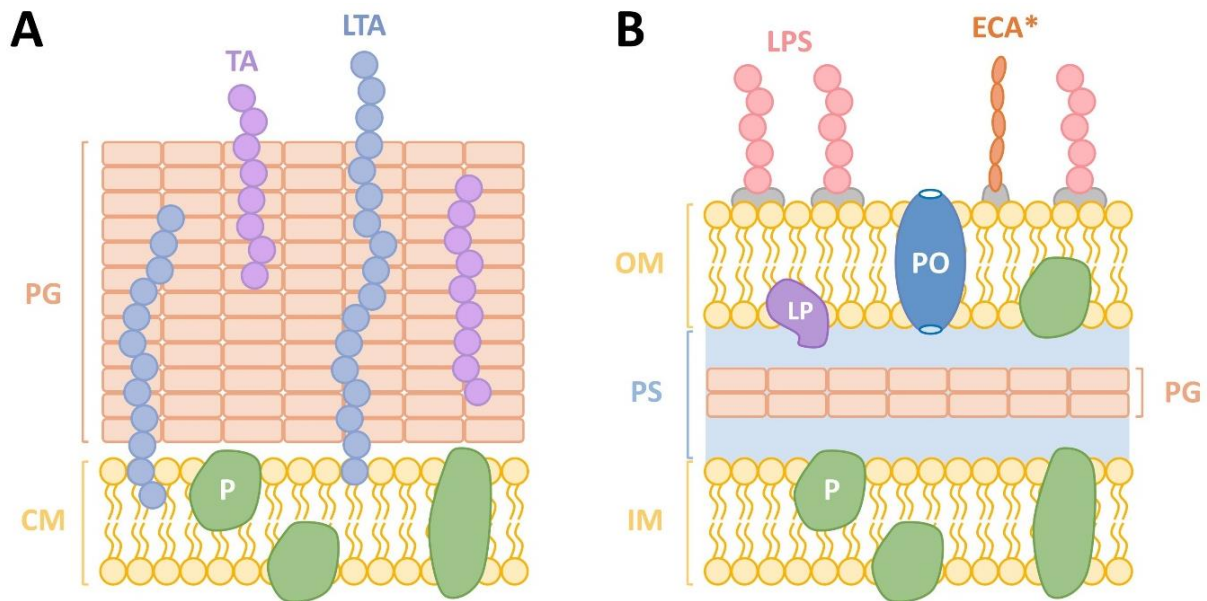


**Figure 17.** Comparison of the cell wall structure in Gram-positive (A) and Gram-negative (B) bacteria. \*ECA is present only in Enterobacteriaceae. CM – cell membrane, IM – inner membrane, LP – lipoprotein, LTA – lipoteichoic acid, OM – outer membrane, P – protein, PG – peptidoglycan, PO – porin, PS – periplasmic space, TA – teichoic acid. Figure adapted and modified from Miller et al.<sup>189</sup>

The thick cell wall is an excellent physical protective barrier for Gram-positive bacteria. It makes them often less sensitive to stress exposure, when compared to Gram-negative bacteria, because the cell interior and metabolic machinery are better isolated from the environment and less accessible.<sup>177</sup> On the other hand, the cell wall of Gram-negative bacteria, due to the presence of two diverse and metabolically active membranes, forms an advanced and highly selective permeability barrier for molecule and particle uptake, characterized by cooperation of active and passive transport mechanisms.<sup>190</sup>

### 2.3.3. Mechanisms and examples of particle uptake in bacteria

In contrast to well-researched endocytosis-based particle uptake mechanisms in eukaryotic cells, the nature of particle uptake by bacteria remains still poorly understood.<sup>189</sup> This can be explained by a significantly smaller size of the bacterial cell (~1-2  $\mu\text{m}$ ) which limits the applicability of classical microscopic methods, like confocal laser scanning microscopy

(CLSM), which is successfully used to visualise particle uptake by eukaryotic cells, in studies on the uptake by bacteria. Thus, such advanced microscopic methods as high resolution transmission electron microscopy (HRTEM) and super resolution microscopy come here into play.<sup>191-193</sup> Three main uptake mechanisms have been proposed to explain how nanoparticles may pass through the bacterial cell envelope. These are (i) non-specific diffusion (*e.g.*, via  $\beta$ -structured porin channels in Gram-negative bacteria), (ii) non-specific membrane damage (related with cell injury and pathologic changes in the membrane structure) and (iii) specific uptake (suitable also for larger molecules and particles, *e.g.*, mediated by protein-excreting permeases).<sup>194</sup> Non-specific diffusion is believed to be the leading mechanism for particle uptake by bacteria, however, it is limited by cell wall pore diameter and is believed to be suitable only for particles with a diameter  $<20$  nm.<sup>193,194</sup> The average diameter of cell wall pores in *B. subtilis* and *E. coli* is  $\sim 2$  nm and  $\sim 4$  nm, respectively.<sup>195</sup> Mitchell *et al.* postulated, after performing modelling studies, that pore diameter exceeding 15 nm is already lethal to Gram-positive bacteria, which was in agreement with results obtained for lysed *Streptococcus pyogenes*.<sup>179</sup> Moreover, porin-mediated passive diffusion is intended for hydrophilic molecules with a molecular weight ( $M_w$ ) up to 600 Da.<sup>196</sup>

Although studies on particle uptake by bacteria is a dynamically developing research field, literature provides already some reports on particle internalization by bacterial cells. Morones *et al.* concluded that the size range of 1-10 nm is preferential for the uptake of silver (Ag) nanoparticles by different Gram-negative bacterial species (*Salmonella enterica* Typhimurium, *E. coli*, *Vibrio cholerae* and *Pseudomonas aeruginosa*).<sup>197</sup> Kumar *et al.* confirmed the uptake of ultrasmall (5 nm) AuNPs by *E. coli* and *Staphylococcus aureus*, however, in case of this study, the uptake of nanoparticles was probably facilitated by their conjugation with cell-penetrating peptides.<sup>198</sup> Kloepfer *et al.* demonstrated that ultrasmall cadmium-selenium quantum dots ( $<5$  nm) were able to penetrate the cell wall of *B. subtilis* and *E. coli*, however, the proposed internalization mechanism was already lethal and related with bacterial cell membrane injury caused by oxidative stress.<sup>194</sup> Lonhienne *et al.* have shown that even 10 nm AuNPs were taken up by Gram-negative *Gemmata obscuriglobus*. In the case of *G. obscuriglobus*, involvement of a specific particle uptake mechanism was suggested. This bacterium belongs to the phylum *Planctomycetes* and demonstrates occurrence of a unique, among prokaryotes, intracellular membrane system which is similar to the cell compartment network known from eukaryotes. Thus, *G. obscuriglobus* could internalize also larger particles in analogy to endocytosis.<sup>199</sup> Wang *et al.* demonstrated that already 16 nm AuNPs were not taken up by *S. enterica* Typhimurium cells, what is in agreement with the preferential particle

size for the uptake by *S. enterica* Typhimurium cells proposed by Morones *et al.*<sup>197,200</sup> Furthermore, Butler *et al.* did not confirm internalization of 20 nm TiO<sub>2</sub> nanoparticles by *S. enterica* Typhimurium.<sup>201</sup> Finally, Pajerski *et al.* reported that 30 nm AuNPs were already too large to be taken up by Gram-positive *Staphylococcus carnosus* and *B. subtilis*, and Gram-negative *Neisseria subflava* and *Stenotrophomonas maltophilia*.<sup>202</sup>

#### 2.3.4. Metal resistance mechanisms in bacteria

Trace metals (or micronutrients), like iron (Fe), zinc (Zn), copper (Cu), manganese (Mn) or nickel (Ni), play an important role in proper functioning of the bacterial cell and its proliferation. They are cofactors of key enzymes involved in nucleic acid synthesis, cellular respiration and vital metabolic pathways.<sup>203</sup> Furthermore, trace metals influence the biosynthesis of secondary metabolites and form with them functional complexes. Although micronutrients are biologically essential for cell survival, their high concentrations are already cytotoxic.<sup>204,205</sup> High toxicity to cells, even at low concentrations, is observed for metals, like mercury (Hg), cadmium (Cd) or lead (Pb), which are biologically non-essential and have no known role in the living systems.<sup>206-208</sup> Environmental bacteria typically live under strong selective pressure and have to deal with metals which are widespread in aquatic and terrestrial ecosystems.<sup>209,210</sup> In response to environmental stress, bacteria developed different detoxification strategies known as metal resistance mechanisms (**Figure 18**). These can be based on (i) exclusion by permeability barrier, (ii) efflux systems, (iii) intracellular binding to proteins, (iv) enzymatic transformation to less toxic forms and (v) extracellular binding to polymers (biosorption).<sup>211</sup> Bacterial resistance to a variety of metals, including Cu, Zn, Pb, Ni, chromium (Cr), Ag, Au and even radioactive uranium (U) has been reported.<sup>212-219</sup>

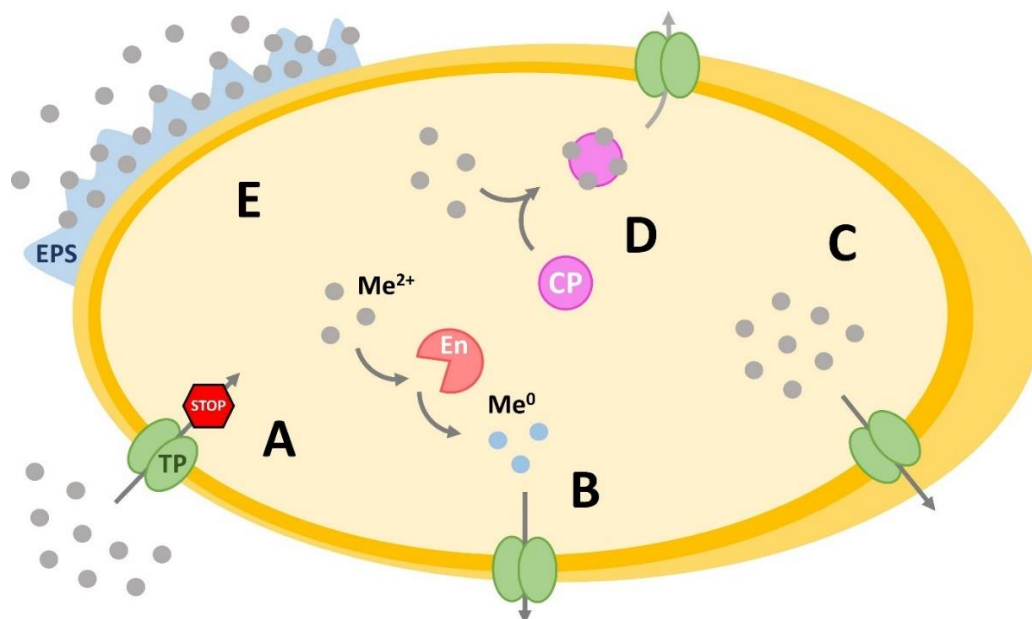


**Figure 18.** Main mechanisms of metal resistance in bacteria. Exclusion by permeability barrier (A), enzymatic detoxification by reduction (B), active efflux (C), intracellular sequestration (D) and biosorption (E). CP – complexing protein, En – enzyme, EPS – extracellular polysaccharide, Me – metal, TP – transporting protein. Figure adapted and modified from Wheaton et al.<sup>220</sup>

Metal resistance is usually encoded in plasmid DNA which means that it can be also easily disseminated in bacterial populations.<sup>221</sup> Metagenomic studies indicate a rich abundance of metal resistance genes in the environmental samples. These genes are evolutionary-conserved and can be acquired by bacteria *via* vertical evolution and horizontal gene transfer.<sup>205</sup> The latter is the primary mechanism involved in the spread of resistance among bacteria and its three forms: conjugation, transduction and transformation, can be distinguished. Horizontal gene transfer is an important strategy of gene pool sharing between cells, resulting in genome diversification and evolutionary progress.<sup>222</sup> Furthermore, genes determining metal and antimicrobial resistance may co-occur on one plasmid (co-resistance). This phenomenon is commonly observed in plasmids determining bacterial resistance to Ag, arsenic (As), Cd, Cu and Hg.<sup>205</sup> Beside co-resistance, other types of a close relation between metal and antimicrobial resistance are cross-resistance and co-regulation. The first is when one gene determines both resistances, whereas the second is when resistances share the regulatory system.<sup>223</sup>

### 2.3.5. Nanomaterials as antibacterial agents

Attractive physicochemical properties, large chemical modification possibilities and ability to work in an ultrasmall size range make nanoparticles promising materials for a variety of biomedical applications, including treatment of bacterial infections. Literature provides many examples of the antimicrobial activity of nanoconjugates, particularly metallic (*e.g.*, Ag, Cu) and metal oxide (Ag<sub>2</sub>O, CuO, ZnO), against pathogenic bacteria.<sup>208,224</sup> This is an emerging research topic nowadays, as in so-called “post-antibiotic era”, due to long-term overuse of antibiotics, generation of drug resistance in bacteria and development of multidrug-resistant “superbugs” (*e.g.*, methicillin-resistant *S. aureus*, vancomycin-resistant *Enterococcus faecium*, fluoroquinolone-resistant *P. aeruginosa*, and extended spectrum  $\beta$ -lactamase-producing *E. coli* and *Klebsiella* sp.) constitutes already a worldwide problem.<sup>225,226</sup>

Nanoparticles are believed to be promising alternatives to antibiotics with important advantages over traditional antimicrobials, like (i) ability to bypass antibiotic resistance mechanisms, (ii) effectiveness towards bacteria possessing more than one drug resistance mechanism, (iii) prevention of biofilm formation and (iv) synergism, when applied in combination with conventional antibiotics, for an enhanced therapeutic effect.<sup>208,224</sup> The antibacterial effect of metallic and metal oxide nanoparticles results mainly from the interaction of toxic metal ions, released from the nanoparticles, with vital biomolecules of bacteria and generation of oxidative stress by the formation of reactive oxygen species. Metal ions can cause damage to the cell envelope, interfere with protein synthesis, inactivate enzymes and disrupt DNA replication.<sup>189,208</sup> The most prominent examples are here silver and copper ions. Divalent copper and monovalent silver show the highest affinity to interact with functional groups of vital proteins among biologically essential and non-essential metals, respectively. This is reflected in high antibacterial activity of these metals, when present in excess.<sup>208</sup>

Nanoparticle materials, even when not cytotoxic by themselves, like gold or some polymers, can be also applied to target bacteria, serving as delivery platforms for antimicrobials with advantage to therapies.<sup>227-229</sup> In this case, unique cell penetration properties of nanocarriers can be utilized to support drug internalization into cell and thus enhance the healing effect. Moreover, nanoparticles tend to increase the permeability of the bacterial cell envelope which improves the antimicrobial cell penetration rate.<sup>230-232</sup> For example, polymeric nanoparticle-mediated delivery of gentamicin and azithromycin resulted in a higher effectiveness against enteropathogenic *S. enterica* Typhimurium, when compared to the inhibitory effect of the antibiotics applied alone.<sup>233,234</sup> A similar effect was observed in *S. aureus*, a skin-associated opportunistic pathogen, for clarithromycin delivered using polymeric nanoparticles.<sup>227</sup> The

antibacterial activity of modified polymeric nanoparticles can be also achieved in another way, not related with loading of the nanoparticles with antimicrobials. For example, they can be functionalized with carbohydrate binding proteins to counteract bacterial adhesion to surfaces. Lectin-coated gliadin nanoparticles were successfully used by Umamaheshwari and Jain to block superficial carbohydrate receptors of *Helicobacter pylori* (causative agent of gastritis) and therefore, such nanoconjugates may prevent bacterial colonization of the gastric mucus and establishment of an infection by *H. pylori*.<sup>235</sup> Demurtas and Perry have shown that amoxicillin (a penicillin family antibiotic) can be used as reducing agent to synthesize antibiotic-coated AuNPs in a size range of 30-40 nm. Gold-conjugated amoxicillin was more efficient in the inhibition of *E. coli* growth than unbound amoxicillin. Practically, nanoparticle-mediated delivery allowed to reduce the antibiotic dose by 1/3 without loss of the antibacterial efficiency.<sup>236</sup> Shaker and Shaaban reported that imipenem- or meropenem-conjugated AuNPs (35 nm) efficiently inhibited growth of carbapenem-resistant *Klebsiella pneumoniae*, *Proteus mirabilis* and *Acinetobacter baumannii* isolated from human urine samples. For example, in *K. pneumoniae*, MIC values for imipenem- and meropenem-loaded AuNPs were 16- and 8-fold lower than MIC values of the corresponding free antibiotics, respectively. Gold nanocarriers themselves did not negatively impact the bacterial growth.<sup>228</sup> Payne *et al.* described a similar observation for kanamycin-coated AuNPs (20 nm) in studies on different bacterial species *Streptococcus bovis*, *Staphylococcus epidermidis*, *Enterobacter aerogenes*, *P. aeruginosa* PA01 and *Yersinia pestis* CO92, including kanamycin-resistant strains *P. aeruginosa* UNC-D and *Y. pestis* CO92::Km. The decrease in MIC values for nanoparticle-bound kanamycin was significant, when compared to MIC values for free kanamycin, with a fold change range of 3-50, depending on the bacterial strain.<sup>237</sup> Fuller *et al.* demonstrated that non-cytotoxic AuNPs (5 nm) loaded with colistin (polymyxin E) acted more inhibitory against *E. coli* cells than free administered colistin. Thus, a therapy based on this principle would allow to decrease the antibiotic dosage for the patient, when compared to current therapy models, ensuring the same high antibacterial effect as observed for free administered colistin sulphate. This is very important, as colistin belongs to the group of “last line” antibiotics (these are carbapenems and polymyxins), which are used to combat multidrug resistant pathogens (typically insensitive to most antibiotic-based therapies), and beside excellent antibacterial efficiency they may cause nephrotoxic and neurotoxic side effects.<sup>229</sup> The application of nano-sized liposomes (spherical vesicles composed of at least one phospholipid bilayer), as drug delivery platforms, utilizes still another strategy of bringing antimicrobials into bacterial cells.<sup>238</sup> Antibiotic-loaded liposomes, due to structural similarity with biological membranes,

can fuse with phospholipid membranes of bacteria and release the therapeutic cargo directly into the bacterial cytoplasm. This enhances drug penetration within the bacterial cell and is a strategy to bypass cell membrane-localized drug resistance mechanisms. The latter are widely distributed among multidrug-resistant pathogens, including clinically relevant biofilm formers, like *P. aeruginosa*.<sup>239,240</sup>

### 3. Materials and devices

#### 3.1. Reagents, fluorophores, media and kits

**Table 1.** List of chemicals, dyes, media and kits used in the research work. *kDa* – kilodalton, *n/a* – not applicable, *p.a.* – pro analysi.

Reagent:	Formula/ composition:	Manufacturer:	Purity:
Agar-Agar Kobe I	$C_{14}H_{24}O_9$	Carl Roth, Germany	n/a
Ammonia solution, aqueous, 30-33%	$NH_4OH$	Carl Roth, Germany	p.a.
Ampicillin sodium salt	$C_{16}H_{18}N_3NaO_4S$	Carl Roth, Germany	$\geq 99\%$
Barium chloride	$BaCl_2$	Sigma-Aldrich, USA	99.9%
Calcium chloride, dihydrate	$CaCl_2 \cdot 2H_2O$	Fluka, Switzerland	$> 99\%$
Calcium lactate, pentahydrate	$C_6H_{10}CaO_6 \cdot 5H_2O$	Sigma-Aldrich, USA	$\geq 99\%$
Citric acid	$C_6H_8O_7$	Fluka, Switzerland	$> 99.5\%$
D-(+)-trehalose, dihydrate	$C_{12}H_{22}O_{11} \cdot 2H_2O$	VWR Life Science, USA	$\geq 99\%$
Diammonium hydrogen phosphate	$(NH_4)_2HPO_4$	VWR Life Science, USA	$\geq 99\%$
Dimethyl sulfoxide (DMSO)	$C_2H_6OS$	Carl Roth, Germany	$\geq 99.5\%$
Dulbecco's phosphate buffered saline (DPBS), 1X	$NaCl, KH_2PO_4,$ $Na_2HPO_4, KCl, H_2O$	Gibco™, USA	n/a
Dyomics(Dy)734-N- hydroxysuccinimide(NHS)-ester	$C_{44}H_{52}N_3O_{17}S_4Na_3$	Dyomics, Germany	n/a
Ethanol, absolute	$C_2H_6O$	Fisher Chemicals, USA	p.a.
Ethylenediaminetetraacetic acid (EDTA)	$C_{10}H_{16}N_2O_8$	Carl Roth, Germany	$\geq 99\%$
Fetal calf serum (FCS)	Mixture of serum biomolecules and inorganic salts	Sigma-Aldrich, USA	n/a
Fluoromount-G™ mounting medium	$NaN_3$ -based	Invitrogen™, USA	n/a

Formaldehyde	CH <sub>2</sub> O	Fluka, Switzerland	p.a.
Glycerol	C <sub>3</sub> H <sub>8</sub> O <sub>3</sub>	Carl Roth, Germany	≥99.5%
Glycine	C <sub>2</sub> H <sub>5</sub> NO <sub>2</sub>	Biomol, Germany	>99%
Hydrochloric acid, 37%	HCl	VWR Life Science, USA	p.a.
Isopropyl-β-D-thiogalactopyranoside (IPTG)	C <sub>9</sub> H <sub>18</sub> O <sub>5</sub> S	Carl Roth, Germany	≥99%
Liquid nitrogen (-196 °C)	N <sub>2</sub>	Air Liquide	n/a
LIVE/DEAD® BacLight™ bacterial viability kit for microscopy (L7012)	SYTO™ 9, propidium iodide	Invitrogen™, USA	n/a
Lysogeny broth (LB), Lennox	Tryptone (10 g L <sup>-1</sup> ), yeast extract (5 g L <sup>-1</sup> ), NaCl (10 g L <sup>-1</sup> )	Carl Roth, Germany	n/a
Magnesium chloride, hexahydrate	MgCl <sub>2</sub> ·6H <sub>2</sub> O	Fluka, Switzerland	99%
(3-Mercaptopropyl)trimethoxysilane (MPS)	C <sub>6</sub> H <sub>16</sub> O <sub>3</sub> SSi	Sigma-Aldrich, USA	95%
Nitric acid, 65%	HNO <sub>3</sub>	Fisher Chemicals, USA	p.a.
Paraformaldehyde, 4%	C <sub>2</sub> H <sub>6</sub> O <sub>2</sub>	Merck Millipore, Germany	≥95%
Polyethyleneimine, branched, M <sub>w</sub> = 25 kDa (PEI)	(C <sub>2</sub> H <sub>5</sub> N) <sub>n</sub>	Sigma-Aldrich, USA	≥99%
PEI-cyanine 5 (Cy5), branched, 1 Cy5 unit per 320 monomer units	As above	Surflay Nanotec, Germany	≥99%
Potassium bromide	KBr	Sigma-Aldrich, USA	≥99%
Sodium chloride	NaCl	Bernd Kraft, Germany	>99.5%
Sodium citrate, dihydrate	HOC(COONa) (CH <sub>2</sub> COONa) <sub>2</sub> ·2H <sub>2</sub> O	Sigma-Aldrich, USA	99%
Sodium hydroxide	NaOH	VWR Life Science, USA	99%
Sodium lactate	NaC <sub>3</sub> H <sub>5</sub> O <sub>3</sub>	Sigma-Aldrich, USA	>99%
Sodium phosphate, heptahydrate	Na <sub>2</sub> HPO <sub>4</sub> ·7H <sub>2</sub> O	Riedel-de-Haën, Germany	99%
Sodium pyruvate	CH <sub>3</sub> COCOONa	Sigma-Aldrich, USA	>99%

Sodium sulfate	Na <sub>2</sub> SO <sub>4</sub>	Fluka, Switzerland	99%
Sodium tartrate, dihydrate	Na <sub>2</sub> C <sub>4</sub> H <sub>4</sub> O <sub>6</sub> ·2H <sub>2</sub> O	Alfa Aesar, Germany	98%
Sulfo- <i>N</i> -succinimidyl 4-(maleimidomethyl)cyclohexane-1-carboxylate (sulfo-SMCC)	C <sub>16</sub> H <sub>17</sub> N <sub>2</sub> NaO <sub>9</sub> S	Iris Biotech, Germany	≥99%
Sulfuric acid, 95%	H <sub>2</sub> SO <sub>4</sub>	Fisher Chemicals, USA	p.a.
Tetraethoxysilane (TEOS)	C <sub>8</sub> H <sub>20</sub> O <sub>4</sub> Si	Sigma-Aldrich, USA	98%

Sterile nuclease-free distilled water Ultrapure™ (Invitrogen™, USA) was used in all syntheses and experiments with nanoparticles. Synthesis and handling of nanoparticles were performed in a nuclease-free environment, under a laboratory hood and a laminar flow cabinet. Workbenches were regularly decontaminated using technical-grade 70% ethanol and RNase AWAY® reagent (Carl Roth, Germany). Ultrapure double-distilled water (ELGA Purelab®, United Kingdom) was used for preparation of nanoparticle suspensions for the measurements by dynamic light scattering (DLS) and zeta-potential ( $\zeta$ -potential), and atomic absorption spectroscopy (AAS). For re-suspension and handling of freeze-dried siRNA, sterile nuclease-free water, provided by the manufacturer (Santa Cruz Biotechnology, USA), was used.

For preparation of the simulated lysosomal medium, all reagents were dissolved in Ultrapure™ water by magnetic stirring. The pH of the medium was adjusted to 4.7 with HCl. The medium was sterilized by filtration (0.2  $\mu$ m pore size) and stored at 4 °C.

### 3.2. Biomolecules

**Table 2.** List of biomolecules (antibodies, peptides, siRNA) used for preparation of bioactive CaP nanoparticles. Ab – antibody, CD69 – Cluster of Differentiation 69, CTRL – control, IgG – immunoglobulin G, nt – nucleotide, TAMRA – carboxytetramethylrhodamine.

Biomolecule:	Sequence:	M <sub>w</sub> :	Manufacturer:
Functional siRNA (anti-NF- $\kappa$ B p65), siRNAf (sc-29411)	5'-CCAUGGAGUCCAGUACUUt-3' 5'-UCAGCACCAUCAACUUUGAtt-3' 5'-CGAAGUGCGUACACAUUCUtt-3' 5'-GGAUCCUGUACACCUUGAtt-3'	13.8 kDa	Santa Cruz Biotechnology, USA

Control siRNA, siRNAc (sc-37007)	Not available (20-25 nt) (proprietary)	13.8 kDa	Santa Cruz Biotechnology, USA
cRGDfK peptide	cyclo(Arg-Gly-Asp-D-Phe-Lys)	0.603 kDa	BACHEM, Switzerland
TAMRA-KKK- (VELPPP) <sub>3</sub> peptide* (TAMRAp)	(TAMRA)-Lys-Lys-Lys-(Val-Glu-Leu- Pro-Pro-Pro) <sub>3</sub>	2.7 kDa	CASLO ApS, Denmark
$\kappa$ isotype control IgG Ab (IgG- $\kappa$ -IC)	n/a	150 kDa	Invitrogen™, USA
Anti-CD69 anti- mouse IgG Ab (IgG-anti-CD69)	n/a	150 kDa	BioLegend®, USA
Anti-CD69- CTRL anti- mouse IgG Ab (IgG-anti-CD69- CTRL)	n/a	150 kDa	BioLegend®, USA

\*Non-commercial product. Synthesis upon request.

### 3.3. Laboratory materials

Biosphere® plus sterile disposable labware, *i.e.*, pipette filter tips (0.0005-1 mL), screw cap microtubes (1.5 mL) and SafeSeal reaction tubes (1.5 mL), characterized by the highest chemical and microbiological purity, was used for nanoparticle synthesis and handling. For all other experimental purposes standard disposable labware, *i.e.*, pipette tips (0.0005-10 mL), reaction tubes (1.5 mL, 5 mL) and screw cap “falcon-type” tubes (15 mL, 50 mL), was used. Before using, the non-Biosphere® disposable labware was sterilized by autoclaving (121 °C, 15 psi, 20 min), each time when studies with living cells were planned. Chemically pure, but not sterile, reaction tubes (1.5 mL) were used to store tooth enamel powders. Disposable serological pipettes (5 mL, 10 mL, 25 mL) and screw cap tubes were sterile. Disposable sterile syringe filters Filtropur S 0.2 (0.2  $\mu$ m pore size) were used for sterilization of synthesis solutions. Disposable sterile short (1.20 x 40 mm; 18 G x 1<sup>1/2</sup>) and long (0.80 x 120 mm; 21 G x 4<sup>3/4</sup>) Sterican® needles were used during nanoparticle synthesis for solution injection into the reaction environment. Disposable sterile Injekt® Luer Solo syringes (10 mL, 20 mL) were used

together with syringe filters for sterilization of temperature-sensitive reagent solutions. All disposable medical equipment was purchased from the company B. Braun (Germany). Short and long glass Pasteur pipettes were purchased from the company Brand® (Germany). Glass labware, *i.e.*, beakers, conical flasks and Pasteur pipettes, and magnetic stirring rods were heat-sterilized and depyrogenated (250 °C, 1 h), before using, in a heating oven. Amicon® Ultra 0.5 mL and Amicon® Ultra 4 mL centrifugal filters Ultracel®-3K (Merck Millipore, Ireland), made of regenerated cellulose 3,000 NMWL (nominal molecular weight limit), were used for purification of antibodies and the PEI-Dy734 conjugate, respectively. In microbiological experiments, sterile inoculation loops (10 µL) and disposable Petri dishes (92 x 16 mm) were used for cultivation and passaging of bacteria. All works with bacteria were performed under sterile conditions (next to a burner) and using sterile labware (disposable and glass materials). Working surfaces were regularly disinfected either with technical-grade 70% ethanol or with 1% Ultrisol® F (Dr. Schumacher, Germany). All disposable labware was purchased from the company Sarstedt (Germany).

### 3.4. Glass materials for fluorescence microscopy

Before usage, glass microscope slides (76 x 26 mm<sup>2</sup>; Thermo Scientific, USA) and cover slips (18 x 8 mm<sup>2</sup>; thickness 170 ± 5 µm; Carl Roth, Germany) were ultrasonically cleaned and degreased with technical-grade absolute ethanol and ultrapure water (ELGA Purelab®), and left covered to dry.

### 3.5. Bacterial strains, growth media and cultivation conditions

Different *E. coli* strains were used in studies on the interactions between ultrasmall AuNPs and bacterial cells. These were: non-fluorescent DH5α strain (parental strain), green-fluorescent eGFP-expressing strain DH5α-eGFP (genetically-modified parental strain) and red-fluorescent DsRed2-expressing strain TOP10 (genetically-modified). The latter was a kind gift from Prof. Dr. Wiebke Hansen (Institute of Medical Microbiology, University Hospital Essen, University of Duisburg-Essen, Germany). The parental *E. coli* DH5α strain was cultivated in LB medium, whereas genetically-modified *E. coli* strains DH5α-eGFP and TOP10 required an LB medium supplemented with ampicillin (100 mg L<sup>-1</sup>), as fluorescent protein expression in modified bacteria was encoded by ampicillin resistance-carrying plasmid DNA. Solid LB medium was prepared by addition of Agar-Agar Kobe I (15 g L<sup>-1</sup>) to liquid LB medium. All growth media were prepared using ultrapure water (ELGA Purelab®) and sterilized by autoclaving (121 °C, 15 psi, 20 min). The same ultrapure, but sterilized, water was used for handling of bacterial

cells. If necessary, sterile-filtered ampicillin was added to pre-cooled LB medium (warm but not hot) to prevent thermal degradation of the antibiotic and maintain its biofunctionality in the medium. All bacterial strains were grown at 37 °C, either in an incubator (on LB plates) or in an orbital shaker (in flasks with liquid LB). For all experiments using *E. coli* strains DH5 $\alpha$  and DH5 $\alpha$ -eGFP, log-phase bacterial cultures were prepared from overnight cultures. In brief, fresh medium was inoculated with 2 volume% of the overnight bacterial culture and grown until the fresh culture reached the optical density (OD<sub>600</sub>) of ~0.6 (measured turbidimetrically at wavelength  $\lambda_{\text{max}} = 600$  nm). This took place after ~4 h of incubation with intensive shaking. McFarland turbidity standards were freshly made, in accordance with commercially available protocols, and used as reference solutions for culture density measurements. For all experiments with *E. coli* TOP10 strain, 48 h cultures were used as the intense expression of the DsRed2 fluorescent protein in TOP10 cells was observed first after ~48 h of growth. Dense stationary-phase bacterial cultures were then diluted with fresh growth medium to obtain cultures with an OD<sub>600</sub> of ~0.6. To determine the viability of bacterial cultures, expressed as number of colony forming units (CFU) re-calculated to the number of cells per mL, bacterial colonies were counted using a digital colony counter.

### 3.6. Laboratory devices

**Table 3.** List of laboratory devices used in the research work. EU – endotoxin unit, UV – ultraviolet light, Vis – visible light.

Device:	Manufacturer:	Model:
Analytical balance	Kern & Sohn, Germany	ABS 220-4N
Atomic absorption spectrometer	Thermo Scientific™, USA	iCE™ 3000 M-Series
Autoclave	SHP Steriltechnik, Germany	LABOKLAV 25
Automatic pipettes (0.0005-10 mL)	Eppendorf, Germany	Research® plus
Cell density meter	WPA Biowave, United Kingdom	CO8000
Cell incubator	Thermo Scientific™, USA	Heratherm™ Compact

Centrifuge	Andreas Hettich, Germany	Rotofix 32A + 1624 rotor
Centrifuge	Thermo Scientific™, USA	Multifuge X1R + TX-400 swinging bucket rotor (4 x 400 mL)
Confocal laser scanning microscope	Leica Microsystems, Germany	TCS SP8 HCS A + HC PL APO 63x/1.4 CS2 oil objective
Digital colony counter	Stuart®, United Kingdom	SC6+
DLS and $\zeta$ -potential instrument	Malvern Panalytical, United Kingdom	Zetasizer Ultra + DTS1070 disposable cuvette
Electroporator	Bio-Rad Laboratories, USA	GenePulser® Xcell™ + GenePulser® cuvette (2 mm)
Elemental analyzer	EuroVector, Italy	EA3100
Fluorescence microscope	Keyence Corporation, Japan	Biorevo BZ-9000
Fluorescence spectrometer	Agilent Technologies, USA	Cary Eclipse + Hellma® Analytics QS Quartz microcuvette (10 mm)
Freeze-dryer	Martin Christ, Germany	Christ Alpha 2-4 LSC
Heating oven	Memmert, Germany	UF110
Infrared (IR) spectrometer	Bruker Corporation, USA	Vertex 70
Laboratory freezer	Philipp Kirsch, Germany	Froster-Labex-96
Laboratory fridge	Philipp Kirsch, Germany	Labex-105
Laboratory hood	Waldner Laboreinrichtungen, Germany	MC6 Secuflow®
Laminar flow cabinet (safety class II)	Thermo Scientific™, USA	MSC-Advantage™ 1.2
Magnetic stirrers	IKA®, Germany	RCT classic/RCT basic/RET basic
Mini centrifuge	Biozym® Scientific, Germany	Sprout™

Orbital shaker	Thermo Scientific™, USA	MaxQ™ 4000
Peristaltic pumps	Ismatec®, Germany	Reglo
pH meter	WTW®, Germany	pH 340 + SenTix® 41 electrode
Precision grinder with jewelry diamond drills	Proxxon, Germany	Micromot FBS 230/E
Scanning electron microscope with energy-dispersive X-ray detector	FEI™, USA	ESEM Quanta™ 400 FEG
Single wheel grinder and polisher	ATM Qness, Germany	Saphir 520
Sputter coater	Cressington Scientific Instruments, England	Sputter Coater 108
Structured illumination microscope	Carl Zeiss, Germany	Elyra PS.1 + $\alpha$ Plan-Apochromat 100x/1.46 DIC M27 oil objective
Thermogravimetric analyzer	Netzsch, Germany	STA 449 F3 Jupiter®
Thermomixer	Oehmen Labortechnik, Germany	HLC
Ultracentrifuge	Thermo Scientific™, USA	Heraeus® Fresco™ 21 + ClickSeal™ rotor (24 x 1.5/2.0 mL)
Ultra-low temperature laboratory freezer (-80 °C)	Thermo Scientific™, USA	Heraeus® HERAfreeze™
Ultrasonic bath	Bandelin Electronic, Germany	Sonorex™ RK-100
Ultrasonic bath	Elma Schmidbauer, Germany	Elmasonic S10
Ultrasonic sonotrode	Hielscher Ultrasonics, Germany	UP50H + MS1 sonotrode
UV spectrometer	Agilent Technologies, USA	Varian Cary® 300 Bio + Hellma® Analytics QS Quartz cuvette (10 mm)
UV/Vis spectrophotometer	DeNovix®, USA	DS-11 FX+ (NanoDrop)

Vacuum hydraulic press	Perkin Elmer, USA (press) + KNF Neuberger, Germany (vacuum pump)	-
Vis spectrophotometer	Charles River Laboratories, USA	Endosafe® nexgen-PTS™ + PTS2001F cartridges (0.01 – 0.1 EU mL <sup>-1</sup> )
Vortex	Scientific Industries™, USA	Genie® 2
X-ray powder diffractometer	Bruker Corporation, USA	D8 Advance

### 3.7. Software

For data acquisition and analysis, standard software provided by device manufacturers was used. For analysis of scanning electron micrographs, the ImageJ software (Wayne Rasband, National Institutes of Health, USA) was used. Origin 2019b (OriginLab® Corporation, USA) and Microsoft® PowerPoint (Microsoft®, USA) software was used for data analysis and graphical presentation.

## 4. Methods, samples and experimental procedures

### 4.1. Project I – Bioactive calcium phosphate nanoparticles for NF- $\kappa$ B silencing

#### 4.1.1. Syntheses of calcium phosphate nanoparticles

All types of CaP nanoparticles, presented in this thesis, were synthesized according to Kozlova *et al.*, with modifications of syntheses depending on nanoparticle formulations.<sup>241</sup>

##### 4.1.1.1. Fluorescent calcium phosphate nanoparticles for dissolution studies

Two types of Cy5-labelled CaP nanoparticles were synthesized by wet-chemical precipitation. These were “basic” non-functionalized nanoparticles (CaP/PEI-Cy5) and silica-functionalized (CaP/PEI-Cy5/SiO<sub>2</sub>) nanoparticles (**Figure 19**). The nanoparticles were used in experiments on dissolution kinetics of CaP nanoparticles in the simulated lysosomal medium and in water (as reference).

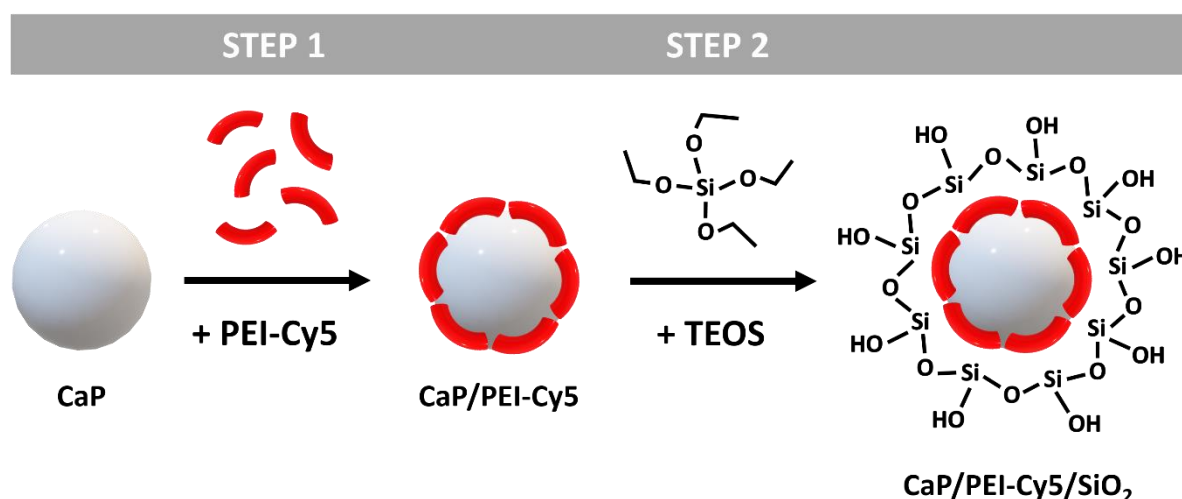


**Figure 19.** Schematic representation of the synthesis of Cy5-labelled CaP nanoparticles without (CaP/PEI-Cy5) and with (CaP/PEI-Cy5/SiO<sub>2</sub>) silica shell.

Aqueous solutions of calcium lactate pentahydrate (18 mM; pH = 10), diammonium hydrogen phosphate (10.8 mM; pH = 10) and PEI-Cy5 (2 mg mL<sup>-1</sup>; diluted with unlabelled PEI in a volume ratio of one part PEI-Cy5 to four parts PEI) were simultaneously added with peristaltic pumps at a volume ratio of 5:5:7 mL min<sup>-1</sup>, respectively, to a strongly stirred beaker (100 mL) containing 20 mL water. The rapidly formed nanoparticle dispersion (CaP/PEI-Cy5) was stirred for the next 20 min at room temperature (RT) in darkness. For further silica functionalization of the “basic” nanoparticles, 1 mL of CaP/PEI-Cy5 nanoparticle dispersion was immediately

added to a stirred mixture of 4 mL absolute ethanol, 5  $\mu\text{L}$  TEOS and 10  $\mu\text{L}$  aqueous ammonia solution (7.8%), and further stirred overnight at RT under light exclusion. After this time, the nanoparticles (CaP/PEI-Cy5/SiO<sub>2</sub>) were collected by centrifugation (4,000 rpm; 30 min; RT) and the nanoparticle pellet was re-dispersed in 1 mL water, followed by vortexing and ultrasonication (cycle 0.8; amplitude 70%; 30 s). The supernatant was also collected and analyzed by UV/Vis spectrophotometry for the presence of PEI-Cy5 (at  $\lambda_{\text{max}} = 639 \text{ nm}$ ), using the NanoDrop instrument (2  $\mu\text{L}$  of sample), to determine the total PEI concentration in the nanoparticles. It was calculated based on the detected PEI-Cy5 concentration multiplied by the dilution factor 1:5. Beforehand, a calibration curve of water-dissolved PEI-Cy5 was prepared (**Figure 20**). Nanoparticle dispersions were immediately used to perform dissolution experiments, to avoid rapid agglomeration of the non-functionalized nanoparticles.<sup>242</sup>

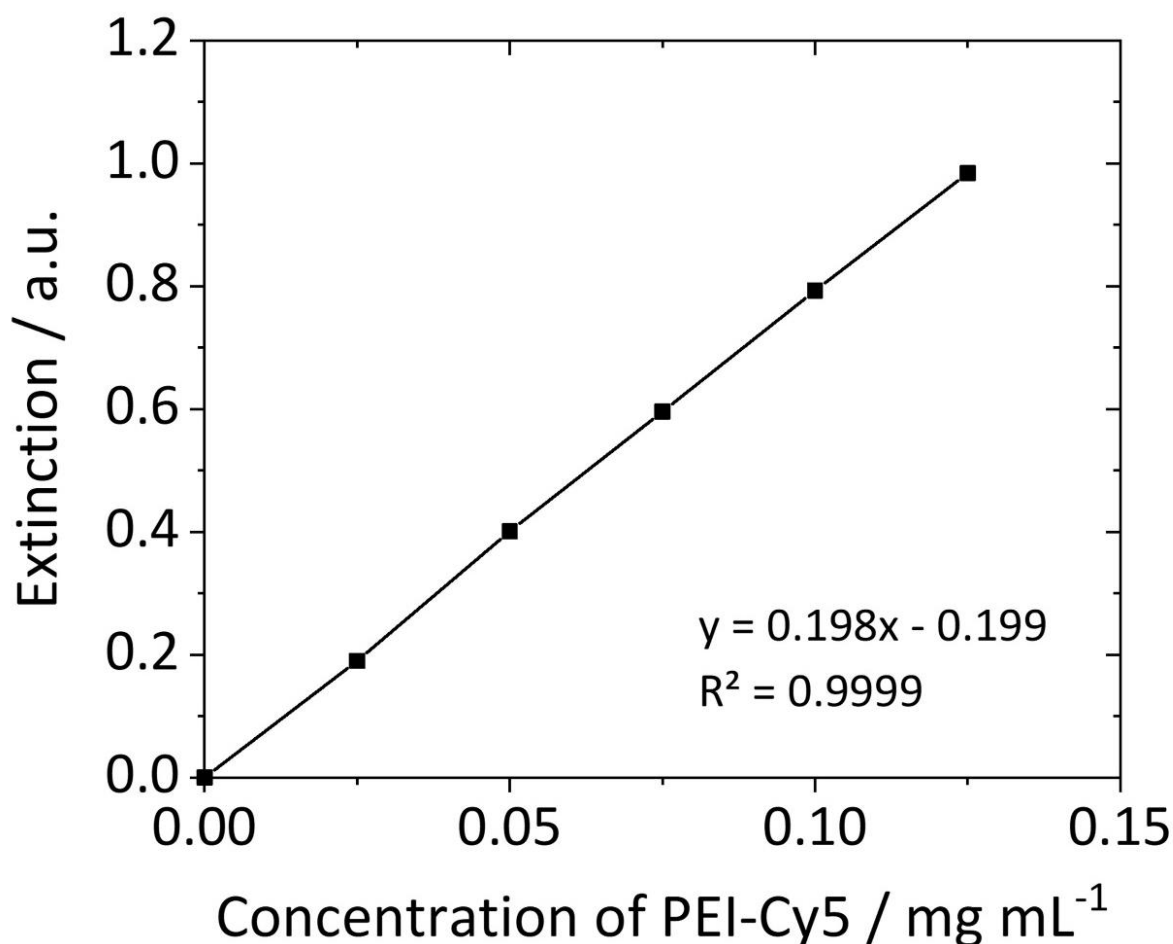


**Figure 20.** UV/Vis calibration curve of water-dissolved PEI-Cy5 determined at  $\lambda_{\text{max}} = 639 \text{ nm}$ .

#### 4.1.1.2. Bioactive fluorescent calcium phosphate nanoparticles for gene silencing of NF- $\kappa$ B p65

Bioactive fluorescently-labelled (with Cy5 or Dy734) and siRNA-loaded CaP nanoparticles were synthesized by wet-chemical precipitation. These were CaP/PEI-Cy5/siRNAf/SiO<sub>2</sub> or CaP/PEI-Dy734/siRNAf/SiO<sub>2</sub> (nanoparticles loaded with functional siRNA for gene silencing of NF- $\kappa$ B p65) and CaP/PEI-Cy5/siRNAc/SiO<sub>2</sub> or CaP/PEI-Dy734/siRNAc/SiO<sub>2</sub> (nanoparticles loaded with control siRNA and without the gene silencing effect). All types of the nanoparticles were silica-functionalized to protect the incorporated siRNA from enzymatic degradation and maintain nanoparticle stability in biological media. Cy5- and Dy734-labelled siRNA-loaded CaP nanoparticles were used in *in vitro* (studies in murine monocytes) and *in vivo* (studies in mice) experiments, respectively. As reference nanoparticles, non-bioactive fluorescent CaP/PEI-Cy5/SiO<sub>2</sub> or CaP/PEI-Dy734/SiO<sub>2</sub> nanoparticles were used in the experiments. Furthermore, CaP/PEI-Cy5/SiO<sub>2</sub> nanoparticles were also used to study the uptake by murine blood compartment cells.

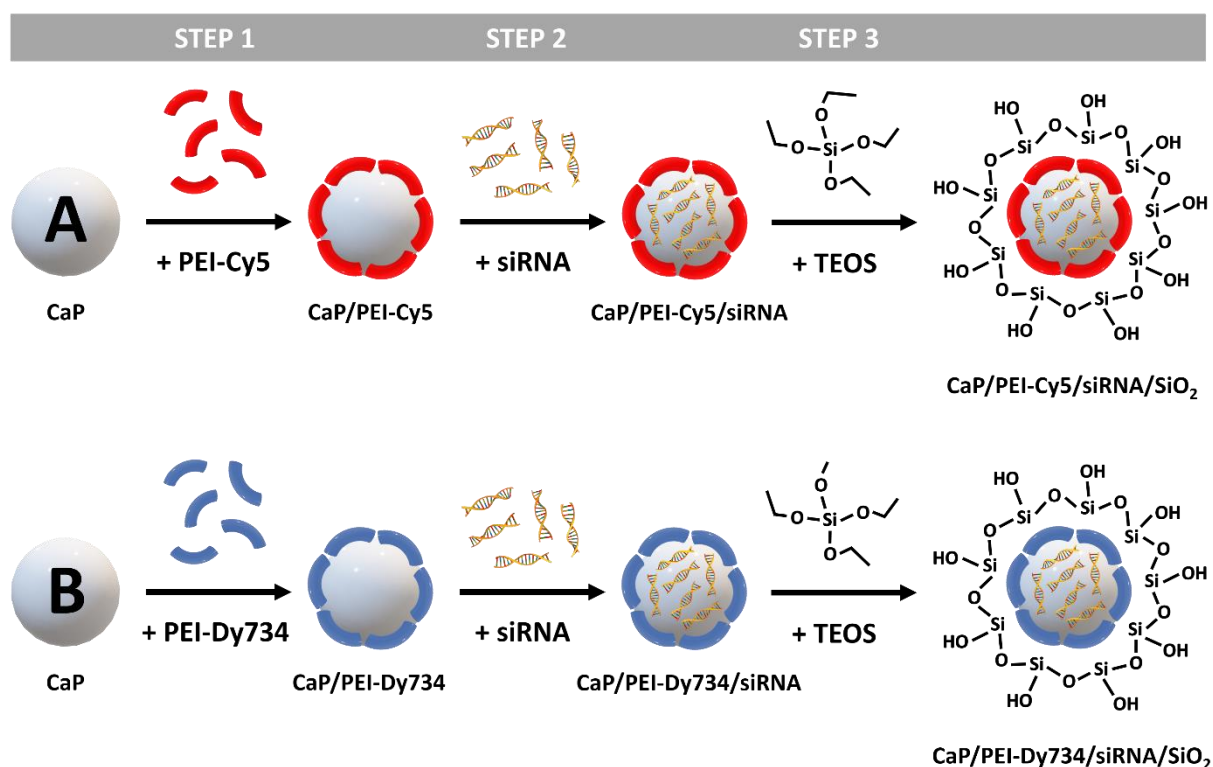


**Figure 21.** Schematic representation of the synthesis of fluorescent siRNA-loaded CaP nanoparticles for gene silencing studies. The nanoparticles were labelled either with the Cy5 dye for nanoparticle imaging *in vitro* (A; CaP/PEI-Cy5/siRNA/SiO<sub>2</sub>) or with the Dy734 dye for nanoparticle imaging *in vivo* (B; CaP/PEI-Dy734/siRNA/SiO<sub>2</sub>).

In general, the synthesis of siRNA-loaded CaP nanoparticles was based on the protocol described in chapter 4.1.1.1. for synthesis of non-bioactive CaP nanoparticles. For nanoparticle loading with siRNA, an additional step in the synthesis was performed (**Figure 21**). After the first step of synthesis (CaP core + labelled PEI), before silica functionalization of the nanoparticles, 0.9 mL of CaP/PEI-Cy5 or CaP/PEI-Dy734 nanoparticle dispersion was mixed with 0.1 mL siRNA ( $0.36 \text{ mg mL}^{-1}$ ) in a 1.5 mL reaction tube and stirred for 30 min at RT in darkness. During this time, negatively-charged siRNA molecules were incorporated onto positively-charged CaP nanoparticles, due to electrostatic complexation. Next, 1 mL of fluorescent and siRNA-loaded CaP nanoparticles was used for further silica functionalization of the nanoparticles (as described in the previous chapter for synthesis of unloaded CaP nanoparticles). To avoid biomolecule damage and loss of biological functionality after centrifugation, the nanoparticle pellet was ultrasonicated only for 4 s (keeping the same cycle and amplitude conditions as for re-dispersion of the non-bioactive CaP nanoparticles). 0.04 mL D-(+)-trehalose dihydrate solution ( $0.5 \text{ g mL}^{-1}$ ) was added to 1 mL of CaP/PEI-Cy5/siRNA/SiO<sub>2</sub> or CaP/PEI-Dy734/siRNA/SiO<sub>2</sub> nanoparticle dispersion, as cryoprotective agent, followed by shock freezing in liquid nitrogen and freeze-drying of the nanoparticles for 72 h at 0.37 mbar and -10 °C. Colloidal stability of lyophilized CaP nanoparticles was checked by performing DLS and  $\zeta$ -potential measurements, and possible pyrogenicity of the nanoparticles was evaluated by analyzing the content of endotoxins in the nanoparticles using the Endosafe<sup>®</sup> instrument, based on the principle of the limulus amoebocyte lysate chromogenic assay. Endotoxins (or LPS) are major outer membrane components of the cell wall of Gram-negative bacteria. Lyophilized nanoparticles were stored at -80 °C. Immediately before application in biological studies, the nanoparticles were re-dispersed in the same volume of ultrapure water as present before freeze-drying and thoroughly vortexed. The efficiency of siRNA loading onto the nanoparticles was determined by UV/Vis spectrophotometry by analyzing the supernatant, obtained after nanoparticle centrifugation, for the presence of free siRNA, using the NanoDrop instrument. It was assumed that the fraction of siRNA that was not found in the supernatant had been incorporated onto the nanoparticles. UV/Vis spectrophotometry was also applied to assess PEI content in the nanoparticles. Bioactive Cy5-labelled CaP nanoparticles were synthesized in 1 mL scale, whereas synthesis of bioactive Dy734-labelled CaP nanoparticles was upscaled 20-fold, as for the *in vivo* studies in mice much more nanoparticle material was needed.

### 4.1.1.3. Bioactive fluorescent and ligand-decorated calcium phosphate nanoparticles for gene silencing of NF- $\kappa$ B p65 and cell targeting studies

Bioactive fluorescent ligand-decorated and siRNA-loaded CaP nanoparticles were synthesized by wet-chemical precipitation. The nanoparticles were labelled with Cy5, loaded with functional or control siRNA, coated with silica shell and surface-decorated with peptides or antibodies. Silica functionalization of the nanoparticles, beside already mentioned protection of the siRNA cargo and maintaining nanoparticle stability in biological media, enabled also their further chemical modification. Silica surface of the nanoparticles was covalently-functionalized by silanization with thiol groups for surface decoration of the nanoparticles with peptides/antibodies. The synthesis route of ligand-decorated CaP nanoparticles was composed of five steps, where the first three steps were the same as in the synthesis of fluorescent siRNA-loaded CaP nanoparticles for gene silencing experiments, described in chapter 4.1.1.2. (Figure 22).

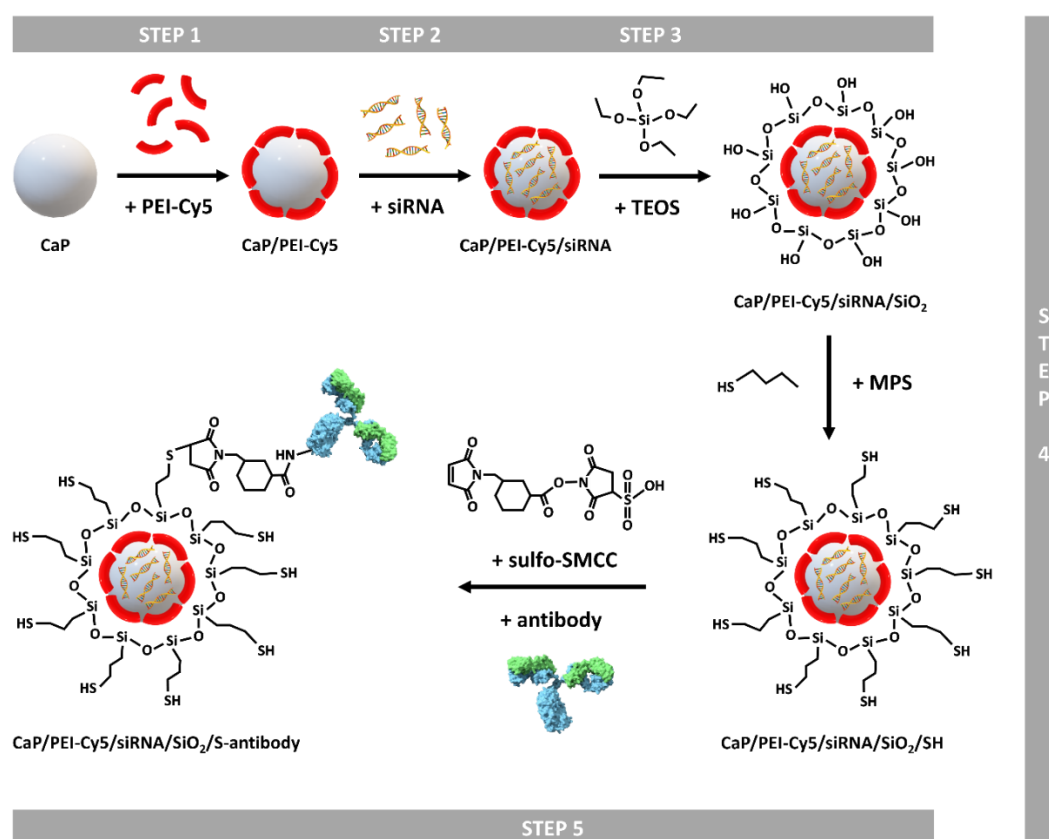


**Figure 22.** Schematic representation of the synthesis of fluorescent antibody-decorated and siRNA-loaded CaP nanoparticles (CaP/PEI-Cy5/siRNA/SiO<sub>2</sub>/S-Ab) for *in vitro* gene silencing and cell targeting studies. Peptide-decorated CaP nanoparticles were synthesized in the same way. Image of the antibody was adapted from [static.turbosquid.com](http://static.turbosquid.com).

For thiol functionalization, 2 mL of fluorescent siRNA-loaded (CaP/PEI-Cy5/siRNA/SiO<sub>2</sub>) or unloaded (CaP/PEI-Cy5/SiO<sub>2</sub>) nanoparticles were added to a stirred mixture of 10  $\mu$ L MPS (conjugation reagent) and 8 mL absolute ethanol, and further stirred overnight at RT under light exclusion. SH-functionalized nanoparticles (CaP/PEI-Cy5/siRNA/SiO<sub>2</sub>/SH or CaP/PEI-Cy5/SiO<sub>2</sub>/SH) were then collected by centrifugation (4,000 rpm; 30 min; RT), and the nanoparticle pellet was double-concentrated by re-dispersion in 1 mL of ultrapure water, followed by vortexing and ultrasonication. The supernatant, obtained after nanoparticle centrifugation, was analyzed for the presence of free siRNA, using the NanoDrop instrument. 1 mL of thiol-functionalized nanoparticles were mixed with 0.5 mL activated peptides/antibodies and incubated for the next 24 h at 4 °C in darkness. Prior to coupling with the nanoparticles, ligands were activated in a reaction with a heterobifunctional cross-linker sulfo-SMCC, which contains an NHS-ester and a maleimide functional group. This enables covalent conjugation, *via* cross-linker, between amine-containing peptides/antibodies and sulfhydryl-coated CaP nanoparticles. 0.5 mL peptide/antibody solution (0.5 mg mL<sup>-1</sup>) was mixed with 0.25 mL sulfo-SMCC (4 mM) and left for activation for 4 h at RT without stirring. Next, the ligand-cross-linker complex was purified by spin filtration (Amicon<sup>®</sup> Ultra 0.5 mL) to remove the free sulfo-SMCC. First, the spin filter was activated by adding 0.4 mL ultrapure water and ultracentrifugation (12,000 rpm; 15 min; 4 °C). Second, the complex was spin-filtered by ultracentrifugation and washed with 0.4 mL ultrapure water and ultracentrifuged again. Finally, the spin filter was turned around, placed in a new reaction tube and shortly centrifuged (3,000 rpm; 2 min; 4 °C) to detach and collect the purified complex (activated ligand). Before the complex was added to thiol-functionalized nanoparticles, it was analyzed using the NanoDrop instrument to determine the final peptide/antibody concentration in the ligand stock solution. After the coupling reaction, the nanoparticles were collected by ultracentrifugation (14,800 rpm; 30 min; 4 °C) and the nanoparticle pellet was re-dispersed in 1 mL water, followed by vortexing and ultrasonication (4 s). The supernatant, obtained after nanoparticle ultracentrifugation, was analyzed for the presence of free peptides or antibodies at  $\lambda_{\text{max}} = 205$  nm (E0.1%; 31.00 mg mL<sup>-1</sup>) or 280 nm (E1%; 13.70 g 100 mL<sup>-1</sup>), respectively, using the NanoDrop instrument, to determine the peptide/antibody concentration on the nanoparticles. Supernatant obtained after each synthesis step of biomolecule-loaded nanoparticles was analyzed for the presence of free siRNA, to monitor possible siRNA loss during the multi-step synthesis. Finally, CaP nanoparticles were aliquoted, freeze-dried and stored at -80 °C before application in biological experiments.

Ligand decoration of the nanoparticles was performed to enhance nanoparticle uptake by the target cells. For surface decoration of the nanoparticles, depending on the type of target cells, peptides or antibodies were used. Nanoparticle-coating with cRGDfK peptides was applied to favor the uptake of nanoparticles by SVEC4-10 cells, whereas coating with IgG-anti-CD69 antibodies was applied to improve the uptake of nanoparticles by lymphocytes, particularly by TK-1 cells. The following bioactive nanoparticle types were synthesized: CaP/PEI-Cy5/siRNAf/SiO<sub>2</sub>/S-cRGDfK, CaP/PEI-Cy5/siRNAc/SiO<sub>2</sub>/S-cRGDfK, CaP/PEI-Cy5/siRNAf/SiO<sub>2</sub>/S-IgG-anti-CD69 and CaP/PEI-Cy5/siRNAc/SiO<sub>2</sub>/S-IgG-anti-CD69.

Additionally, different types of reference nanoparticles were synthesized. These were nanoparticles coated with IgG-anti-CD69-CTRL antibodies and loaded with siRNA (CaP/PEI-Cy5/siRNAf/SiO<sub>2</sub>/S-IgG-anti-CD69-CTRL, CaP/PEI-Cy5/siRNAc/SiO<sub>2</sub>/S-IgG-anti-CD69-CTRL), nanoparticles with various ligand decoration but without siRNA loading (CaP/PEI-Cy5/SiO<sub>2</sub>/S-cRGDfK, CaP/PEI-Cy5/SiO<sub>2</sub>/S-IgG-anti-CD69 and CaP/PEI-Cy5/SiO<sub>2</sub>/S-IgG-anti-CD69-CTRL), as well as non-decorated and unloaded thiol-functionalized nanoparticles (CaP/PEI-Cy5/SiO<sub>2</sub>/SH). To mimic the last synthesis step, related with ligand decoration of the nanoparticles, and to obtain an equally-treated control sample, thiol-terminated nanoparticles (CaP/PEI-Cy5/SiO<sub>2</sub>/SH/H<sub>2</sub>O) were incubated for 24 h in ultrapure water. Moreover, CaP nanoparticles decorated with model IgG- $\kappa$ -isotype control antibodies (CaP/PEI-Cy5/SiO<sub>2</sub>/S-IgG- $\kappa$ -IC) were synthesized as reference nanoparticles for studies on the specificity of the cellular uptake.

#### ***4.1.1.4. Fluorescent calcium phosphate nanoparticles for tracking studies***

Fluorescent dual-labelled (with Cy5 and TAMRA) and single-labelled (either with Cy5 or with TAMRA) CaP nanoparticles were synthesized by wet-chemical precipitation. These were nanoparticles stabilized with fluorescent PEI-Cy5 and loaded with fluorescent TAMRA-conjugated peptides (TAMRAp) (CaP/PEI-Cy5/TAMRAp/SiO<sub>2</sub>), nanoparticles stabilized with non-fluorescent PEI and loaded with TAMRAp (CaP/PEI/TAMRAp/SiO<sub>2</sub>), and nanoparticles stabilized with fluorescent PEI-Cy5 and without TAMRAp loading (CaP/PEI-Cy5/SiO<sub>2</sub>). All types of the nanoparticles were silica-functionalized for protection of the peptide cargo from enzymatic degradation, if applicable, and for maintaining nanoparticle stability in biological media. The nanoparticles were applied in *in vitro* experiments on intracellular tracking inside J774A.1 cells. Both fluorescent dyes used in the experiments were detectable with UV/Vis spectrophotometry in the visible range of light: TAMRA (excitation = 552 nm; emission = 578 nm) and Cy5 (excitation = 651 nm; emission = 670 nm) without the risk of cross-talk in CLSM

imaging. TAMRAp, due to size and anionic similarity to the therapeutic siRNA, was used as model biomolecule to mimic intracellular route and processing of siRNA (used in gene silencing studies), and evaluate co-localization of the peptides and endolysosomes in the monocytes.<sup>243</sup>

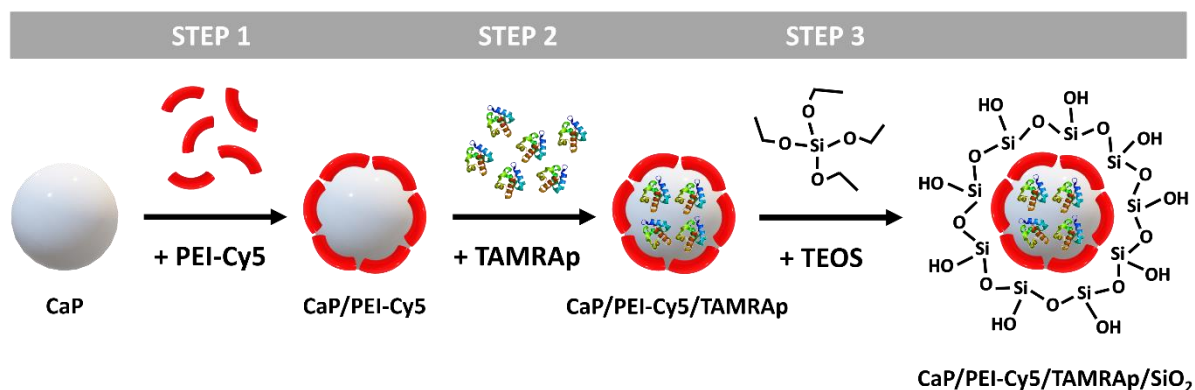


**Figure 23.** Schematic representation of the synthesis of fluorescent dual-labelled CaP nanoparticles for intracellular tracking experiments. Image of the peptide was adapted from [autismspectrumnews.org](http://autismspectrumnews.org).

In general, the synthesis of fluorescent peptide-loaded CaP nanoparticles was based on the protocol described in chapter 4.1.1.2. for synthesis of fluorescent siRNA-loaded CaP nanoparticles for gene silencing experiments (**Figure 23**). Loading with TAMRAp was performed in the same way as loading with siRNA, at a mass concentration of the peptide equal to the mass concentration of siRNA. The efficiency of nanoparticle loading with the peptides was determined by UV/Vis spectrophotometry based on detection of the free TAMRAp in the supernatant (at  $\lambda_{\max} = 205$  nm) after nanoparticle synthesis, using the NanoDrop instrument. It was assumed that the fraction of the peptide that was not found in the supernatant had been incorporated onto the nanoparticles. Single-labelled CaP nanoparticles were used as reference nanoparticles and to optimize settings for CLSM imaging.

#### 4.1.2. Dissolution experiments of CaP nanoparticles

A very important property of nanoparticles, in particular when applied in cell studies, is stability in biological media. This factor influences, for example, the drug release rate from the nanoparticles and is critical to obtain a sufficient drug concentration in the target site, and thus achieve an optimal therapeutic effect. Stability of fluorescent silica-functionalized (CaP/PEI-Cy5/SiO<sub>2</sub>) and unfunctionalized (CaP/PEI-Cy5) nanoparticles (described in chapter 4.1.1.1.)

was examined under lysosomal conditions. This was of particular importance because silica-coated CaP nanoparticles were later used in *in vitro* and *in vivo* studies, as carriers of therapeutic siRNA for gene silencing of NF- $\kappa$ B p65, and underwent lysosomal degradation in murine cells. Dissolution experiments were performed to mimic the acidic environment of the lysosomes and evaluate stability of the nanoparticles at lysosomal pH (4.5-5.5).<sup>244</sup> The experiments were carried out as follows: 1 mL of CaP nanoparticles without (CaP/PEI-Cy5) and with (CaP/PEI-Cy5/SiO<sub>2</sub>) silica shell was taken directly after synthesis and ultracentrifuged (14,800 rpm; 30 min; RT). The supernatant was collected and analyzed by UV/Vis spectrophotometry to evaluate loss of the Cy5 signal, due to ultracentrifugation. Nanoparticle pellets were then re-dispersed in 1 mL of the simulated lysosomal medium (pH 4.7) or in water (pH 7, as reference), in 1.5 mL reaction tubes, vortexed and incubated at 37 °C (body temperature) up to 48 h in darkness.<sup>245</sup> The measurement timepoints for the dissolution experiments were 1, 2, 3, 24 and 48 h after re-dispersion of the nanoparticles. At each timepoint, the sample was vortexed and ultracentrifuged. The supernatant was removed, and the nanoparticle pellet was dissolved in 10  $\mu$ L H<sub>2</sub>O:HCl (3:1) mixture and analyzed by UV/Vis (at  $\lambda_{\text{max}} = 639$  nm) for detection of the Cy5 signal, and calculation of the remaining amount of PEI-Cy5 which was still bound to the nanoparticles.<sup>242</sup> This corresponded to the dissolution rate of CaP nanoparticles at lysosomal and neutral pH.

#### **4.1.3. Preparation of Dy734-conjugated polyethyleneimine**

For whole body computed tomography imaging of nanoparticle-treated mice, CaP nanoparticles were labelled with the near-infrared (NIR) Dy734 dye instead of the far-red fluorophore (Cy5). A stable coupling between the NIR dye and CaP nanoparticles was desired. Dy734 fluorophore (in form of an NHS-ester) was covalently-attached *via* an amide bond to non-fluorescent PEI, based on the protocol described by Kollenda *et al.*<sup>246</sup> The conjugation reaction was performed as follows: 50 mg PEI were dissolved in 2.45 mL of DPBS and 0.05 mL (0.5 mg) Dy734-NHS-ester in DMSO was added to PEI solution. The coupling reaction was performed overnight with stirring at RT under light exclusion. After the reaction was completed, the dye-polymer complex was purified by spin filtration (Amicon<sup>®</sup> Ultra 4 mL) to remove the free Dy734 fluorophore. The complex was spin-filtered by centrifugation (4,000 rpm; 30 min; RT), washed twice with 3.5 mL ultrapure water and centrifuged each time. Next, the labelled polymer was shock frozen in liquid nitrogen and freeze-dried for 7 days (prolonged lyophilization time was necessary due to high density of the polymer). The possible loss of labelled PEI during sample purification was evaluated from the gravimetric difference of masses between PEI added to

the reaction and freeze-dried PEI-Dy734. Lyophilized PEI-Dy734 was dissolved in ultrapure water and the concentration of the labelled polymer in the stock solution was adjusted accordingly to synthesis requirements.

#### 4.1.4. Methods for nanoparticle characterization

All types of CaP nanoparticles, described in this thesis, were completely characterized by different analytical methods used in inorganic chemistry and scanning electron microscopy (SEM). DLS, using the Smoluchowski approximation, and  $\zeta$ -potential were used to study nanoparticle size, dispersion state (mono- or polydisperse) and colloidal stability, after each step of synthesis, as well as after nanoparticle lyophilization. For fluorescently-labelled nanoparticles, DLS measurements were performed using a fluorescence filter correction, to block undesirable emissions from the fluorescence and improve signal-to-noise ratio. Morphology and size of the nanoparticles were studied independently by SEM. Nanoparticle size determined by DLS was larger, when compared to SEM, due to the fact that in DLS, nanoparticles are measured in a colloidal state (hydrodynamic size), whereas in SEM the nanoparticles are measured in a dried state (size of the inorganic core without hydration shell). AAS was used to determine calcium and phosphate content in the nanoparticles. UV/Vis spectrophotometry was applied to determine PEI and biomolecule (antibodies, peptides, siRNA) concentrations in the nanoparticles, as well as to assess labelling of the fluorescent nanoparticles. Fluorescence spectroscopy was used to confirm the binding of Dy734 to PEI, validate fluorescence of Dy734-labelled nanoparticles and study possible cross-talk between fluorescent dyes Cy5 and TAMRA, with regard to dual-labelled nanoparticles. Microbial purity of nanoparticles, which were used for further biological experiments (*in vitro* and *in vivo*), was determined by Vis spectrophotometry (in the limulus amoebocyte lysate assay). Concentration of the nanoparticles, expressed as number of particles per mL of colloidal dispersion, was calculated based on the results obtained from SEM (nanoparticle radius) and AAS (calcium concentration in the nanoparticles), and the properties of hydroxyapatite, using the following equation:

$$N(\text{nanoparticles}) = \frac{[\text{Ca}] \cdot 2.51 \cdot 3}{\rho(\text{HA}) \cdot 4 \cdot \pi \cdot r^3}$$

$N(\text{nanoparticles})$  – number of nanoparticles

$[\text{Ca}]$  – calcium concentration in the nanoparticles (by AAS)

$\rho(HA)$  – density of hydroxyapatite ( $3.14 \text{ g cm}^{-3}$ )

$r$  – nanoparticle radius (by SEM)

For calculation purposes it was assumed that homogeneous spherical hydroxyapatite nanoparticles were formed in the syntheses. The factor 2.51 derived from the ratio of calcium in hydroxyapatite  $\frac{502.31 \text{ g mol}^{-1}}{5 \cdot 40.08 \text{ g mol}^{-1}}$  and multiplication by 3 originated from the formula for sphere volume determination  $V = \frac{4}{3} \cdot \pi \cdot r^3$ .

#### **4.1.5. Biological methods, cell lines and animals**

Biological *in vitro* and *in vivo* studies using CaP nanoparticles described in this thesis were performed by M.Sc. Elena K. Müller at Research Center Lobeda (University Hospital Jena, Germany) under supervision of Prof. Dr. Ingrid Hilger (Department of Experimental Radiology, Institute of Diagnostic and Interventional Radiology, University Hospital Jena). *In vitro* studies were performed using four different lines of murine blood compartment cells, which are key players in inflammatory processes. These were: monocytes (line: J774A.1), endothelial cells (line: SVEC4-10), B-lymphocytes (line: MOPC-315) and T-lymphocytes (line: TK-1). *In vivo* studies were performed in 8-week-old mice (strain: BALB/cJRj) with induced acute colitis (as model inflammatory disease) and in healthy mice, as control group.

##### **4.1.5.1. *In vitro* methods**

Nanoparticle uptake by cells and cytotoxicity were analyzed by flow cytometry with annexin-V-staining. Flow cytometry was also applied for characterization of the targets for ligands used for surface decoration of CaP nanoparticles and studies on nanoparticle uptake specificity by performing competition experiments with the ligands. CLSM was used to investigate the uptake of labelled nanoparticles by cells and to track them intracellularly. NF- $\kappa$ B p65 gene and protein expression levels were studied by real-time quantitative PCR (qPCR) and Western Blot, respectively, to evaluate the effect of gene silencing by nanoparticle-delivered siRNA. The impact of the nanoparticles on cellular cytokine expression levels was analyzed by the enzyme-linked immunosorbent assay (ELISA, LEGENDplex™).

#### **4.1.5.2. In vivo methods**

Mice were treated with dextran sodium sulfate to induce model acute intestinal inflammation (colitis).<sup>247</sup> The assessment of colitis severity was done based on determination of the disease activity index, which included three main animal body observation parameters: weight loss, stool consistency and rectal bleedings, studies on the colon length and hemogram analyzes. Biodistribution of the labelled nanoparticles, after intravenous tail injection into mice ( $2 \text{ mg}_{\text{siRNA}} \text{ kg}_{\text{bodyweight}}^{-1}$ ), was studied by *in vivo* and *ex vivo* whole body computed tomography imaging (IVIS<sup>®</sup> SpectrumCT, Perkin Elmer, USA) in anesthetized mice in compliance with the principles of ethical treatment of animals during laboratory experiments. The method is dedicated to pre-clinical 2D and 3D imaging of bioluminescence and fluorescence signals in small animals. The distribution of nanoparticles in the organs was analyzed accordingly, after mice were sacrificed. The assessment of inflammation in murine colon tissue was done based on immunostaining of paraffin tissue sections towards the detection of p65, I $\kappa$ B $\alpha$ , cytokine-inducible nitric oxide synthase (INOS), cyclooxygenase-2 (COX-2) and B-cell lymphoma-2 (Bcl-2) proteins, and recognition of histopathologic changes in the tissue by hematoxylin and eosin staining. The expression of inflammatory proteins in colon tissue and colonic leukocytes was studied by Western Blot. ELISA was used to detect presence of the inflammation marker Lipocalin-2 in feces, as well as to analyze the expression of inflammatory cytokines in the colon tissue and blood plasma (LEGENDplex<sup>™</sup>).

## **4.2. Project II – Chemistry of fossilized proboscidean enamel**

### **4.2.1. Proboscidean samples**

All studied proboscidean teeth samples (fossilized and recent) were identified and provided by Prof. Rajeev Patnaik (Department of Geology, Panjab University, Chandigarh, India). Most of the fossilized teeth were found by Prof. Patnaik in the Indian part of the Siwalik Hills (or the Siwaliks), which are located in the Himachal Pradesh State in North India (**Figure 24**).

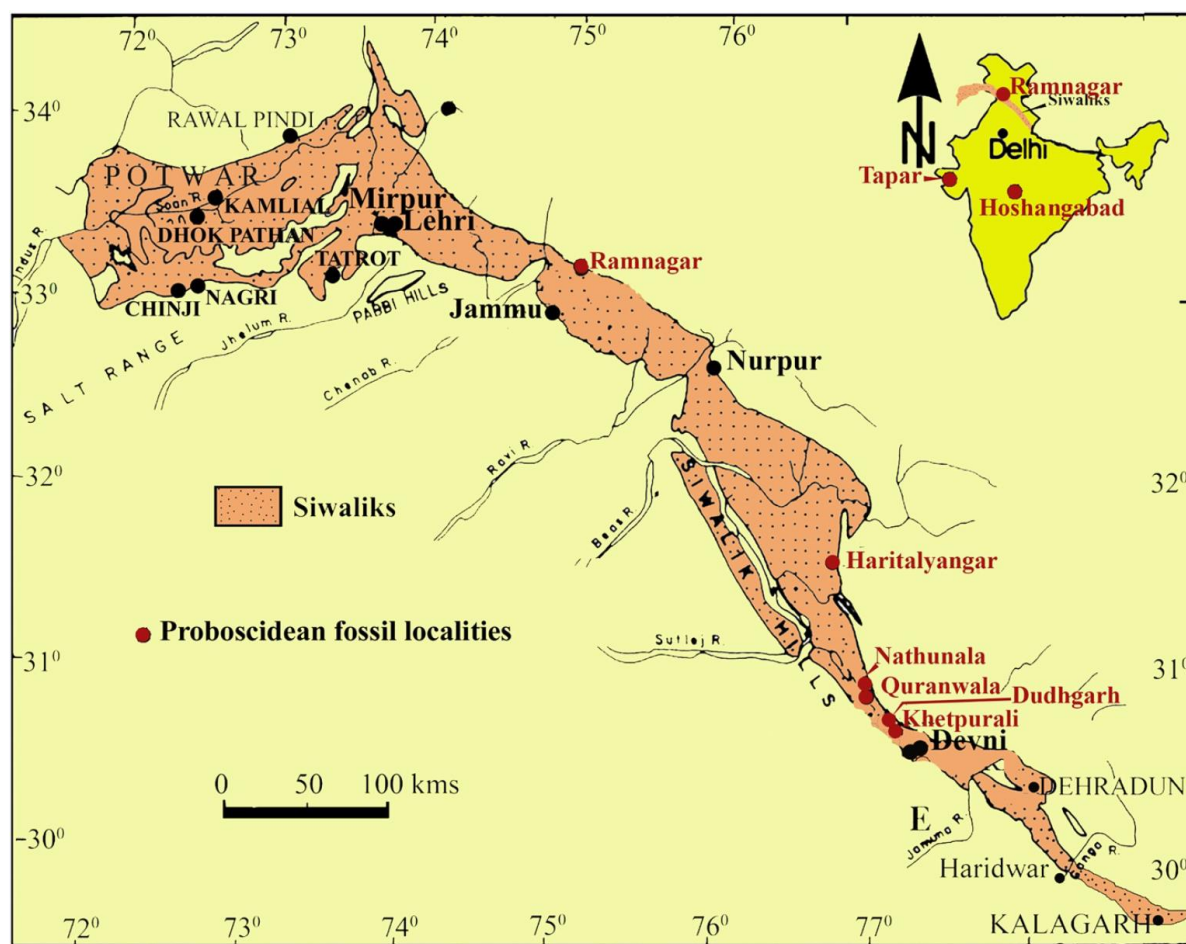


**Figure 24.** Fossil excavation localities in the Siwaliks (India). kms – kilometers. Figure adapted from Białas et al.<sup>248</sup>

These foothills of Himalaya are well-known for a rich paleodiversity of *Proboscidea* and occurrence of many Miocene-Pleistocene remains of extinct vertebrates.<sup>249-252</sup> These fossils are extremely valuable in studies on the paleoclimate, paleoenvironment and geological evolution of Himalaya. Together with Kutch (Western India) and Narmada Valley (Central India), the Siwaliks represent Neogene and Quaternary deposits of India, which are known for the abundance of late proboscidean fossils. In these studies, three enamel samples of early African elephants *Moeritherium* sp. and *Palaeomastodon* sp., found in Fayum Basin (Egypt), were additionally investigated for comparison purposes. Proboscidean remains of the age corresponding to the Egyptian samples (Eocene-dated) could not be found in India. An overview of investigated samples is presented in **Figure 25**, whereas their detailed description is summarized in **Table 4**. The samples covered the time range of ~34 Ma, from Eocene to the recent times (**Figure 26**).

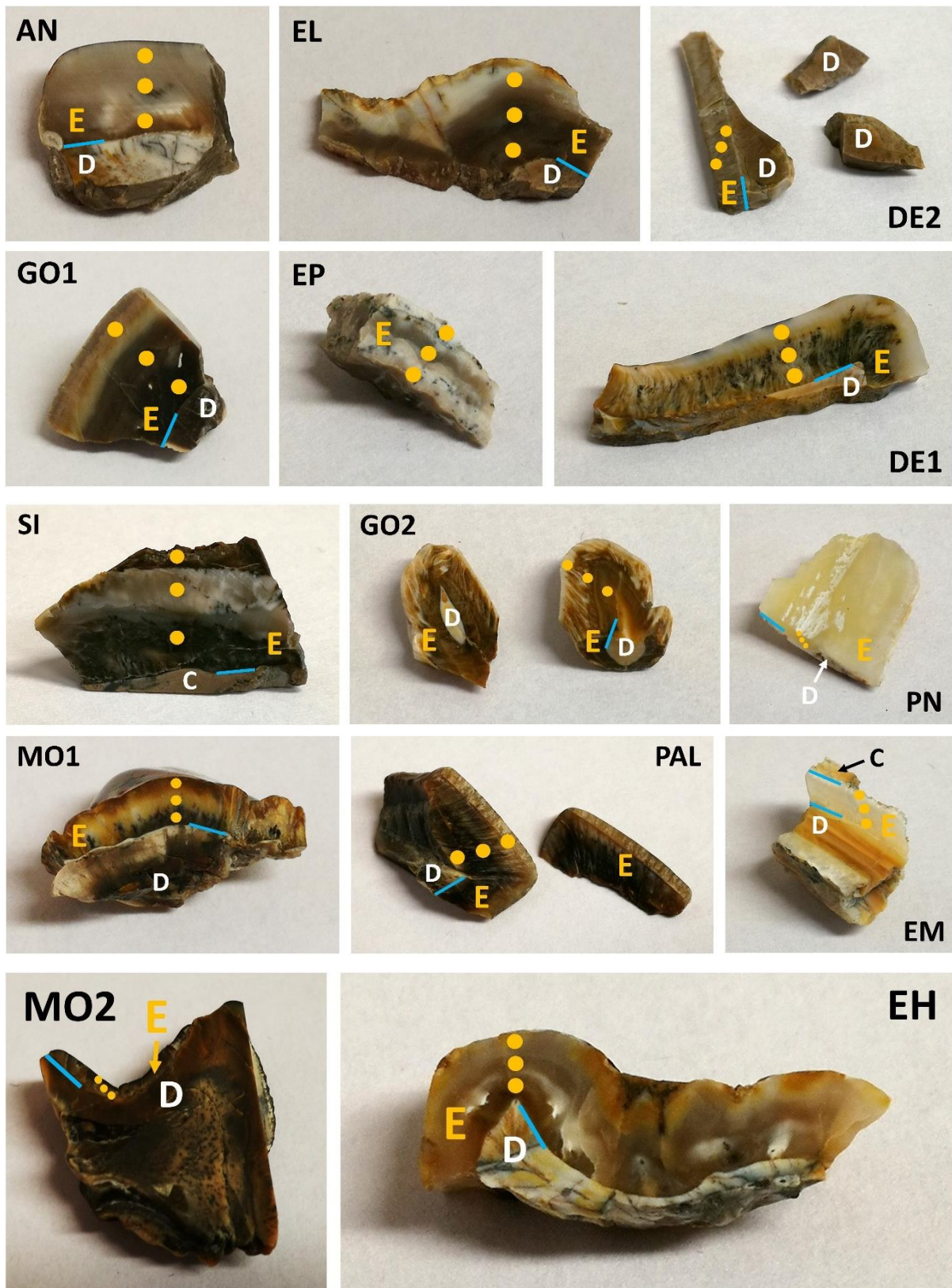


**Figure 25.** Photos of proboscidean tooth fragments used in these studies. 13 fossilized samples and 1 recent sample (EM) were investigated. The sample code is presented in **Table 4**. Most samples were composed of dentin (D) and enamel (E). Sample SI instead of dentin contained cement (C) and sample EM, beside enamel, was made of both dentin and cement. In studies

using SEM and energy-dispersive X-ray (EDX) spectroscopy, in each sample, three enamel regions (inner, middle, outer) were analyzed. They are marked with yellow dots. The blue line depicts localization of EDJ/enamel-cement junction (ECJ) in the samples.

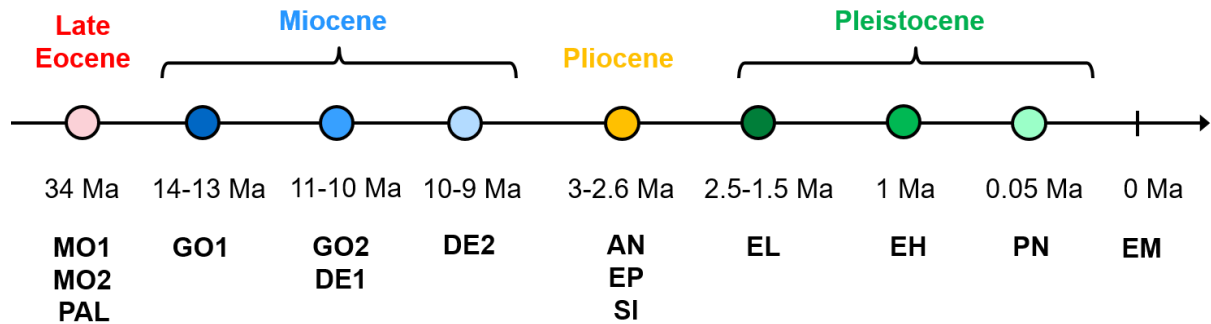


**Figure 26.** The age of studied Proboscidea on the geologic time scale. Ma – millions of years.

**Table 4.** Detailed description of the investigated proboscidean tooth samples.

Sample:	Taxa:	Stratigraphy:	Location:	Age / Ma:
MO1	<i>Moeritherium</i> sp.	Late Eocene, Birket Qarun Formation	Fayum, Egypt	~34
MO2	<i>Moeritherium</i> sp.	Late Eocene, Birket Qarun Formation	Fayum, Egypt	~34
PAL	<i>Palaeomastodon</i> sp.	Late Eocene, Birket Qarun Formation	Fayum, Egypt	~34
GO1	<i>Gomphotherium</i> sp.	Middle Miocene, Chinji Formation	Kulwanta (Ramnagar), India	~14-13
GO2	<i>Gomphotherium</i> sp.	Late Miocene, Khari Nadi Formation	Tapar (Kutch), India	~11-10
DE1	<i>Deinotherium</i> sp.	Late Miocene, Khari Nadi Formation	Tapar (Kutch), India	~11-10
DE2	<i>Deinotherium</i> sp.	Late Miocene, Dhok Pathan Formation	Haritalyangar, India	~10-9
AN	<i>Anancus</i> sp.	Late Pliocene, Tatrot Formation	Khetpurali, India	~3-2.6
SI	<i>Stegodon insignis</i>	Late Pliocene, Tatrot Formation	Nathunala, India	~3-2.6
EP	<i>Elephas platycephalus</i>	Late Pliocene, Tatrot Formation	Quranwala, India	~3-2.6
EL	<i>Elephas</i> sp.	Early Pleistocene, Pinjor Formation	Quranwala, India	~2.5-1.5
EH	<i>Elephas hysudricus</i>	Middle Pleistocene, Boulder Conglomerate	Dudhgarh, India	~1
PN	<i>Palaeoloxodon namadicus</i>	Late Pleistocene, Surajkund Formation	Hoshnagabad, India	~0.05
EM	<i>E. maximus</i>	Recent	Simlipal, India	0

#### 4.2.2. Preparation of samples and enamel characterization methods

Pulverized proboscidean enamel, obtained by precise drilling of tooth samples in the enamel region with jewelry diamond drills, was used for performing combustion analysis, and

measurements by AAS, ion-selective potentiometry, IR spectroscopy, thermogravimetry (TG), UV spectroscopy and X-ray powder diffraction (XRD).

Whole enamel samples were investigated by SEM combined with EDX. The samples were polished using an aqueous polycrystalline diamond suspension (ATM Qness; grain size: 3  $\mu\text{m}$ ), etched with 5% nitric acid (diluted from 65%) in absolute ethanol for 1 min, washed with ultrapure water (ELGA Purelab<sup>®</sup>) in an ultrasonic bath for 1 min, rinsed with absolute ethanol, heat-dried and sputter-coated with gold and palladium (80:20) for 30 s under vacuum. The microstructure of enamel and local distribution of selected elements in the enamel were analyzed by SEM (ESEM Quanta<sup>™</sup> 400 FEG) combined with EDX (SUTW-sapphire detector; resolution: 128.81; Lsec: 50) at an accelerating voltage of 15 kV. To determine the average diameter of crystals in the enamel, 100 crystals were measured from a SEM micrograph (for each sample). EDX was used to determine the content of aluminum (Al), calcium, chlorine (Cl), iron and silicon (Si) in different enamel regions (inner, middle, outer). For studies on the local distribution of selected elements, EDX mapping of whole tooth fragments containing dentin/cement and enamel was applied. The analysis was carried out in EDJ/ECJ region for 15 h, in the direction from tooth interior (dentin/cement) towards tooth surface (enamel). Combustion analysis was carried out to determine the content of carbon (C), hydrogen, nitrogen (N) and sulfur (S) in the enamel. For further elemental analyses, 50 mg of sample powder was dissolved in hydrochloric acid (37%) and the content of calcium, magnesium and sodium were determined by AAS, whereas the content of phosphate was determined by UV spectroscopy, as  $\text{PO}_4^{3-}$ -molybdenum blue complex. The amount of fluorine (F) in the enamel samples was determined, upon request, by Analytische Laboratorien (Lindlar, Germany) using an ion-selective potentiometer (pH/ION 735, WTW<sup>®</sup>, Germany). TG analyses were carried out to determine the content of adsorbed water, organic compounds and carbonated apatite in enamel samples. The measurements were performed in open alumina crucibles (using 20 mg of sample powder), in a dynamic oxygen atmosphere, with a heating rate of 2 K  $\text{min}^{-1}$  and in the temperature range of 30-1,400 °C. In order to investigate the type of substitution in carbonated apatite, IR spectroscopy was applied. For the analysis, 2 mg of pulverized enamel were ground with 200 mg of KBr (1:100) in an agate mortar, to very fine powder and pressed under vacuum at pressure of 5 t for 5 min to produce transparent pellet ( $\text{\O}$  13 mm). IR measurements were performed in the wavenumber range of 4,000-400  $\text{cm}^{-1}$ . Identification of the crystalline phase of apatite and possible diagenetic formation of other crystalline compounds in fossilized enamel, as well as quantification of the lattice parameters and crystallite size by Rietveld refinement were performed by XRD. The fine enamel powder was deposited on a flat silicon

single crystal sample holder to minimize scattering after dispersing the powder in ethanol for better homogenization. The samples were investigated in Bragg-Brentano geometry in a rotation mode with CuK $\alpha$  radiation (1.54 Å; 40 kV; 40 mA). XRD analyses were performed for 5-90 °2 $\theta$ , step size 0.01 °, counting time 0.6 s at each step, for a total measurement time of 90 min. The phase analysis was performed with the reference patterns of fluorapatite (#15-0876) from the ICDD database. For the determination of the lattice parameters  $a$ ,  $c$  and the crystallite size of hexagonal apatite, Rietveld refinement was performed by Dr. Oleg Prymak (Inorganic Chemistry, University of Duisburg-Essen). The instrumental correction of the diffractometer parameters was done by measuring a model sample (LaB6; NIST; SRM 660b;  $a = 4.16$  Å). Additionally, to evaluate the degree of diagenetic alteration of fossilized enamel, stable oxygen isotope ( $\delta^{18}\text{O}$ ) studies on eight proboscidean and one rhinocerotid enamel samples were performed in collaboration with Prof. Debayoti Paul (Department of Earth Sciences, Indian Institute of Technology, Kanpur, India) (**Table 15**). The samples originated from the same Neogene-Quaternary locations in India as proboscidean samples studied for the elemental composition and microstructure (**Table 4**). Isotope analyses were carried out using a TC/EA (high temperature conversion elemental analyzer) instrument combined with an isotope ratio mass spectrometer (Delta V Plus IRMS, Thermo-Finnigan, Germany) in a continuous flow mode.

### **4.3. Project III – Interactions between ultrasmall gold nanoparticles and bacteria**

#### **4.3.1. Ultrasmall fluorescent gold nanoparticles for studies with bacteria**

AuNPs, in cluster size range (diameter 1-3 nm),<sup>253</sup> were used in studies on particle uptake by bacteria. The ultrasmall nanoparticles (~2 nm) were fluorescently-labelled with bright and photostable fluorophores: sulfo-cyanine 3-alkyne (Cy3), 5-fluorescein-alkyne (FAM), fluorescein isothiocyanate (FITC) and Alexa Fluor<sup>®</sup> (AF) 647 (AF647), which are well suitable for advanced microscopic imaging using CLSM and structured illumination microscopy (SIM) (**Table 5**). Dyes used in these studies were purchased from the company Invitrogen<sup>™</sup> (USA).

*Table 5. Fluorophores applied in these studies and experimental conditions for dye excitation and emission by fluorescence microscopy.*

Dye:	Excitation (nm):	Emission (nm):	Visible color:	Laser line and power:	Imaging method:
AF647	650	665		Diode 642 nm (150 mW)	SIM
Cy3	550	570		Argon 514 nm (20 mW)	CLSM
DsRed2	561	587		DPSS 561 nm (20 mW)	CLSM
eGFP	488	509		Argon 488 nm (20 mW)/ OPSL 488 nm (200 mW)	CLSM/SIM
FAM	495	516		Argon 488 nm (20 mW)	CLSM
FITC	495	518		Argon 488 nm (20 mW)	CLSM
Propidium iodide	535	615		Argon 514 nm (20 mW)	CLSM

Most of used fluorophores (Cy3, FAM, AF647) were covalently-attached to AuNPs by click chemistry *via* copper-catalyzed azide-alkyne cycloaddition (CuAAC).<sup>254-256</sup> In contrast, FITC-labelled nanoparticles were prepared in a two-step synthesis in which, first, the ultrasmall AuNPs were functionalized with glutathione (GSH), and second, FITC was coupled to primary functional -NH<sub>2</sub> group of GSH.<sup>257,258</sup> The gold content in nanoparticle dispersions was determined by AAS and re-calculated to the number of AuNPs per volume unit. Concentration of the nanoparticles, expressed as number of particles per mL of colloidal dispersion, was calculated based on the results obtained from HRTEM and differential centrifugal sedimentation (nanoparticle radius) and AAS (gold concentration in the nanoparticles), and the properties of gold, using the following equation:

$$N(\text{nanoparticles}) = \frac{[\text{Au}] \cdot 3}{\rho(\text{Au}) \cdot 4 \cdot \pi \cdot r^3}$$

$N(\text{nanoparticles})$  – number of nanoparticles

$[\text{Au}]$  – gold concentration in the nanoparticles (by AAS)

$\rho(\text{Au})$  – density of gold (19.32 g cm<sup>-3</sup>)

$r$  – nanoparticle radius (by HRTEM and differential centrifugal sedimentation)

For calculation purposes it was assumed that homogeneous spherical gold nanoparticles were formed in the syntheses and multiplication by 3 originated from the formula for sphere volume determination  $V = \frac{4}{3} \cdot \pi \cdot r^3$ .

The amount of dye molecules attached to the nanoparticles was determined by UV/Vis spectrophotometry and fluorescence spectroscopy, using calibration curves for dye solutions. The ultrasmall fluorescent AuNPs, applied in studies on the interactions with *E. coli* cells, were provided by Dr. Selina van der Meer (Au-Click-Cy3, Au-Click-FAM), Dr. Tatjana Ruks (Au-GSH-FITC) and M.Sc. Kai Klein (Au-Click-AF647) (Inorganic Chemistry, University of Duisburg-Essen).

#### 4.3.2. Preparation of electrocompetent *E. coli* cells

Bacterial cells were made competent (which means ready to take up foreign DNA from the environment) for electrotransformation as follows: 50 mL of log-phase *E. coli* DH5 $\alpha$  culture were incubated on ice for 15 min and collected by centrifugation (4,000 rpm; 10 min; 4 °C). In order to wash cells and remove growth medium impurities, the bacterial pellet was re-suspended first in 50 mL and next in 25 mL of cold (4 °C) ultrapure water, vortexed and centrifuged. Next, the pellet was re-suspended in 5 mL of cold (4 °C) water:glycerol (9:1) mixture, vortexed and centrifuged. Finally, the pellet was re-suspended in 2.5 mL of cold water:glycerol mixture (as above), vortexed and aliquoted. Electrocompetent *E. coli* DH5 $\alpha$  cells were immediately frozen and stored at -80 °C until usage.

#### 4.3.3. Electrotransformation of *E. coli* cells

For the transformation of bacterial cells, 39  $\mu$ L of electrocompetent *E. coli* DH5 $\alpha$  cells were thoroughly mixed by pipetting with 1  $\mu$ L (115 ng) eGFP- and ampicillin resistance-carrying plasmid DNA (pGEX-6P-1-eGFP; **Figure 27**) and incubated for 1 min on ice. Next, the sample was transferred to a pre-cooled electroporation cuvette and rapidly transformed with an electric pulse (25  $\mu$ F; 1.8 kV; 5 ms). After electroporation, 0.9 mL of LB medium, pre-warmed to 37 °C, was immediately added to transformed bacteria, the cell suspension was transferred into a new reaction tube and incubated with intensive shaking in a thermomixer at 37 °C for 1 h. Next, the culture was centrifuged (4,000 rpm; 10 min; RT), 2/3 of the supernatant was removed, and the remaining 1/3 volume of the supernatant was used to re-suspend the bacterial pellet. 0.1 mL of the bacterial suspension was spread-plated on ampicillin-supplemented LB plate and

incubated overnight at 37 °C for selective isolation of eGFP-positive bacterial colonies. A log-phase liquid culture of transformed *E. coli* DH5 $\alpha$ -eGFP cells was grown by single-colony inoculation (after performing streak plating), mixed with glycerol as cryoprotectant (1/4; v/v), aliquoted, immediately frozen and stored at -80 °C until usage.

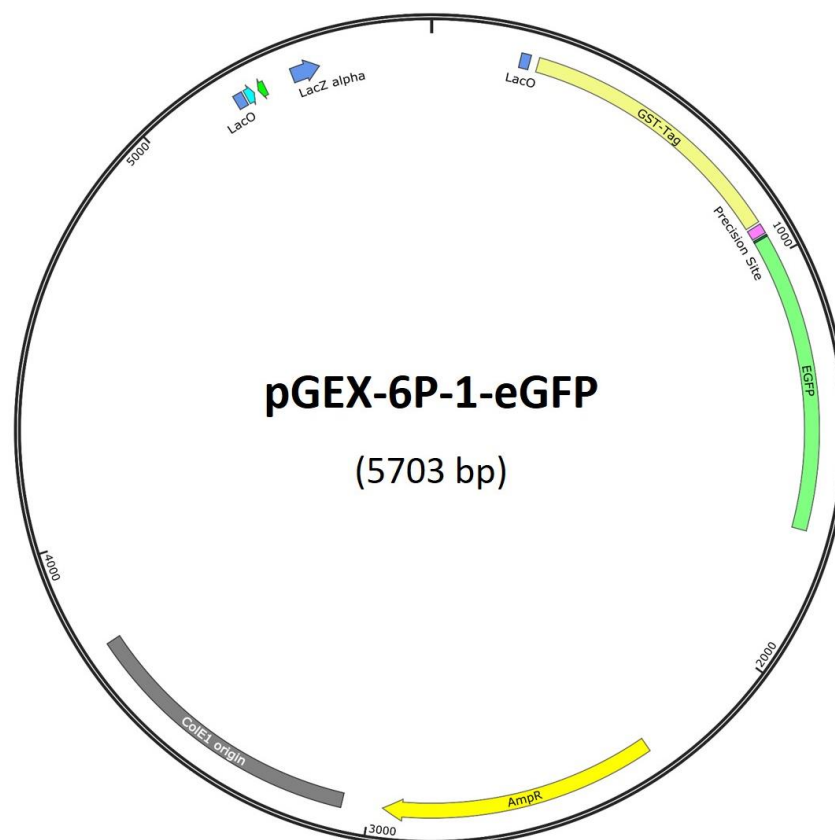


**Figure 27.** Molecular map of pGEX-6P-1-eGFP plasmid used for electrotransformation of *E. coli* DH5 $\alpha$  cells. The expression of plasmid-encoded genes was controlled by the Lac operon. Amp<sup>R</sup> – ampicillin resistance, bp – base pair, ColE1 – colicin E1 plasmid DNA, GST – GSH-S-transferase. The map was provided by Dr. Sebastian Kollenda (Inorganic Chemistry, University of Duisburg-Essen).

#### 4.3.4. Stimulation of eGFP expression in bacteria

For stimulation of eGFP expression in bacteria, IPTG was used. On the molecular level, IPTG mimics allolactose, which is the natural activator of Lac operon transcription. The activation results in expression of proteins encoded by genes controlled by the Lac.<sup>259</sup> In brief, IPTG was added to 50 mL of log-phase *E. coli* DH5 $\alpha$ -eGFP culture (derived from an overnight culture) to a concentration of 0.4 mM IPTG in the cell culture. Next, bacteria were grown overnight

under light exclusion at 30 °C with orbital shaking (130 rpm). Fluorescence microscopy was applied to assess fluorescent protein expression in bacterial cells. In case of *E. coli* TOP10, the expression of fluorescent DsRed2 protein was not stimulated externally, as eGFP, and was constant in bacteria during the growth. Thus, TOP10 strain required prolonged cultivation periods and stationary-phase cultures of these bacteria were used for all experiments.

#### 4.3.5. Incubation of bacteria with ultrasmall gold nanoparticles for CLSM imaging

For uptake studies, 0.2 mL ( $1 \cdot 10^9$  CFU mL<sup>-1</sup>) of log-phase cultures of *E. coli* strains DH5 $\alpha$ -eGFP and TOP10 were mixed with dispersions of Cy3-labelled (10  $\mu$ L; 0.5 mg<sub>Au</sub> mL<sup>-1</sup>) and FAM-labelled (70  $\mu$ L; 0.07 mg<sub>Au</sub> mL<sup>-1</sup>) ultrasmall AuNPs, respectively. This ensured the final dose of gold for the incubation with bacteria ( $\sim 25$   $\mu$ g<sub>Au</sub> mL<sup>-1</sup>), independently on the nanoparticle formulation. By assuming an average nanoparticle diameter of 2 nm, this corresponded to  $3.1 \cdot 10^{14}$  nanoparticles mL<sup>-1</sup>. Furthermore, taking into account the culture density of  $1 \cdot 10^9$  bacterial cells mL<sup>-1</sup>, the initial dose of AuNPs was  $3.1 \cdot 10^5$  particles per bacterial cell. Bacteria were incubated with the nanoparticles (Au-Click-Cy3, Au-Click-FAM) for 2 h at 37 °C in darkness and prepared for CLSM imaging. 20  $\mu$ L of the sample were placed on a glass cover slip and left to dry at RT. Next, bacteria were fixed (killed) with 4% paraformaldehyde (pH 7.4) for 8 min at 37 °C, the sample was carefully washed twice with ultrapure water and again left to dry at RT. Finally, 20  $\mu$ L of the Fluoromount-G™ mounting medium were placed on a glass microscope slide and the cover slip (with the dried sample) was very carefully immersed in the mounting medium, avoiding air bubbles. After 24 h, edges of the cover slip were secured with transparent nail polish, to prevent desiccation of the mounting medium, and to enable a long-term storage of the sample at 4 °C in darkness without losing its fluorescent properties. Samples prepared in that way were studied by CLSM. Microscope laser settings for fluorescent imaging are described in **Table 5**. The samples were observed under oil immersion, at a magnification of 63x. To identify nanoparticles taken up by bacterial cells, z-stacks were acquired (step size 0.1  $\mu$ m). To study possible cross-talk between fluorescent signals of labelled bacteria and nanoparticles, control samples of just bacteria and just nanoparticles were prepared and analyzed by CLSM using the same microscope settings as for the uptake studies.

For comparison purposes, reference samples of bacteria incubated just with water-dissolved fluorescent dyes (Cy3 and FAM) were prepared. All experimental conditions were the same as for the uptake studies. Aqueous fluorophore solutions of the same volume as nanoparticle dispersions were used. *E. coli* DH5 $\alpha$ -eGFP and TOP10 cells were mixed with 10  $\mu$ L of 50  $\mu$ M Cy3 solution (final dye concentration in the reaction tube: 2.5  $\mu$ M) and 70  $\mu$ L of 20  $\mu$ M FAM

solution (final dye concentration in the reaction tube: 7  $\mu\text{M}$ ), respectively. Imaging of the samples was performed by CLSM, as described above for the uptake studies.

#### **4.3.6. Studies on gold nanoparticle cytotoxicity in bacteria**

To evaluate the potential cytotoxicity of ultrasmall AuNPs to bacteria, non-fluorescent *E. coli* DH5 $\alpha$  cells were incubated with FITC-labelled AuNPs (20  $\mu\text{L}$ ; 0.25  $\text{mg}_{\text{Au}} \text{mL}^{-1}$ ) under the same conditions as for the uptake studies. After incubation, prior to preparation of the samples for CLSM imaging (as described in chapter 4.3.5.), bacterial cultures were additionally stained with propidium iodide, according to the manufacturer's protocol (Invitrogen<sup>TM</sup>, USA), for detection of dead cells. Thus, only one part of the staining kit was used. Propidium iodide is a membrane-impermeant dye, which binds to double-stranded DNA by intercalation and is used as dead cell marker in commercially available LIVE/DEAD staining kits.<sup>260</sup> Important is, that propidium iodide staining of bacteria was done before cell fixation. Microscope laser settings for CLSM imaging are described in **Table 5**.

#### **4.3.7. Incubation of bacteria with ultrasmall gold nanoparticles for SIM imaging**

For uptake studies, 0.2 mL ( $1.5 \cdot 10^8 \text{ CFU mL}^{-1}$ ) of log-phase culture of *E. coli* DH5 $\alpha$ -eGFP was mixed with a dispersion of AF647-labelled (5  $\mu\text{L}$ ; 1  $\text{mg}_{\text{Au}} \text{mL}^{-1}$ ) ultrasmall AuNPs. This gave the gold dose of  $\sim 25 \mu\text{g}_{\text{Au}} \text{mL}^{-1}$  which, assuming an average nanoparticle diameter of 2 nm, corresponded to the number of  $3.1 \cdot 10^{14}$  nanoparticles  $\text{mL}^{-1}$ . Furthermore, taking into account the culture density of  $1.5 \cdot 10^8$  bacterial cells  $\text{mL}^{-1}$ , the initial dose of AuNPs was  $2.1 \cdot 10^6$  particles per bacterial cell. Bacteria were incubated with the nanoparticles (Au-Click-AF647) for 1 h and 3 h at 37 °C in darkness, and prepared for SIM imaging. Preparation and storage procedure for SIM samples was the same as for the CLSM samples (described in chapter 4.3.5.). Microscope laser settings for SIM imaging are described in **Table 5**. The samples were observed under oil immersion, at a magnification of 100x. To identify nanoparticles taken up by bacterial cells, z-stacks were acquired (step size 0.1  $\mu\text{m}$ ). To study the possibility of cross-talk between fluorescent signals of labelled bacteria and nanoparticles, control samples of just bacteria and just nanoparticles were prepared and analyzed by SIM using the same microscope settings as for the uptake studies. SIM processing of the images was performed with the ZEN system 2012 software (Carl Zeiss, Germany).

#### 4.3.8. Incubation of bacteria with ultrasmall gold nanoparticles for FACS studies

For fluorescence-assisted cell sorting (FACS) analyses, 1 mL ( $1.5 \cdot 10^8$  CFU mL<sup>-1</sup>) of log-phase *E. coli* DH5 $\alpha$ -eGFP culture was mixed with dispersions of AF647-labelled (5, 10, 20, 40 and 80  $\mu$ L; 1 mg<sub>Au</sub> mL<sup>-1</sup>) ultrasmall AuNPs. By assuming an average nanoparticle diameter of 2 nm, this corresponded to the number of  $6.2 \cdot 10^{13}$  to  $9.9 \cdot 10^{14}$  nanoparticles mL<sup>-1</sup>. Taking into account the CFU value of the bacterial culture, the initial dose of AuNPs could be re-calculated to  $4.1 \cdot 10^5$  to  $6.6 \cdot 10^6$  particles per bacterial cell. Bacteria were incubated with the nanoparticles (Au-Click-AF647) for 1 h at 37 °C in darkness. Next, bacteria were paraformaldehyde-fixed and washed twice with ultrapure water. During fixation and washing steps, bacterial cells were harvested by centrifugation (4,000 rpm; 10 min; RT). Finally, the bacterial pellets were re-suspended in 0.3 mL of cold (4 °C) FACS buffer (DPBS supplemented with 2% FCS and 2 mM EDTA). All samples were prepared and measured in triplicates. As nanoparticle-negative control in the uptake studies, non-exposed to nanoparticles *E. coli* DH5 $\alpha$ -eGFP cells were used. The uptake of fluorescent ultrasmall AuNPs by bacteria was quantified with a flow cytometer (LSR II, BD Biosciences, USA). The frequency of nanoparticle-positive and eGFP-expressing bacteria, as well as mean fluorescence intensity (MFI) were analyzed using the DIVA software (BD Biosciences, USA). Statistical analysis was performed by ordinary one-way ANOVA, followed by Tukey's multiple comparisons test. FACS analyses were carried out in collaboration with Dr. Torben Knuschke (Institute of Medical Microbiology, University Hospital Essen).

## 5. Results and discussion

### 5.1. Project I – Bioactive calcium phosphate (CaP) nanoparticles for NF- $\kappa$ B silencing

#### 5.1.1. Characterization of CaP nanoparticles for dissolution studies

Fluorescent CaP nanoparticles used in *in vitro* dissolution experiments were “basic” nanoparticles with a simple structure, when compared to other types of CaP nanoparticles described in this thesis, however, they served as model to mimic the intracellular behavior of nanoparticles after internalization into lysosomes. The nanoparticles were spherical, monodisperse, positively-charged and colloidally stable (**Figures 28-29; Table 6**). Two types of nanoparticles were applied to study dissolution kinetics of CaP nanoparticles under acidic lysosomal conditions. These were unfunctionalized nanoparticles (CaP/PEI-Cy5) and nanoparticles functionalized with silica shell (CaP/PEI-Cy5/SiO<sub>2</sub>). The nanoparticles were re-dispersed and incubated either in the simulated lysosomal medium (pH 4.7) or in water (pH 7). The dissolution rate in the simulated lysosomal medium and in water was significantly higher for non-functionalized nanoparticles. This confirmed the importance of the silica shell, as a protective layer, for CaP nanoparticles and their potential biomolecule cargo. The dissolution rate of silica-functionalized nanoparticles was slower during first three hours of incubation in the simulated lysosomal medium, when compared to the unfunctionalized nanoparticles (**Figure 30**). This is beneficial for a prolonged release rate of the biomolecules from the nanoparticles. Furthermore, it allows to obtain a stable concentration of the therapeutic in the target site, for a longer period of time, and thus achieve an optimal healing effect. However, it has to be underlined, that acidic conditions strongly favored dissolution of CaP nanoparticles, independently on their formulation.

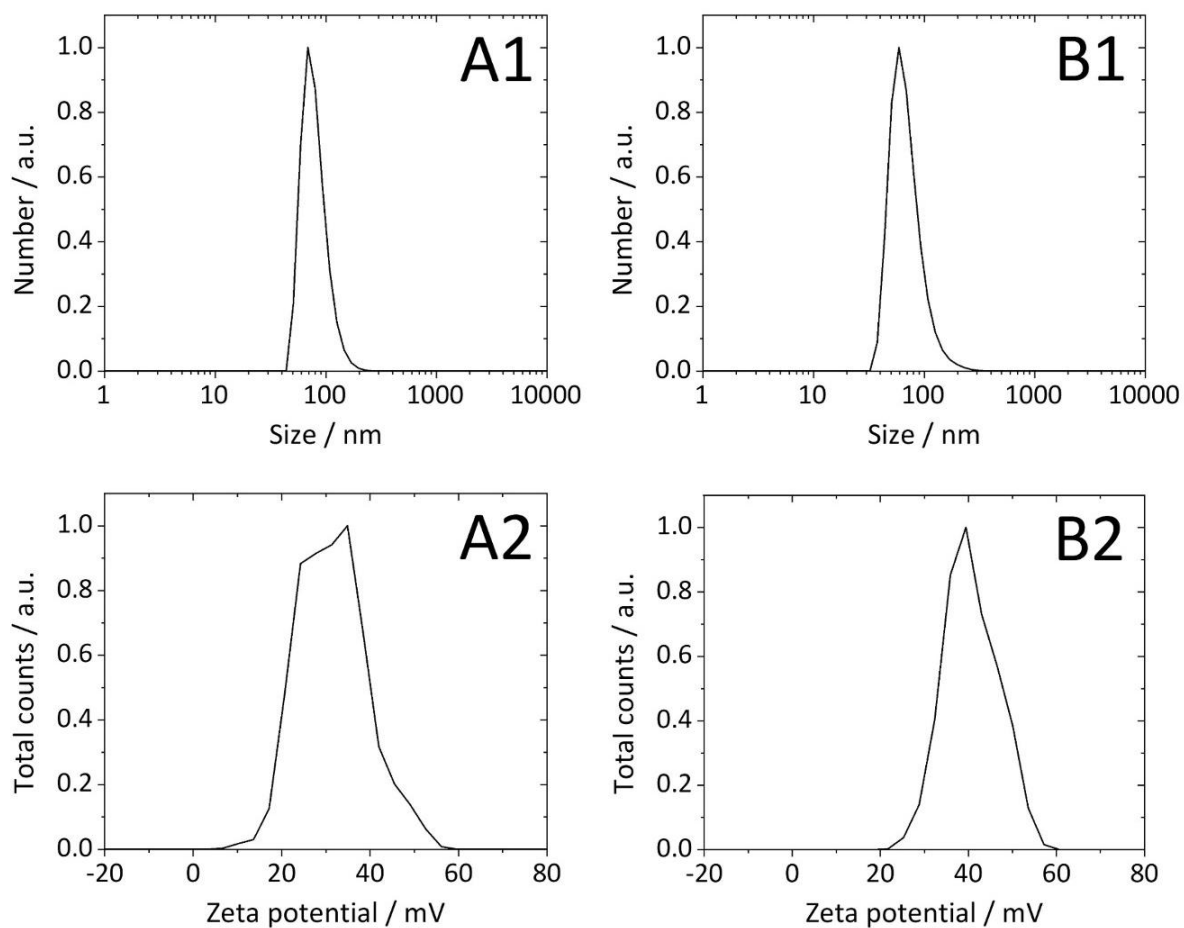


**Figure 28.** Normalized particle size distributions (**A1-B1**) and the corresponding  $\zeta$ -potentials (**A2-B2**) of fluorescent CaP nanoparticles without (**A1, A2**; CaP/PEI-Cy5) and with (**B1, B2**; CaP/PEI-Cy5/SiO<sub>2</sub>) silica shell, used in dissolution studies.

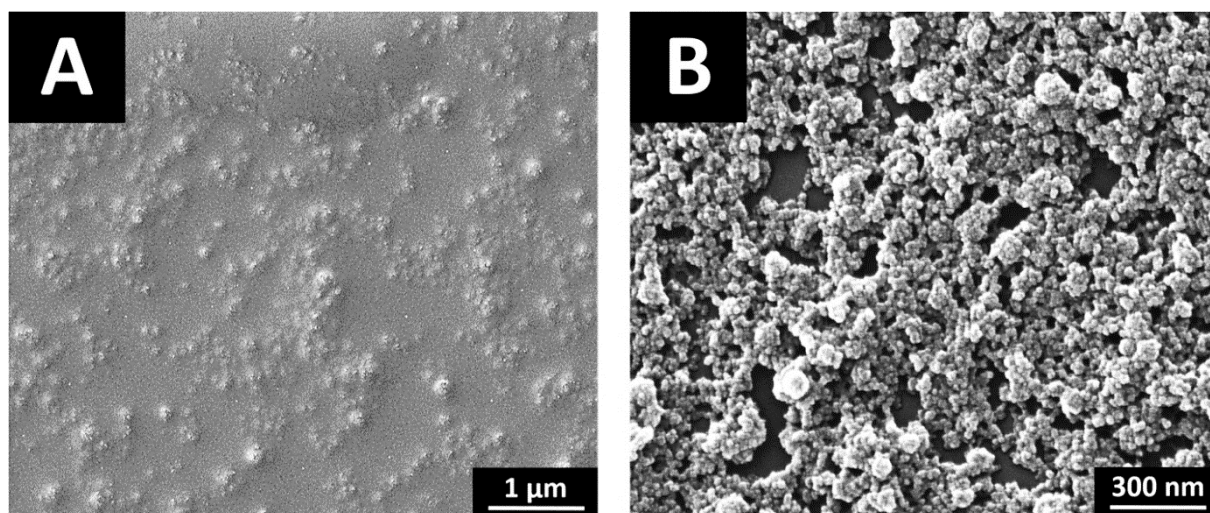


**Figure 29.** SEM micrographs of fluorescent CaP nanoparticles without (**A**; CaP/PEI-Cy5) and with (**B**; CaP/PEI-Cy5/SiO<sub>2</sub>) silica shell, used in dissolution experiments.

**Table 6.** Characterization data of CaP nanoparticles used in dissolution studies. conc. – concentration, PDI – polydispersity index.

Characterization parameter:	CaP/PEI-Cy5	CaP/PEI-Cy5/SiO <sub>2</sub>
Size by SEM / nm	24 ± 7	64 ± 7
Size by DLS / nm	107 ± 1	138 ± 28
PDI	0.07 ± 0.01	0.33 ± 0.09
ζ-potential / mV	32 ± 1	24 ± 3
Ca <sup>2+</sup> conc. / μg mL <sup>-1</sup>	117	55
PO <sub>4</sub> <sup>3-</sup> conc. / μg mL <sup>-1</sup>	230	-
CaP conc. / μg mL <sup>-1</sup>	293	138
PEI conc. / μg mL <sup>-1</sup>	136	170
Particle conc. / mL <sup>-1</sup>	1.29·10 <sup>13</sup>	3.21·10 <sup>11</sup>

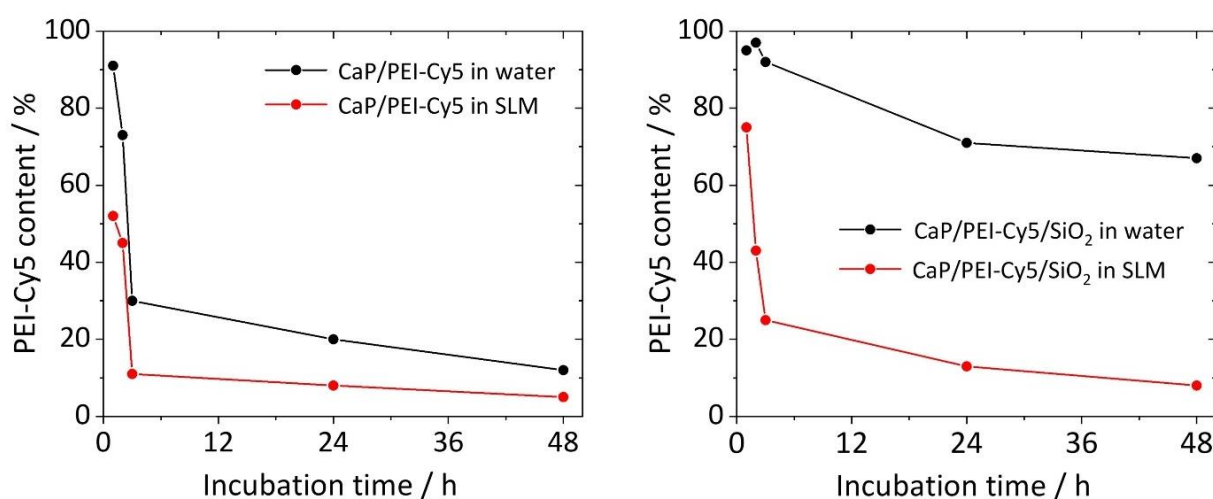


**Figure 30.** Dissolution kinetics of unfunctionalized (**left**; CaP/PEI-Cy5) and silica-functionalized (**right**; CaP/PEI-Cy5/SiO<sub>2</sub>) CaP nanoparticles after incubation in the simulated lysosomal medium (pH 4.7; **red curve**) and in water (pH 7; **black curve**) at 37 °C in darkness. Percentage of PEI-Cy5 content in the nanoparticles was determined by UV/Vis spectrophotometry. SLM – simulated lysosomal medium.

### 5.1.2. Characterization of CaP nanoparticles for gene silencing of NF-κB p65

Fluorescent bioactive (siRNA-loaded) CaP nanoparticles were used in *in vitro* and *in vivo* experiments on gene silencing of NF-κB p65 in inflamed murine monocytes and mice with acute intestinal inflammation (dextran sodium sulfate-induced colitis), respectively. On the

molecular level, nanoparticle-delivered siRNA inhibited the expression of the p65 subunit of NF- $\kappa$ B, which resulted in downregulation of NF- $\kappa$ B expression (**Figure 31**).

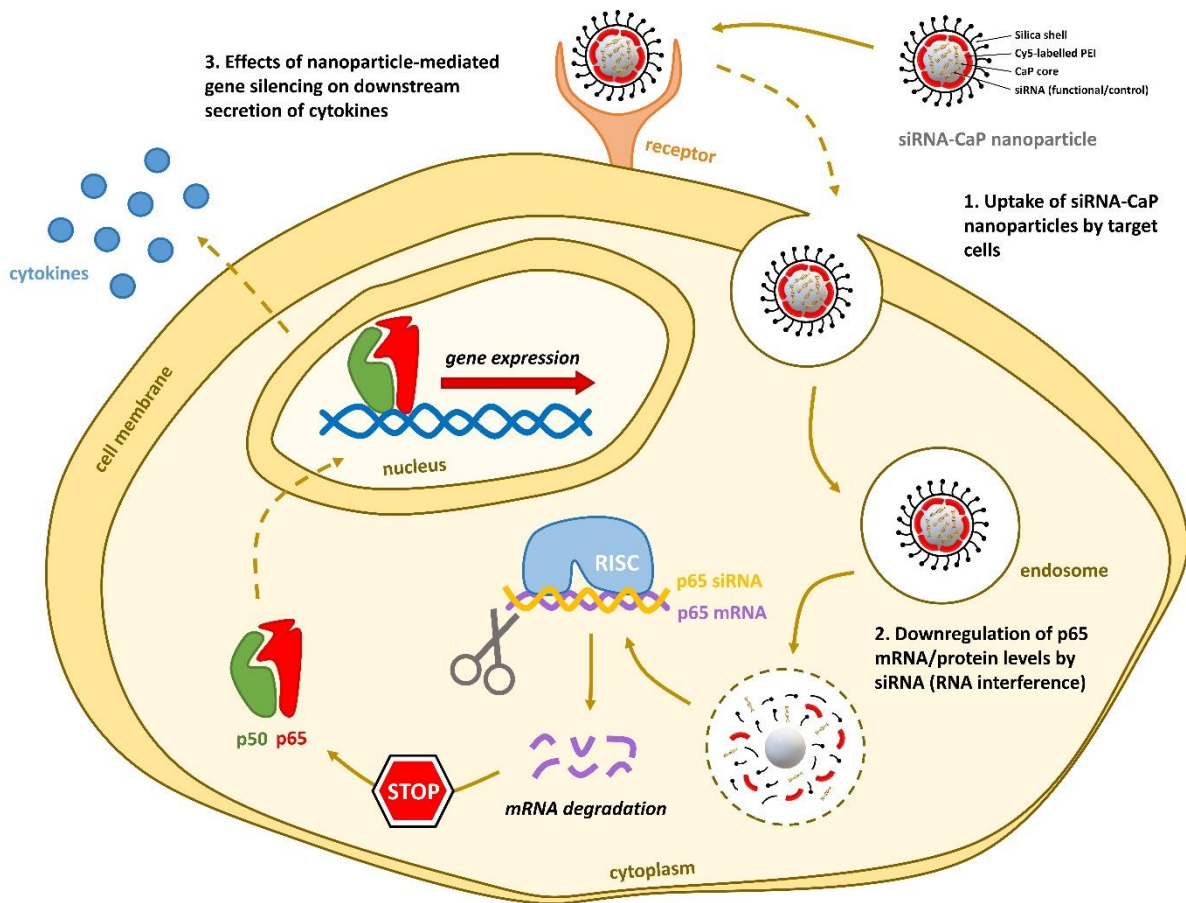


**Figure 31.** Molecular principle of NF- $\kappa$ B downregulation in cells using nanoparticle-delivered siRNA. Detailed description of the molecular mode of action of NF- $\kappa$ B is presented in chapter 2.1.6. p – protein.

All types of CaP nanoparticles used in NF- $\kappa$ B p65 gene silencing experiments were silica-functionalized for maximum biomolecule protection. In *in vitro* studies on gene silencing, Cy5-labelled nanoparticles were applied, as the Cy5 dye is a bright and photostable far-red fluorophore well-suited for CLSM imaging. These were: CaP nanoparticles loaded with functional anti-NF- $\kappa$ B p65 siRNA (CaP/PEI-Cy5/siRNAf/SiO<sub>2</sub>), nanoparticles loaded with control siRNA without the gene silencing effect (CaP/PEI-Cy5/siRNAc/SiO<sub>2</sub>) and reference nanoparticles without siRNA loading (CaP/PEI-Cy5/SiO<sub>2</sub>). In *in vivo* gene silencing experiments, similar siRNA-loaded CaP nanoparticle formulations were prepared, with the difference that instead of PEI-Cy5 the nanoparticles were stabilized and labelled with PEI-Dy734. These were: CaP/PEI-Dy734/siRNAf/SiO<sub>2</sub>, CaP/PEI-Dy734/siRNAc/SiO<sub>2</sub> and

CaP/PEI-Dy734/SiO<sub>2</sub> nanoparticles, accordingly. Dy734 is a bright and photostable NIR fluorophore well-suited for whole body computed tomography imaging. The great advantage of working in the NIR emission range is that animal tissues generate minimal autofluorescence during NIR imaging. Furthermore, strong tissue penetration and minimal light scattering of the NIR emission allows to study *in vivo* biodistribution of NIR-labelled CaP nanoparticles in mice in a non-invasive way with high resolution.<sup>261</sup> Prior to nanoparticle preparation, PEI-Dy734 conjugation reaction was performed (chapter 4.1.3.), based on the protocol described by Kollenda *et al.*, to obtain a labelled polymer with covalently-attached NIR dye.<sup>246</sup> No loss of PEI during sample processing was detected. The final concentration of PEI-Dy734 stock solution was 20 mg mL<sup>-1</sup>. A comparison of the fluorescence emission spectra of the free Dy734 dye and PEI-Dy734 conjugate revealed that attachment of the NIR fluorophore to the polymer almost did not alter emission properties of the dye, as only a marginal shift (1 nm) of the emission maximum was observed. Furthermore, the emission peak of polymer-attached fluorophore was narrow and more wavelength-specific than the emission peak of the free dye. PEI-Dy734 excited at  $\lambda = 720$  nm demonstrated strong fluorescence in the NIR range, with an emission maximum at  $\lambda = 749$  nm (**Figure 32**).

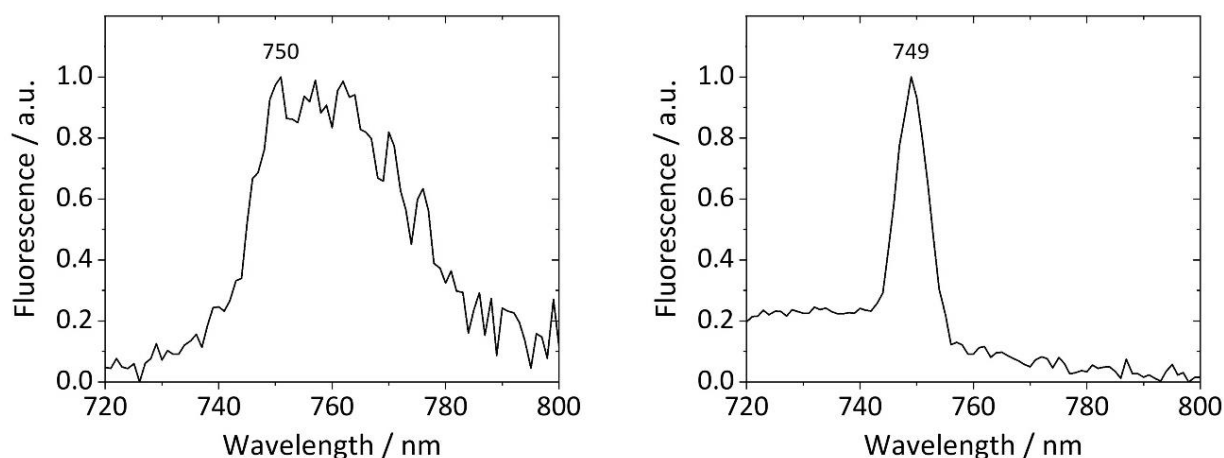


**Figure 32.** Fluorescence emission spectra of the free Dy734 dye (**left**) and PEI-conjugated Dy734 (**right**) with emission maxima at  $\lambda = 750$  nm and 749 nm, respectively. The samples were excited at  $\lambda = 720$  nm.

All nanoparticles used in NF- $\kappa$ B p65 gene silencing studies were spherical, monodisperse, positively-charged and colloidally stable (**Figures 33-36; Tables 7-8**).

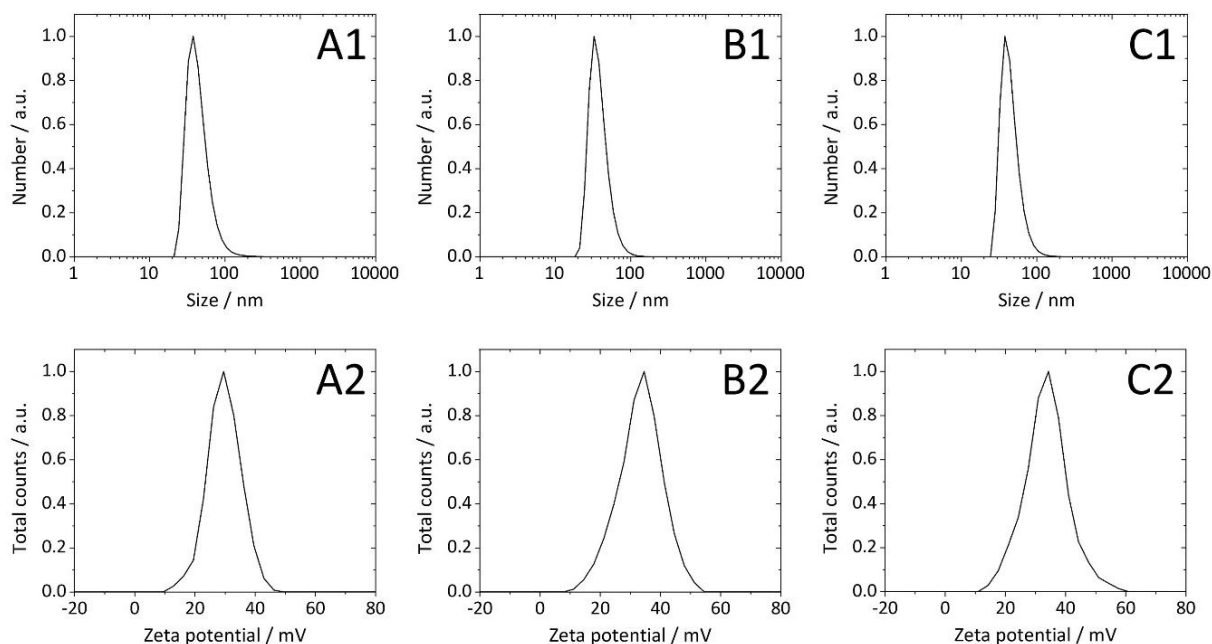


**Figure 33.** Normalized particle size distributions (A1-C1) and the corresponding  $\zeta$ -potentials (A2-C2) of representative Cy5-labelled CaP nanoparticles, from typical synthesis batches, loaded with functional siRNA (A1, A2; CaP/PEI-Cy5/siRNAf/SiO<sub>2</sub>) or with control siRNA (B1, B2; CaP/PEI-Cy5/siRNAc/SiO<sub>2</sub>) and of reference nanoparticles without siRNA loading (C1, C2; CaP/PEI-Cy5/SiO<sub>2</sub>). The nanoparticles were applied in *in vitro* gene silencing studies.

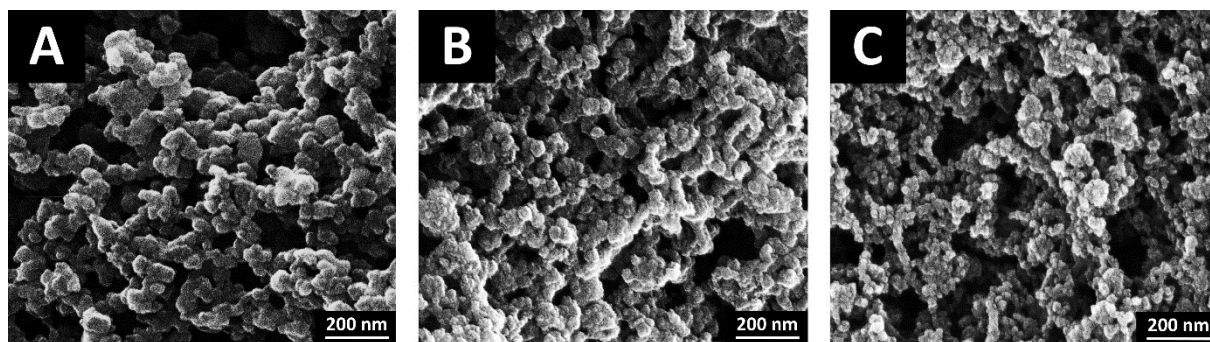


**Figure 34.** SEM micrographs of representative Cy5-labelled CaP nanoparticles, from typical synthesis batches, loaded with functional siRNA (A; CaP/PEI-Cy5/siRNAf/SiO<sub>2</sub>) or with control siRNA (B; CaP/PEI-Cy5/siRNAc/SiO<sub>2</sub>) and of reference nanoparticles without siRNA loading (C; CaP/PEI-Cy5/SiO<sub>2</sub>). The nanoparticles were applied in *in vitro* gene silencing experiments.

**Table 7.** Characterization data of representative CaP nanoparticles, from typical synthesis batches, used in *in vitro* gene silencing studies.

Characterization parameter:	CaP/PEI-Cy5/siRNAf/SiO <sub>2</sub>	CaP/PEI-Cy5/siRNAc/SiO <sub>2</sub>	CaP/PEI-Cy5/SiO <sub>2</sub>
Size by SEM / nm	53 ± 9	52 ± 7	62 ± 8
Size by DLS / nm	273 ± 27	250 ± 25	146 ± 15
PDI	0.26 ± 0.04	0.25 ± 0.01	0.27 ± 0.06
ζ-potential / mV	25 ± 3	27 ± 3	26 ± 3
Ca <sup>2+</sup> conc. / μg mL <sup>-1</sup>	40	37	52
CaP conc. / μg mL <sup>-1</sup>	100	93	130
siRNA conc. / μg mL <sup>-1</sup>	36	35	-
siRNA per particle	3,980	3,950	-
PEI conc. / μg mL <sup>-1</sup>	62	93	65
Endotoxins / EU mL <sup>-1</sup>	0.04	0.03	0.05
Particle conc. / mL <sup>-1</sup>	4.02·10 <sup>11</sup>	4.03·10 <sup>11</sup>	3.35·10 <sup>11</sup>

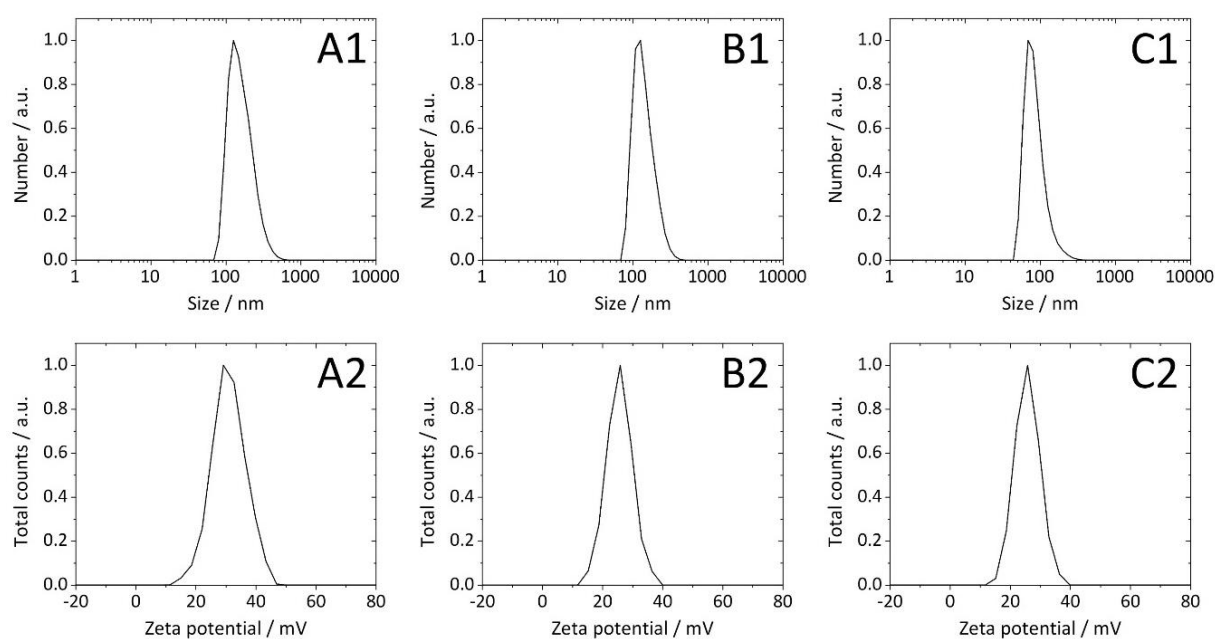


**Figure 35.** Normalized particle size distributions (A1-C1) and the corresponding ζ-potentials (A2-C2) of representative Dy734-labelled CaP nanoparticles, from typical synthesis batches, loaded with functional siRNA (A1, A2; CaP/PEI-Dy734/siRNAf/SiO<sub>2</sub>) or with control siRNA (B1, B2; CaP/PEI-Dy734/siRNAc/SiO<sub>2</sub>) and of reference nanoparticles without siRNA loading (C1, C2; CaP/PEI-Dy734/SiO<sub>2</sub>). The nanoparticles were applied in *in vivo* gene silencing studies.

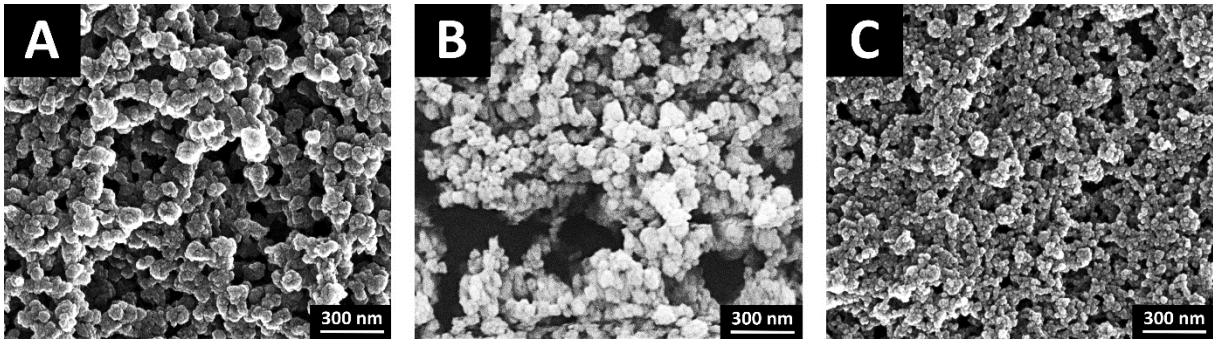


**Figure 36.** SEM micrographs of representative Dy734-labelled CaP nanoparticles, from typical synthesis batches, loaded with functional siRNA (A; CaP/PEI-Dy734/siRNAf/SiO<sub>2</sub>) or with control siRNA (B; CaP/PEI-Dy734/siRNAc/SiO<sub>2</sub>) and of reference nanoparticles without siRNA loading (C; CaP/PEI-Dy734/SiO<sub>2</sub>). The nanoparticles were applied in *in vivo* gene silencing experiments.

**Table 8.** Characterization data of representative CaP nanoparticles, from typical synthesis batches, used in *in vivo* gene silencing studies.

Characterization parameter:	CaP/PEI-Dy734/siRNAf/SiO <sub>2</sub>	CaP/PEI-Dy734/siRNAc/SiO <sub>2</sub>	CaP/PEI-Dy734/SiO <sub>2</sub>
Size by SEM / nm	80 ± 9	85 ± 8	33 ± 2
Size by DLS / nm	253 ± 3	190 ± 2	124 ± 1
PDI	0.18 ± 0.02	0.18 ± 0.02	0.24 ± 0.01
ζ-potential / mV	22 ± 1	25 ± 1	25 ± 3
Ca <sup>2+</sup> conc. / μg mL <sup>-1</sup>	46	55	43
CaP conc. / μg mL <sup>-1</sup>	115	138	108
siRNA conc. / μg mL <sup>-1</sup>	36	27	-
siRNA per particle	11,896	8,818	-
PEI conc. / μg mL <sup>-1</sup>	240	240	240
Endotoxins / EU mL <sup>-1</sup>	0.04	0.05	0.07
Particle conc. / mL <sup>-1</sup>	3.94·10 <sup>10</sup>	3.29·10 <sup>10</sup>	5.61·10 <sup>11</sup>

Bioactive nanoparticles were efficiently loaded with siRNA (with a typical biomolecule incorporation rate of 95-100%) and demonstrated strong fluorescence with either Cy5-specific ( $\lambda = 600-650$  nm) or Dy734-specific ( $\lambda = 749$  nm) emission maxima (**Figure 37**). As expected, biomolecule-loaded CaP nanoparticles were larger than the unloaded nanoparticles. Independently on the type of siRNA used for loading, the nanoparticles showed comparable characterization parameters. All nanoparticles were also non-pyrogenic ( $<0.1$  EU mL<sup>-1</sup>). This

is the quality criterion which must be met if the nanoparticles shall be applied in biological experiments. The nanoparticles should be then biocompatible and should not induce, by themselves, an inflammatory response of the cells. A number of synthesis batches of fluorescent (Cy5- or Dy734-labelled) siRNA-loaded CaP nanoparticles was performed. The obtained results for different nanoparticle batches were comparable and the syntheses were reproducible. 20-fold upscaling of the synthesis of bioactive Dy734-labelled nanoparticles did not adversely affect parameters and quality of the nanoparticles, and characterization results of these nanoparticles were comparable to those of the nanoparticles synthesized in a 1 mL scale.

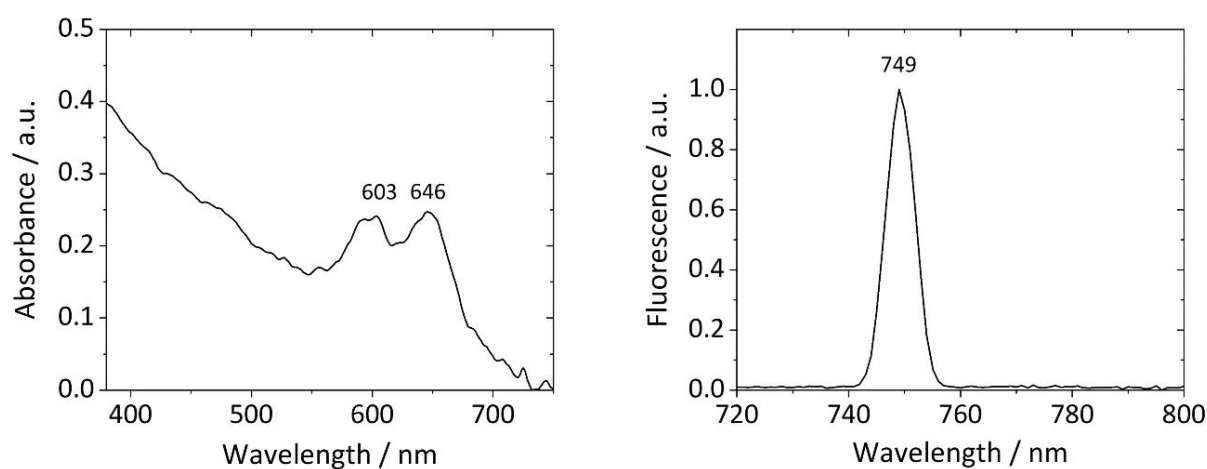


**Figure 37.** UV/Vis absorption spectrum of representative Cy5-labelled CaP nanoparticles (CaP/PEI-Cy5/SiO<sub>2</sub>) showed two Cy5-specific absorption bands at  $\lambda_{max} = 603$  nm and 646 nm (**left**). Fluorescence emission spectrum of representative Dy734-labelled CaP nanoparticles (CaP/PEI-Dy734/SiO<sub>2</sub>) showed a single and narrow Dy734-specific emission band at  $\lambda_{max} = 749$  nm (**right**). The NIR sample was excited at  $\lambda = 720$  nm.

### 5.1.3. Characterization of CaP nanoparticles for tracking studies

Fluorescent nanoparticles, dual-labelled with TAMRA and Cy5 (CaP/PEI-Cy5/TAMRAp/SiO<sub>2</sub>), were used in *in vitro* experiments for intracellular tracking of the nanoparticles inside murine monocytes. As control nanoparticles, single-labelled, either with TAMRA (CaP/PEI/TAMRAp/SiO<sub>2</sub>) or with Cy5 (CaP/PEI-Cy5/SiO<sub>2</sub>), nanoparticles were used. The negatively-charged short TAMRAp served as nanoparticle cargo and a model molecule to mimic siRNA. This permitted extensive microscopic studies on co-localization of the nanoparticles with endolysosomes in J774A.1 cells, which would not be possible with very expensive labelled siRNA. All types of CaP nanoparticles used in intracellular tracking studies

were spherical, monodisperse, positively-charged and colloiddally stable (**Figures 38-39; Table 9**). These nanoparticles were also silica-functionalized.

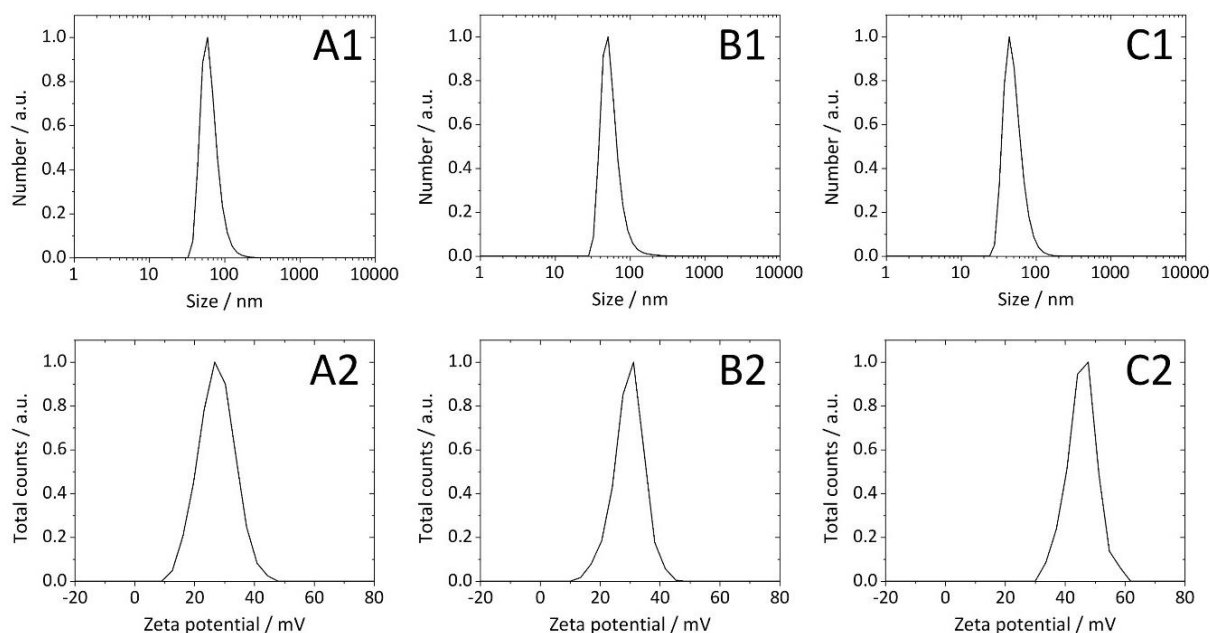


**Figure 38.** Normalized particle size distributions (**A1-C1**) and the corresponding  $\zeta$ -potentials (**A2-C2**) of dual-labelled with Cy5 and TAMRA (**A1, A2**; CaP/PEI-Cy5/TAMRAp/SiO<sub>2</sub>), single-labelled with TAMRA (**B1, B2**; CaP/PEI/TAMRAp/SiO<sub>2</sub>) and single-labelled with Cy5 (**C1, C2**; CaP/PEI-Cy5/SiO<sub>2</sub>) CaP nanoparticles. The nanoparticles were applied in *in vitro* intracellular tracking studies.

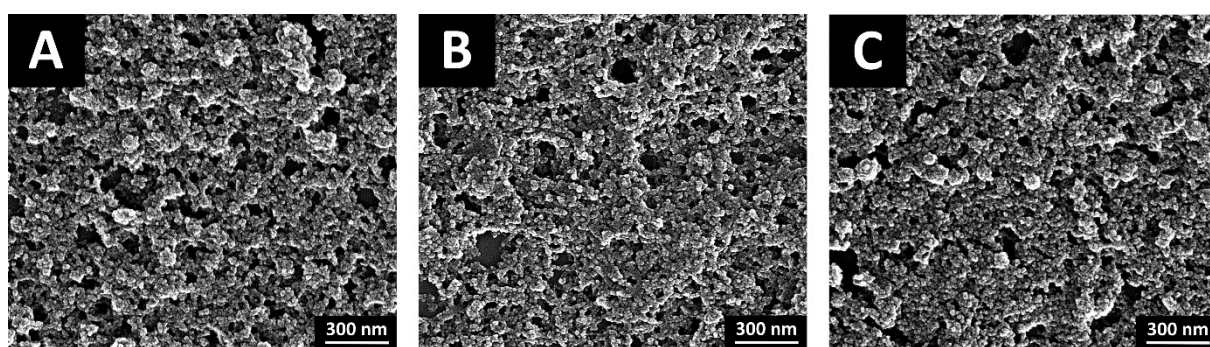


**Figure 39.** SEM micrographs of dual-labelled with Cy5 and TAMRA (**A**; CaP/PEI-Cy5/TAMRAp/SiO<sub>2</sub>), single-labelled with TAMRA (**B**; CaP/PEI/TAMRAp/SiO<sub>2</sub>) and single-labelled with Cy5 (**C**; CaP/PEI-Cy5/SiO<sub>2</sub>) CaP nanoparticles used in *in vitro* intracellular tracking experiments.

**Table 9.** Characterization data of CaP nanoparticles used in *in vitro* intracellular tracking studies.

Characterization parameter:	CaP/PEI-Cy5/TAMRAp/SiO <sub>2</sub>	CaP/PEI/TAMRAp/SiO <sub>2</sub>	CaP/PEI-Cy5/SiO <sub>2</sub>
Size by SEM / nm	66 ± 11	36 ± 3	61 ± 11
Size by DLS / nm	121 ± 7	156 ± 1	105 ± 11
PDI	0.25 ± 0.03	0.35 ± 0.01	0.33 ± 0.07
ζ-potential / mV	25 ± 1	25 ± 1	24 ± 3
Ca <sup>2+</sup> conc. / μg mL <sup>-1</sup>	24	27	27
CaP conc. / μg mL <sup>-1</sup>	60	68	68
Peptide conc. / μg mL <sup>-1</sup>	26	30	-
Peptides per particle	45,328	7,545	-
PEI conc. / μg mL <sup>-1</sup>	180	-	176
Endotoxins / EU mL <sup>-1</sup>	0.01	0.02	0.01
Particle conc. / mL <sup>-1</sup>	1.28·10 <sup>11</sup>	8.84·10 <sup>11</sup>	1.91·10 <sup>11</sup>

Peptide loading of the nanoparticles was efficient (with the incorporation rate of 70-80%) and allowed to obtain a bright fluorescence signal of the TAMRA dye in microscopic imaging. The advantage of using TAMRA fluorophore is that the dye is photostable and ensures a pH insensitive fluorescence emission.<sup>262</sup> Furthermore, when compared to far-red Cy5 dye, TAMRA shows emission in the orange-red range of light. Therefore, the risk of possible cross-talk between fluorescent channels for Cy5 and TAMRA detection in microscopic studies was excluded. Furthermore, fluorescence spectroscopy analyses of the TAMRAp and PEI-Cy5 (1:3) mixture demonstrated that there was no quenching effect between the two fluorophores and, in the presence of TAMRA, fluorescence emission maximum of Cy5 was only slightly shifted (4 nm) (**Figure 40**). The ratio of fluorophore volumes in the mixture reflected the ratio of fluorophores in CaP nanoparticles. The nanoparticles used in intracellular tracking studies were non-pyrogenic (<0.1 EU mL<sup>-1</sup>).

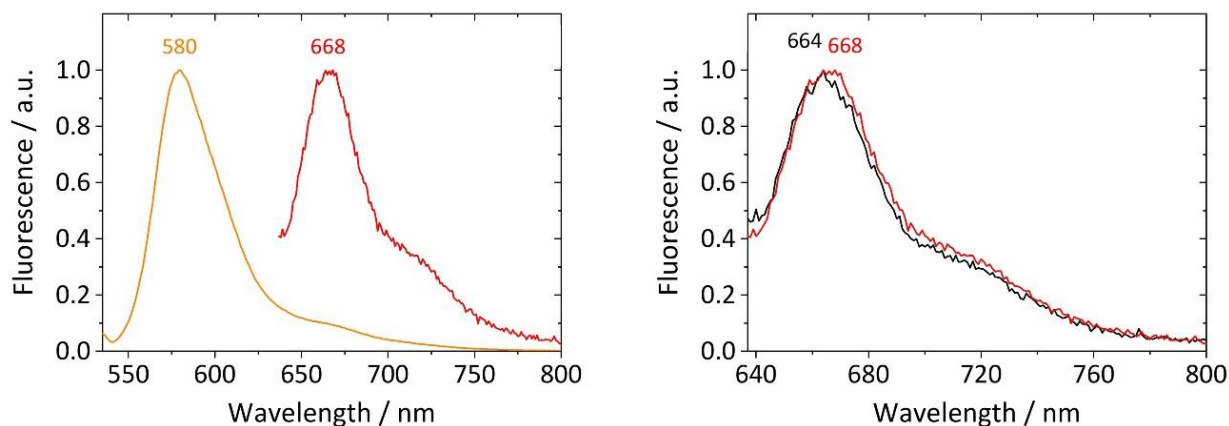


**Figure 40.** Fluorescence emission spectra of the TAMRA and PEI-Cy5 (1:3) mixture with dye-specific emission maxima for TAMRA (orange curve) and Cy5 (red curve) (left). The sample was excited at  $\lambda = 535$  nm and 637 nm for TAMRA and Cy5 emission, respectively. The overlay of fluorescence emission spectra of the mixture of TAMRA and PEI-Cy5 (red curve), and just PEI-Cy5 (black curve) excited at  $\lambda = 637$  nm for Cy5 emission (right).

#### 5.1.4. Characterization of ligand-decorated CaP nanoparticles for gene silencing of NF- $\kappa$ B p65 and cell targeting studies

Fluorescent ligand-decorated and siRNA-loaded CaP nanoparticles were applied in *in vitro* cell targeting experiments and gene silencing studies. Before siRNA-loaded nanoparticles were prepared, unloaded ligand-decorated nanoparticles were synthesized and used in preliminary studies on the cellular uptake of nanoparticles (enhanced by ligand decoration of the nanoparticle surface). Nanoparticles decorated with cRGDfK peptides (CaP/PEI-Cy5/SiO<sub>2</sub>/S-cRGDfK) and IgG-anti-CD69 antibodies (CaP/PEI-Cy5/SiO<sub>2</sub>/S-IgG-anti-CD69) were prepared for the targeting of endothelial cells, and B- and T-lymphocytes, respectively. In endothelial cells, cRGDfK peptides interact with  $\alpha_v\beta_3$  integrin receptors, whereas IgG antibodies, used for targeting of lymphocytes, bind to CD69 receptors exposed on the surface of activated B- and T-cells.<sup>263,264</sup> Additionally, nanoparticles decorated with murine IgG- $\kappa$ -IC antibodies (CaP/PEI-Cy5/SiO<sub>2</sub>/S-IgG- $\kappa$ -IC) were synthesized to study whether the enhanced uptake of antibody-decorated nanoparticles by murine cells had a specific or a non-specific nature and depended on the ligand type. Reference nanoparticles in these studies were thiol-functionalized nanoparticles without surface decoration (CaP/PEI-Cy5/SiO<sub>2</sub>/SH), as well as thiol-terminated nanoparticles which were additionally incubated in water for 24 h at 4 °C to mimic the reaction conditions for ligand decoration during synthesis (CaP/PEI-Cy5/SiO<sub>2</sub>/SH/H<sub>2</sub>O). All types of

silica-functionalized nanoparticles, used in cell targeting experiments, were spherical, monodisperse, positively-charged and colloiddally stable (**Figures 41-42; Table 10**).

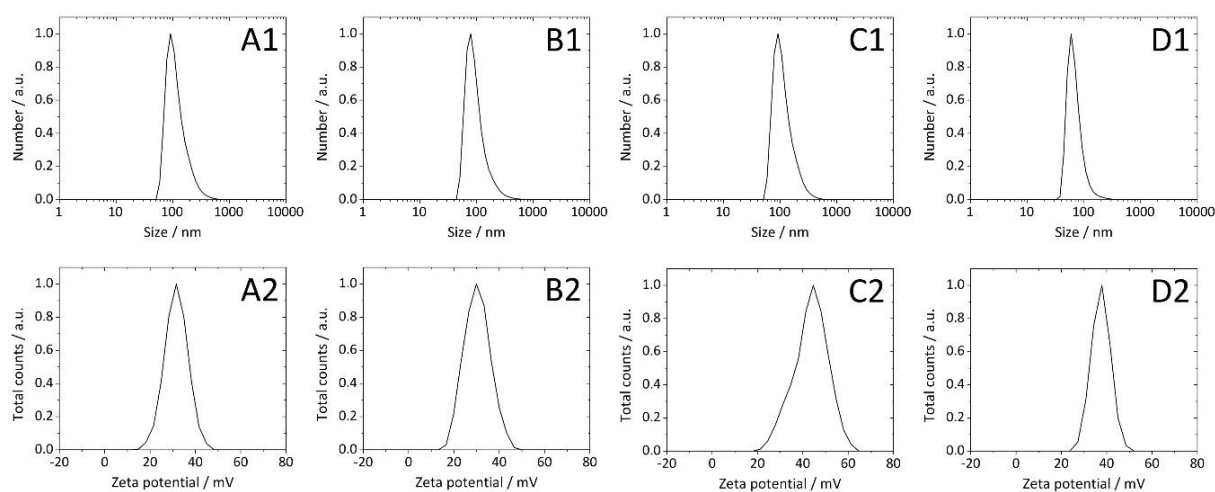


**Figure 41.** Normalized particle size distributions (**A1-D1**) and the corresponding  $\zeta$ -potentials (**A2-D2**) of fluorescent CaP nanoparticles decorated with cRGDfK peptides (**A1, A2**; CaP/PEI-Cy5/SiO<sub>2</sub>/S-cRGDfK), IgG-anti-CD69 antibodies (**B1, B2**; CaP/PEI-Cy5/SiO<sub>2</sub>/S-IgG-anti-CD69), IgG-anti-CD69-CTRL antibodies (**C1, C2**; CaP/PEI-Cy5/SiO<sub>2</sub>/S-IgG-anti-CD69-CTRL) and IgG- $\kappa$ -IC antibodies (**D1, D2**; CaP/PEI-Cy5/SiO<sub>2</sub>/S-IgG- $\kappa$ -IC). The nanoparticles were applied in *in vitro* cell targeting studies.

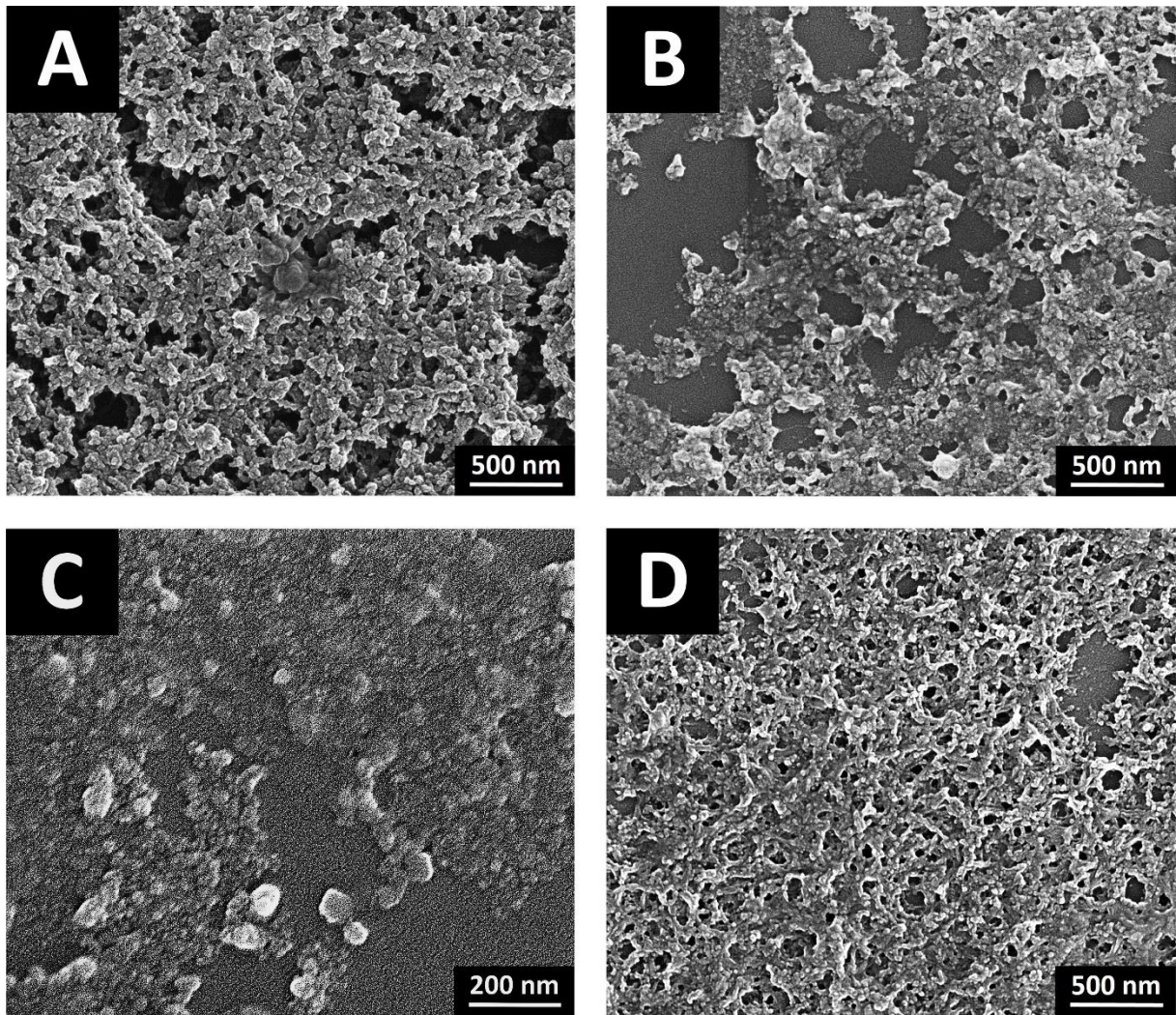


**Figure 42.** SEM micrographs of fluorescent CaP nanoparticles decorated with cRGDfK peptides (A; CaP/PEI-Cy5/SiO<sub>2</sub>/S-cRGDfK), IgG-anti-CD69 antibodies (B; CaP/PEI-Cy5/SiO<sub>2</sub>/S-IgG-anti-CD69), IgG-anti-CD69-CTRL antibodies (C; CaP/PEI-Cy5/SiO<sub>2</sub>/S-IgG-anti-CD69-CTRL) and IgG-κ-IC antibodies (D; CaP/PEI-Cy5/SiO<sub>2</sub>/S-IgG-κ-IC). The nanoparticles were applied in *in vitro* cell targeting experiments.

**Table 10.** Characterization data of ligand-decorated CaP nanoparticles used in in vitro cell targeting studies. \*calcium concentration below AAS detection limit. \*\*estimated data based on the result of calcium concentration below AAS detection limit.

Characterization parameter:	CaP/PEI-Cy5/SiO <sub>2</sub> /S-cRGDFK	CaP/PEI-Cy5/SiO <sub>2</sub> /S-IgG-anti-CD69	CaP/PEI-Cy5/SiO <sub>2</sub> /S-IgG-anti-CD69-CTRL	CaP/PEI-Cy5/SiO <sub>2</sub> /S-IgG-κ-IC
Size by SEM / nm	49 ± 9	36 ± 3	44 ± 7	36 ± 3
Size by DLS / nm	212 ± 3	212 ± 4	206 ± 6	145 ± 4
PDI	0.20 ± 0.03	0.28 ± 0.03	0.27 ± 0.04	0.25 ± 0.02
ζ-potential / mV	31 ± 2	31 ± 2	43 ± 1	34 ± 4
Ca <sup>2+</sup> conc. / μg mL <sup>-1</sup>	19	13	<7*	13
CaP conc. / μg mL <sup>-1</sup>	48	33	<18**	33
Peptide/Ab conc. / μg mL <sup>-1</sup>	92	120	121	153
Peptides/Ab per particle	3.7·10 <sup>5</sup>	1,088	>3,876**	1,424
PEI conc. / μg mL <sup>-1</sup>	102	127	146	138
Endotoxins / EU mL <sup>-1</sup>	0.03	0.04	0.02	0.09
Particle conc. / mL <sup>-1</sup>	2.52·10 <sup>11</sup>	4.44·10 <sup>11</sup>	<1.26·10 <sup>11</sup> **	4.32·10 <sup>11</sup>

Characterization data have shown that independently on the type of ligand used for surface decoration, the nanoparticles demonstrated comparable characterization parameters. However, the multi-step synthesis of ligand-decorated nanoparticles revealed the problem of calcium loss from the nanoparticles. Thus, ligand-decorated nanoparticles demonstrated, in some cases, a very low calcium concentration, which was already below AAS detection limit and therefore, some of nanoparticle characterization parameters, like CaP content, siRNA/ligands per nanoparticle and nanoparticle concentration, could not be determined accurately. The reason of calcium loss during nanoparticle synthesis was found out after performing additional

experiments with monitoring (by AAS) the calcium content in the nanoparticles (without biomolecule loading) after each step of synthesis (**Figure 43**).

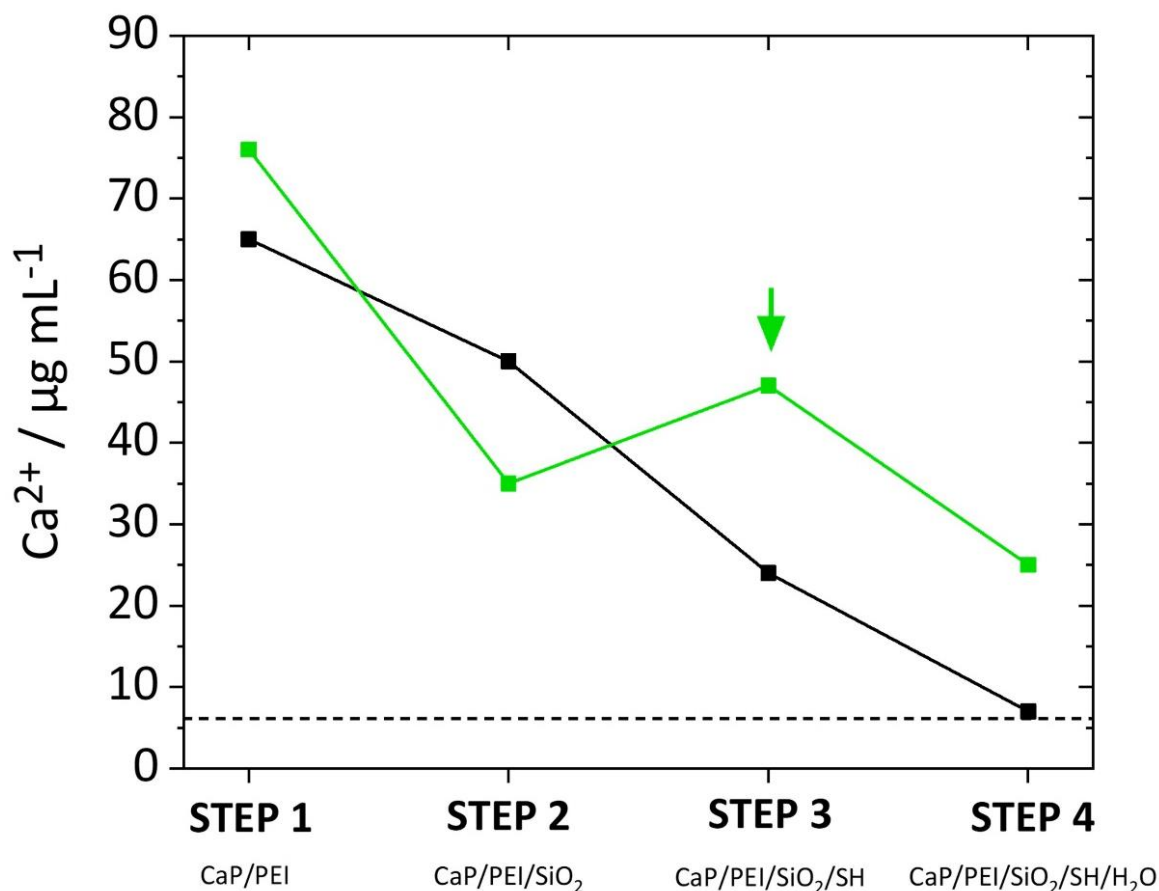


**Figure 43.** Kinetics of calcium loss from representative unloaded CaP nanoparticles during a model multi-step synthesis (steps 1-4). Course of the standard synthesis without (**black curve**) and with (**green curve**) double concentration of the nanoparticles in the third step of synthesis (indicated with an arrow). The level of AAS detection limit for calcium is marked with the dashed line.

A reproducible tendency of ~25-60% loss of calcium content from the nanoparticles, per synthesis step, was due to nanoparticle re-dispersion in water and purification by washing with centrifugation. Therefore, multiple re-dispersions of nanoparticles in water, during the multi-step synthesis, were responsible for the observed low calcium concentration in some of the nanoparticle formulations. Silica functionalization of the nanoparticles did not prevent loss of calcium, which was significant also in functionalized nanoparticles (up to 71% of calcium loss) (**Figure 44**).

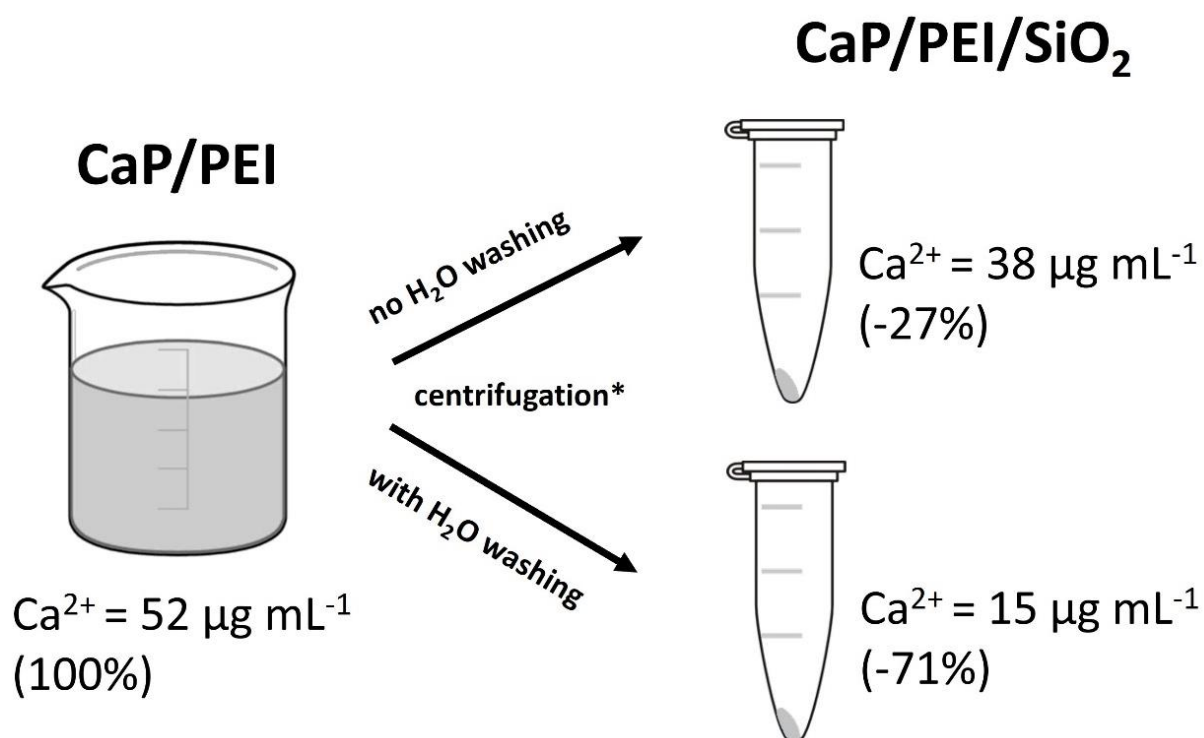


**Figure 44.** Demonstration of calcium loss from CaP nanoparticles during synthesis. Unfunctionalized (CaP/PEI) and silica-functionalized (CaP/PEI/SiO<sub>2</sub>) nanoparticles were investigated. Nanoparticle pellets, obtained after centrifugation, were analyzed by AAS for calcium content. \*centrifugation conditions: 4,000 rpm; 30 min; RT.

Therefore, all possible purification steps *via* washing were excluded and double concentration of thiol-functionalized nanoparticle samples was introduced to obtain as much calcium as possible in the nanoparticles, particularly in the multi-step syntheses of ligand-decorated nanoparticles. In most cases, double concentration of nanoparticles during synthesis enabled to increase the content of calcium in peptide/antibody-decorated nanoparticles 2- to 3-fold.

Washing of the nanoparticles and introduction of ultracentrifugation in the last step of the multi-step synthesis (ligand decoration of nanoparticles) did not adversely affect other characterization parameters of the nanoparticles, like size, dispersion state and colloidal stability. Ligand-decorated CaP nanoparticles, without siRNA loading, generally demonstrated a very high efficiency of surface decoration. For coating with cRGDfK peptides, and IgG-anti-CD69 and IgG-anti-CD69-CTRL antibodies, the decoration rate was close to 100%, whereas for IgG- $\kappa$ -IC antibodies it was 54%. Ligand-decorated and siRNA-loaded CaP nanoparticles showed a characterization profile comparable to the unloaded nanoparticles (**Figures 45-48; Tables 11-12**).

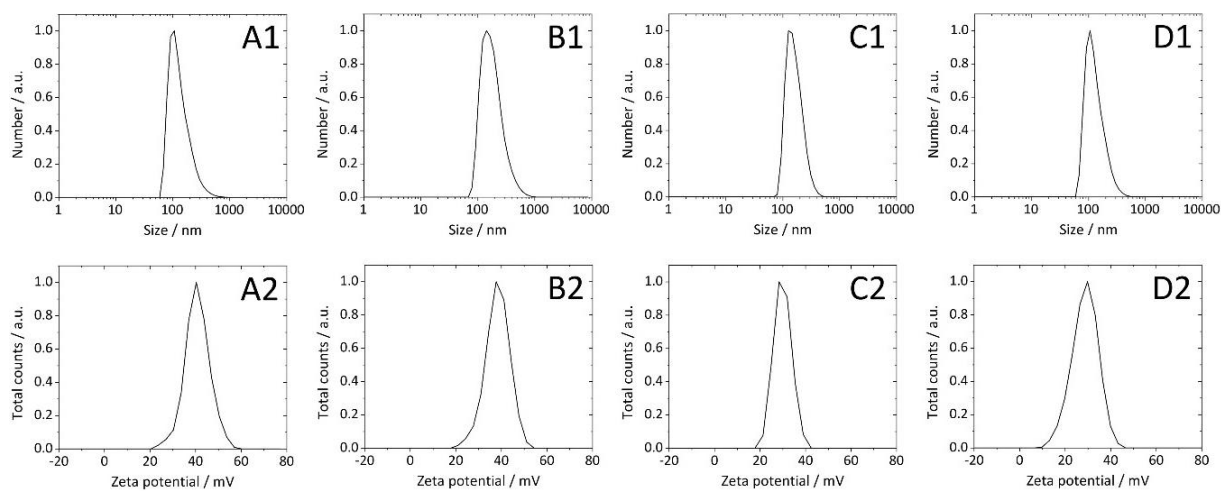


**Figure 45.** Normalized particle size distributions (**A1-D1**) and the corresponding  $\zeta$ -potentials (**A2-D2**) of fluorescent CaP nanoparticles decorated with cRGDfK peptides and loaded with functional siRNA (**A1, A2**; CaP/PEI-Cy5/siRNAf/SiO<sub>2</sub>/S-cRGDfK) or with control siRNA (**B1, B2**; CaP/PEI-Cy5/siRNAc/SiO<sub>2</sub>/S-cRGDfK), and of two types of reference nanoparticles without peptide decoration and siRNA loading: CaP/PEI-Cy5/SiO<sub>2</sub>/SH/H<sub>2</sub>O (**C1, C2**) and CaP/PEI-Cy5/SiO<sub>2</sub>/SH (**D1, D2**). The nanoparticles were applied in *in vitro* cell targeting and gene silencing studies.

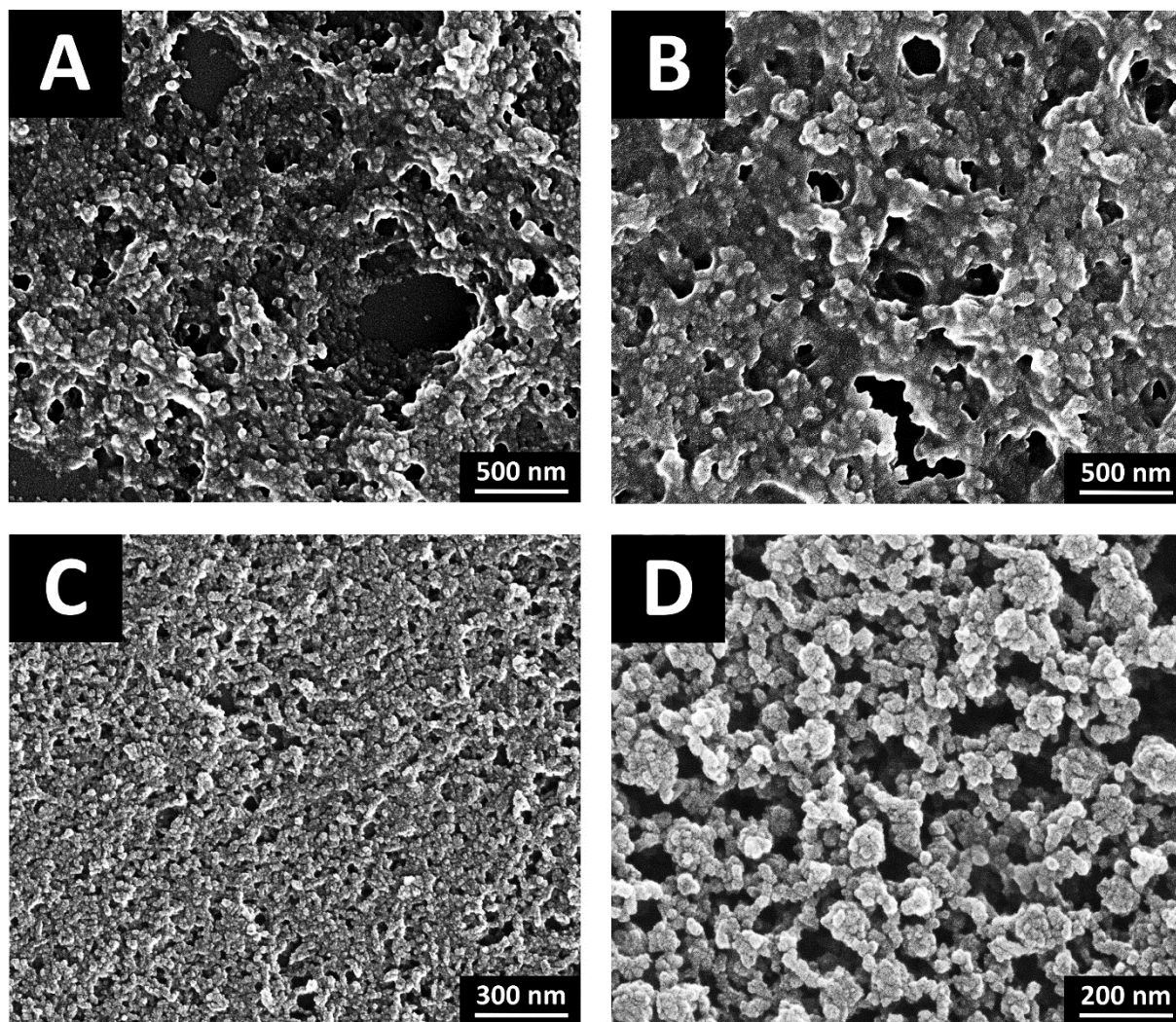


**Figure 46.** SEM micrographs of fluorescent CaP nanoparticles decorated with cRGDfK peptides and loaded with functional siRNA (A; CaP/PEI-Cy5/siRNAf/SiO<sub>2</sub>/S-cRGDfK) or with control siRNA (B; CaP/PEI-Cy5/siRNAc/SiO<sub>2</sub>/S-cRGDfK) and of two types of reference nanoparticles without peptide decoration and siRNA loading: CaP/PEI-Cy5/SiO<sub>2</sub>/SH/H<sub>2</sub>O (C) and CaP/PEI-Cy5/SiO<sub>2</sub>/SH (D). The nanoparticles were applied in in vitro cell targeting and gene silencing experiments.

**Table 11.** Characterization data of ligand-decorated and siRNA-loaded CaP nanoparticles, and of the corresponding reference nanoparticles (undecorated and unloaded) used in in vitro cell targeting and gene silencing studies. Nanoparticles without ligand decoration and siRNA loading (CaP/PEI-Cy5/SiO<sub>2</sub>/SH/H<sub>2</sub>O, CaP/PEI-Cy5/SiO<sub>2</sub>/SH) were used as reference nanoparticles to all types of ligand-decorated nanoparticles (with and without siRNA loading). \*calcium concentration below AAS detection limit. \*\*estimated data based on the result of calcium concentration below AAS detection limit.

Characterization parameter:	CaP/PEI-Cy5/siRNAf/SiO <sub>2</sub> /S-cRGDfK	CaP/PEI-Cy5/siRNAc/SiO <sub>2</sub> /S-cRGDfK	CaP/PEI-Cy5/SiO <sub>2</sub> /SH/H <sub>2</sub> O	CaP/PEI-Cy5/SiO <sub>2</sub> /SH
Size by SEM / nm	59 ± 8	67 ± 7	30 ± 4	39 ± 4
Size by DLS / nm	230 ± 4	325 ± 25	192 ± 76	211 ± 3
PDI	0.24 ± 0.04	0.35 ± 0.04	0.48 ± 0.01	0.23 ± 0.01
ζ-potential / mV	41 ± 1	39 ± 1	31 ± 3	29 ± 1
Ca <sup>2+</sup> conc. / μg mL <sup>-1</sup>	<7*	<7*	14	41
CaP conc. / μg mL <sup>-1</sup>	<18**	<18**	35	103
siRNA conc. / μg mL <sup>-1</sup>	33	20	-	-
siRNA per particle	>28,744**	>25,511**	-	-
Peptide conc. / μg mL <sup>-1</sup>	95	100	-	-
Peptides per particle	>1.8·10 <sup>6</sup> **	>2.8·10 <sup>6</sup> **	-	-
PEI conc. / μg mL <sup>-1</sup>	146	174	148	126
Endotoxins / EU mL <sup>-1</sup>	0.02	0.02	0.03	0.04
Particle conc. / mL <sup>-1</sup>	<5.13·10 <sup>10</sup> **	<3.62·10 <sup>10</sup> **	7.85·10 <sup>11</sup>	1.03·10 <sup>12</sup>

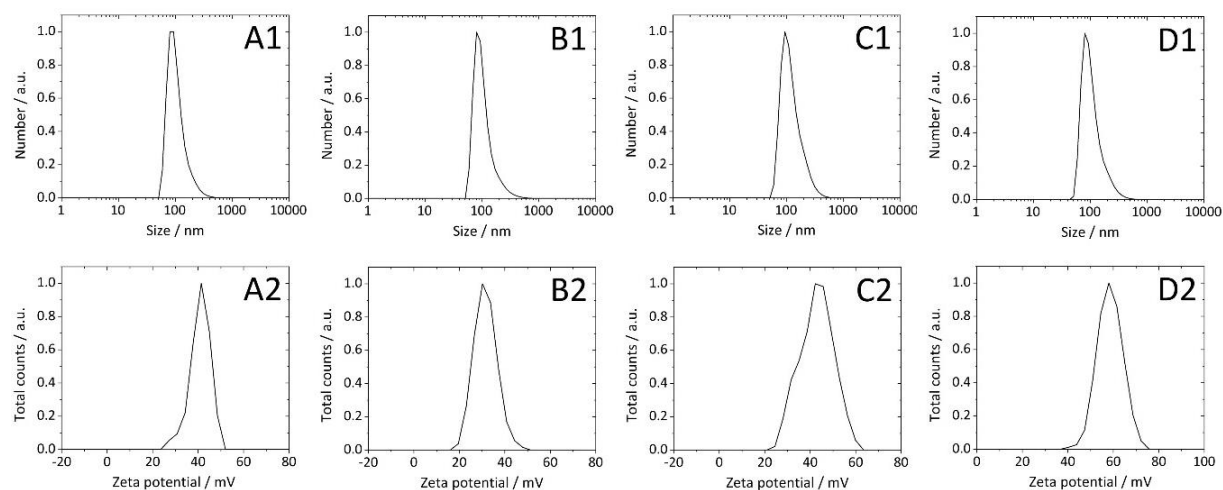


**Figure 47.** Normalized particle size distributions (**A1-D1**) and the corresponding  $\zeta$ -potentials (**A2-D2**) of fluorescent CaP nanoparticles decorated with IgG-anti-CD69 antibodies and loaded with functional siRNA (**A1, A2**; CaP/PEI-Cy5/siRNAf/SiO<sub>2</sub>/S-IgG-anti-CD69) or with control siRNA (**C1, C2**; CaP/PEI-Cy5/siRNAc/SiO<sub>2</sub>/S-IgG-anti-CD69), and of CaP nanoparticles decorated with IgG-anti-CD69-CTRL antibodies and loaded with functional siRNA (**B1, B2**; CaP/PEI-Cy5/siRNAf/SiO<sub>2</sub>/S-IgG-anti-CD69-CTRL) or with control siRNA (**D1, D2**; CaP/PEI-Cy5/siRNAc/SiO<sub>2</sub>/S-IgG-anti-CD69-CTRL). The nanoparticles were applied in in vitro cell targeting and gene silencing studies.

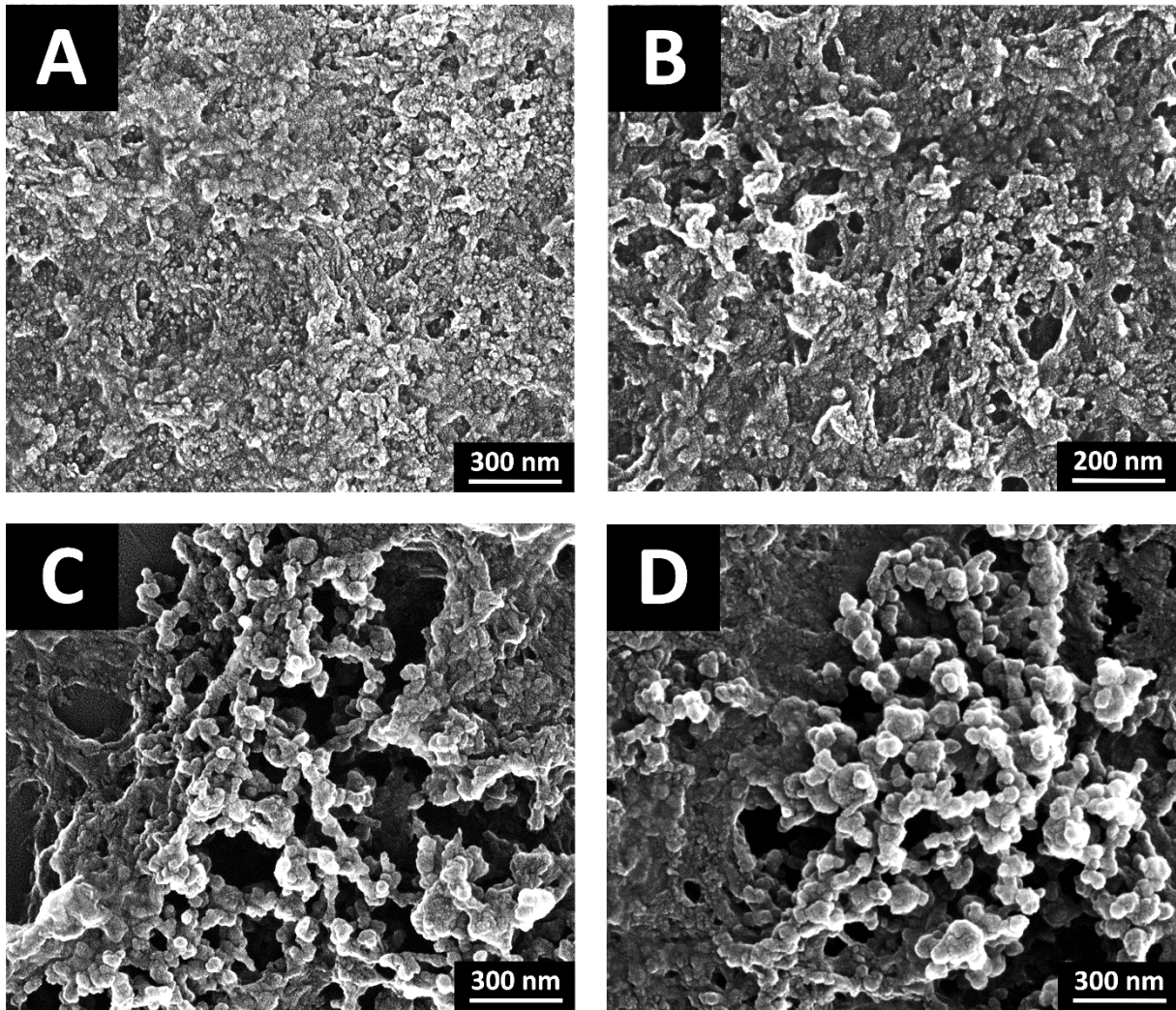


**Figure 48.** SEM micrographs of fluorescent CaP nanoparticles decorated with IgG-anti-CD69 antibodies and loaded with functional siRNA (A; CaP/PEI-Cy5/siRNAf/SiO<sub>2</sub>/S-IgG-anti-CD69) or with control siRNA (C; CaP/PEI-Cy5/siRNAc/SiO<sub>2</sub>/S-IgG-anti-CD69), and of CaP nanoparticles decorated with IgG-anti-CD69-CTRL antibodies and loaded with functional siRNA (B; CaP/PEI-Cy5/siRNAf/SiO<sub>2</sub>/S-IgG-anti-CD69-CTRL) or with control siRNA (D; CaP/PEI-Cy5/siRNAc/SiO<sub>2</sub>/S-IgG-anti-CD69-CTRL). The nanoparticles were applied in *in vitro* cell targeting and gene silencing experiments.

**Table 12.** Characterization data of ligand-decorated and siRNA-loaded CaP nanoparticles used in *in vitro* cell targeting and gene silencing studies. Characterization of undecorated and unloaded reference nanoparticles is presented in **Table 11**.

Characterization parameter:	CaP/PEI-Cy5/siRNAf/SiO <sub>2</sub> /S-IgG-anti-CD69	CaP/PEI-Cy5/siRNAf/SiO <sub>2</sub> /S-IgG-anti-CD69-CTRL	CaP/PEI-Cy5/siRNAc/SiO <sub>2</sub> /S-IgG-anti-CD69	CaP/PEI-Cy5/siRNAc/SiO <sub>2</sub> /S-IgG-anti-CD69-CTRL
Size by SEM / nm	38 ± 5	36 ± 4	50 ± 6	62 ± 9
Size by DLS / nm	189 ± 7	224 ± 11	205 ± 7	218 ± 1
PDI	0.26 ± 0.06	0.33 ± 0.06	0.20 ± 0.04	0.28 ± 0.02
ζ-potential / mV	37 ± 4	32 ± 1	29 ± 1	27 ± 1
Ca <sup>2+</sup> conc. / μg mL <sup>-1</sup>	13	20	34	16
CaP conc. / μg mL <sup>-1</sup>	33	51	86	41
siRNA conc. / μg mL <sup>-1</sup>	33	29	29	29
siRNA per particle	4,135	2,008	3,165	12,824
Ab conc. / μg mL <sup>-1</sup>	137	160	267	243
Ab per particle	1,487	1,006	2,580	9,476
PEI conc. / μg mL <sup>-1</sup>	111	176	141	158
Endotoxins / EU mL <sup>-1</sup>	0.01	0.01	0.02	0.07
Particle conc. / mL <sup>-1</sup>	3.62·10 <sup>11</sup>	6.37·10 <sup>11</sup>	4.17·10 <sup>11</sup>	1.03·10 <sup>11</sup>

CaP nanoparticles loaded with siRNA were larger than the nanoparticles without biomolecule cargo. The efficiency of siRNA incorporation onto the nanoparticles varied between 56-90% (which was less than in non-decorated and siRNA-loaded fluorescent CaP nanoparticles described in chapter 5.1.2.), whereas antibodies were bound with 45-50% efficiency, which was constant and did not depend on the type of antibody. A ~50% decrease in antibody binding efficiency was observed for siRNA-loaded nanoparticles, when compared to the unloaded nanoparticles. Only in cRGDfK-decorated nanoparticles, the efficiency of peptide binding was almost identical in unloaded and siRNA-loaded nanoparticles. All nanoparticles were pyrogen free (<0.1 EU mL<sup>-1</sup>). It has to be underlined that, despite introduced synthesis modifications, it

was difficult to control calcium content in the nanoparticles during multi-step syntheses and ensure reproducible and relatively constant values for this characterization parameter of CaP nanoparticles.

#### **5.1.5. Review of the biological results for CaP nanoparticles described in this thesis**

Biological experiments with CaP nanoparticles were performed and their results provided by M.Sc. Elena K. Müller (Research Center Lobeda, University Hospital Jena). Presented figures were adapted from a joint manuscript.<sup>242</sup> At the time of writing of this thesis, results of *in vitro* cell targeting and gene silencing experiments, as well as results of *in vivo* gene silencing studies were still under evaluation and not available for presentation in this thesis.

In general, fluorescent silica-functionalized CaP nanoparticles were readily taken up by most of studied murine blood compartment cells (monocytes, endothelial cells, B-lymphocytes) and demonstrated a low degree of cytotoxicity. Poor nanoparticle uptake was observed only in T-lymphocytes (<20% of cell population was nanoparticle-positive) (**Figure 49**).

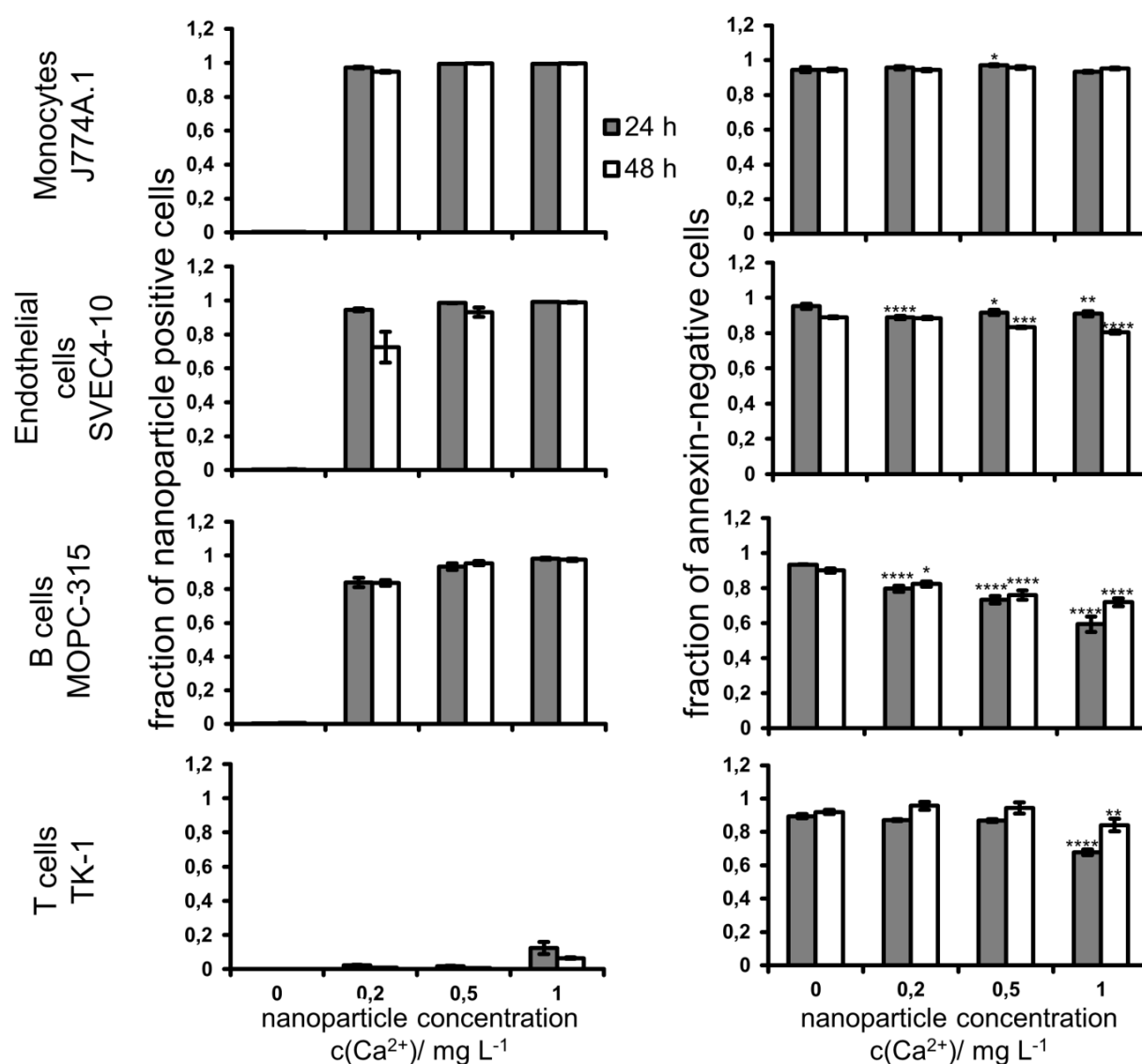


**Figure 49.** Uptake behavior (*left*) and impact on cell viability (*right*) of silica-functionalized CaP nanoparticles (CaP/PEI-Cy5/SiO<sub>2</sub>). Cells were exposed to different concentrations of the nanoparticles (up to 1 mg<sub>Ca</sub> L<sup>-1</sup>) and incubated up to 48 h, prior to flow cytometry analysis (N=3). For the fraction of annexin-negative cells: significant difference to non-treated control (set to 1) with  $p < 0.0001$  (\*\*\*\*),  $p < 0.001$  (\*\*\*) or  $p < 0.01$  (\*\*) or  $p < 0.05$  (\*). c – concentration.

The efficient cellular uptake of fluorescent silica-functionalized CaP nanoparticles was further studied in detail in the monocytes. Cells were incubated with the nanoparticles (NP) in the presence of different endocytosis inhibitors and also at 4 °C to prevent energy-dependent nanoparticle uptake. As control, cells were incubated with the nanoparticles, but in absence of the inhibitors. These were: cytochalasin D (inhibitor of microtubule re-arrangement), Wortmannin (inhibitor of macropinocytosis) and chlorpromazine (inhibitor of clathrin-mediated endocytosis). The uptake by monocytes was mainly driven by energy-dependent mechanisms and partially by processes related to phagocytosis and clathrin-mediated endocytosis. CLSM imaging confirmed efficient uptake of the nanoparticles by monocytes in all studied uptake models (**Figure 50**).

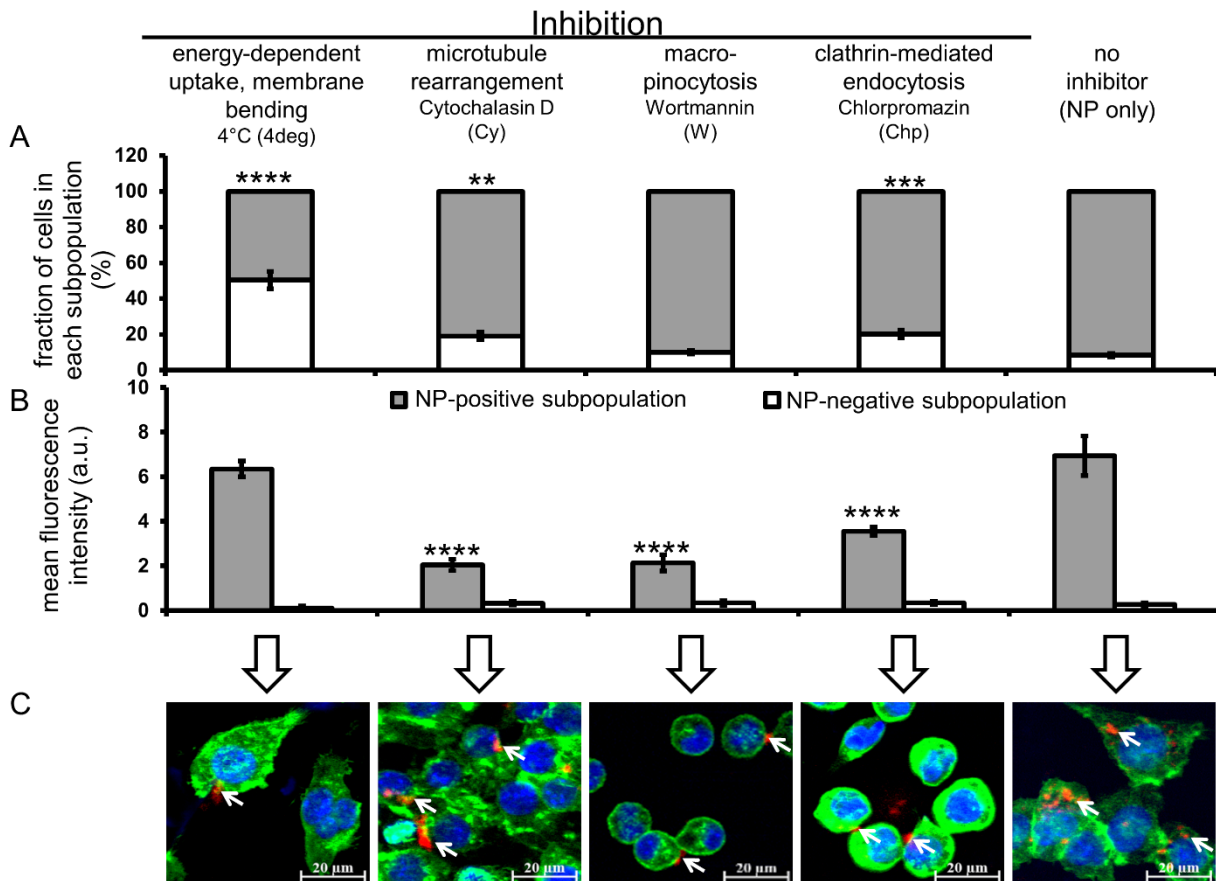


**Figure 50.** Murine monocytes efficiently internalized silica-functionalized CaP nanoparticles (CaP/PEI-Cy5/SiO<sub>2</sub>) after 3 h of incubation. The nanoparticle concentration was 0.5 mg<sub>Ca</sub> L<sup>-1</sup>. (A) Nanoparticle uptake capacity expressed by fractions of nanoparticle-positive and nanoparticle-negative cells, relative to the total cell count (whole cell population). (B) Single-cell uptake capacity measured by MFI per cell (Cy5 signal from the nanoparticles). *p*-values indicate significant differences to the control cells (nanoparticle-exposed cells in the absence

of inhibitors, at 37 °C) with  $p < 0.0001$ (\*\*\*\*),  $p < 0.001$ (\*\*\*) or  $p < 0.01$ (\*\*) ( $N=3$ ) (C) Representative CLSM images of each experimental group of cells (representing a different uptake model) treated with the corresponding endocytosis inhibitors. Red (Cy5): **nanoparticles** (indicated with arrows), blue (Hoechst 33258): **cell nuclei** and green (Phalloidin-AF488): **actin cytoskeleton**. Scale bar corresponds to 20  $\mu\text{m}$ .

The intracellular route of dual-labelled fluorescent CaP nanoparticles (NP) was studied, after uptake by monocytes, using CLSM. The nanoparticles were loaded with TAMRAp, which served as model of siRNA and mimicked its processing in cells. The experiments revealed a high degree of co-localization of the nanoparticles with cell endolysosomes, which could be observed already after 1 h of incubation. After 6 h of incubation, nearly 90% of cell population possessed nanoparticle-positive endolysosomes. In the time range between 24-72 h of incubation, co-localization consequently decreased, and the peptide cargo could be detected in the cell cytoplasm, indicating degradation of CaP nanoparticles inside the endolysosomes and release of transported peptides (Figure 51). If the nanoparticle cargo would be siRNA, liberated biomolecules would induce gene silencing.

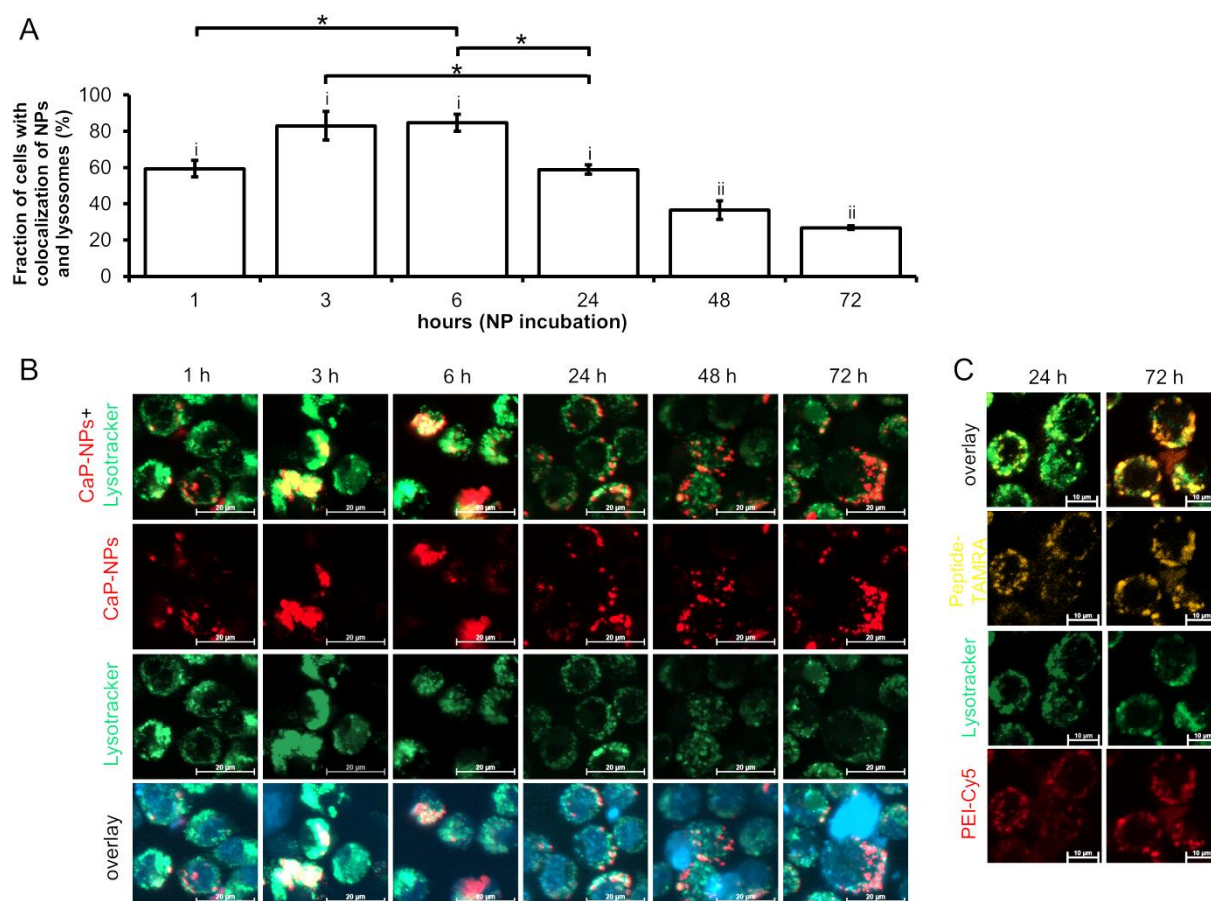


**Figure 51.** CaP nanoparticles were co-localized with monocyte endolysosomes and the nanoparticle cargo (TAMRAp) was released into the cell cytoplasm after 72 h of incubation. (A) Semi-quantitative analysis of cells incubated with silica-functionalized nanoparticles (CaP/PEI-Cy5/SiO<sub>2</sub>). The nanoparticle concentration was 0.5 mg<sub>Ca</sub> L<sup>-1</sup>. Fraction of cells with nanoparticles co-localized with the endolysosomes, normalized to all nanoparticle-positive cells. (B) Maximum intensity projections (MIP) of representative z-stacks from CLSM imaging. Red (Cy5): **nanoparticles**, blue (Hoechst 33258): **cell nuclei** and green (Lyso-Tracker® Green DND-26): **endolysosomes**. Mean and standard deviation of the mean of 3 (i) or 2 (ii) independent experiments with  $p < 0.05$  (\*). Scale bar corresponds to 20 μm. (C) Co-localization of dual-labelled CaP/PEI-Cy5/TAMRAp/SiO<sub>2</sub> nanoparticles with the endolysosomes. Red (Cy5): **nanoparticles**, blue (Hoechst 33258): **cell nuclei**, green (Lyso-Tracker® Green DND-26): **endolysosomes** and orange (TAMRA): **peptide cargo**. Scale bar corresponds to 10 μm.

The effect of gene silencing of NF-κB p65 could be observed on the level of p65 mRNA and p65 protein in inflamed (LPS-primed) monocytes (**Figure 52**). Nanoparticle-delivered functional siRNA reversed the expression of p65 protein almost back to the non-inflammatory state. In contrast, the downregulation effect of p65 did not occur in the presence of either nanoparticles carrying control siRNA or reference nanoparticles without siRNA cargo, or even free functional siRNA transfected into cells using Lipofectamine®, which is a model transfection agent that facilitates nucleic acid delivery into cells.<sup>265</sup> Free functional siRNA, due to the lack of protection, was probably rapidly degraded by the cell nucleases. The results of efficient silencing of NF-κB p65 by siRNA supported conclusions of nanoparticle tracking experiments. After endolysosomal degradation of the nanoparticles, their released into cell cytoplasm cargo remains bioactive (functional) and interacts with the cell gene expression machinery.

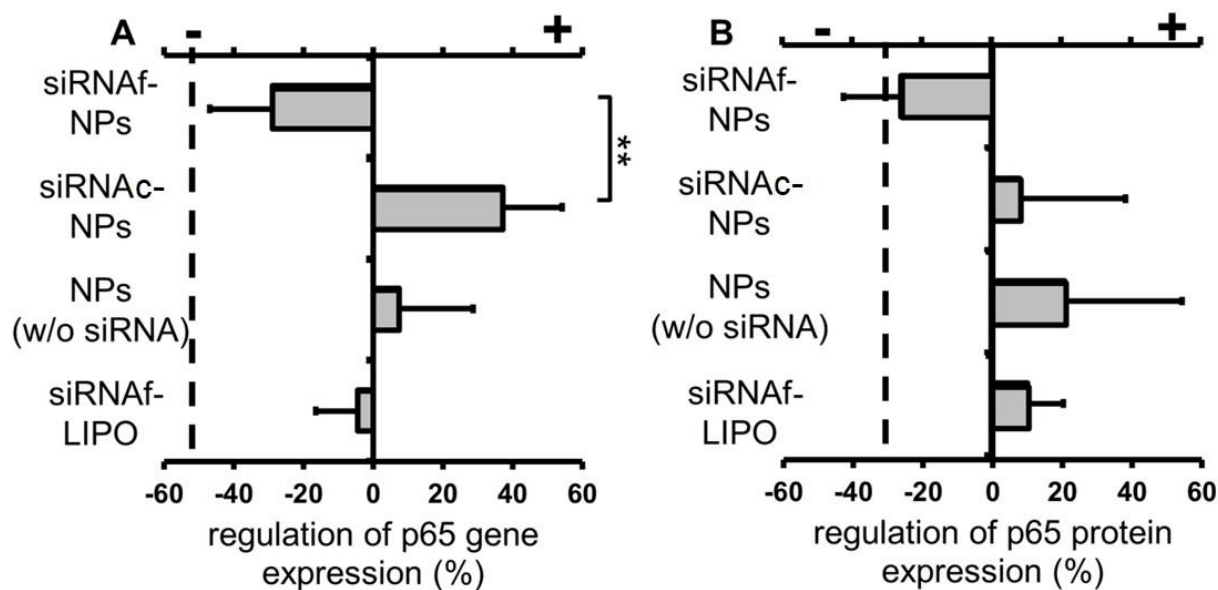


**Figure 52.** Regulation of NF- $\kappa$ B p65 gene (A) and protein (B) expression in inflamed monocytes. The regulation was defined as ratio of p65 expression with respect to the inflammatory condition (LPS-primed cells, absence of nanoparticles) set to zero. “+ regulation” = upregulation, “- regulation” = downregulation. The dashed line depicts the non-inflammatory state of cells (immune homeostasis). siRNAf-NPs – nanoparticles loaded with functional siRNA (CaP/PEI-Cy5/siRNAf/SiO<sub>2</sub>), siRNAc-NPs – nanoparticles loaded with control siRNA (CaP/PEI-Cy5/siRNAc/SiO<sub>2</sub>), NPs (w/o siRNA) – nanoparticles without siRNA loading (CaP/PEI-Cy5/SiO<sub>2</sub>) and siRNAf-LIPO – functional siRNA transfected into cells using Lipofectamine<sup>®</sup>, with  $p < 0.01$  (\*\*).

Furthermore, downregulation of NF- $\kappa$ B p65 expression in LPS-primed monocytes, after exposure to CaP nanoparticles loaded with functional siRNA, had an impact on secretion of cytokines: TNF- $\alpha$ , IL-6 and interferon beta (IFN- $\beta$ ), which regulation is related to p65. A significant downregulation of cytokine expression towards the non-inflammatory state was detected, however, this effect cannot be attributed exclusively to nanoparticles carrying functional siRNA, as downregulation of cytokine secretion was also observed in inflamed cells exposed to nanoparticles loaded with control siRNA, as well as to reference unloaded nanoparticles (**Figure 53**). This would rather suggest the impact of other nanoparticle components (calcium, phosphate, PEI, silica or trace amounts of trehalose), released into the cytoplasm after endolysosomal degradation of the nanoparticles, on cytokine downregulation effect.

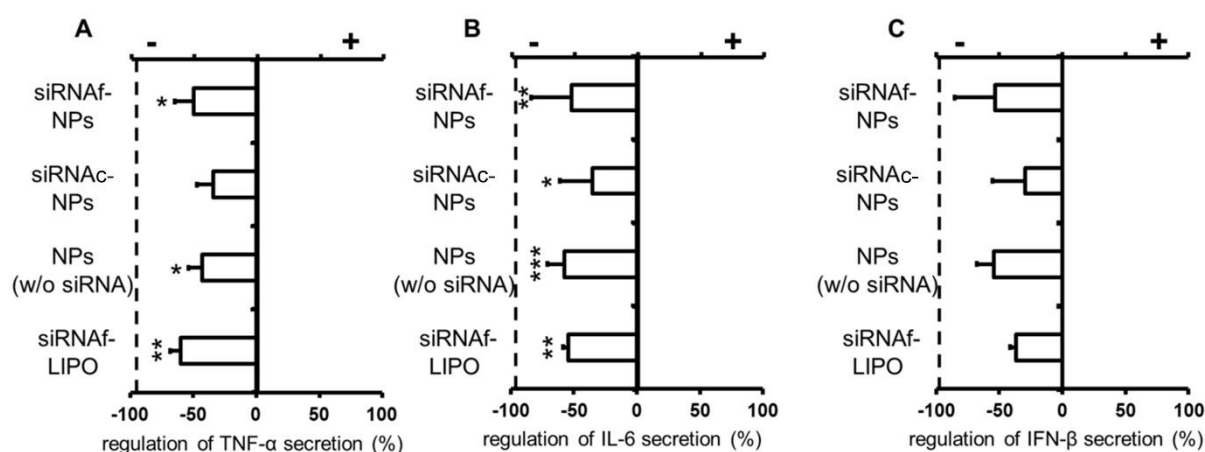


**Figure 53.** Downregulation of cytokine expression after exposure of inflamed monocytes to different CaP nanoparticles (used in *in vitro* gene silencing studies) and free functional siRNA, as reference. The regulation is defined here as ratio of cytokine secretion with respect to the inflammatory state (LPS-primed cells, absence of nanoparticles) set to zero. “+ regulation” = upregulation, “- regulation” = downregulation. The levels of TNF- $\alpha$  (A), IL-6 (B) and IFN- $\beta$  (C) were measured in the cell supernatants. siRNAf-NPs – nanoparticles loaded with functional siRNA (CaP/PEI-Cy5/siRNAf/SiO<sub>2</sub>), siRNAc-NPs – nanoparticles loaded with control siRNA (CaP/PEI-Cy5/siRNAc/SiO<sub>2</sub>), NPs (w/o siRNA) – nanoparticles without siRNA loading (CaP/PEI-Cy5/SiO<sub>2</sub>) and siRNAf-LIPO – functional siRNA transfected into cells using Lipofectamine<sup>®</sup>. *p*-values indicate a significant difference of secretion compared to the inflammatory condition without the nanoparticles, with  $p < 0.05$  (\*),  $p < 0.01$  (\*\*),  $p < 0.001$  (\*\*\*) or  $p < 0.0001$  (\*\*\*\*) ( $N=3$ ).

## 5.2. Project II – Chemistry of fossilized proboscidean enamel

### 5.2.1. Chemical characterization of fossilized proboscidean enamel

#### 5.2.1.1. Elemental analyses

The results of calcium and phosphate content in proboscidean enamel are summarized in **Figure 54**. These data can be further re-calculated to calcium-to-phosphate (Ca<sup>2+</sup>/PO<sub>4</sub><sup>3-</sup>) molar ratio in enamel, which is an indication of the CaP phase in enamel.

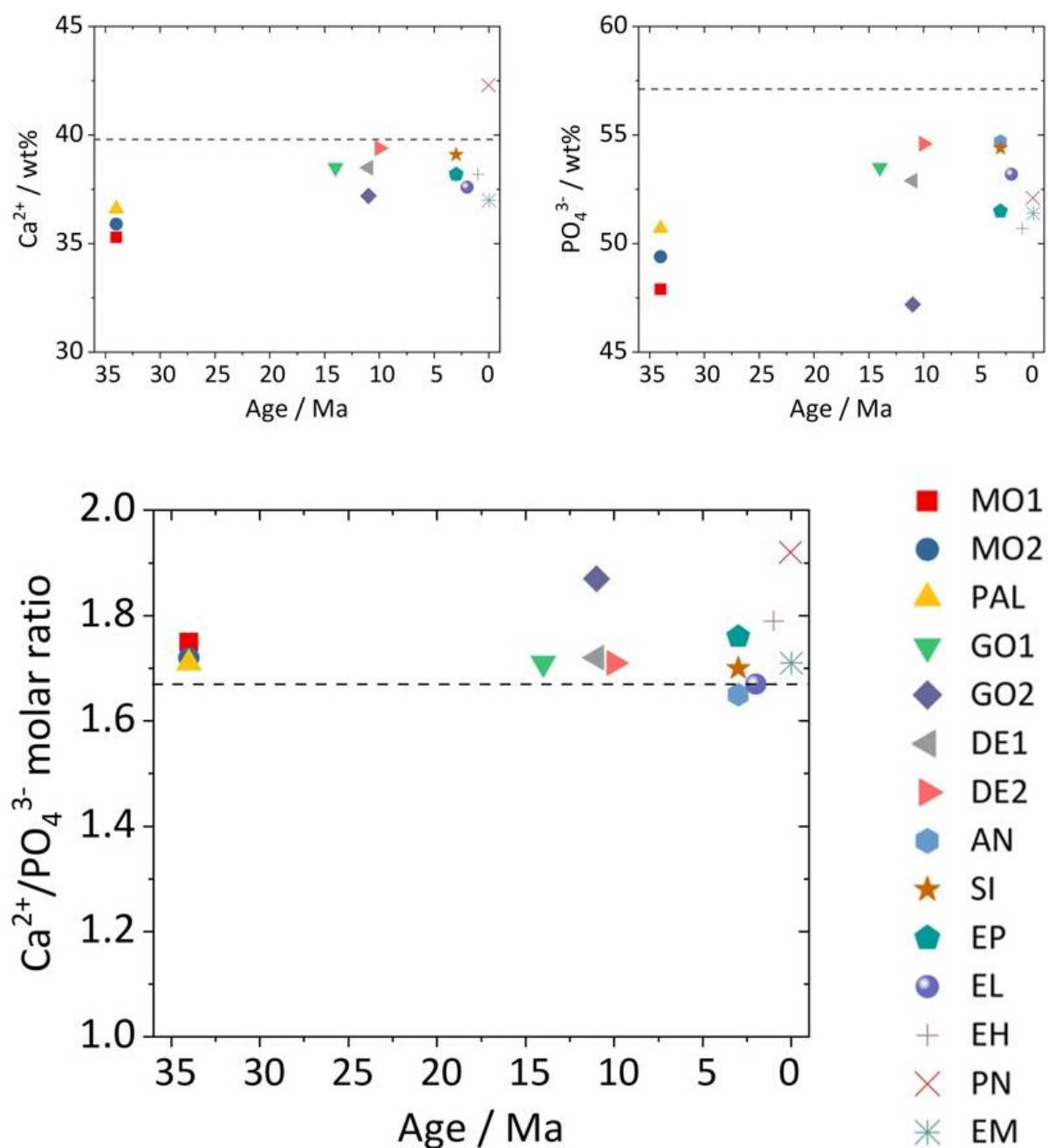


**Figure 54.** The summary of calcium (*left graph*) and phosphate (*right graph*) contents, as well as of calcium-to-phosphate molar ratio (*lower graph*) in enamel bioapatite. Theoretical contents of calcium and phosphate, and their molar ratio in pure hydroxyapatite are marked in the graphs with dashed lines.

The content of calcium and phosphate in enamel bioapatite were stable over the time, and no significant age-related differences between samples were observed with regard to this feature. A similar tendency as in proboscidean enamel was also reported in shark enamel.<sup>97,98,266</sup> The content of calcium and phosphate, and calcium-to-phosphate molar ratio in proboscidean

enamel bioapatite were close to the theoretical values in pure hydroxyapatite, which are 39.9 wt%, 56.7 wt% and 1.67, respectively. However, the observed lowered values, in particular for the phosphate content, were already an indication of ionic substitutions in bioapatite. Examples of such substitutions may be magnesium for calcium, fluoride (F<sup>-</sup>)/carbonate for hydroxide (A-type substitution) and hydrogenphosphate/carbonate for phosphate (B-type substitution).<sup>267</sup> Low values of the light elements (carbon, hydrogen, nitrogen, sulfur) in bioapatite indicated low organic content in fossilized enamel, which was about 1-2 wt% of carbon and 0.3-0.5 wt% of hydrogen. The fluoride content in fossilized proboscidean enamel was significantly higher than in the enamel of the recent elephant. This is compliant with the report of Roche *et al.* who investigated fossilized tooth enamel of different Miocene-Pliocene mammals, including proboscideans.<sup>268</sup> Similarly, as in the case of calcium and phosphate content, also fluoride content in fossilized proboscidean enamel demonstrated no significant age-dependency between studied samples. This agrees with the general assumption that there is no clear relationship between fluoride content and fossilization time.<sup>267,268</sup> The content of fluoride in fossilized proboscidean enamel may be species-specific and is probably not influenced by environmental fluoride, similarly as it is in fossilized fish enamel.<sup>269</sup> No clear age-relationship was also found for the content of other elements, like magnesium, sodium, carbon, hydrogen and chlorine. There were no significant differences between fossilized samples of different age in the content of silicon, iron and aluminum, which are elements of diagenetic origin in enamel bioapatite. This observation indicates considerable resistance of enamel to environmentally-driven chemical alteration and diagenesis during fossilization. All elemental analysis data for fossilized and recent (non-fossilized) enamel samples obtained by combustion analysis (carbon, hydrogen, nitrogen, sulfur), AAS (calcium, sodium, magnesium), ion-selective potentiometry (fluorine), UV spectroscopy (phosphate) and EDX (aluminum, chlorine, iron, silicon) are summarized in **Table 13**.

**Table 13.** Characterization data of the chemical composition of proboscidean enamel. \*\*\* – detection limit.

Sample:	Ca <sup>2+</sup> / wt%:	PO <sub>4</sub> <sup>3-</sup> / wt%:	F / wt%:	Na / wt%:	Mg / wt%:	C / wt%:	H / wt%:	S / wt%:	N / wt%:	Al / wt%:	Cl / wt%:	Fe / wt%:	Si / wt%:	Ca <sup>2+</sup> /PO <sub>4</sub> <sup>3-</sup> molar ratio:
MO1	35.3	47.9	1.47	0.62	0.11	1.51	0.45	<***	<***	0.79	<***	0.82	0.79	1.75:1
MO2	35.9	49.4	1.00	0.61	0.13	1.19	0.30	0.46	<***	0.50	0.33	0.93	0.86	1.72:1
PAL	36.6	50.7	0.95	0.78	0.15	1.71	0.45	<***	<***	0.16	<***	1.08	0.36	1.71:1
GO1	38.5	53.5	0.75	0.41	0.11	1.14	0.32	<***	<***	0.41	0.32	0.57	0.54	1.71:1
GO2	37.2	47.2	2.01	0.68	0.09	1.72	0.43	<***	<***	0.14	0.02	1.64	0.37	1.87:1
DE1	38.5	52.9	0.32	0.62	0.15	1.09	0.40	<***	<***	0.45	0.48	0.69	0.54	1.72:1
DE2	39.4	54.6	0.78	0.49	0.08	1.23	0.39	<***	<***	0.26	0.26	<***	0.43	1.71:1
AN	38.2	54.7	0.42	0.45	0.12	0.97	0.33	<***	<***	0.25	0.30	0.44	0.33	1.65:1
SI	39.1	54.4	0.40	0.55	0.13	1.07	0.34	<***	<***	0.08	0.15	<***	0.28	1.70:1
EP	38.2	51.5	0.97	0.57	0.10	1.63	0.41	<***	<***	0.24	0.14	0.44	0.52	1.76:1
EL	37.6	53.2	0.65	0.46	0.10	1.08	0.34	<***	<***	0.30	0.21	0.60	0.31	1.67:1
EH	38.2	50.7	0.92	0.54	0.12	1.72	0.45	<***	<***	0.34	0.31	0.69	0.47	1.79:1
PN	42.3	52.1	0.58	0.59	0.15	2.05	0.51	<***	<***	0.47	0.46	0.57	0.59	1.92:1
EM	37.0	51.4	0.04	0.63	0.24	1.48	0.41	<***	<***	0.41	<***	0.43	0.59	1.71:1

Beside general elemental composition of the enamel, the local distribution of fluorine and sodium was investigated by EDX mapping in representative fossilized tooth fragments. The mapping region covered the upper dentin/cement, EDJ/ECJ and the inner enamel, as well as part of the outer enamel. Differences in the local distribution of studied elements between dentin/cement and enamel were observed within proboscidean teeth (**Figure 55**).

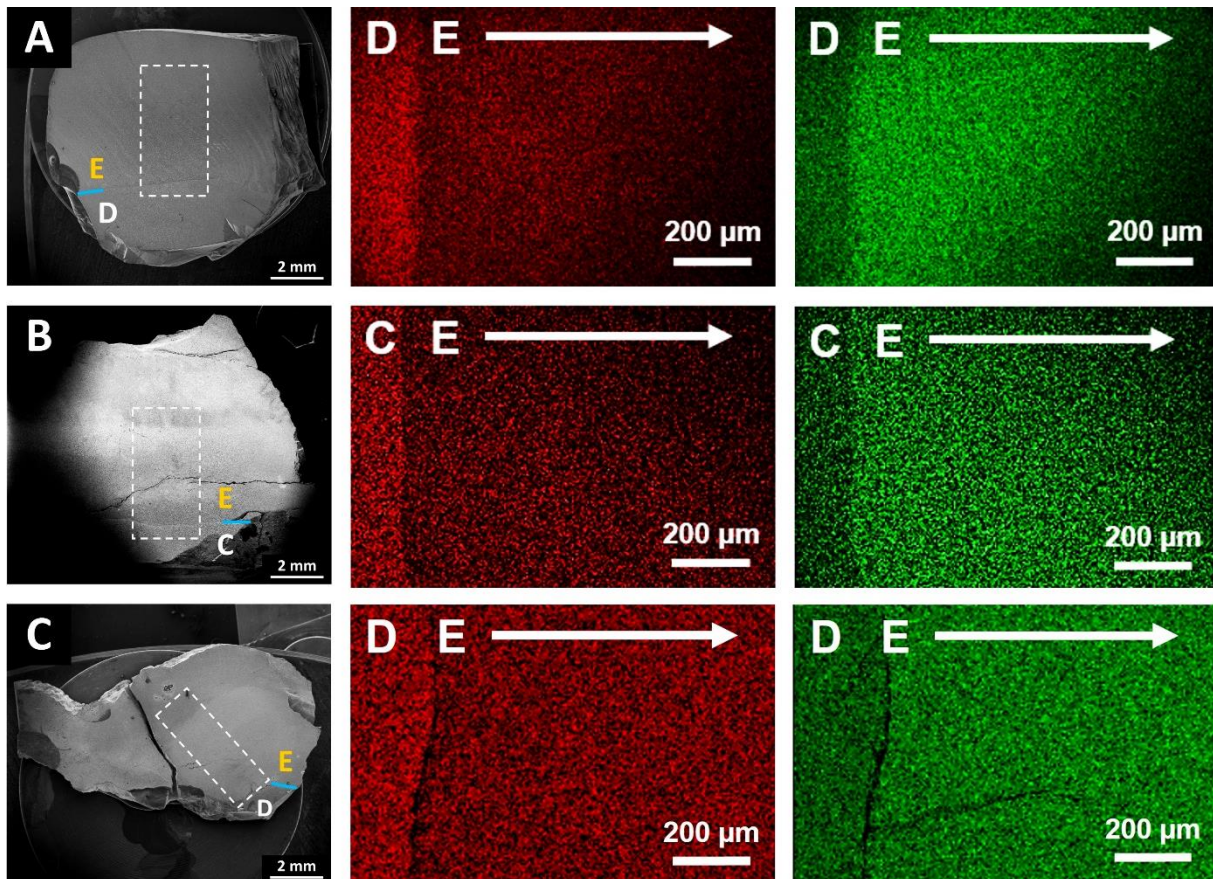


**Figure 55.** EDX mapping of the local distribution of elements in fossilized proboscidean teeth. Samples AN (A), SI (B) and EL (C) were investigated. SEM micrographs of whole tooth fragments (*left*) present the mapping regions (marked with dashed lines). The *blue line* indicates localization of EDJ/ECJ in the samples. Results of the local distribution of fluorine (*red*) and sodium (*green*) in dentin/cement and enamel are presented. The brighter the region was, the more element was present in it. C – cement, D – dentin, E – enamel.

Generally, more fluorine was found in dentin/cement, whereas enamel was richer in sodium. Furthermore, the amount of fluorine in the enamel was depth-dependent and decreased towards the outer enamel and the tooth surface. This observation agrees with an earlier report of Wilmers and Bargmann on variations of substituting elements over enamel thickness.<sup>270</sup> Nakagaki *et al.*

observed a similar tendency with regard to fluorine distribution in recent human teeth and Dauphin and Williams reported presence of sodium-enriched enamel, when compared to dentin, in fossilized teeth of Pleistocene rodents.<sup>271-273</sup>

### 5.2.1.2. TG and IR analyses

TG analyses gave further information on the composition of proboscidean enamel. TG results were re-calculated to the content of carbonate in enamel bioapatite.<sup>274</sup> All studied samples demonstrated similar thermogram curve patterns, with an average mass loss of ~10% and average carbonate content of ~2 wt% (**Figure 56; Table 14**).

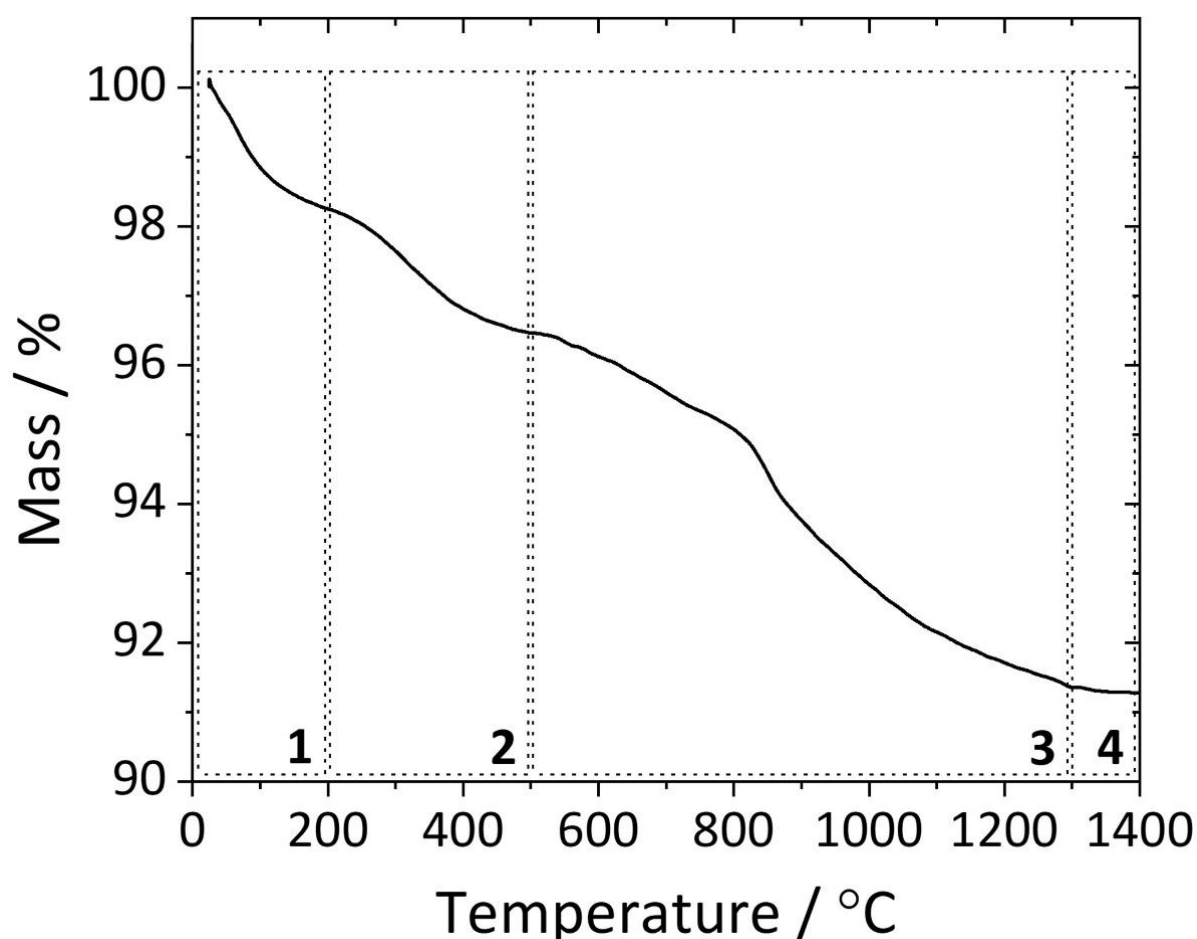


**Figure 56.** Representative thermogram of proboscidean enamel (EP sample). **Region 1:** release of physically-adsorbed water. **Region 2:** combustion of the organic material and release of structural water. **Region 3:** release of CO<sub>2</sub> from enamel bioapatite. **Region 4:** remaining pure inorganic material (bioapatite). During heating of the sample up to 1,400 °C a total mass loss of ~9% (water, organics) was detected.

**Table 14.** Summary of the data of crystallite size and diameter of crystals (by XRD and SEM, respectively), apatite substitution type (B/A) and ratio (by IR spectroscopy), and the content of carbonate (by TG) in investigated proboscidean enamel samples.

Sample:	Crystallite size (XRD) / nm:	Diameter of crystals (SEM) / nm:	B/A substitution ratio:	CO <sub>3</sub> <sup>2-</sup> / wt%:
MO1	52 ± 1	63 ± 14	2.0:1	2.0
MO2	39 ± 1	56 ± 10	3.0:1	1.4
PAL	39 ± 1	55 ± 10	2.5:1	0.7
GO1	35 ± 1	72 ± 12	2.5:1	1.4
GO2	24 ± 1	48 ± 9	2.5:1	3.4
DE1	24 ± 1	68 ± 11	2.5:1	1.4
DE2	32 ± 1	50 ± 11	3.0:1	1.4
AN	36 ± 1	43 ± 6	1.5:1	2.7
SI	44 ± 1	71 ± 12	3.0:1	2.0
EP	24 ± 1	48 ± 9	3.0:1	2.0
EL	38 ± 1	61 ± 11	3.0:1	2.0
EH	39 ± 1	58 ± 11	2.5:1	2.7
PN	37 ± 1	57 ± 10	3.0:1	2.0
EM	40 ± 1	56 ± 11	3.0:1	2.0

Proboscidean enamel contained less carbonate than is typically found in bioapatite of recent teeth (3-7 wt%), however, the results were already in the range of carbonate content in fossilized shark teeth.<sup>89,96,135,275</sup> No significant correlation between the age of the sample and its carbonate content was found. Furthermore, proboscidean enamel contained low amounts of the organic material. This agreed well with elemental analysis results of the light elements (carbon, hydrogen) in the enamel (presented in **Table 13**).

IR analyses gave insight into the substitution of carbonate in the apatite lattice and have shown that in all studied proboscidean enamel samples, independently on their age, B-type substitution (carbonate on phosphate positions) of carbonated bioapatite was preferential to A-type substitution (carbonate on hydroxide positions), although both substitution types were found in the enamel bioapatite (**Figure 57**; **Table 14**).<sup>276</sup>

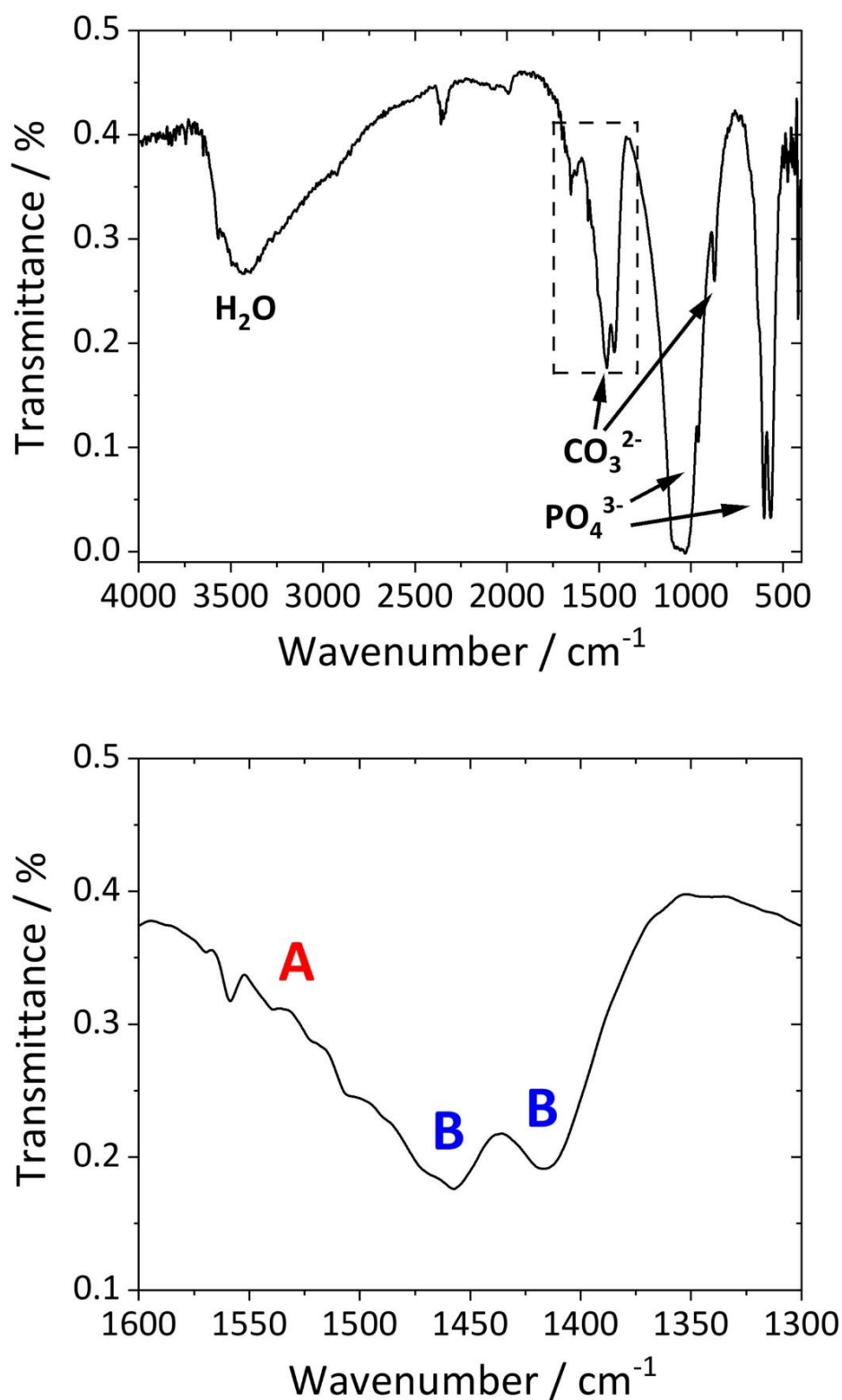


**Figure 57.** Representative IR spectrum of proboscidean enamel (DE2 sample). The **upper graph** presents the whole IR spectrum of the sample in a wavenumber measurement range 4,000-400  $\text{cm}^{-1}$ , whereas the **lower graph** presents the enlarged spectrum region 1,600-1,300  $\text{cm}^{-1}$  (marked in the upper graph with the dashed line), which shows the type (A/B) of carbonated bioapatite substitution.<sup>277-279</sup>

Thermograms and IR spectra of all other studied proboscidean enamel samples are presented in chapter 5.2.3. in Figures 64-65 of the Supplementary information, respectively.

### 5.2.1.3. XRD analyses

XRD analyses provided detailed information on crystalline phase of enamel bioapatite and changes of its lattice parameters. Performing detailed Rietveld refinement allowed to determine crystallite size in bioapatite, which was later compared with the crystal diameter studied parallel by SEM. The enamel showed a common for proboscideans XRD curve pattern of nanocrystalline apatite (Figure 58).

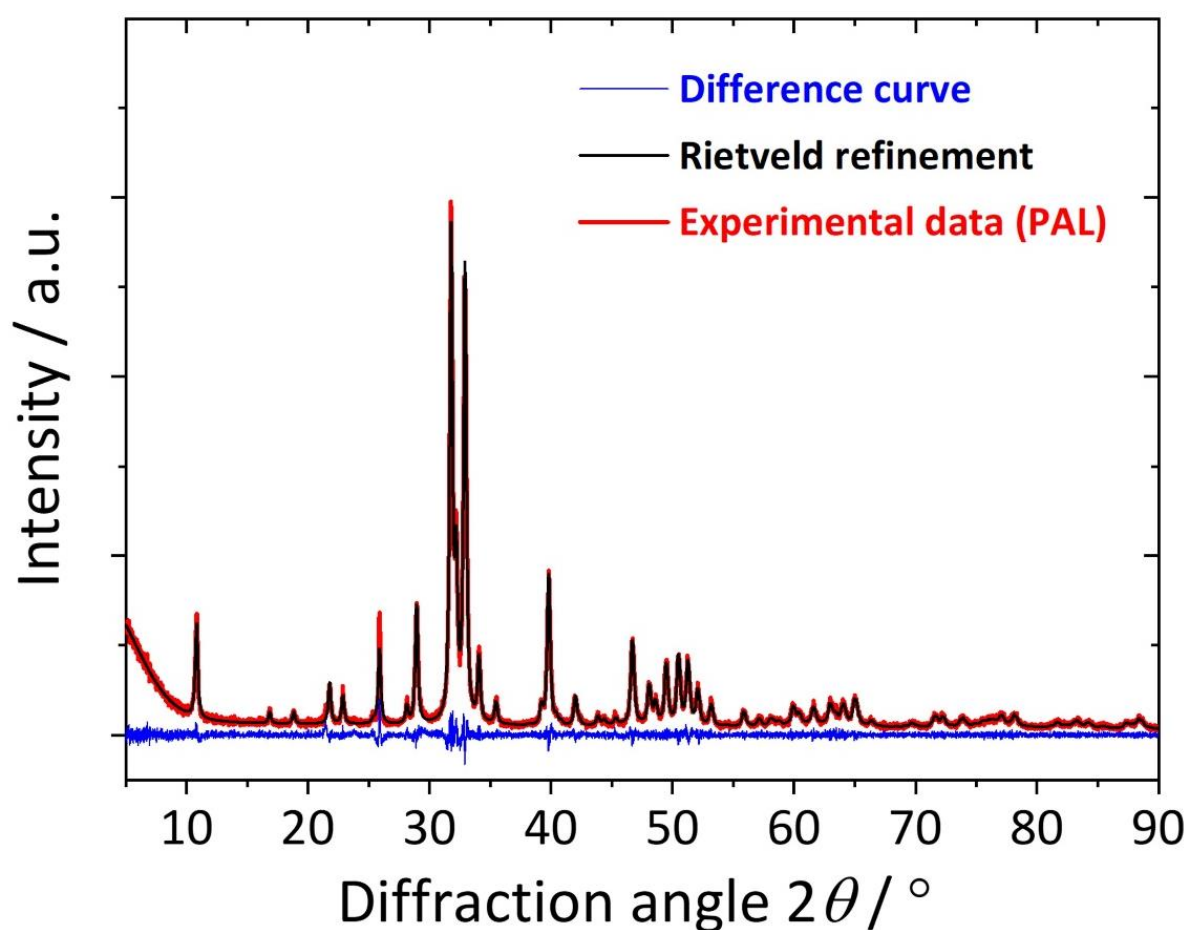


**Figure 58.** Representative XRD powder diffractogram of proboscidean enamel (PAL sample), including Rietveld refinement with hydroxyapatite structure.

In an earlier study, Sakae *et al.* reported that XRD curve pattern of the enamel of extinct proboscideans (Eocene-Pleistocene) showed similarity with the XRD pattern of human enamel.<sup>267</sup> From the broad diffraction peaks (which are typical for small crystallites) the

crystallite size was calculated.<sup>280</sup> Moreover, XRD results confirmed occurrence of ionic substitution of the enamel bioapatite, which was reflected in changes of apatite lattice parameters, in particular the increase of the  $a$ -axis length, due to substitution, when compared to pure hydroxyapatite. This was also compliant with interpretation of elemental analysis data. Furthermore, no significant age-related changes were found by analyzing and comparing the values of XRD-determined crystallite size and SEM-determined crystal diameter of enamel bioapatite (**Figure 59**).

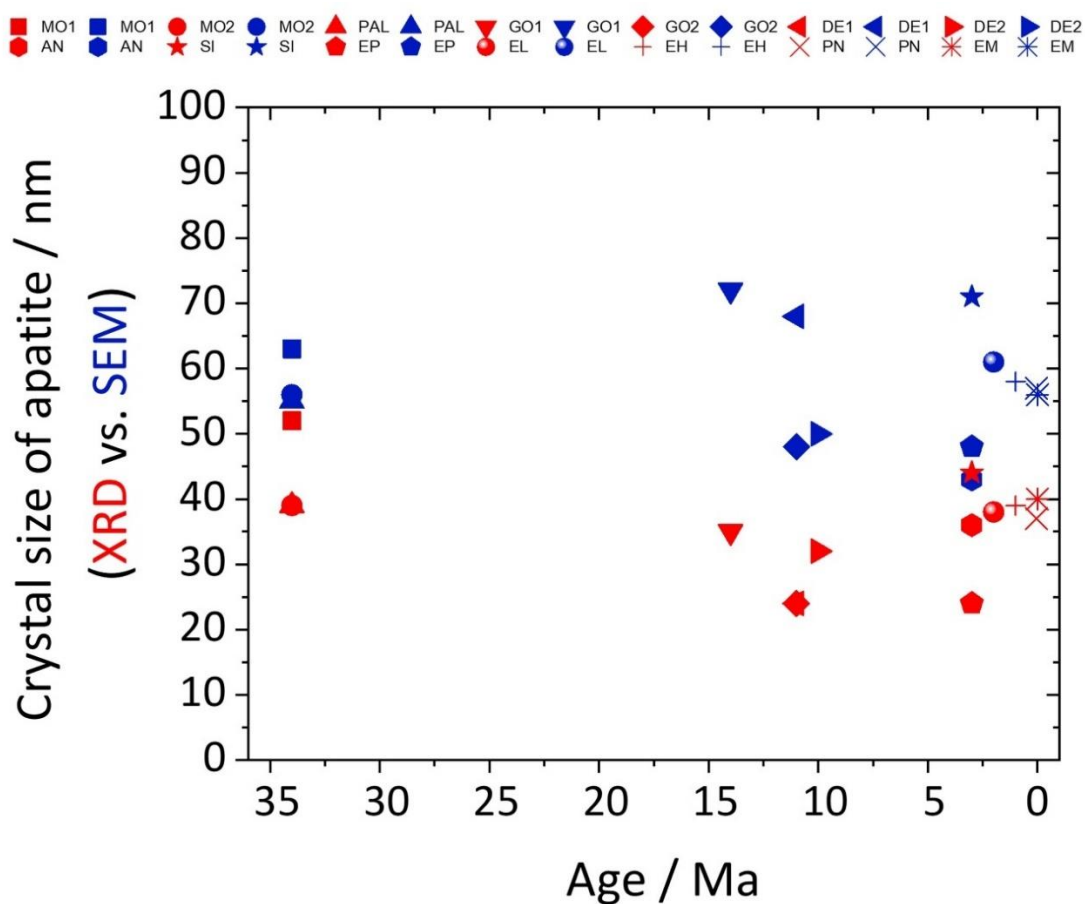


**Figure 59.** Comparison of the results of crystallite size and crystal diameter in proboscidean enamel bioapatite studied by XRD (red) and SEM (blue), respectively.

Differences in the results for size determination can be explained with the specificity of measurement principle of the applied methods. Using XRD the diameter of crystallites, which are crystal building domains, is determined, whereas by SEM the diameter of crystals is analyzed. The latter, if it is not a single crystal made of just 1 crystallite, is usually composed of more crystallites, which are measured by SEM together within the whole crystal. This results in generally higher size determination values obtained by SEM, when compared to XRD. The

average size of bioapatite crystallites and crystals in fossilized proboscidean enamel was 30-40 nm and 40-70 nm by XRD and SEM, respectively (**Table 14**). Furthermore, no other crystalline phases indicating possible diagenetic alteration of proboscidean enamel were found by XRD. Powder diffractograms of all other studied proboscidean enamel samples are presented in chapter 5.2.3. in **Figure 66** of the **Supplementary information**.

#### 5.2.1.4. Stable oxygen isotope ( $\delta^{18}\text{O}$ ) studies

In paleontological studies on the diagenetic alteration of hydroxyapatite in fossilized samples, analyses of oxygen isotopic composition of carbonate ( $\delta^{18}\text{O}\text{-CO}_3^{2-}$ ) and phosphate ( $\delta^{18}\text{O}\text{-PO}_4^{3-}$ ) are preferential. Due to lower strength, the C-O bond is more susceptible to diagenesis and chemical alteration than the P-O bond. The relationship between the  $\delta^{18}\text{O}$  isotope of carbonate and phosphate ( $\Delta_{\text{CO}_3\text{-PO}_4}$ ) is a diagnostic marker to evaluate the level of preservation of the primary isotopic composition of enamel bioapatite, taking into account also alteration of diagenetic origin.<sup>281,282</sup> It is considered that  $\Delta_{\text{CO}_3\text{-PO}_4}$  of  $\sim 9\%$  stands for good preservation of fossilized bioapatite, characterized by minor diagenetic alteration.<sup>283</sup>  $\Delta_{\text{CO}_3\text{-PO}_4}$  values for enamel samples analyzed in these studies (Miocene-Pleistocene) were in the range 10-14%, which indicated presence of diagenetic alteration, however, this sample property was not age-related (**Table 15**).

**Table 15.** Stable oxygen isotope ratios for structural phosphate ( $\delta^{18}\text{O}\text{-PO}_4^{3-}$ ) and carbonate ( $\delta^{18}\text{O}\text{-CO}_3^{2-}$ ) in enamel bioapatite of proboscideans and rhinoceros. VSMOW – Vienna Standard Mean Ocean Water.

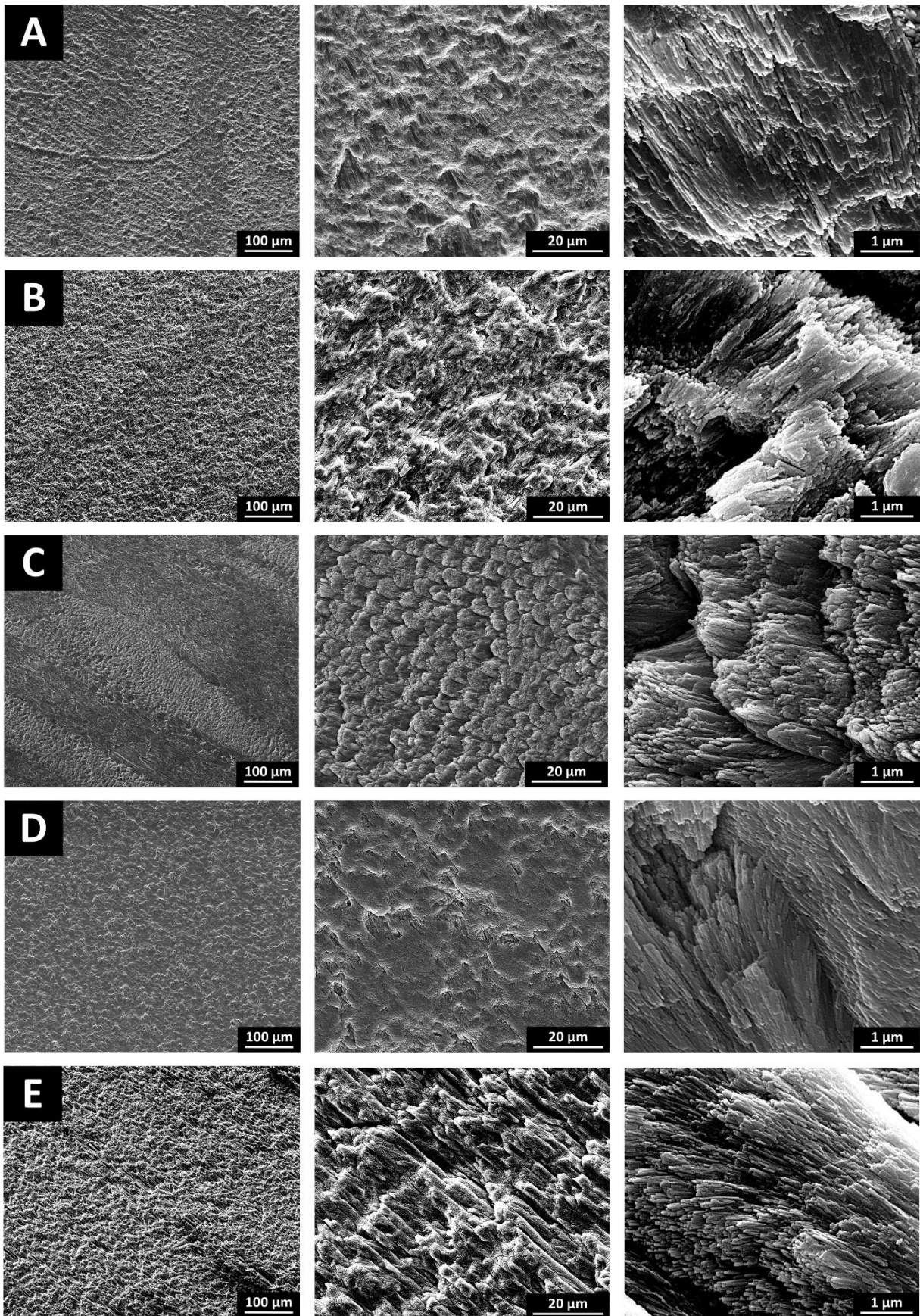
Sample:	Taxa:	Age / Ma:	$\delta^{18}\text{O}\text{-PO}_4^{3-}$ [‰, VSMOW]	$\delta^{18}\text{O}\text{-CO}_3^{2-}$ [‰, VSMOW]	$\Delta_{\text{CO}_3\text{-PO}_4}$
RB41	<i>Rhinocerotidae</i>	~14-13	7.3	17.8	10.5
GO1	<i>Gomphotheridae</i>	~14-13	7.1	20.2	13.1
DD1	<i>Deinotherium</i> sp.	~11	8.9	22.0	13.1
EP	<i>E. platycephalus</i>	~3.0-2.6	14.5	26.0	11.5
B608	<i>Elephas planifrons</i>	~3.0-2.6	10.9	25.1	14.2
A155	<i>Elephas planifrons</i>	~2.5-1.5	14.1	23.8	9.7
EL	<i>E. hysudricus</i>	~1.5	14.3	25.2	10.9
VPL/B 2060	<i>E. hysudricus</i>	~0.5	11.9	24.6	12.7
PN	<i>P. namadicus</i>	~0.05	17.3	31.0	13.7

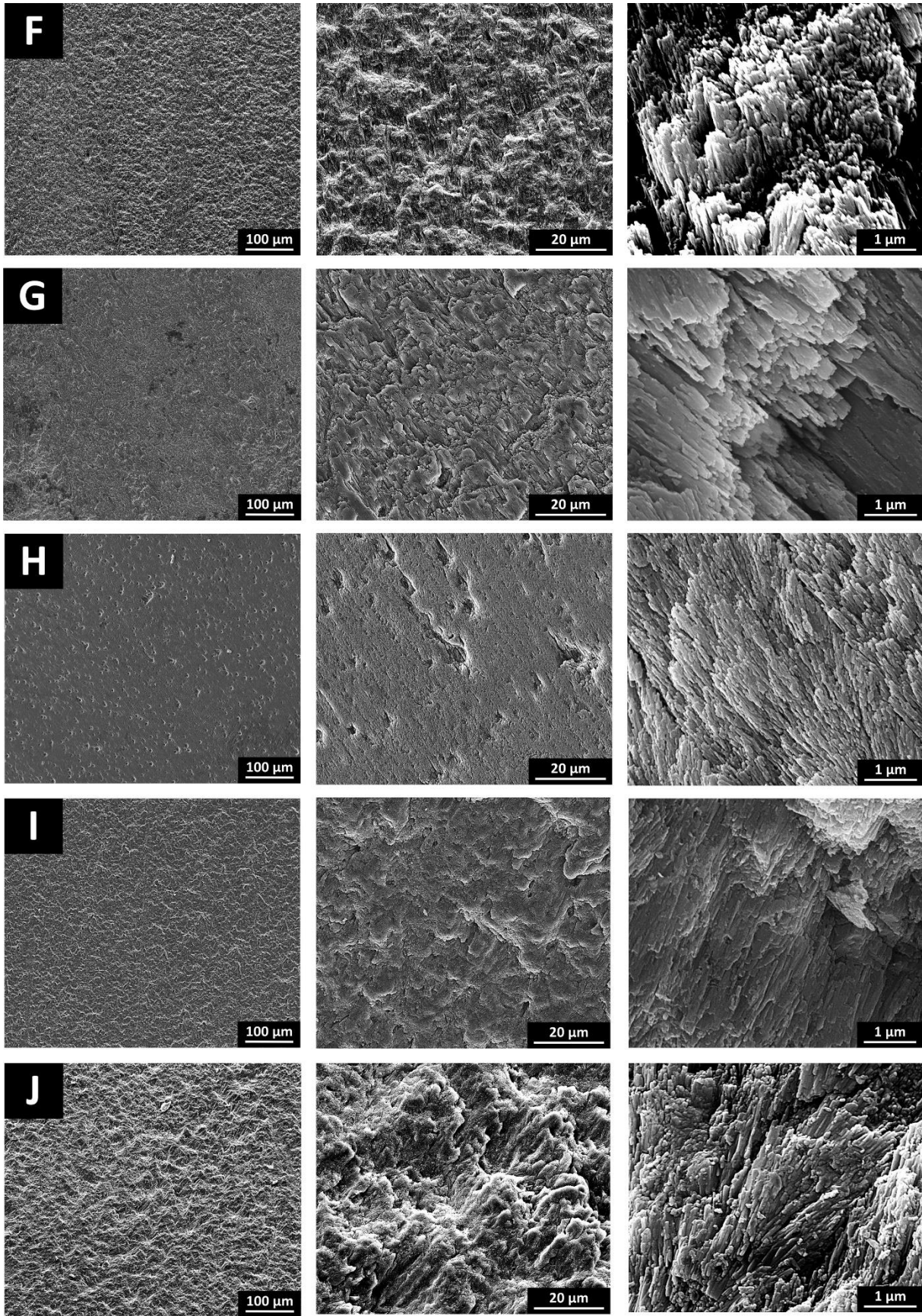
Enamel apatite, when compared to dentin apatite, is less susceptible to diagenesis, due to larger crystal size and lower organic content. Stable isotope data for mammalian herbivore teeth provide valuable information about the animal's diet and physiology, and the environment.<sup>284-</sup>

286

### **5.2.2. Microstructure of fossilized proboscidean enamel**

All studied proboscidean enamel samples showed a very well-preserved microstructure, even the oldest samples from Egypt (~34 Ma). The process of sample preparation for SEM imaging, especially the steps of diamond polishing and acid etching of the samples, did not significantly alter the microstructure of enamel, enabling to preserve its unique prismatic architecture (**Figures 60-61**).





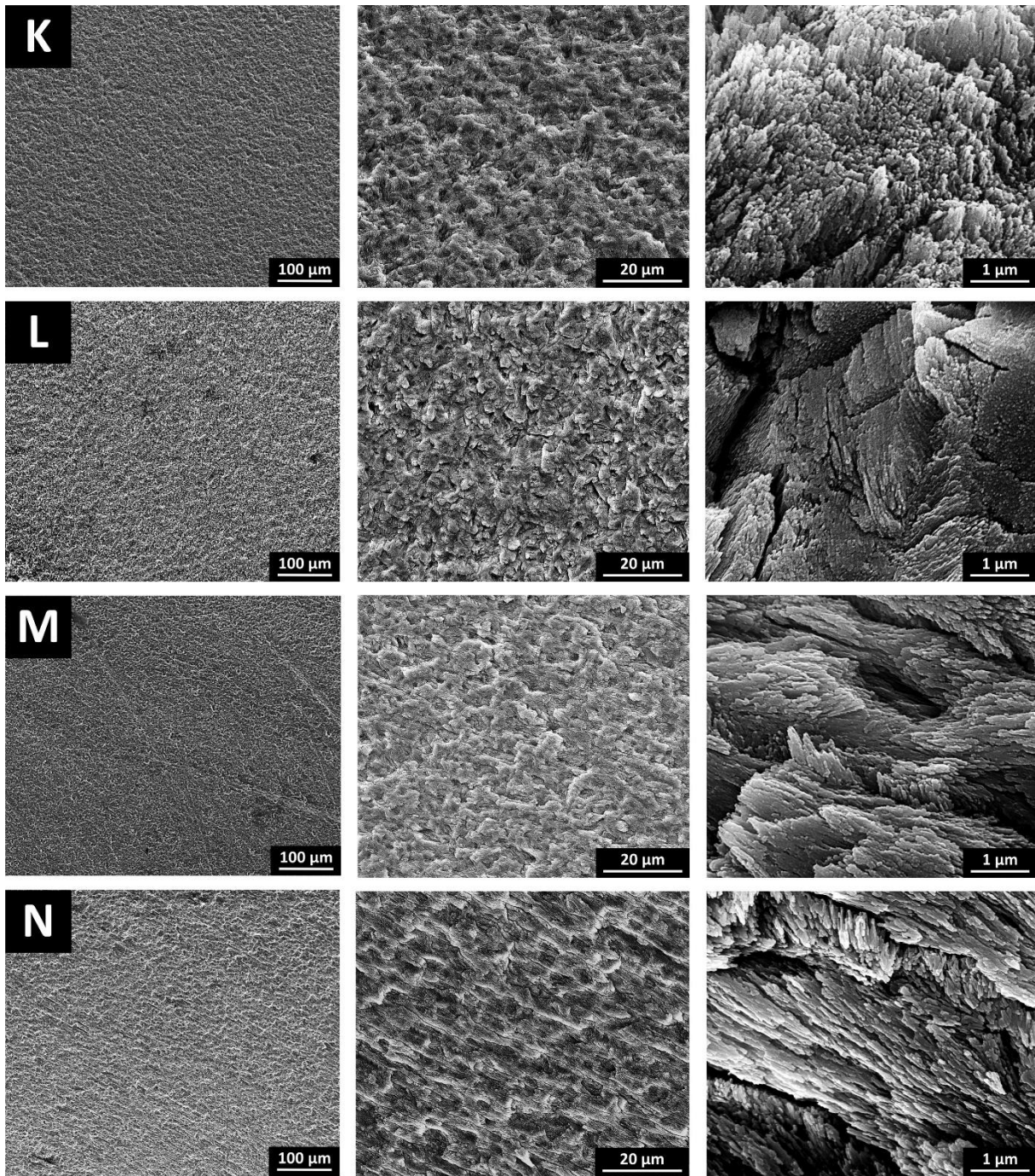


**Figure 60.** SEM micrographs presenting the microstructure of proboscidean enamel samples: MO1(A), MO2 (B), PAL (C), GO1 (D), GO2 (E), DE1 (F), DE2 (G), AN (H), SI (I), EP (J), EL (K), EH (L), PN (M) and EM (N), with an increasing magnification (500x; 3,000x; 50,000x) from left to right.

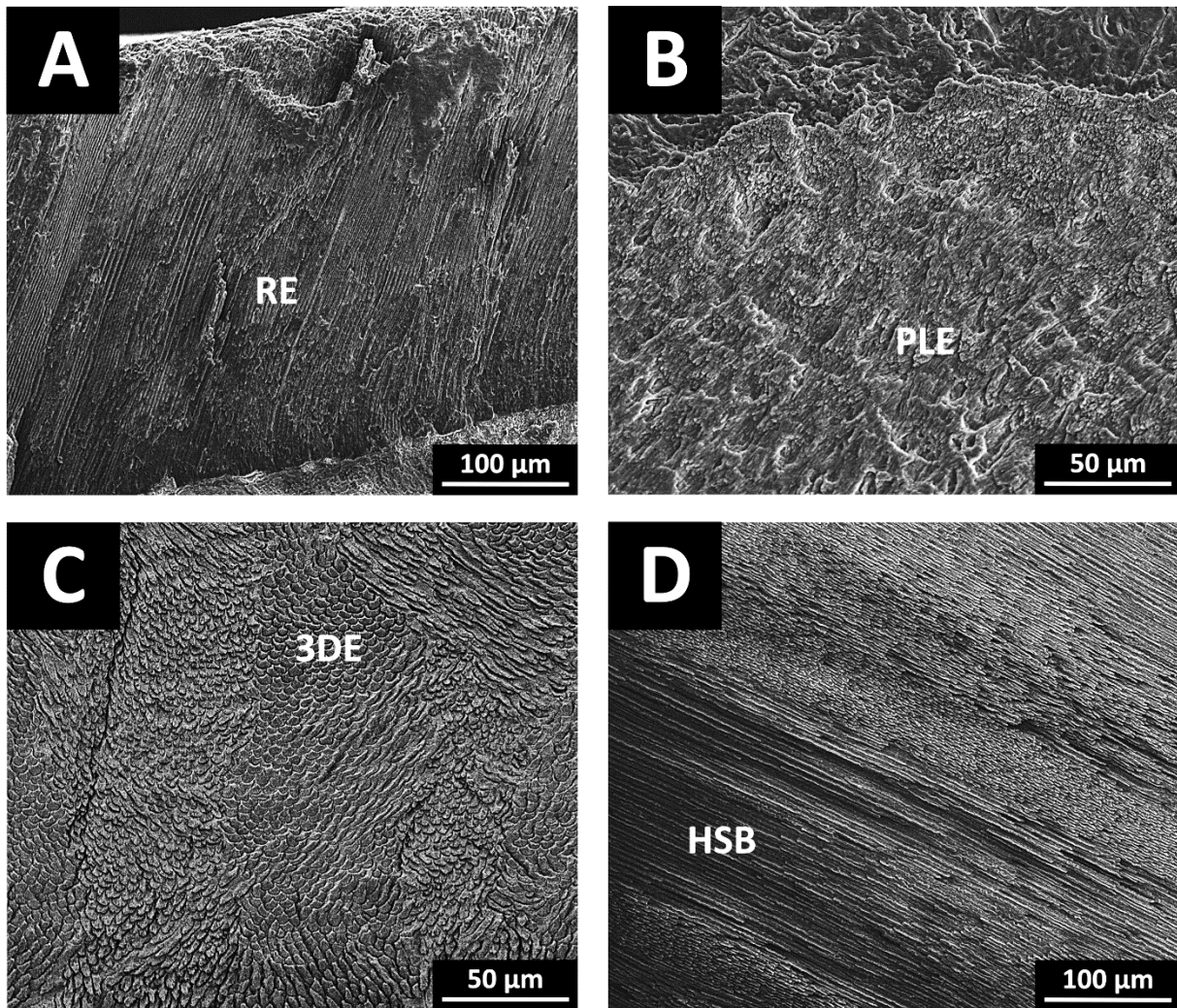


**Figure 61.** SEM micrographs presenting typical types of proboscidean enamel. These are: RE in the sample MO2 (A), PLE in the sample SI (B), 3DE in the sample PN (C) and HSB in the sample EM (D).

SEM analyses of fossilized proboscidean teeth clearly demonstrated the evolutionary trend of enamel differentiation. The early proboscideans from Eocene (*Moeritherium* sp., *Palaeomastodon* sp.) had 2-layered enamel with a primitive “schmelzmuster” composed of RE and HSB, and the keyhole prism cross-section pattern. These observations are compliant with earlier reports on enamel microstructure of extinct African *Proboscidea*.<sup>102,143,145</sup> The enamel of Miocene proboscideans (*Gomphotherium* sp., *Deinotherium* sp.) was already 3-layered with an advanced “schmelzmuster” composed of 3DE, beside RE and HSB, and the fan-shaped prism cross-section pattern. Earlier studies on Miocene elephants confirmed these observations for *Gomphotheridae*, however, some authors reported also occurrence of the primitive keyhole prism cross-section pattern, combined either with single-layered enamel (3DE) or 3-layered

enamel (RE, HSB, 3DE), like in *Deinotheridae*.<sup>143,145,287</sup> In Pliocene proboscideans, the enamel was either 3-layered (RE, HSB, 3DE), as in *Anancus* sp., or even 4-layered (RE, HSB, 3DE, PLE), like in *S. insignis* and *E. platycephalus*. In the enamel of *Anancus* sp. fan-shaped prism cross-section pattern was found, in enamel of *E. platycephalus* the ginkgo-leaf prism pattern was present, whereas in the enamel of *S. insignis* both primitive keyhole and advanced ginkgo-leaf patterns were identified. The observations for *Anancus* sp. and *S. insignis* are in accordance with earlier reports on 3-layered enamel of these Pliocene proboscideans, however, presence of PLE in the enamel profile of *S. insignis* is reported here for the first time.<sup>139</sup> Pleistocene *P. namadicus* demonstrated presence of 3-layered enamel (3DE, RE, PLE) with ginkgo-leaf prism cross-section pattern. Finally, extant *E. maximus* demonstrated 4-layered enamel (RE, HSB, PLE, 3DE) with ginkgo-leaf motif of the prism pattern, which is compliant with the previous report on the microstructure of enamel of the recent Asian elephant, however, presence of PLE in the enamel of this species, again, is reported here for the first time (**Figures 62-63**).<sup>139</sup> Generally, in hypsodont proboscideans (*Elephas* sp., *P. namadicus*) 3DE was particularly well-developed and dominated the enamel “schmelzmuster”, as well as an extensive development of PLE was observed in these animals.

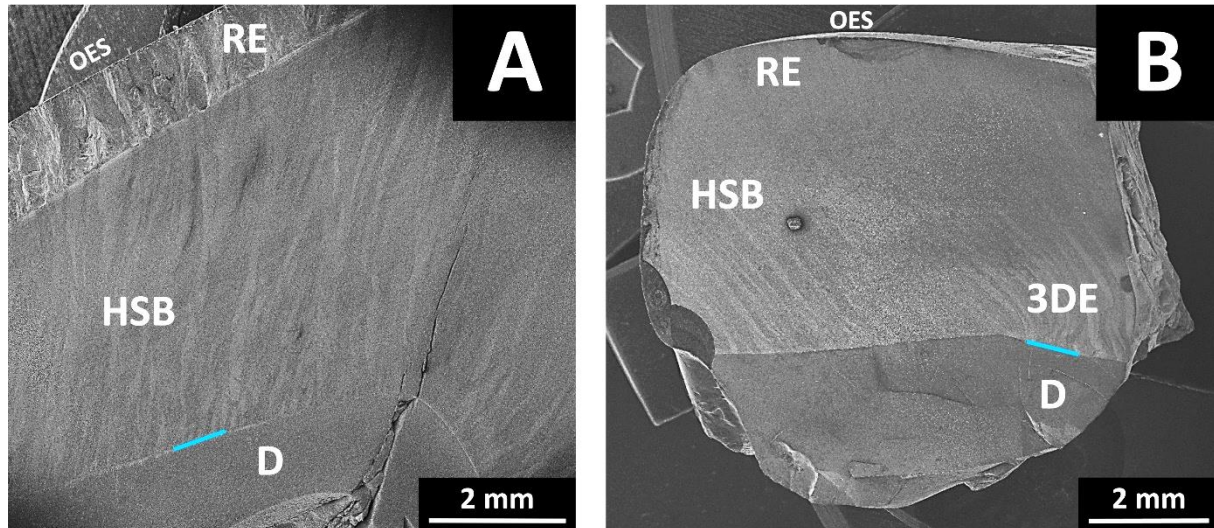


**Figure 62.** SEM micrographs presenting typical in proboscideans enamel type combinations within tooth and the direction of enamel differentiation in proboscidean evolution. These are: primitive 2-layered (RE, HSB) enamel “schmelzmuster” in the older PAL sample from Eocene (A) and advanced 3-layered (RE, HSB, 3DE) enamel “schmelzmuster” in the younger AN sample from Pliocene (B). The blue line depicts localization of EDJ in the samples. D – dentin, OES – outer enamel surface.

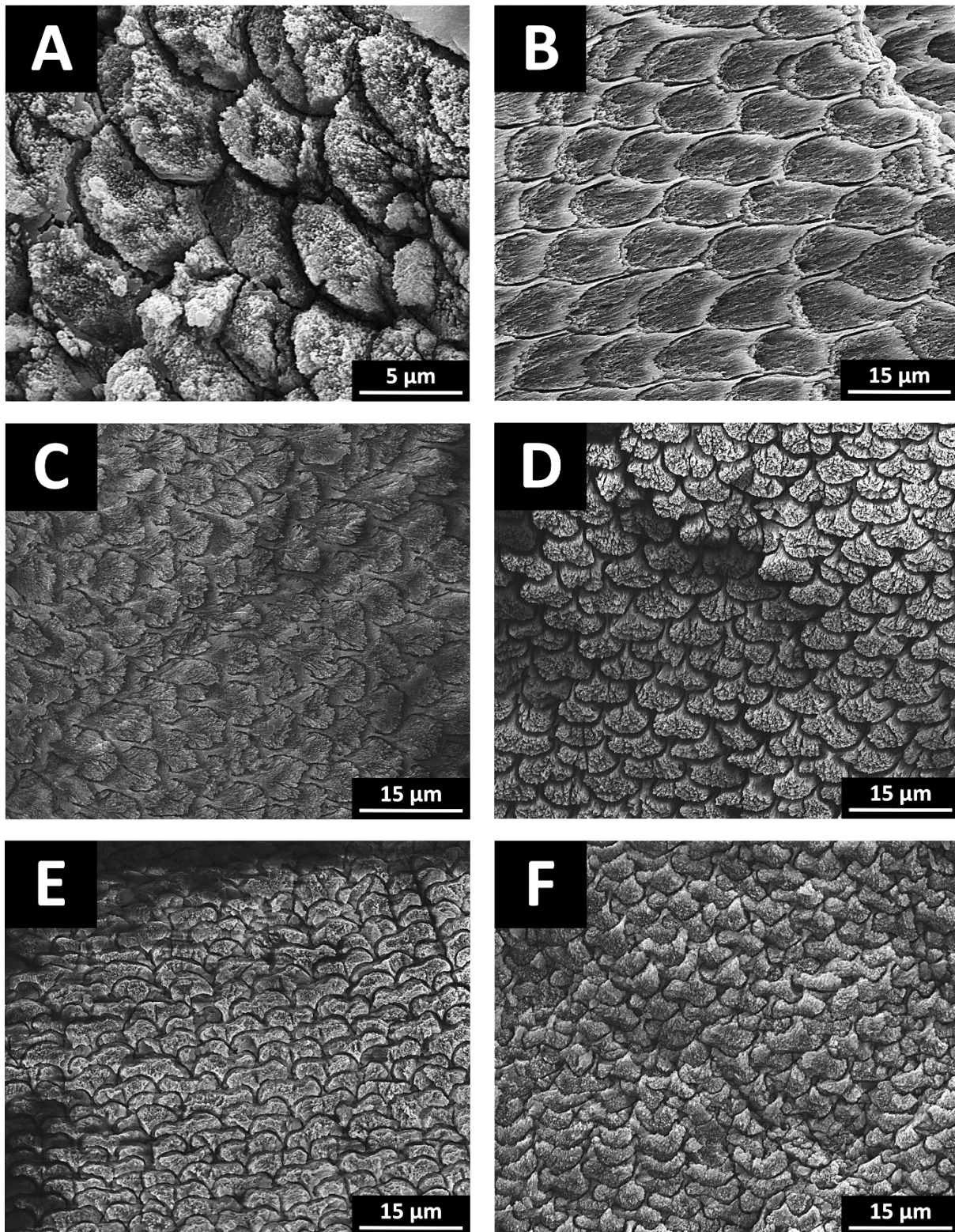


**Figure 63.** SEM micrographs presenting enamel prism cross-section patterns in proboscidean samples: MO2 (A), PAL (B), GO1 (C), DE1 (D), SI (E) and EP (F). These are: keyhole (A, B; Late Eocene samples), fan-shaped (C, D; Middle Miocene samples) and ginkgo-leaf (E, F; Late Pliocene samples) prism pattern motifs.

## 5.2.3. Supplementary information

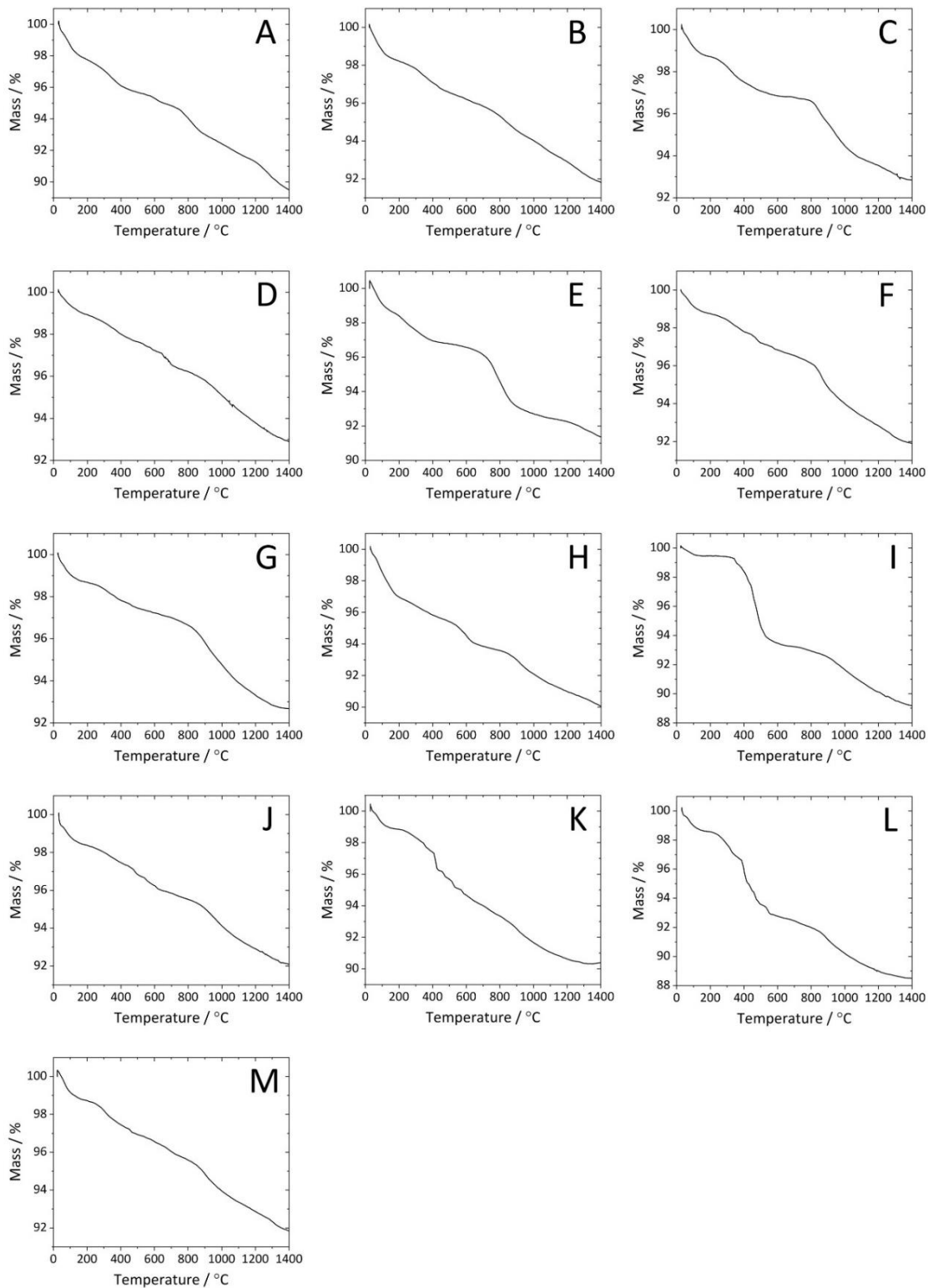


**Figure 64.** Thermograms of the remaining investigated proboscidean enamel samples: MO1 (A), MO2 (B), PAL (C), GO1 (D), GO2 (E), DE1 (F), DE2 (G), AN (H), SI (I), EL (J), EH (K), PN (L) and EM (M).

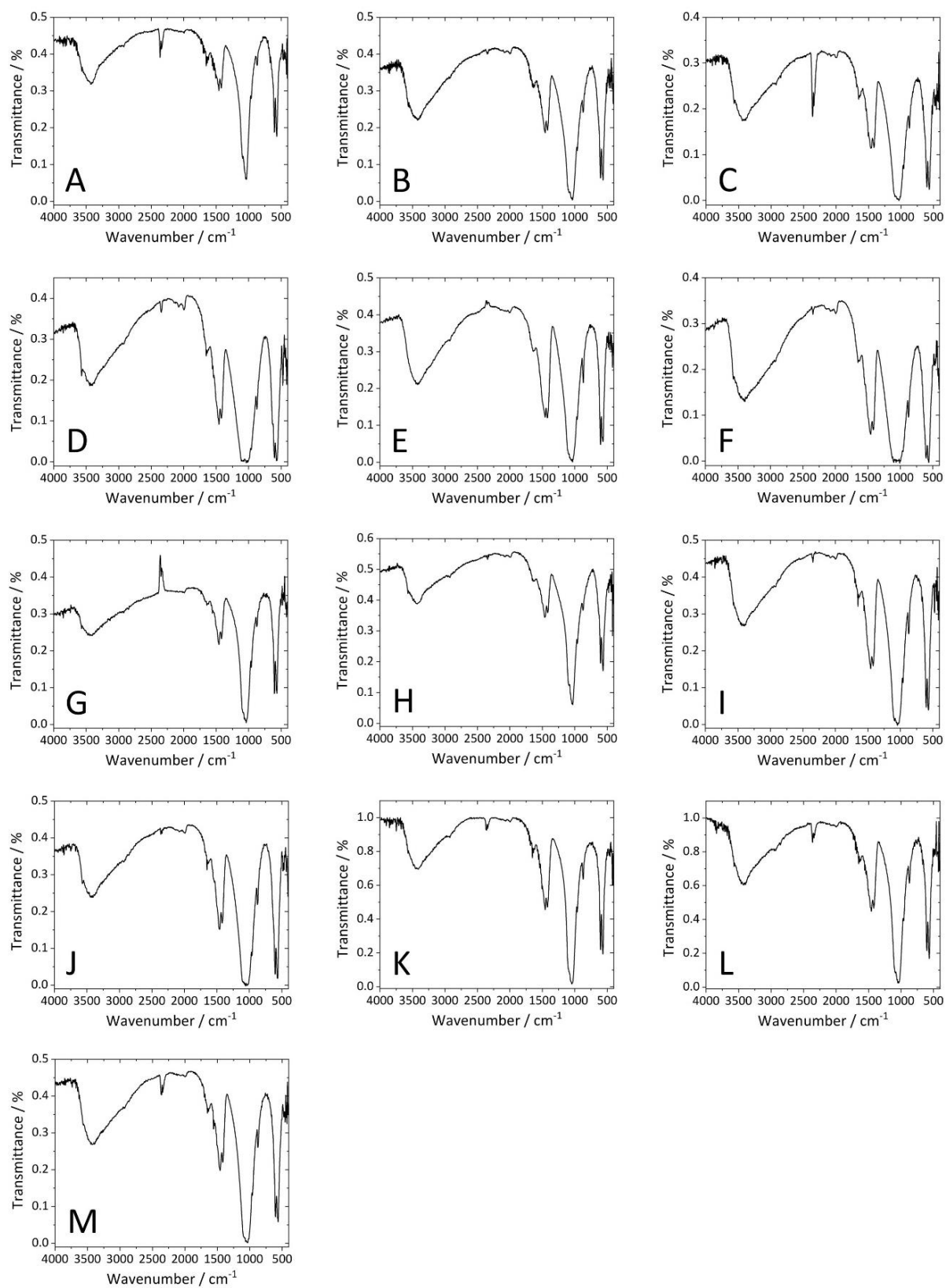


**Figure 65.** IR spectra of the remaining investigated proboscidean enamel samples: MO1 (A), MO2 (B), PAL (C), GO1 (D), GO2 (E), DEI (F), AN (G), SI (H), EP (I), EL (J), EH (K), PN (L) and EM (M).

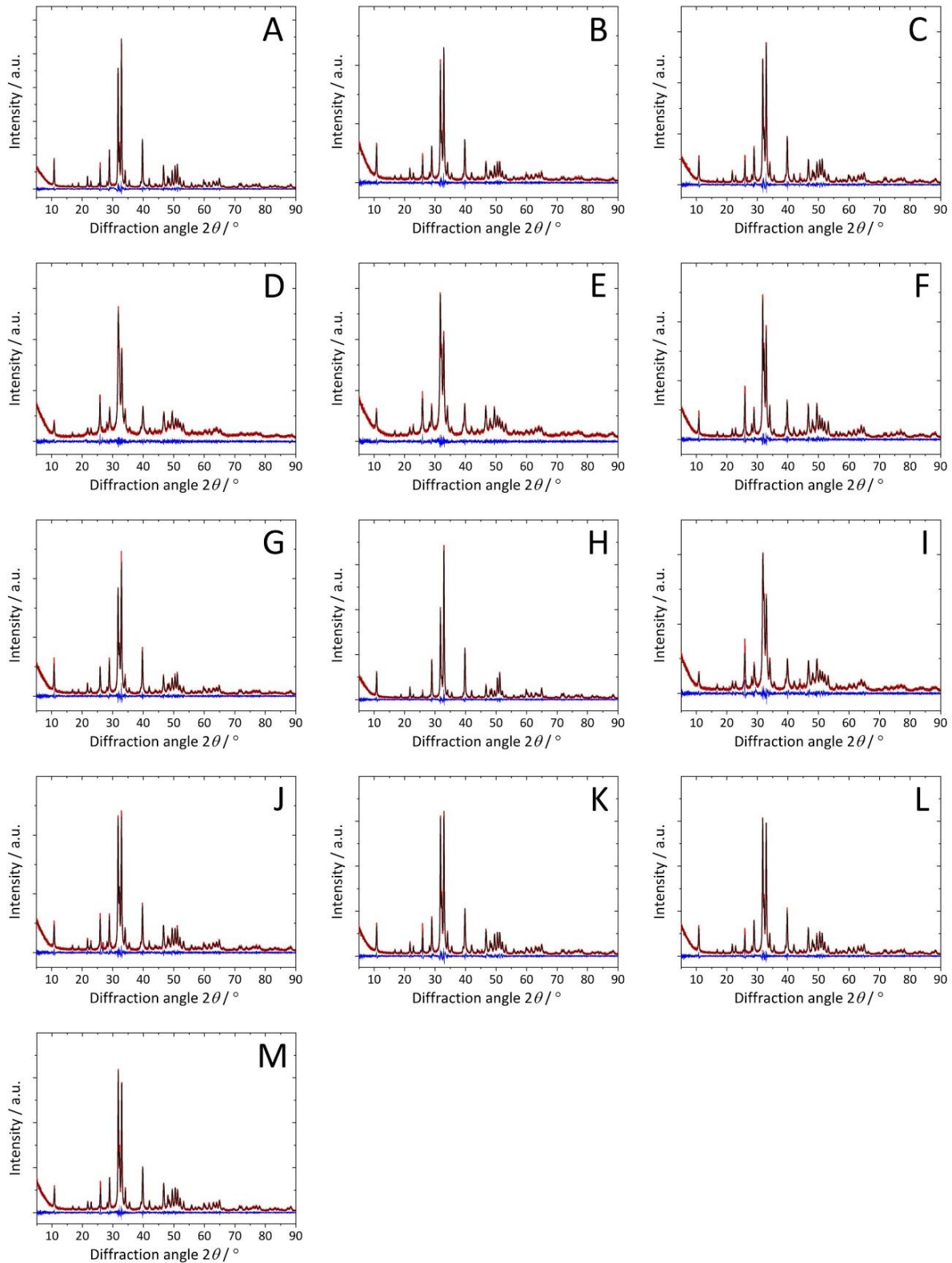


**Figure 66.** Powder diffractograms of the remaining investigated proboscidean enamel samples: MO1 (A), MO2 (B), GO1 (C), GO2 (D), DE1 (E), DE2 (F), AN (G), SI (H), EP (I), EL (J), EH (K), PN (L) and EM (M). **Red curve** (sample experimental data), **black curve** (Rietveld refinement with hydroxyapatite structure), **blue curve** (difference curve).

### 5.3. Project III – Interactions between ultrasmall gold nanoparticles and bacteria

#### 5.3.1. Characterization of bacterial strains and the ultrasmall gold nanoparticles

The uptake of ultrasmall fluorescent AuNPs by bacterial cells was studied using different advanced microscopic methods. Genetically-modified bacteria, used in these studies, were efficient producers of fluorescent proteins (eGFP, DsRed2) and thus, demonstrated bright and strong fluorescence emitted by cells. *E. coli* bacteria, independently on the strain type, showed typical for *Enterobacteriaceae* rod-shaped morphology with an average cell length of  $\sim 2 \mu\text{m}$ , however, bacteria imaged by SEM probably lost their motility organelle (flagella), due to the specificity of sample preparation for SEM imaging (**Figure 67**).

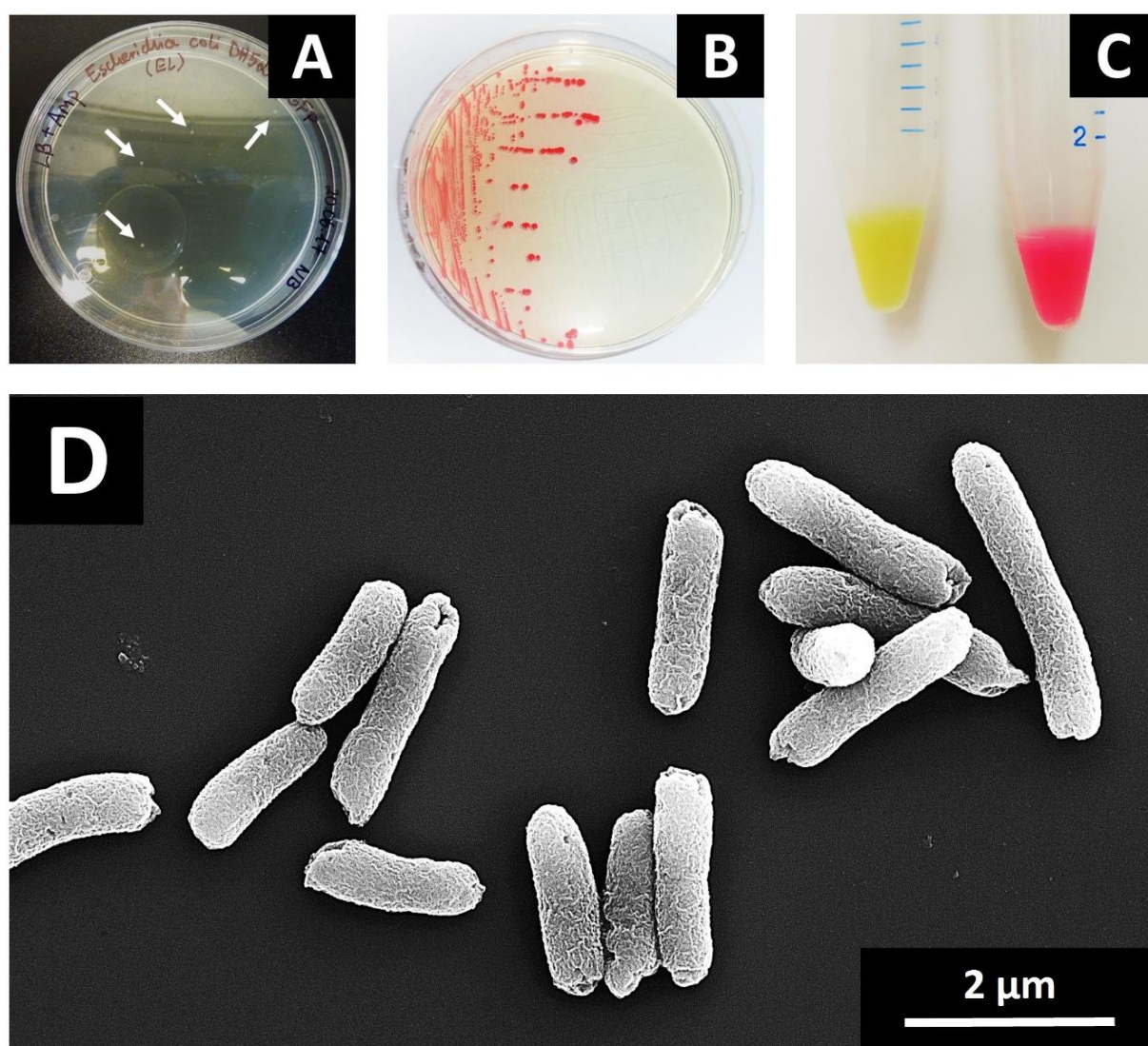


**Figure 67.** Single colonies of eGFP-positive *E. coli* DH5 $\alpha$  cells (indicated with arrows) on a selective LB plate (A), streak plating of DsRed2-expressing *E. coli* TOP10 for single-colony isolation (B), re-suspended pellets of *E. coli* DH5 $\alpha$ -eGFP (yellow-green-fluorescent) and *E.*

*E. coli* TOP10 (red-fluorescent) cells (C), and a representative SEM micrograph of rod-shaped *E. coli* DH5 $\alpha$  cells (D). During sample preparation for SEM imaging, due to multiple washing and centrifugation steps, *E. coli* DH5 $\alpha$  cells probably lost their flagella which can be anchored on one or both poles of the bacterial cell, i.e., arranged mono- or amphitrichously.<sup>288</sup> The SEM image of bacteria was taken by Dr. Kateryna Loza (Inorganic Chemistry, University of Duisburg-Essen).

*E. coli* DH5 $\alpha$  parental strain was successfully made competent and transformed by electroporation to an eGFP-expressing strain (*E. coli* DH5 $\alpha$ -eGFP). The efficient production of fluorescent proteins by bacterial cells, eGFP protein by IPTG-stimulated *E. coli* DH5 $\alpha$ -eGFP and DsRed2 protein by *E. coli* TOP10, was confirmed by fluorescence microscopy (**Figure 68**).

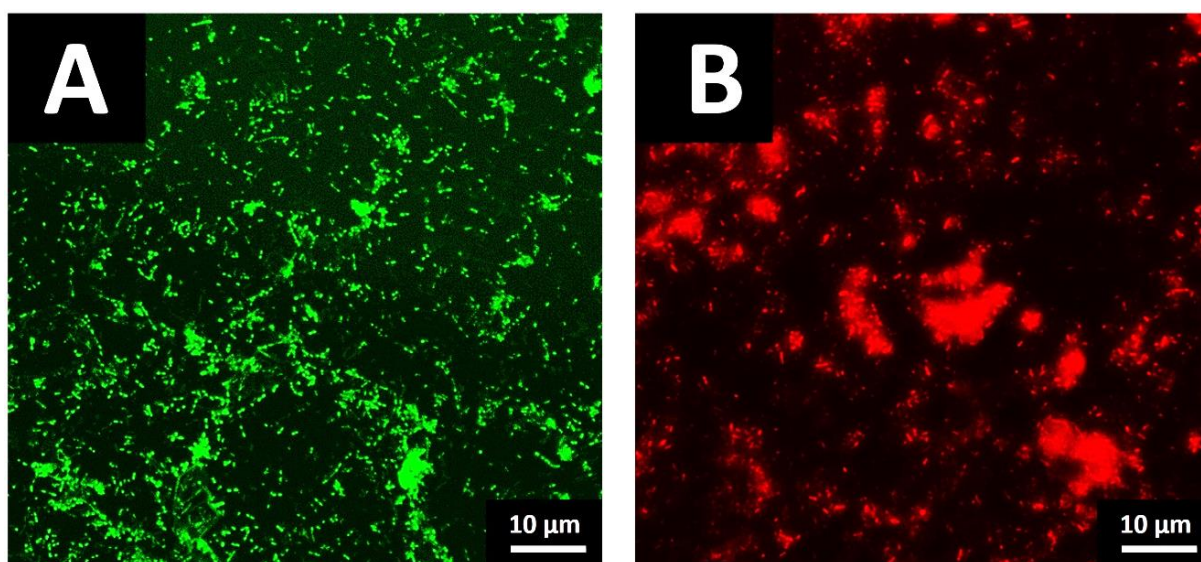


**Figure 68.** Fluorescence microscopy images of eGFP-expressing *E. coli* DH5 $\alpha$ -eGFP (A) and DsRed2-expressing *E. coli* TOP10 (B) cells.

The spherical morphology and average diameter ( $\sim 2$  nm) of ultras-small AuNPs were determined by HRTEM and differential centrifugal sedimentation. Based on these results, the number of dye molecules per nanoparticle and nanoparticle concentrations were determined. Depending on nanoparticle type, the nanoparticles possessed from several to several dozens of fluorophore molecules per particle. The nanoparticle dose, applied in microbiological studies, was in the order from  $10^5$  to  $10^6$  nanoparticles per bacterial cell. Nanoparticles and bacteria were in dispersion, thus many interactions between them took place during incubation. As different types of bacteria and nanoparticles were available for the microscopic studies, regarding the

colour of fluorescence, experimental setups were combined in the way to avoid possible channel cross-talk between fluorescent signals from bacteria and nanoparticles (e.g., red-fluorescent cells were incubated with green-fluorescent nanoparticles).

### 5.3.2. CLSM results on the uptake of gold nanoparticles by bacterial cells

CLSM was applied to study the uptake of ultras-small AuNPs by *E. coli* cells and evaluate possible cytotoxicity of the nanoparticles to bacteria. CLSM images presented in chapters 5.3.2.-5.3.4. were taken by Dr. Viktoriya Sokolova (Inorganic Chemistry, University of Duisburg-Essen). Au-Click-FAM nanoparticles were taken up well by some of the bacteria and localization of the nanoparticles (or nanoparticle agglomerates), after internalization, was mainly in the cell periphery regions. Z-stacks confirmed the intracellular localization of the nanoparticles (Figure 69).

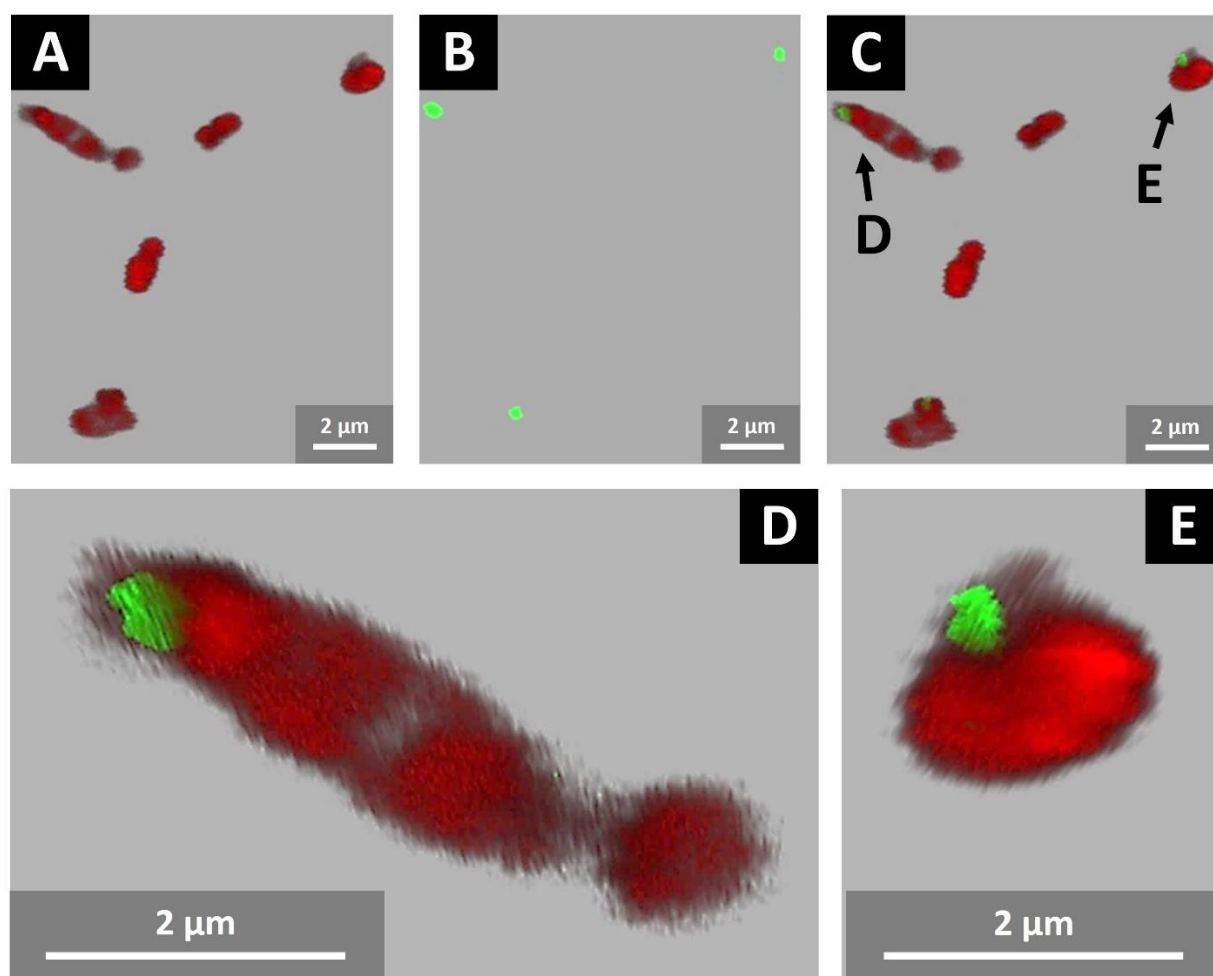


**Figure 69.** CLSM images (z-stacks) of red-fluorescent *E. coli* TOP10 cells incubated with green-fluorescent Au-Click-FAM nanoparticles for 2 h at 37 °C. Bacteria in the DsRed2

channel (A), nanoparticles in the FAM channel (B) and the overlay of fluorescence of bacteria and nanoparticles (C). Images D and E are enlarged regions of the overlay (indicated with arrows) showing nanoparticle-positive cells.

In contrast, water-dissolved FAM dye was not taken up by *E. coli* TOP10 cells (Figure 70). Detachment of the FAM fluorophore from the nanoparticles could be rather excluded, due to the covalent nature of dye-nanoparticle conjugation after performing the CuAAC reaction.<sup>256</sup>

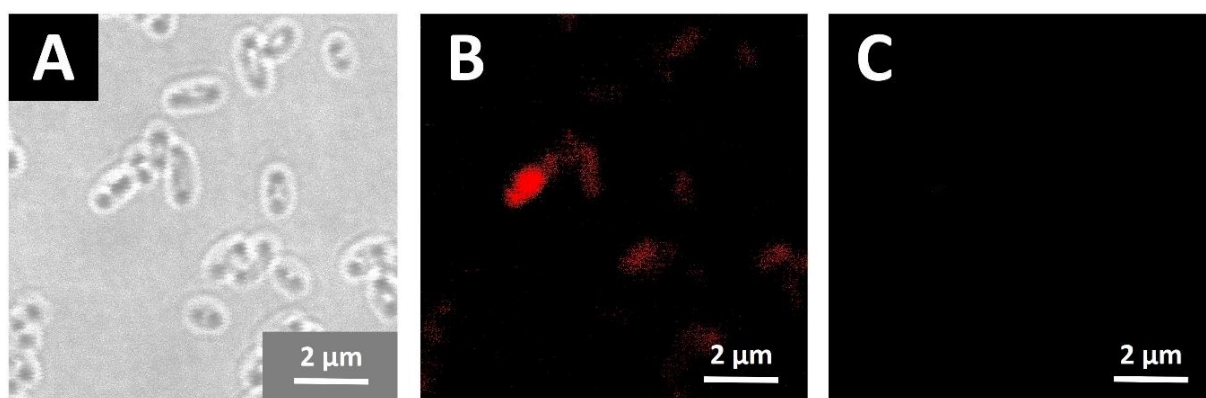


**Figure 70.** CLSM images of red-fluorescent *E. coli* TOP10 cells incubated with water-dissolved green-fluorescent FAM dye for 2 h at 37 °C. The images were taken under the same microscopic conditions as for the sample with FAM-labelled AuNPs. Cells were imaged in the brightfield channel (A), in the DsRed2 channel for bacteria (B) and in the FAM channel for dye/nanoparticles (C).

The uptake of orange-fluorescent Au-Click-Cy3 nanoparticles by green-fluorescent *E. coli* DH5 $\alpha$ -eGFP cells gave similar results as in the case of bacteria incubated with FAM-labelled AuNPs. Again, the nanoparticles were taken up by some cells to a considerable extent. Z-stacks confirmed nanoparticle accumulation within bacteria (Figure 71).

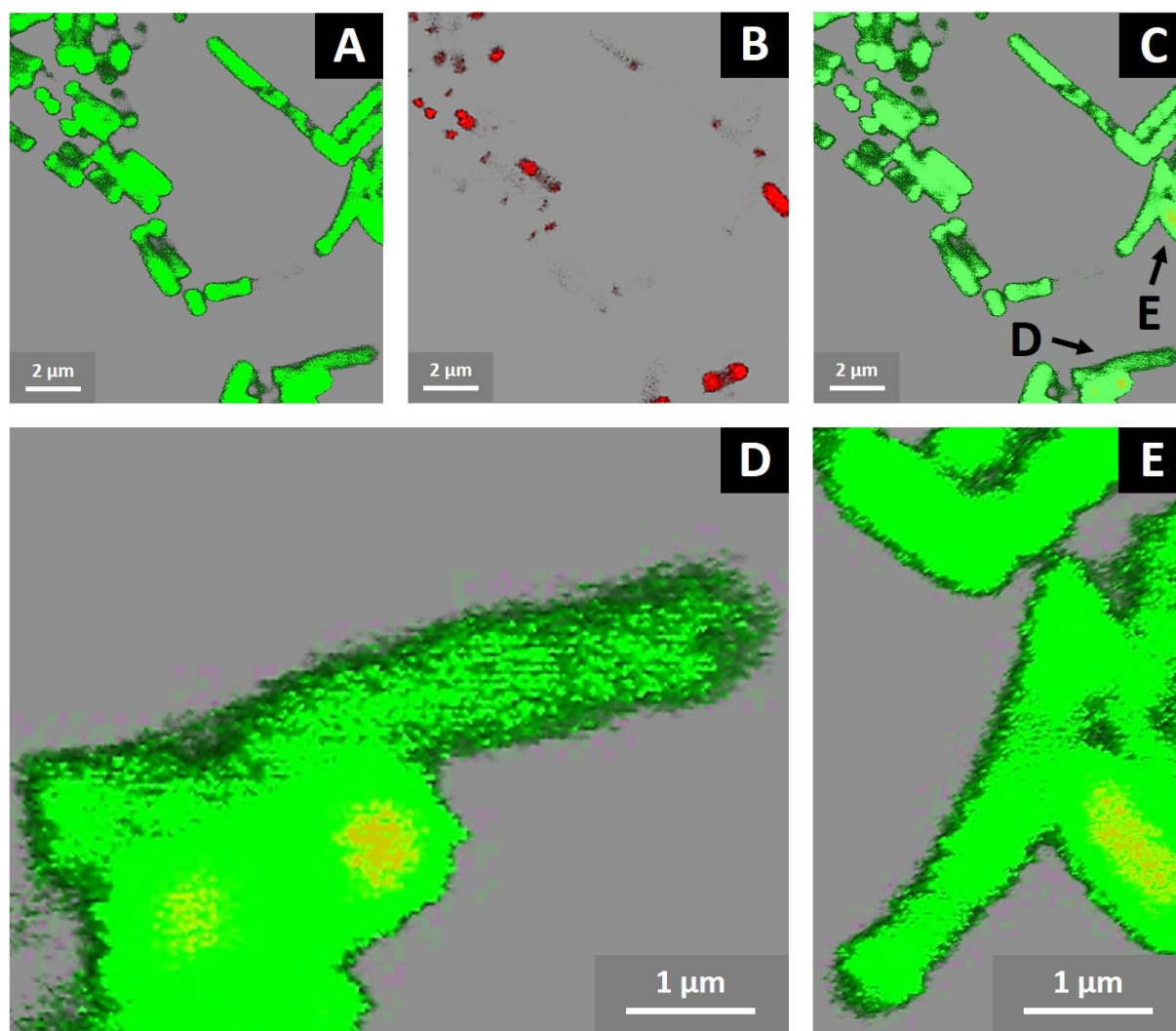


**Figure 71.** CLSM images (z-stacks) of green-fluorescent *E. coli* DH5 $\alpha$ -eGFP cells incubated with orange-fluorescent Au-Click-Cy3 nanoparticles for 2 h at 37 °C. Bacteria in the eGFP channel (A), nanoparticles in the Cy3 channel (B) and the overlay of fluorescence of bacteria and nanoparticles (C). Images D and E are enlarged regions of the overlay (indicated with arrows) showing nanoparticle-positive cells. Although Cy3 is an orange fluorophore, in this figure its colour was changed to red (using the microscope software) for better recognition of the fluorescent signal, when combined with green-labelled bacteria.

Although water-dissolved Cy3 dye was also taken up by bacteria, this was only to some extent and not comparable with the cellular uptake of Cy3-labelled AuNPs (**Figure 72**).

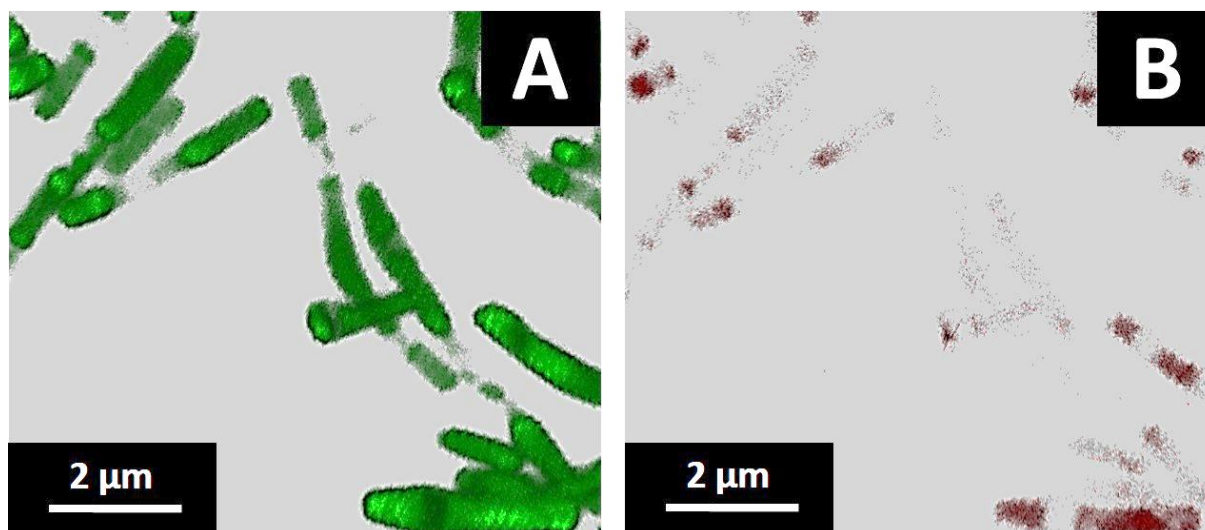


**Figure 72.** CLSM images (z-stacks) of green-fluorescent *E. coli* DH5 $\alpha$ -eGFP cells incubated with water-dissolved orange-fluorescent Cy3 dye for 2 h at 37 °C. The images were taken under the same microscopic conditions as for the sample with Cy3-labelled AuNPs. Cells were imaged in the eGFP channel for bacteria (A) and in the Cy3 channel for dye/nanoparticles (B). Similarly as in **Figure 71**, the Cy3 fluorophore is depicted red, not orange, for better recognition of the fluorescent signal from the nanoparticles.

### 5.3.3. CLSM results on nanoparticle cytotoxicity in bacteria

In biological studies, an important aspect is possible cytotoxicity of the nanomaterials. To evaluate this, non-fluorescent *E. coli* DH5 $\alpha$  cells were incubated with Au-GSH-FITC nanoparticles, under the same experimental conditions as for the uptake of FAM- and Cy3-labelled nanoparticles, and additionally stained, after incubation, with propidium iodide for detection of dead bacteria. AuNPs were not toxic to bacteria, as most of *E. coli* DH5 $\alpha$  cells were alive after incubation with the nanoparticles and only few dead (red-stained) cells were found (**Figure 73**).

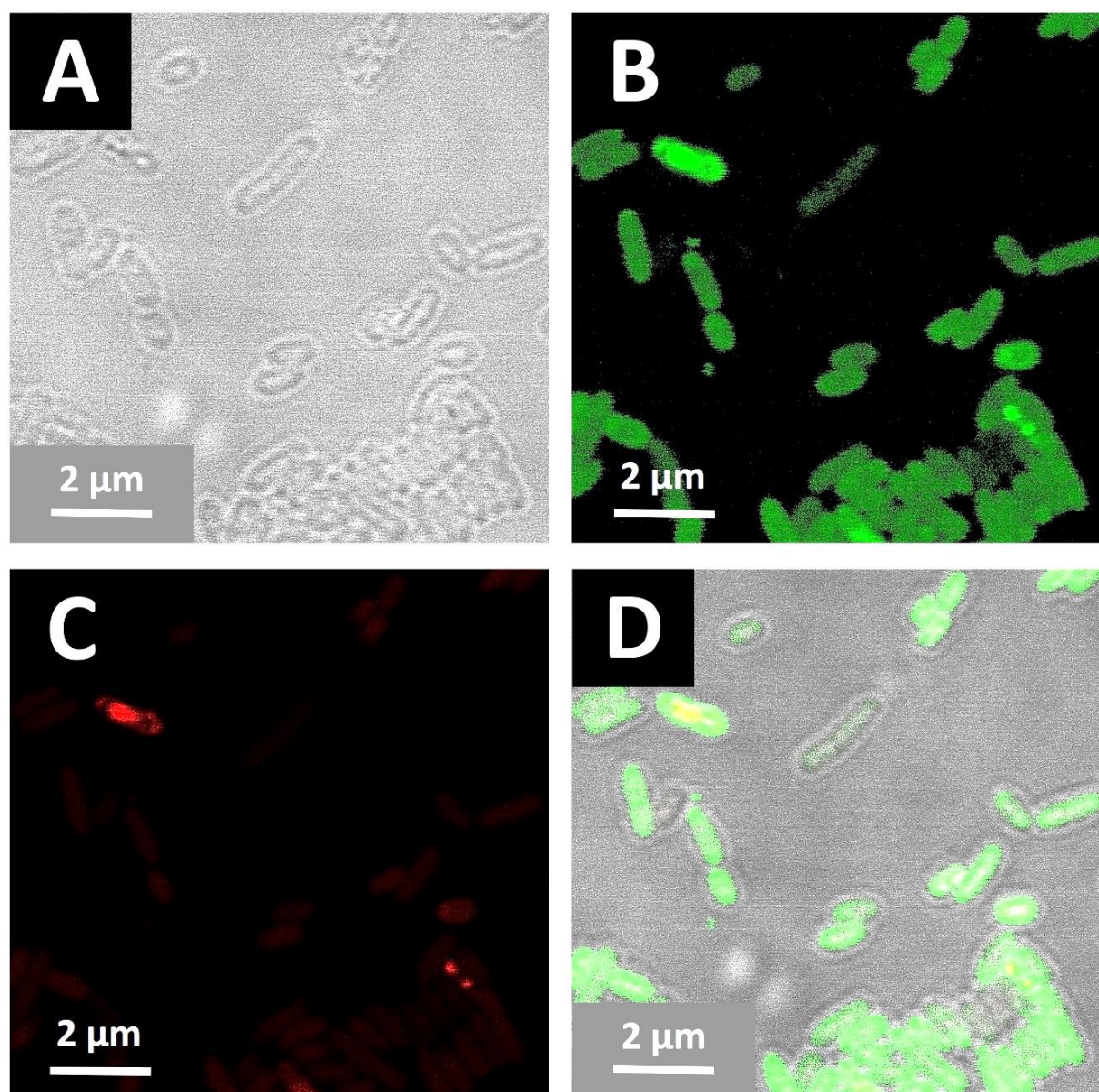


**Figure 73.** CLSM images of non-fluorescent *E. coli* DH5α cells incubated with green-fluorescent Au-GSH-FITC nanoparticles for 2 h at 37 °C, followed by propidium iodide staining of the dead cells (red colour). Bacteria in the brightfield channel (A), nanoparticles (coating bacterial cells) in the FITC channel (B), dead bacteria in propidium iodide channel (C) and the overlay of fluorescence of bacteria and nanoparticles, including brightfield (D).

This conclusion can be additionally supported with the observation that no clear connection between nanoparticle-positive and dead cells was found. This is in agreement with literature and the general assumption that gold is biocompatible and non-cytotoxic.<sup>289-292</sup> For example, Hayden *et al.* reported that ultrasmall AuNPs (2 nm) were not toxic to *E. coli* and Boda *et al.* demonstrated that cluster-sized AuNPs were not harmful to staphylococci (*S. aureus*, *S.*

*epidermidis*), *E. coli* and *P. aeruginosa*.<sup>293,294</sup> Although, FITC-labelled AuNPs were used in cytotoxicity studies on *E. coli* as representative nanoparticles, the harmlessness of other nanoparticle formulations used in these studies (Au-Click-FAM/Cy3/AF647) is expected to be comparable. All of these nanoparticles shared a similar in size and morphology gold core (these are major parameters determining nanoparticle toxicity to cells), and varied just in the type and amount of attached dye molecules.<sup>208,295</sup>

#### 5.3.4. CLSM results of the control samples and possible channel cross-talk

In order to exclude the possible channel cross-talk between fluorescent signals from bacteria and nanoparticles, control samples of bacteria (*E. coli* strains DH5 $\alpha$ , DH5 $\alpha$ -eGFP and TOP10) were prepared and investigated in the channels for nanoparticle imaging (**Figure 74**).

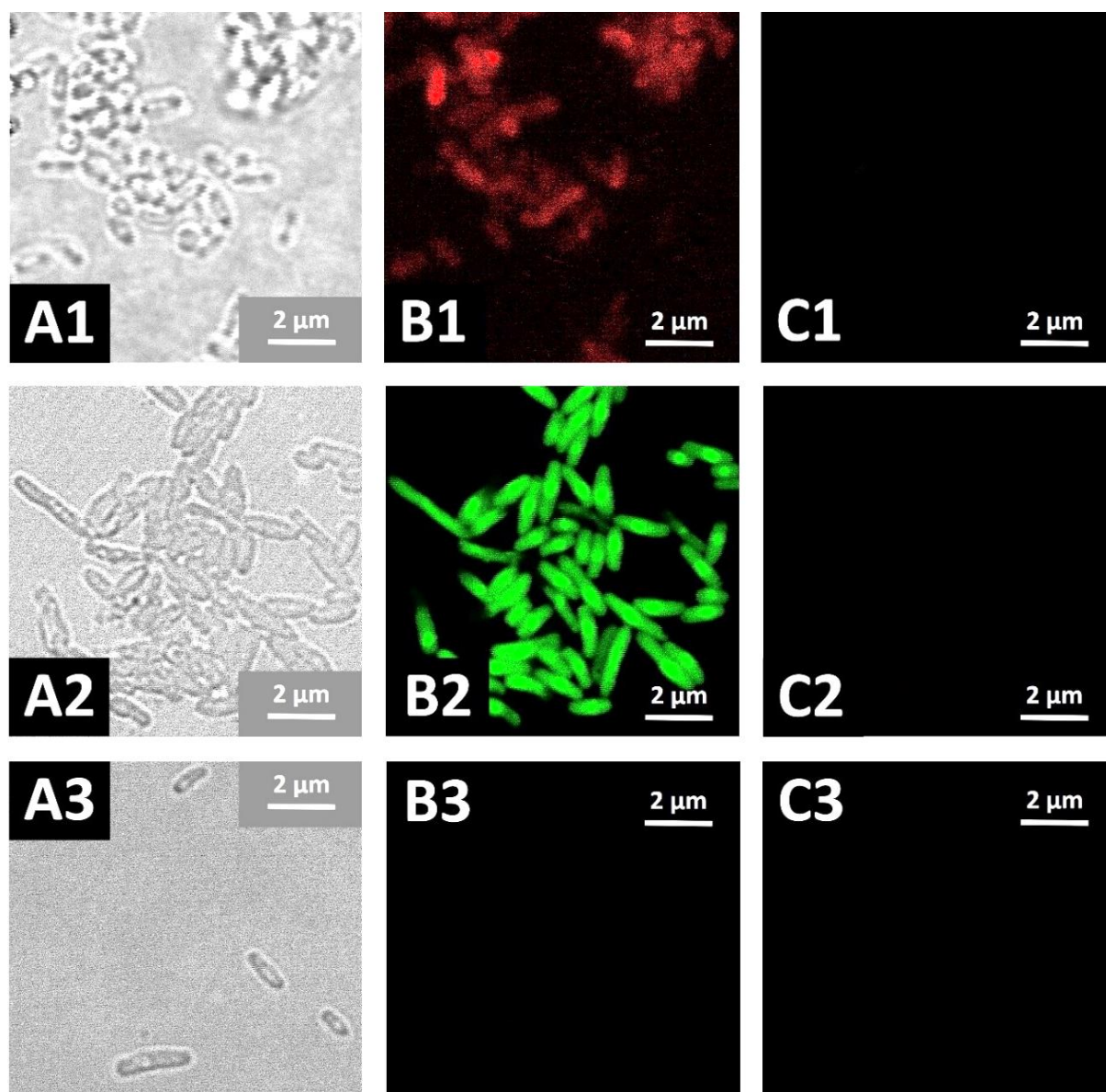


**Figure 74.** CLSM images of the control samples of *E. coli* strains: red-fluorescent TOP10 (1), green-fluorescent DH5 $\alpha$ -eGFP (2) and non-fluorescent DH5 $\alpha$  (3). Depending on the experimental setup, bacteria are presented in the brightfield channel (A1/A2/A3), in the DsRed2/eGFP/propidium iodide channel for cell imaging (B1/B2/B3) and in the FAM/Cy3/FITC channel for nanoparticle imaging (C1/C2/C3).

Similarly, control samples of the nanoparticles (Au-Click-FAM/Cy3, Au-GSH-FITC) were studied in channels for bacteria imaging (data not shown). Bacteria were not visible in the channels for nanoparticles and *vice versa*. These results confirmed the absence of channel cross-talk between fluorescence of bacteria and AuNPs, and thus indicated a proper selection of the experimental setups.

### 5.3.5. SIM results on the uptake of gold nanoparticles by bacterial cells

SIM enabled to investigate the uptake of ultrasmall AuNPs by *E. coli* cells even with a higher magnification and imaging resolution than using conventional CLSM. Therefore, SIM is particularly recommended for the imaging of bacteria, as it operates at 100x magnification, which is a golden standard in microscopy of microbiological samples. When compared to CLSM, SIM improves the imaging resolution by the factor of two.<sup>296</sup> SIM images showed strong red-fluorescence of Au-Click-AF647 nanoparticles inside green-fluorescent *E. coli* DH5 $\alpha$ -eGFP cells. The nanoparticles were efficiently taken up by bacteria already after 1 h of incubation. Signals from single nanoparticles, localized in the intercellular space, were also detected. The nanoparticles were well- and equally-distributed in the cell interior, with no preferential localization in the cell periphery, membrane or center (**Figure 75**).

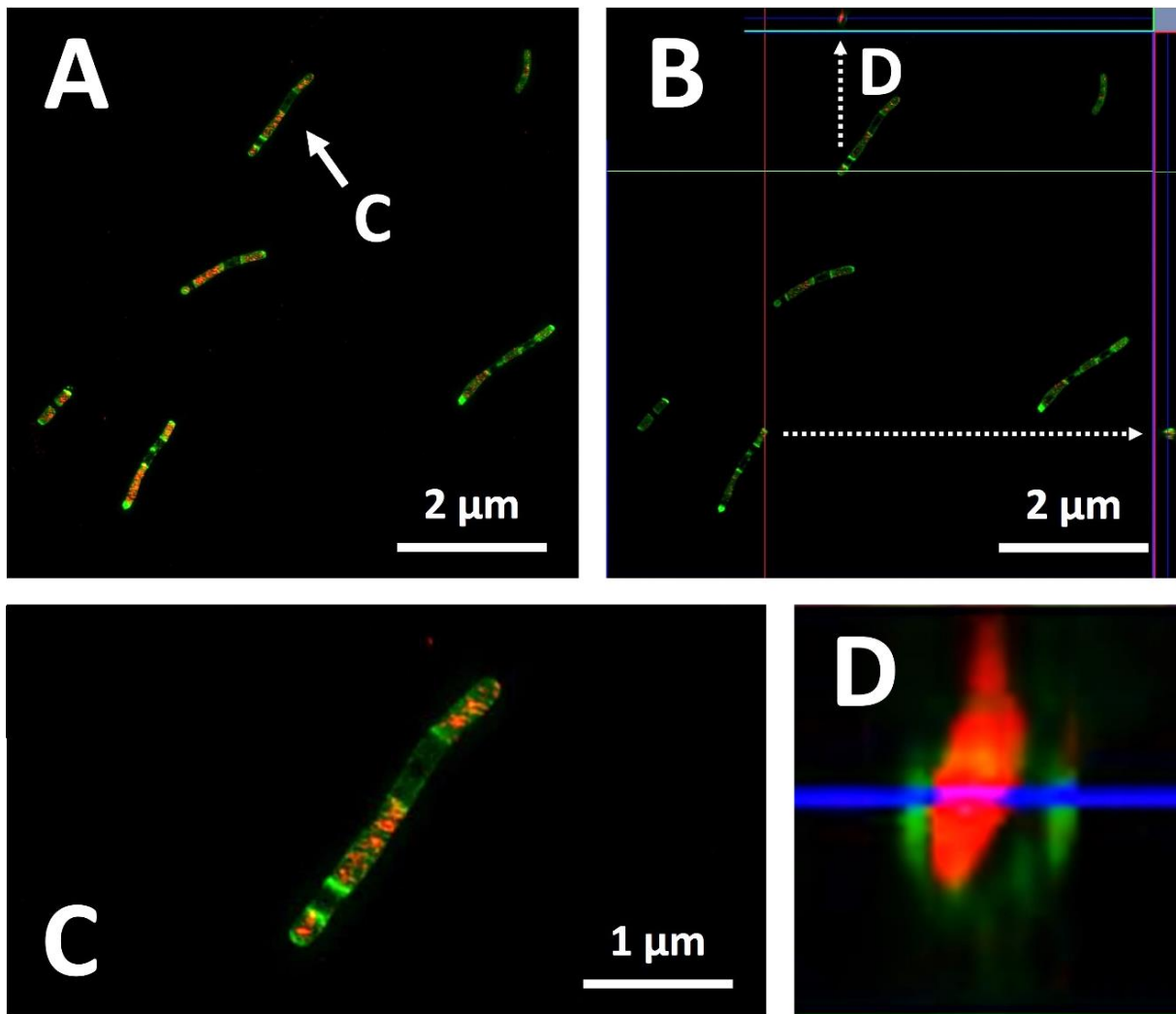


**Figure 75.** SIM images (z-stacks) of green-fluorescent *E. coli* DH5 $\alpha$ -eGFP cells incubated with red-fluorescent Au-Click-AF647 nanoparticles for 1 h at 37 °C. The dashed arrows indicate examples of intracellular uptake of the nanoparticles by bacteria. Presented are the MIP image (A) and the ORTHO projection (B) – for tracking of the nanoparticles inside cells. Images C and D are enlarged regions of the MIP image and the ORTHO projection, respectively (indicated with arrows), showing nanoparticle-positive bacteria.

A similar observation, regarding intracellular distribution of gold nanoclusters, was reported by Zhang *et al.* in acetogenic bacterium *Moorella thermoacetica*.<sup>291</sup> Further cultivation of *E. coli* DH5 $\alpha$ -eGFP cells (until 3 h) resulted in a rapidly increasing number of bacteria, without a significant change in nanoparticle uptake efficiency (**Figure 76**).

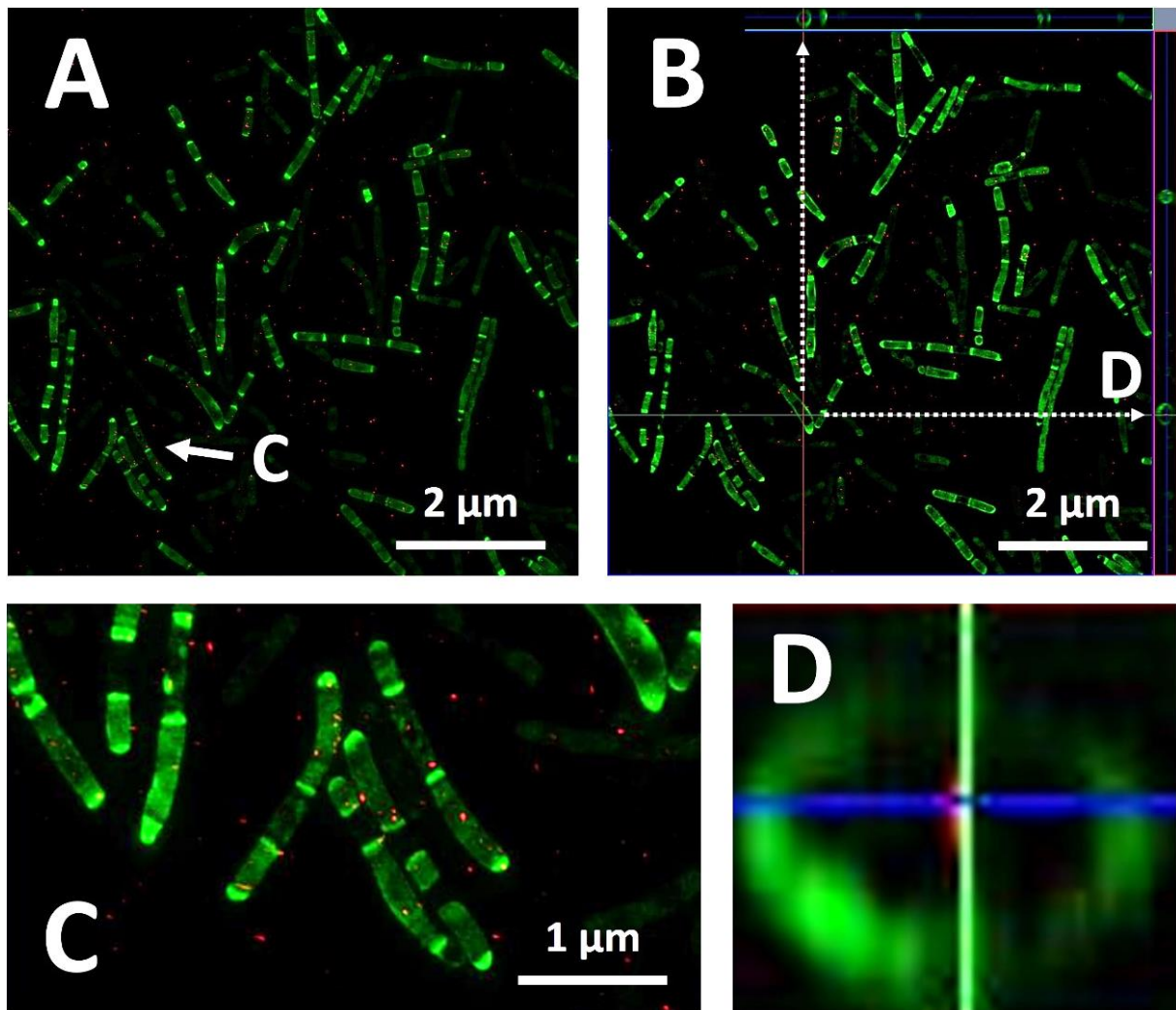


**Figure 76.** SIM images (z-stacks) of green-fluorescent *E. coli* DH5 $\alpha$ -eGFP cells incubated with red-fluorescent Au-Click-AF647 nanoparticles for 3 h at 37 °C. The dashed arrows indicate examples of intracellular uptake of the nanoparticles by bacteria. Presented are the MIP image (A) and the ORTHO projection – for tracking of the nanoparticles inside cells (B). Images C and D are enlarged regions of the MIP image and the ORTHO projection, respectively (indicated with arrows), showing nanoparticle-positive bacteria.

The approximate generation time of *E. coli* under optimal laboratory conditions is  $\sim 20$  min.<sup>297</sup> Due to constant consumption and, at some point, already absence of IPTG in the culture, further generations of eGFP-positive *E. coli* cells did not produce eGFP anymore. Therefore, it was not possible to continue the uptake studies beyond 3 h, despite further viability of the bacterial culture. SIM images are presented as maximum intensity projections (with enhanced fluorescent signals) and ORTHO projections of z-stacks to track the nanoparticles and confirm their intracellular localization in bacteria.

The possible channel cross-talk between fluorescent signals from bacteria and nanoparticles was also studied by SIM. The control sample of *E. coli* DH5 $\alpha$ -eGFP cells was prepared and investigated in the channel for nanoparticle imaging (**Figure 77**).

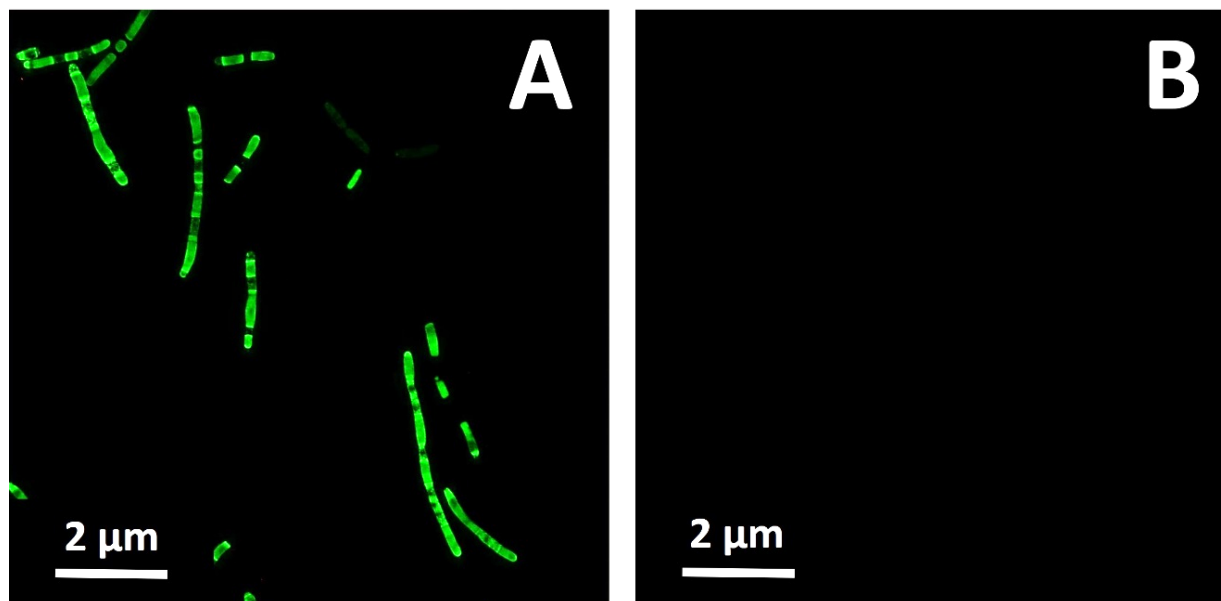


**Figure 77.** SIM images of the control sample of green-fluorescent *E. coli* DH5 $\alpha$ -eGFP cells in the eGFP channel for bacteria imaging (A) and in the AF647 channel for nanoparticle imaging (B).

The control sample of Au-Click-AF647 nanoparticles was also studied in the channel for bacteria imaging (data not shown). No cross-talk between eGFP and AF647 channels was observed. Both bacteria and nanoparticles were not visible in the opposite fluorescence channels, indicating a proper selection of the experimental setup.

Non-fluorescent *E. coli* DH5 $\alpha$  cells were labelled with AF488-NHS-ester (Lumiprobe, Germany) to evaluate, using SIM, the staining protocol for bacteria. eGFP-derived autofluorescence of bacteria is, in some cases, not sufficient for cell imaging using other super resolution microscopy techniques and staining of bacteria with non-bleaching and photoswitchable fluorophores, like Alexa Fluor<sup>®</sup>, is then required. In brief, green-fluorescent *E. coli* DH5 $\alpha$  cells (stained with AF488) were incubated with Au-Click-AF647 nanoparticles for 1 h at 37 °C. Bacteria were labelled, still before incubation with the nanoparticles, according to the protocol described by Turner *et al.*<sup>298</sup> Hydroxysuccinimide-esters of Alexa Fluor<sup>®</sup> dyes are amino specific and bind covalently to free amine functional groups of protein amino acids,

particularly lysines, in bacterial cell membranes.<sup>298,299</sup> Preparation of the samples for SIM imaging (bacteria + nanoparticles) was performed as described in chapter 4.3.7. Fluorescence of AF488 was excited using the same microscope laser settings as for the excitation of eGFP (Table 5). A representative image is presented in Figure 78.

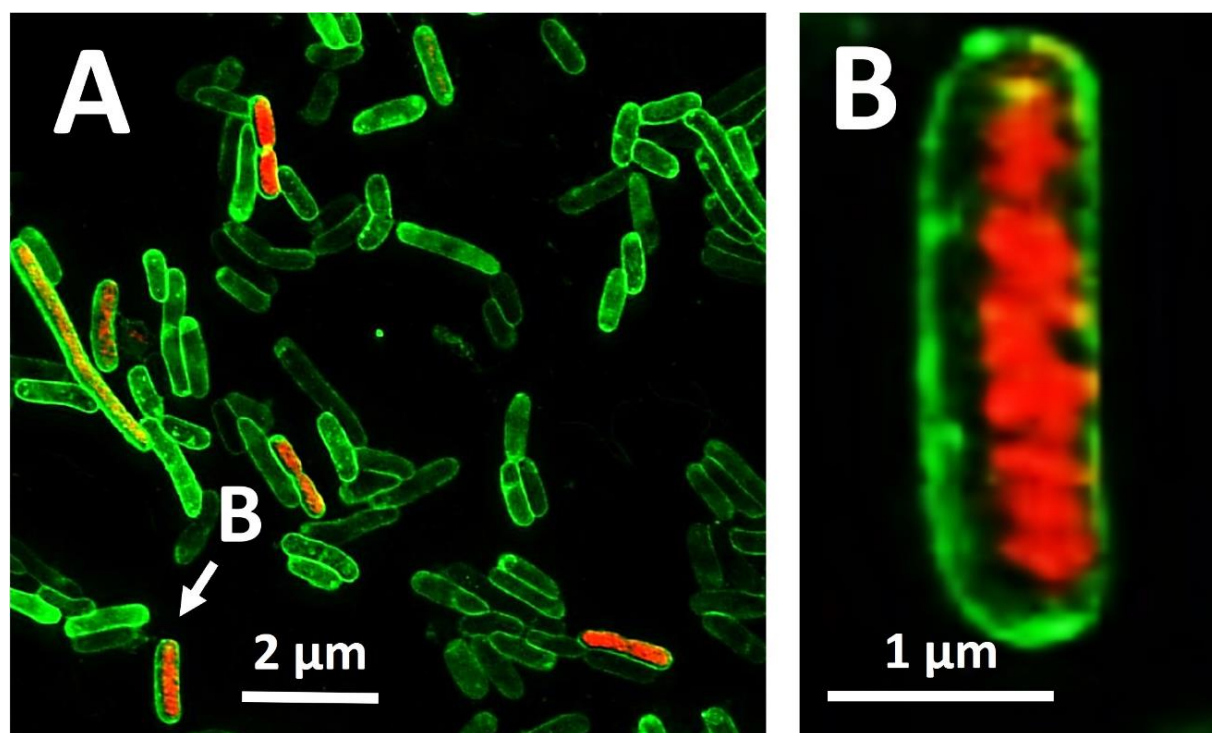


**Figure 78.** SIM image (z-stack) of green-fluorescent *E. coli* DH5 $\alpha$  cells (with AF488-stained membranes) incubated with red-fluorescent Au-Click-AF647 nanoparticles for 1 h at 37 °C. The MIP image (A) presents examples of intracellular uptake of the nanoparticles by bacteria and image B is enlarged region of the MIP image (indicated with an arrow) showing a representative nanoparticle-positive bacterium.

These independent experiments with AF488-labelled bacteria confirmed nanoparticle uptake results observed for fluorescent protein expressing *E. coli*, indicating reproducibility of the previous results. Furthermore, the nature of labelling of the two types of green-fluorescent *E. coli* (eGFP, AF488) can be easily distinguished in the SIM images. As mentioned, eGFP protein is expressed in IPTG-stimulated cells and thus whole bacteria are green, whereas AF488-stained bacteria possess green-labelled cell membranes. This is in agreement with the chemical principle of dye interaction with the bacterial cell.<sup>298,299</sup>

### 5.3.6. FACS results on the uptake of gold nanoparticles by bacterial cells

FACS results confirmed the uptake of ultrasmall nanoparticles (Au-Click-AF647) by *E. coli* DH5 $\alpha$ -eGFP cells (**Figure 79**).

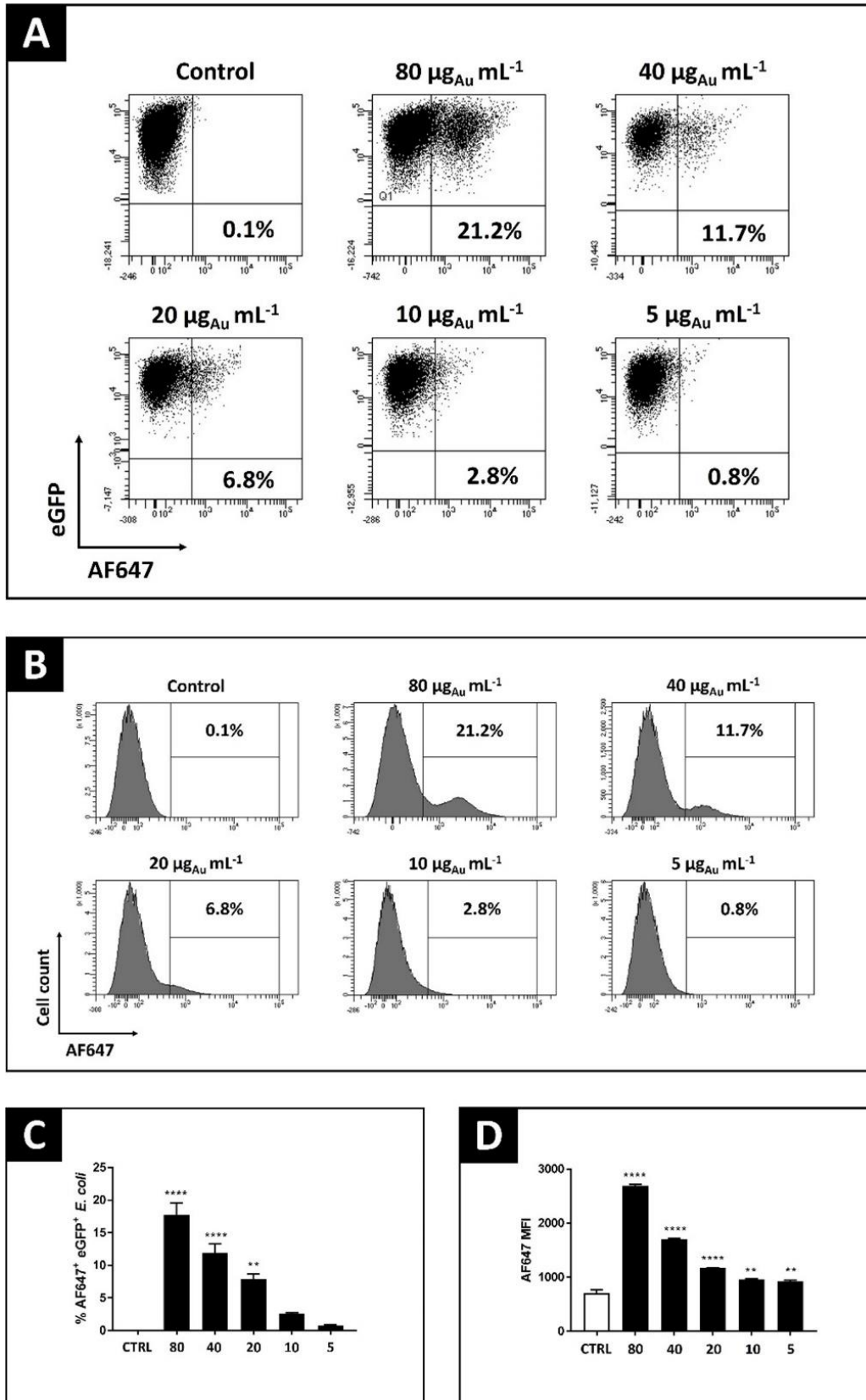


**Figure 79.** FACS results of the uptake of red-fluorescent Au-Click-AF647 nanoparticles by green-fluorescent *E. coli* DH5 $\alpha$ -eGFP cells after 1 h of incubation at 37 °C. Shown are: representative dot plots (A) and histograms (B) after flow cytometry, percentage of nanoparticle-positive (AF647<sup>+</sup>) and green-fluorescent (eGFP<sup>+</sup>) bacteria (C), and MFI values of AF647 (from nanoparticles internalized by cells) (D). *p*-values indicate significant differences to control bacteria (cells not exposed to the nanoparticles, CTRL) with  $p < 0.01$  (\*\*) or  $p < 0.0001$  (\*\*\*\*) ( $N=3$ ). In figures C and D, the gold dose is reflected by a corresponding number (e.g., 5 = 5  $\mu\text{g}_{\text{Au}} \text{mL}^{-1}$ ). Gold doses, to which bacterial cells were exposed, could be recalculated to the following concentrations of the nanoparticles: 5  $\mu\text{g}_{\text{Au}} \text{mL}^{-1}$  ( $6.2 \cdot 10^{13}$  nanoparticles  $\text{mL}^{-1}$ ), 10  $\mu\text{g}_{\text{Au}} \text{mL}^{-1}$  ( $1.2 \cdot 10^{14}$  nanoparticles  $\text{mL}^{-1}$ ), 20  $\mu\text{g}_{\text{Au}} \text{mL}^{-1}$  ( $2.5 \cdot 10^{14}$  nanoparticles  $\text{mL}^{-1}$ ), 40  $\mu\text{g}_{\text{Au}} \text{mL}^{-1}$  ( $5 \cdot 10^{14}$  nanoparticles  $\text{mL}^{-1}$ ) and 80  $\mu\text{g}_{\text{Au}} \text{mL}^{-1}$  ( $9.9 \cdot 10^{14}$  nanoparticles  $\text{mL}^{-1}$ ).

The number of nanoparticle-positive bacteria depended on the nanoparticle dose and increased up to 21.2% for the highest studied nanoparticle concentration ( $9.9 \cdot 10^{14}$  nanoparticles  $\text{mL}^{-1}$ ). Nanoparticle-positive and nanoparticle-negative subpopulations of bacteria could be clearly distinguished. The control sample of untreated bacteria (cells not exposed to the nanoparticles) did not show fluorescence in the channel for nanoparticle imaging, which confirmed absence of cross-talk between fluorescence of bacteria and nanoparticles. Based on FACS results, the efficiency of nanoparticle uptake by bacteria, investigated previously using CLSM and SIM, could be also estimated. Nanoparticle concentrations applied in these experiments were within the range of nanoparticle concentrations studied by FACS. The nanoparticle dose in CLSM and SIM studies was  $3.1 \cdot 10^{14}$  nanoparticles  $\text{mL}^{-1}$  which, according to FACS results, would correspond to ~4-9% of nanoparticle uptake efficiency. This could explain why only some of the bacterial cells were nanoparticle-positive.

## 6. Conclusions

CaP nanoparticles, described in this thesis, addressed a broad range of biological aspects, including cellular uptake, cytotoxicity, targeted delivery, and gene silencing *in vitro* (in murine cells) and *in vivo* (in mice). Generally, all nanoparticles were spherical, monodisperse, colloiddally stable and non-pyrogenic. Their strong positive charge, important for biomolecule loading and cell-nanoparticle interactions, was due to stabilization of the nanoparticles with cationic PEI. The silica shell confirmed its protective role to the nanoparticles and their cargo. The efficiencies of nanoparticle loading (with siRNA/peptides) and decoration (with peptides/antibodies) were high. However, despite following a well-optimized synthesis protocol, multi-step syntheses of ligand-decorated CaP nanoparticles revealed the necessity to control calcium content in the nanoparticles after each step of synthesis and constantly monitor this important nanoparticle characterization parameter during synthesis. Furthermore, modifications in processing of the nanoparticles, during the multi-step synthesis, were introduced to get a final nanoparticle product with the highest possible content of calcium. The syntheses have proved general reproducibility, as nanoparticles synthesized in different synthesis batches demonstrated similar characterization results. The nanoparticles met rigorous criteria to be further applied in biological studies. The nanoparticles were not toxic to murine cells and were rapidly taken up by most of the studied blood compartment cell types. The cellular uptake was mostly based on energy-dependent processes. After endolysosomal degradation of the nanoparticles, their cargo was released into the cell cytoplasm in a bioactive form. The model of siRNA delivery *via* CaP nanoparticles confirmed its effectiveness in biological applications by preserving functionality of the siRNA cargo which, after release from the nanoparticles, efficiently silenced NF- $\kappa$ B p65 in cells. The experiments revealed also some interesting biological aspects, with regard to cell-nanoparticle interactions, that require further in-depth studies, like the influence of unloaded CaP nanoparticles on cytokine secretion profiles. Based on the results described in this part of the thesis it can be concluded that CaP nanoparticles may serve as host-safe and efficient delivery platforms for therapeutic biomolecules. The nanoparticles loaded with anti-NF- $\kappa$ B p65 siRNA were able to suppress pro-inflammatory reactions, by inducing gene silencing of NF- $\kappa$ B p65, and to downregulate expression of key inflammatory mediators. Therefore, CaP nanoparticles, when combined with therapeutic siRNA, are promising agents for the treatment of acute and chronic inflammatory diseases, which are typically characterized by deregulation of NF- $\kappa$ B expression, leading often to its uncontrolled overexpression.<sup>80,300</sup>

Moreover, in the thesis, comprehensive chemical and microscopic studies of fossilized proboscidean enamel are presented. The samples covered the time range from Eocene to Pleistocene and originated from various locations in Egypt and India. Tooth enamel sample of the recent Asian elephant (*E. maximus*) served in these studies as reference for comparison purposes. Chemical analyses have proved general resistance of fossilized proboscidean enamel to diagenetic alteration and confirmed its high grade of preservation. Calcium and phosphate composition of fossilized enamel was stable over the time, independently on sample age, and close to stoichiometric hydroxyapatite. The samples were also characterized by an increased content of fluorine, however, again without clear age-dependency. Moreover, structural analyses revealed low carbonate content in the enamel, and confirmed purity, nanocrystallinity and presence of ionic substitutions (mainly B-type) in the bioapatite. Diagenetic alteration of fossilized enamel was demonstrated using independent analytical methods, however, it was only to a small extent. Detailed microscopic studies on fossilized proboscidean enamel microstructure revealed its well-preserved and mostly prismatic organization. Samples investigated in these studies reflected the evolutionary trend of enamel development and differentiation in proboscideans. These tooth adaptations were related with animal migrations and dietary changes in the past, as results of the Earth's lithosphere and paleoclimate dynamics. The enamel microhistology of the oldest African proboscideans from Eocene (*Moeritherium* sp., *Palaeomastodon* sp.) was relatively primitive, demonstrating a 2-layered "schmelzmuster", whereas the enamel of younger Indian proboscideans from Miocene to Pleistocene showed already an advanced 3- (*Deinotherium* sp., *Gomphotherium* sp., *Anancus* sp., *P. namadicus*) or even 4-layered (*S. insignis*, *E. platycephalus*) "schmelzmuster". The enamel prism cross-section pattern also evolved in the direction from primitive keyhole (in older proboscideans) to advanced fan-shaped or ginkgo-leaf (in younger proboscideans) motifs. Results of the analyses on fossilized proboscidean enamel presented in this thesis, beside new insights into the current understanding of enamel organization in *Deinotherium* sp., *Stegodon* sp. and *E. maximus*, provided also, reported here for the first time, data on enamel microstructure of Indian *Anancus* sp., *S. insignis*, *E. platycephalus* and *P. namadicus*. Furthermore, also for the first time, differences in the local distribution of elements within proboscidean teeth (dentine vs. enamel) were reported. Presented results confirm that fossilized enamel is resistant to external chemical alteration and demonstrates a high grade of microstructure preservation. Thus, it is an excellent material, with advantage over other body hard tissues, like bone, cement or dentin, to perform chemical, microscopic and paleontological studies on extinct animal taxa. Beside data about

---

the animal (age, diet, evolution, migration, physiology, taxonomy), the enamel provides valuable information about the paleoclimate and paleovegetation dynamics.<sup>248,301</sup>

The aim of the last research project described in this thesis was to investigate the interactions between ultrasmall AuNPs and bacteria, and to evaluate whether nanoparticles can be taken up by bacteria without causing lethal effects to cells. This is particularly important, as most of available literature reports focus rather on antimicrobial application of nanoparticles, where the uptake by bacteria, if present, is not spontaneous and typically driven by pathologic changes in the bacterial cell envelope. Cluster-sized AuNPs (~2 nm), used in these studies, were covalently-coupled to different photostable fluorophores (Cy3, FAM, FITC, AF647) either *via* the CuAAC reaction or GSH binding, and applied in biological studies with non-fluorescent (DH5 $\alpha$ ) and autofluorescent (DH5 $\alpha$ -eGFP, TOP10) *E. coli* strains. The green-fluorescent *E. coli* DH5 $\alpha$ -eGFP strain was derived from the non-fluorescent parental *E. coli* DH5 $\alpha$  strain, after its successful electrotransformation with eGFP-encoding plasmid DNA. The interactions between fluorescent nanoparticles and bacteria were studied using CLSM, SIM and FACS. FAM-labelled nanoparticles were taken up by *E. coli* TOP10 cells, whereas Cy3- and AF647-labelled nanoparticles were internalized by *E. coli* DH5 $\alpha$ -eGFP cells. The application of labelled nanoparticles showed an advantage over staining bacteria with water-dissolved dyes. Furthermore, there was no cross-talk between the fluorescent signals from bacteria and nanoparticles. Cytotoxicity studies demonstrated that ultrasmall AuNPs were not toxic to bacteria. Nanoparticle uptake efficiency by cells was dose-dependent, as shown in flow cytometry experiments. Based on available literature data on particle uptake mechanisms in bacteria, it can be hypothesized that ultrasmall AuNPs were internalized by *E. coli* cells *via* non-specific pore-mediated diffusion, where particle size is the exclusion parameter, and cluster-sized nanoparticles, used in these studies, met criteria to be taken up by bacteria in that way. Fluorescently-labelled ultrasmall AuNPs are promising tools to study the uptake of particles from the environment by bacteria, without causing harmful effects to the cells. Results of this project lead to a better understanding of the living cell phenomenon and the action of noble metal nanoparticles in biological systems. Furthermore, biocompatible ultrasmall AuNPs, characterized by high chemical modification possibilities, can be used as nanocarriers (with proven cell penetration ability) for the delivery of antimicrobials into bacterial cells, and thus have the potential to be an alternative to conventional methods used in combating bacterial infections, including severe ones caused by multidrug-resistant strains.

## 7. Summary

Interdisciplinary research projects presented in this doctoral thesis concern broadly-defined application of inorganic nanoparticles in studies on the interactions with living cells (eukaryotic and prokaryotic), as well as show how inorganic chemistry, and its analytical methods, can be used in investigations of biological nanostructures.

In the first project, calcium phosphate nanoparticles, as inorganic nanoplatfoms, were used for the delivery of therapeutic siRNA into eukaryotic cells. The siRNA was destined to silence the expression of the p65 subunit of NF- $\kappa$ B. The latter is an important transcription factor involved in cell inflammatory and immune response. The nanoparticles showed good physicochemical properties, were efficiently loaded with therapeutic siRNA and fulfilled quality criteria to be further applied in biological experiments. *In vitro* studies carried out in different types of murine blood compartment cells demonstrated that the nanoparticles were not cytotoxic and were readily internalized by cells. Nanoparticle-delivered siRNA effectively inhibited the expression of NF- $\kappa$ B p65 in the inflamed cells. The downregulation effect could be observed on the cellular level of p65 mRNA and p65 protein expression. Interestingly, a downregulation effect on the expression of key cytokines (TNF- $\alpha$ , IL-6, INF- $\beta$ ) induced by unloaded calcium phosphate nanocarriers could be also demonstrated. This observation opened a new perspective in the understanding of complex cell-nanoparticle interactions. The importance of superficial functionalization of calcium phosphate nanoparticles with silica shell was confirmed in the dissolution studies, whereas co-localization experiments enabled in-depth investigations of intracellular processing of the nanoparticles and their biomolecule cargo. Silica functionalization of calcium phosphate nanoparticles enabled also decoration of the nanoparticles with ligands, to improve nanoparticle uptake by the target cells. Stabilization of the nanoparticles with a near-infrared-labelled polymer extended the application range of siRNA-loaded calcium phosphate nanoparticles also to *in vivo* research in mice, indicating the therapeutic potential of biocompatible and biomolecule-loaded inorganic nanocarriers in experimental gene therapy, based on regulation of the NF- $\kappa$ B expression on a molecular level. The second project, described in this thesis, concerned extensive compositional and microstructural studies on tooth enamel of proboscideans, with a particular focus on the enamel of extinct elephant taxa. Studied fossils (tooth fragments) were found in Egypt and India, and had the age up to 34 millions of years (the samples covered the time range of Tertiary and Quaternary). Compositional analyses confirmed that highly-mineralized enamel was only little sensitive to chemical alteration and demonstrated a similar elemental composition over the time. Substitution-related changes in the enamel bioapatite were identified, however, they were

mostly not related with the sample age. Diagenetic alteration of the enamel, although detected, was not significant. Microscopic investigations revealed that the enamel microstructure was well-preserved. The spectrum of investigated samples allowed to observe the process of proboscidean enamel evolution, with regard to development and differentiation of its prismatic microstructure, and evolution of prism cross-section patterns. Tooth adaptations in proboscideans were driven by changes of the paleoclimate, which forced animals to migrate, occupy new habitats and modify their diet, depending on conditions prevailing in the paleoecosystems. Results of the project indicate that the enamel, with its extraordinary resistance to chemical alteration of external origin, is an attractive material, among other available mineralized animal hard tissues, for paleontological studies and provides a wealth of information which are helpful in understanding animal evolution and adaptation mechanisms, and reconstructing the paleoclimate and paleoenvironments.

In the third and last project presented in this thesis, the interactions between inorganic nanoparticles and bacterial cells (*Escherichia coli* strains) were studied. For this purpose, ultrasmall gold nanoparticles were applied. Great possibilities of chemical modification of the nanoparticle surface were utilized to covalently decorate the nanoparticles with photostable fluorophores. The project assumed application of cluster-sized gold nanoparticles to enhance, due to the ultrasmall size, the uptake of nanoparticles by autofluorescent bacteria. For high quality 3D imaging of the samples, advanced fluorescence microscopy techniques were used, such as confocal laser scanning microscopy and super resolution microscopy. Successful internalization of the nanoparticles by bacterial cells could be demonstrated in all studied experimental setups. Incubation with the nanoparticles did not adversely affect the viability of bacterial cultures, including nanoparticle-positive cells, indicating non-cytotoxicity of the ultrasmall gold nanoparticles. The efficiency of nanoparticle uptake by bacteria depended on particle concentration in the environment. The advantage of the application of nanoparticle-coupled fluorophores over free dyes, in this kind of microbiological studies, was also demonstrated. The ultrasmall gold nanoparticles have proved the ability to penetrate the bacterial cell envelope, without causing lethal effects to cells, and demonstrated high chemical modification possibilities, which makes them potential candidates for application in the treatment of bacterial infections, *e.g.*, after coupling with appropriate antimicrobials. Results presented in this thesis indicate that fluorescent ultrasmall gold nanoparticles contribute to a better understanding of the nature of interactions between nanoparticles and prokaryotic cells, which is less studied than in eukaryotic cells, in particular with regard to non-lethal uptake.

## 8. Zusammenfassung

In der vorliegenden Arbeit wurden Ergebnisse von drei interdisziplinären Forschungsprojekten präsentiert. Sie betreffen die Anwendung anorganischer Nanopartikel zur Untersuchung ihrer Wechselwirkungen mit lebenden Zellen, sowohl eukaryotischen als auch prokaryotischen, sowie den Einsatz der analytischen Methoden aus anorganischer Chemie zur Untersuchung biologischer Nanostrukturen verknüpfen.

Das erste Projekt umfasste die Anwendung anorganischer Nanoplatfformen für den Transport therapeutischer Biomoleküle in eukaryotische Zellen. Um dies zu erreichen, wurden Calciumphosphat-Nanopartikel als Träger für siRNA verwendet, die den Zweck hatte, die Expression der p65-Untereinheit des NF- $\kappa$ B stummzuschalten. NF- $\kappa$ B ist ein wichtiger Transkriptionsfaktor, der an der Entzündungs- und Immunantwort von Zellen beteiligt ist. Die Nanopartikel zeigten gute physikalisch-chemische Eigenschaften, konnten effizient mit therapeutischer siRNA beladen werden und erfüllten Qualitätskriterien für die weitere Anwendung in biologischen Experimenten. *In vitro* Studien, die an verschiedenen Arten von Blutzellen der Maus durchgeführt wurden, zeigten, dass die Nanopartikel nicht zytotoxisch waren und von den Zellen aufgenommen wurden. Die siRNA hemmte die Expression von NF- $\kappa$ B p65 in den entzündeten Zellen effizient und der Herunterregulationseffekt konnte auf Ebene von p65-mRNA und p65-Protein beobachtet werden. Interessanterweise konnte auch ein weiterer Herunterregulationseffekt auf die Expressionsprofile der Schlüsselzytokine (TNF- $\alpha$ , IL-6, INF- $\beta$ ) der unbeladenen Calciumphosphat-Nanoträger nachgewiesen werden. Diese Beobachtung eröffnete eine neue Perspektive zum Verständnis komplexer Zell-Nanopartikel-Wechselwirkungen. Die Bedeutung der Oberflächenfunktionalisierung von Calciumphosphat-Nanopartikeln mit einer Silica-Schalle wurde in den durchgeführten Auflösungsstudien bestätigt, während Co-Lokalisierungsexperimente eine eingehende Verfolgung der Partikelaufnahme bis zur Freisetzung der Biomoleküle innerhalb der Zelle ermöglichten. Die Silica-Funktionalisierung von Calciumphosphat-Nanopartikeln ermöglichte auch die Dekoration der Nanopartikel mit Liganden, um die Aufnahme durch Zielzellen zu verbessern. Die Stabilisierung der Nanopartikel mit einem Nahinfrarot-markierten Polymer erweiterte den Anwendungsbereich von siRNA-beladenen Calciumphosphat-Nanopartikeln auf die *in vivo* Forschung an Mäusen, was auf ein therapeutisches Potenzial von biokompatiblen und biomolekülbeladenen anorganischen Nanoträgern in der experimentellen Gentherapie und Regulation von NF- $\kappa$ B Expression auf molekularer Ebene hindeutet.

Das zweite Projekt, das in dieser Dissertation beschrieben wurde, umfasste umfangreich die Zusammensetzung und die mikrostrukturellen Studien des Zahnschmelzes von Rüsseltieren,

mit dem Fokus auf den Zahnschmelz ausgestorbener Elefantenarten. Untersuchte Fossilien (Zahnfragmente) wurden in Ägypten und Indien ausgegraben und hatten ein Alter von bis zu 34 Millionen Jahren (decken den Zeitbereich von Tertiär und Quartär ab). Die Analysen der Probenzusammensetzung bestätigten, dass hochmineralisierter Zahnschmelz weniger empfindlich gegenüber chemischen Veränderungen war und im Laufe der Zeit eine ähnliche Zusammensetzung besaß. Substitutionsbedingte Veränderungen des Schmelz-Bioapatits wurden identifiziert, waren jedoch meist nicht mit dem Probenalter verbunden. Die diagenetische Veränderung des Schmelzes war nicht signifikant. Mikroskopische Untersuchungen zeigten, dass die Zahnschmelzmikrostruktur gut beibehalten wurde. Das Spektrum der untersuchten Proben ermöglichte es, den Prozess der Zahnschmelzentwicklung des Rüssels im Hinblick auf die Entwicklung und Differenzierung seiner prismatischen Mikrostruktur und des Querschnittsmusters von Prismen zu beobachten. Zahnanpassungen bei Rüsseltieren wurden durch Veränderungen des Paläoklimas getrieben, die die Tiere zum Wandern gezwungen waren, um neue Lebensräume zu besetzen und ihre Ernährung abhängig von den Bedingungen in den Paläoökosystemen anzupassen. Die Ergebnisse des Projekts zeigten, dass der Zahnschmelz mit seiner außergewöhnlichen Beständigkeit gegenüber chemischen Veränderungen äußeren Ursprungs, neben anderen verfügbaren mineralisierten tierischen Hartgeweben, ein attraktives Material für paläontologische Studien darstellt. Weiterhin liefert er wichtige Informationen, die zum Verständnis der Evolution und der Anpassungsmechanismen von Tieren beitragen und zur Rekonstruktion des Paläoklimas und der Bedingungen, die in Paläoumgebungen herrschten, hilfreich sind.

Im dritten und letzten Projekt wurden zur Untersuchung der Wechselwirkungen zwischen anorganischen Nanopartikeln und Bakterienzellen (*Escherichia coli* Stämme) ultrakleine Goldnanopartikel eingesetzt. Dabei wurden große Möglichkeiten der chemischen Modifikation der Nanopartikeloberfläche genutzt, um die Nanopartikel kovalent mit photostabilen Fluorophoren zu dekorieren. Das Projekt ging von der Anwendung von Goldnanopartikeln in Clustergröße aus, um ihre Aufnahme durch autofluoreszierende Bakterien zu ermöglichen. Für die hochwertige 3D-Bildgebung von Proben wurden fortgeschrittene Techniken der Fluoreszenzmikroskopie wie die konfokale Laser-Scanning-Mikroskopie und die Superauflösungsmikroskopie angewendet. In allen untersuchten Versuchsansätzen konnte eine erfolgreiche Aufnahme der Nanopartikel in Bakterienzellen nachgewiesen werden. Die Inkubation mit den Nanopartikeln hatte keinen negativen Einfluss auf die Viabilität der bakteriellen Kulturen, einschließlich Nanopartikel-positiver Zellen, was auf keine zytotoxische Wirkung der ultrakleinen Goldnanopartikel hinweist. Die Effizienz der Aufnahme von

Nanopartikeln durch Bakterien hing von der Partikelkonzentration in der Umgebung ab. Der Vorteil der Anwendung von Nanopartikel-gekoppelten Fluorophoren gegenüber freien Farbstoffen in dieser Art mikrobiologischer Untersuchungen konnte ebenfalls gezeigt werden. Die ultrakleinen Goldnanopartikel waren in der Lage, die bakterielle Zellhülle zu penetrieren, ohne tödliche Wirkungen auf Zellen auszuüben, und zeigten hohe chemische Modifikationsmöglichkeiten, was sie zu potenziellen Kandidaten für die Behandlung bakterieller Infektionen macht, z. B. nach Kopplung mit geeigneten antimikrobiellen Stoffen. Fluoreszierende ultrakleine Goldnanopartikel tragen zu einem besseren Verständnis der Wechselwirkungen zwischen Nanopartikeln und prokaryotischen Zellen bei. Diese Interaktionen sind weniger untersucht als im Fall von eukaryotischen Zellen, insbesondere in Hinblick auf die nicht letale Aufnahme.

## 9. Podsumowanie

Interdyscyplinarne projekty badawcze przedstawione w tej pracy doktorskiej dotyczą szeroko pojętego zastosowania nieorganicznych nanocząstek w badaniach ich oddziaływania z komórkami żywymi, zarówno eukariotycznymi, jak i prokariotycznymi, jak również pokazują w jaki sposób chemia nieorganiczna i jej metody analityczne są pomocne w badaniach biologicznych nanostruktur.

Pierwszy z projektów zakładał zastosowanie nieorganicznych nanoplatform w dostarczaniu terapeutycznych biomolekuł do komórek eukariotycznych. W tym celu, nanocząstki fosforanu wapnia użyto jako nośników dla siRNA, specyficznego do wyciszenia ekspresji podjednostki p65 NF- $\kappa$ B. Ten ostatni to ważny czynnik transkrypcyjny, uczestniczący w zapalnej i immunologicznej odpowiedzi komórki. Zastosowane w projekcie nanocząstki charakteryzowały się odpowiednimi właściwościami fizykochemicznymi, były wydajnie sprzężone z terapeutycznym siRNA i spełniały wymagania jakościowe dla zastosowania w badaniach biologicznych. Przeprowadzone z wykorzystaniem różnych rodzajów mysich komórek krwi eksperymenty *in vitro* wykazały, że nanocząstki fosforanu wapnia nie były cytotoksyczne i były wychwytywane przez komórki, natomiast dostarczone za ich pośrednictwem siRNA wydajnie hamowało ekspresję NF- $\kappa$ B p65 w komórkach znajdujących się w stanie zapalnym. Efekt ten można było zaobserwować zarówno na poziomie komórkowej ekspresji mRNA p65, jak i białka p65. Co ciekawe, zjawisko wyciszenia ekspresji udało się wykazać również dla kluczowych cytokin (TNF- $\alpha$ , IL-6, INF- $\beta$ ) przy zastosowaniu niesprzężonych z biomolekułami nanonośników fosforanu wapnia. Obserwacja ta pozwala na lepsze zrozumienie złożonych oddziaływań pomiędzy nanocząstkami, a komórkami. Istotną rolę opłaszczania nanocząstek fosforanu wapnia przy użyciu krzemionki wykazano w badaniach rozpuszczalności, a eksperymenty kolokalizacji pozwoliły na przeprowadzenie pogłębionych badań nad wewnątrzkomórkowym przetwarzaniem nanocząstek i sprzężonych z nimi biomolekuł. Funkcjonalizacja nanocząstek płaszczem krzemionkowym umożliwiła ponadto dekorację powierzchni nanocząstek ligandami, w celu poprawienia wydajności wychwytu nanocząstek przez komórki docelowe. Stabilizacja nanocząstek polimerem znakowanym barwnikiem bliskiej podczerwieni rozszerzyła zakres aplikacyjny nanonośników fosforanu wapnia, sprzężonych z siRNA, na badania *in vivo* w organizmach myszy, potwierdzając tym samym potencjał terapeutyczny biokompatybilnych i niosących biomolekuły nieorganicznych nanocząstek w eksperymentalnej terapii genowej opartej na regulacji ekspresji NF- $\kappa$ B na poziomie molekularnym.

Drugi z projektów, opisany w niniejszej pracy, dotyczył obszernych badań składu chemicznego i mikrostruktury szkliwa zębów trąbowców, ze szczególnym uwzględnieniem szkliwa pochodzącego od wymarłych gatunków słońi. Badane skamieliny (fragmenty zębów) pochodziły z Egiptu i Indii, i charakteryzowały się wiekiem do 34 milionów lat (pokrywały więc czas Trzeciorzędu i Czwartorzędu). Analizy składu potwierdziły, że wysoce zmineralizowane szkliwo było jedynie w niewielkim stopniu wrażliwe na modyfikacje chemiczne i wykazywało porównywalny skład, niezależnie od wieku próby. Zmiany o charakterze substytucji w bioapatycie szkliwa zostały wykazane, jednakże w większości przypadków nie były one zależne od upływu czasu. Modyfikacje pochodzenia diagenetycznego były obecne w skamieniałym szkliwie, natomiast nie były one znaczące. Analizy mikroskopowe wykazały, że mikrostruktura szkliwa była bardzo dobrze zachowana. Spektrum dobranych prób pozwoliło zaobserwować proces ewolucji szkliwa trąbowców, zarówno w kontekście rozwoju i różnicowania jego pryzmatycznej mikrostruktury, jak i ewolucji wzoru przekroju poprzecznego pryzm. Adaptacje zębów stanowiły ewolucyjną odpowiedź trąbowców na zmiany paleoklimatu, które zmuszały zwierzęta do migracji, zajmowania nowych siedlisk i dostosowywania ich diety do warunków panujących w paleoekosystemach. Wyniki projektu wskazują, że szkliwo, ze swoją wyjątkową odpornością na zmiany chemiczne pochodzenia zewnętrznego, stanowi atrakcyjny materiał, spośród innych dostępnych zmineralizowanych tkanek twardych zwierząt, dla badań paleontologicznych i dostarcza bogactwa informacji pomocnych w rozumieniu ewolucji zwierząt i ich mechanizmów adaptacyjnych oraz rekonstrukcji paleoklimatu i paleośrodowisk.

W trzecim i zarazem ostatnim projekcie przedstawionym w tej pracy, zastosowano ultramałe nanocząstki złota, aby badać oddziaływania między komórkami bakterii (szczepami *Escherichia coli*), a nieorganicznymi nanonośnikami. Wykorzystano tutaj znakomite możliwości chemicznej modyfikacji powierzchni nanocząstek, aby kowalencyjnie udekorować je fotostabilnymi barwnikami. Projekt zakładał zastosowanie nanocząstek złota, w klasterowym zakresie wielkości, tak aby umożliwić ich wychwyt przez autofluorescencyjne komórki bakterii. Dla uzyskania wysokiej jakości obrazowania prób w trójwymiarze, wykorzystano zaawansowane techniki mikroskopii fluorescencyjnej, takie jak mikroskopia konfokalna i mikroskopia superrozdzielczości. Wychwyt nanocząstek przez komórki bakterii został wykazany we wszystkich badanych eksperymentalnych konfiguracjach. Inkubacja z nanocząstkami nie miała również negatywnego wpływu na żywotność kultur bakterii, w tym komórek, które wychwyciły nanocząstki (komórki pozytywne), potwierdzając tym samym brak cytotoksyczności ultramałych nanocząstek złota. Wydajność wychwyty nanocząstek przez

bakterie była zależna od stężenia cząstek w środowisku. Wykazano również przewagę zastosowania barwników sprzężonych z nanocząstkami nad wolnymi barwnikami, w tego rodzaju badaniach mikrobiologicznych. Ultramałe nanocząstki złota charakteryzowała zdolność penetracji ściany komórkowej bakterii, bez działania letalnego wobec komórek, i duże możliwości chemicznej modyfikacji, co czyni je potencjalnymi kandydatami w leczeniu infekcji bakteryjnych, np. po sprzężeniu z odpowiednimi substancjami przeciwdrobnoustrojowymi. Zaprezentowane wyniki potwierdzają, że znakowane fluorescencyjnie ultramałe nanocząstki złota przyczyniają się do lepszego zrozumienia natury oddziaływań między nanocząstkami i komórkami prokariotycznymi, która jest słabiej poznana niż w przypadku komórek eukariotycznych, szczególnie w kwestii ich nieletalnego wychwytu.

## 10. References

- (1) Eliaz, N.; Metoki, N. Calcium phosphate bioceramics: a review of their history, structure, properties, coating technologies and biomedical applications. *Materials (Basel)* **2017**, *10*, 334.
- (2) Epple, M. Review of potential health risks associated with nanoscopic calcium phosphate. *Acta Biomater.* **2018**, *77*, 1-14.
- (3) Catauro, M.; Papale, F.; Sapio, L.; Naviglio, S. Biological influence of Ca/P ratio on calcium phosphate coatings by sol-gel processing. *Mater. Sci. Eng. C* **2016**, *65*, 188-193.
- (4) Bonjour, J. P. Calcium and phosphate: a duet of ions playing for bone health. *J. Am. Coll. Nutr.* **2011**, *30*, 438S-448S.
- (5) Sotiropoulou, P.; Fountos, G.; Martini, N.; Koukou, V.; Michail, C.; Kandarakis, I.; Nikiforidis, G. Bone calcium/phosphorus ratio determination using dual energy X-ray method. *Phys. Med.* **2015**, *31*, 307-313.
- (6) Barltrop, D.; Hillier, R. Calcium and phosphorus content of transitional and mature human milk. *Acta Paediatr.* **1974**, *63*, 347-350.
- (7) Rao, A.; Cölfen, H.: Chapter 2 – Morphology control and molecular templates in biomineralization. In *Biomineralization and biomaterials. Fundamentals and applications*; Aparicio, C., Ginebra, M. P., Eds.; Woodhead Publishing/Elsevier: Cambridge, United Kingdom, **2016**; pp 51-93.
- (8) Lin, W.; Zhang, W.; Paterson, G. A.; Zhu, Q.; Zhao, X.; Knight, R.; Bazylnski, D. A.; Roberts, A. P.; Pan, Y. Expanding magnetic organelle biogenesis in the domain *Bacteria. Microbiome* **2020**, *8*, 152.
- (9) Tamura, N.; Gilbert, P. U. P. A.: Chapter 21 – X-ray microdiffraction of biominerals. In *Research methods in biomineralization science*; De Yoreo, J. J., Ed.; Methods in Enzymology; Academic Press/Elsevier: New York, USA, **2013**; pp 501-531.
- (10) Zhang, Y.; Wang, Y. The effect of hydroxyapatite presence on the degree of conversion and polymerization rate in a model self-etching adhesive. *Dent. Mater.* **2012**, *28*, 237-244.
- (11) Wopenka, B.; Pasteris, J. D. A mineralogical perspective on the apatite in bone. *Mater. Sci. Eng. C* **2005**, *25*, 131-143.
- (12) Wegst, U. G. K.; Bai, H.; Saiz, E.; Tomsia, A. P.; Ritchie, R. O. Bioinspired structural materials. *Nature Mater.* **2015**, *14*, 23-36.

- 
- (13) Habraken, W.; Habibovic, P.; Epple, M.; Bohner, M. Calcium phosphates in biomedical applications: materials for the future? *Mater. Today* **2016**, *19*, 69-87.
- (14) Chen, W.; Wang, Q.; Meng, S.; Yang, P.; Jiang, L.; Zou, X.; Li, Z.; Hu, S. Temperature-related changes of Ca and P release in synthesized hydroxylapatite, geological fluorapatite and bone bioapatite. *Chem. Geol.* **2017**, *451*, 183-188.
- (15) Hemeg, H. A. Nanomaterials for alternative antibacterial therapy. *Int. J. Nanomedicine* **2017**, *12*, 8211-8225.
- (16) Dadfar, S. M.; Roemhild, K.; Drude, N. I.; von Stillfried, S.; Knüchel, R.; Kiessling, F.; Lammers, T. Iron oxide nanoparticles: diagnostic, therapeutic and theranostic applications. *Adv. Drug Deliv. Rev.* **2019**, *138*, 302-325.
- (17) Piao, Y.; Bei, H. P.; Tam, A.; Yang, Y.; Zhang, Q.; Yang, M.; Zhao, X.: Chapter 6 – Calcium phosphate nanoparticle-based systems for therapeutic delivery. In *Theranostic bionanomaterials. Micro and nano technologies*; Cui, W., Zhao, X., Eds.; Elsevier: Amsterdam, The Netherlands, **2019**; pp 147-164.
- (18) Yang, Q.; Zhou, Y.; Chen, J.; Huang, N.; Wang, Z.; Cheng, Y. Gene therapy for drug-resistant glioblastoma via lipid-polymer hybrid nanoparticles combined with focused ultrasound. *Int. J. Nanomedicine* **2021**, *16*, 185-199.
- (19) Rotan, O.; Severin, K. N.; Pöpsel, S.; Peetsch, A.; Merdanovic, M.; Ehrmann, M.; Epple, M. Uptake of the proteins HTRA1 and HTRA2 by cells mediated by calcium phosphate nanoparticles. *Beilstein J. Nanotechnol.* **2017**, *8*, 381-393.
- (20) Kumari, S.; Mg, S.; Mayor, S. Endocytosis unplugged: multiple ways to enter the cell. *Cell Res.* **2010**, *20*, 256-275.
- (21) Petros, R. A.; DeSimone, J. M. Strategies in the design of nanoparticles for therapeutic applications. *Nat. Rev. Drug Discov.* **2010**, *9*, 615-627.
- (22) Rathore, B.; Sunwoo, K.; Jangili, P.; Kim, J.; Kim, J. H.; Huang, M.; Xiong, J.; Sharma, A.; Yang, Z.; Qu, J.; Kim, J. S. Nanomaterial designing strategies related to cell lysosome and their biomedical applications: a review. *Biomaterials* **2019**, *211*, 25-47.
- (23) Levingstone, T. J.; Herbaj, S.; Dunne, N. J. Calcium phosphate nanoparticles for therapeutic applications in bone regeneration. *Nanomaterials* **2019**, *9*, 1570.
- (24) Farouq, M. A. H.; Al Qaraghuli, M. M.; Kubiak-Ossowska, K.; Ferro, V. A.; Mulheran, P. A. Biomolecular interactions with nanoparticles: applications for coronavirus disease 2019. *Curr. Opin. Colloid Interface Sci.* **2021**, *54*, 101461.

- 
- (25) Tengjisi; Hui, Y.; Yang, G.; Fu, C.; Liu, Y.; Zhao, C. X. Biomimetic core-shell silica nanoparticles using a dual-functional peptide. *J. Colloid Interface Sci.* **2021**, *581*, 185-194.
- (26) Lin, K.; Wu, C.; Chang, J. Advances in synthesis of calcium phosphate crystals with controlled size and shape. *Acta Biomater.* **2014**, *10*, 4071-4102.
- (27) Wu, Z.; Yang, S.; Wu, W. Shape control of inorganic nanoparticles from solution. *Nanoscale* **2016**, *8*, 1237-1259.
- (28) Xiao, W.; Gao, H. The impact of protein corona on the behavior and targeting capability of nanoparticle-based delivery system. *Int. J. Pharm.* **2018**, *552*, 328-339.
- (29) Guindani, C.; Frey, M. L.; Simon, J.; Koynov, K.; Schultze, J.; Ferreira, S. R. S.; Araújo, P. H. H.; de Oliveira, D.; Wurm, F. R.; Mailänder, V.; Landfester, K. Covalently binding of bovine serum albumin to unsaturated poly(globalide-co- $\epsilon$ -caprolactone) nanoparticles by thiol-ene reactions. *Macromol. Biosci.* **2019**, *19*, 1900145.
- (30) Wang, K.; Kievit, F. M.; Zhang, M. Nanoparticles for cancer gene therapy: recent advances, challenges and strategies. *Pharmacol. Res.* **2016**, *114*, 56-66.
- (31) Röthlisberger, P.; Hollenstein, M. Aptamer chemistry. *Adv. Drug Deliv. Rev.* **2018**, *134*, 3-21.
- (32) Li, J.; Chen, Y. C.; Tseng, Y. C.; Mozumdar, S.; Huang, L. Biodegradable calcium phosphate nanoparticle with lipid coating for systemic siRNA delivery. *J. Control. Release* **2010**, *142*, 416-421.
- (33) Hu, B.; Zhong, L.; Weng, Y.; Peng, L.; Huang, Y.; Zhao, Y.; Liang, X. J. Therapeutic siRNA: state of the art. *Signal Transduct. Target. Ther.* **2020**, *5*, 101.
- (34) Devarasu, T.; Saad, R.; Ouadi, A.; Frisch, B.; Robinet, E.; Laquerrière, P.; Voegel, J. C.; Baumert, T.; Ogier, J.; Meyer, F. Potent calcium phosphate nanoparticle surface coating for *in vitro* and *in vivo* siRNA delivery: a step toward multifunctional nanovectors. *J. Mater. Chem. B* **2013**, *1*, 4692-4700.
- (35) Frede, A.; Neuhaus, B.; Klopffleisch, R.; Walker, C.; Buer, J.; Müller, W.; Epple, M.; Westendorf, A. M. Colonic gene silencing using siRNA-loaded calcium phosphate/PLGA nanoparticles ameliorates intestinal inflammation *in vivo*. *J. Control. Release* **2016**, *222*, 86-96.
- (36) Kara, G.; Parlar, A.; Cakmak, M. C.; Cokol, M.; Denkbaz, E. B.; Bakan, F. Silencing of survivin and cyclin B1 through siRNA-loaded arginine modified calcium phosphate nanoparticles for non-small-cell lung cancer therapy. *Colloids Surf. B Biointerfaces* **2020**, *196*, 111340.

- (37) Tenkumo, T.; Rojas-Sánchez, L.; Vanegas Sáenz, J. R.; Ogawa, T.; Miyashita, M.; Yoda, N.; Prymak, O.; Sokolova, V.; Sasaki, K.; Epple, M. Reduction of inflammation in a chronic periodontitis model in rats by TNF- $\alpha$  gene silencing with a topically applied siRNA-loaded calcium phosphate paste. *Acta Biomater.* **2020**, *105*, 263-279.
- (38) Zhao, X. Y.; Zhu, Y. J.; Chen, F.; Wu, J. Calcium phosphate nanocarriers dual-loaded with bovine serum albumin and ibuprofen: facile synthesis, sequential drug loading and sustained drug release. *Chem. Asian J.* **2012**, *7*, 1610-1615.
- (39) Madhumathi, K.; Rubaiya, Y.; Doble, M.; Venkateswari, R.; Sampath Kumar, T. S. Antibacterial, anti-inflammatory and bone-regenerative dual-drug-loaded calcium phosphate nanocarriers – *in vitro* and *in vivo* studies. *Drug Deliv. Transl. Res.* **2018**, *8*, 1066-1077.
- (40) Bisso, S.; Mura, S.; Castagner, B.; Couvreur, P.; Leroux, J. C. Dual delivery of nucleic acids and PEGylated-bisphosphonates *via* calcium phosphate nanoparticles. *Eur. J. Pharm. Biopharm.* **2019**, *142*, 142-152.
- (41) Mukherjee, R.; Patra, M.; Dutta, D.; Banik, M.; Basu, T. Tetracycline-loaded calcium phosphate nanoparticle (Tet-CPNP): rejuvenation of an obsolete antibiotic to further action. *Biochim. Biophys. Acta* **2016**, *1860*, 1929-1941.
- (42) Pan, X.; Chen, S.; Li, D.; Rao, W.; Zheng, Y.; Yang, Z.; Li, L.; Guan, X.; Chen, Z. The synergistic antibacterial mechanism of gentamicin-loaded CaCO<sub>3</sub> nanoparticles. *Front. Chem.* **2018**, *5*, 130.
- (43) Rivas, M.; del Valle, L. J.; Rodríguez-Rivero, A. M.; Turon, P.; Puiggali, J.; Alemán, C. Loading of antibiotic into biocoated hydroxyapatite nanoparticles: smart antitumor platforms with regulated release. *ACS Biomater. Sci. Eng.* **2018**, *4*, 3234-3245.
- (44) Wang, D.; Farhana, A.: *Biochemistry, RNA structure*; StatPearls Publishing: Treasure Island, USA, **2021**.
- (45) Šponer, J.; Bussi, G.; Krepl, M.; Banáš, P.; Bottaro, S.; Cunha, R. A.; Gil-Ley, A.; Pinamonti, G.; Poblete, S.; Jurečka, P.; Walter, N. G.; Otyepka, M. RNA structural dynamics as captured by molecular simulations: a comprehensive overview. *Chem. Rev.* **2018**, *118*, 4177-4338.
- (46) Alberts, B.; Johnson, A.; Lewis, J.; Raff, M.; Roberts, K.; Walter, P.: *Molecular biology of the cell. 4<sup>th</sup> edition*; Garland Science/Taylor & Francis: New York, USA, **2002**. pp. 1-1462.
- (47) Payne, S. Introduction to RNA viruses. *Viruses* **2017**, 97-105.

- (48) Lodish, H.; Berk, A.; Zipursky, S. L.; Matsudaira, P.; Baltimore, D.; Darnell, J.: *Molecular cell biology. 4<sup>th</sup> edition*; W. H. Freeman and Co./Macmillan Publishers: New York, USA, **2000**. pp. 1-1184.
- (49) Ciechanover, A.; Orian, A.; Schwartz, A. L. Ubiquitin-mediated proteolysis: biological regulation *via* destruction. *Bioessays* **2000**, *22*, 442-451.
- (50) Hoppe, T. Life and destruction: ubiquitin-mediated proteolysis in aging and longevity. *F1000 Biol. Rep.* **2010**, *2*, 79.
- (51) Yoon, J. H.; Abdelmohsen, K.; Kim, J.; Yang, X.; Martindale, J. L.; Tominaga-Yamanaka, K.; White, E. J.; Orjalo, A. V.; Rinn, J. L.; Kreft, S. G.; Wilson, G. M.; Gorospe, M. Scaffold function of long non-coding RNA HOTAIR in protein ubiquitination. *Nat. Commun.* **2013**, *4*, 2939.
- (52) Bratkovič, T.; Božič, J.; Rogelj, B. Functional diversity of small nucleolar RNAs. *Nucleic Acids Res.* **2020**, *48*, 1627-1651.
- (53) Siomi, M. C.; Sato, K.; Pezic, D.; Aravin, A. A. PIWI-interacting small RNAs: the vanguard of genome defence. *Nat. Rev. Mol. Cell Biol.* **2011**, *12*, 246-258.
- (54) Iwasaki, Y. W.; Siomi, M. C.; Siomi, H. PIWI-interacting RNA: its biogenesis and functions. *Annu. Rev. Biochem.* **2015**, *84*, 405-433.
- (55) Jin, F.; Guo, Z. Emerging role of a novel small non-coding regulatory RNA: tRNA-derived small RNA. *ExRNA* **2019**, *1*, 39.
- (56) Park, J.; Ahn, S. H.; Shin, M. G.; Kim, H. K.; Chang, S. tRNA-derived small RNAs: novel epigenetic regulators. *Cancers (Basel)* **2020**, *12*, 2773.
- (57) Green, D.; Dalmay, T.; Chapman, T. Microguards and micromessengers of the genome. *Heredity (Edinb.)* **2016**, *116*, 125-134.
- (58) Montgomery, M. K. RNA interference: unraveling a mystery. *Nat. Struct. Mol. Biol.* **2006**, *13*, 1039-1041.
- (59) Ketting, R. F.; Fischer, S. E.; Bernstein, E.; Sijen, T.; Hannon, G. J.; Plasterk, R. H. Dicer functions in RNA interference and in synthesis of small RNA involved in developmental timing in *C. elegans*. *Genes Dev.* **2001**, *15*, 2654-2659.
- (60) Agrawal, N.; Dasaradhi, P. V. N.; Mohammed, A.; Malhotra, P.; Bhatnagar, R. K.; Mukherjee, S. K. RNA interference: biology, mechanism and applications. *Microbiol. Mol. Biol. Rev.* **2003**, *67*, 657-685.
- (61) Peters, L.; Meister, G. Argonaute proteins: mediators of RNA silencing. *Mol. Cell* **2007**, *26*, 611-623.

- 
- (62) Li, S.; Wang, L.; Fu, B.; Berman, M. A.; Diallo, A.; Dorf, M. E. TRIM65 regulates microRNA activity by ubiquitination of TNRC6. *Proc. Natl. Acad. Sci. USA* **2014**, *111*, 6970-6975.
- (63) Adams, L. Pri-miRNA processing: structure is key. *Nat. Rev. Genet.* **2017**, *18*, 145.
- (64) Hoy, S. M. Patisiran: first global approval. *Drugs* **2018**, *78*, 1625-1631.
- (65) Weng, Y.; Xiao, H.; Zhang, J.; Liang, X. J.; Huang, Y. RNAi therapeutic and its innovative biotechnological evolution. *Biotechnol. Adv.* **2019**, *37*, 801-825.
- (66) Damase, T. R.; Sukhovshin, R.; Boada, C.; Taraballi, F.; Pettigrew, R. I.; Cooke, J. P. The limitless future of RNA therapeutics. *Front. Bioeng. Biotechnol.* **2021**, *9*, 628137.
- (67) Thi, T. T. H.; Suys, E. J. A.; Lee, J. S.; Nguyen, D. H.; Park, K. D.; Truong, N. P. Lipid-based nanoparticles in the clinic and clinical trials: from cancer nanomedicine to COVID-19 vaccines. *Vaccines (Basel)* **2021**, *9*, 359.
- (68) Aristizábal, B.; González, Á.: Chapter 2 – Innate immune system. In *Autoimmunity: from bench to bedside [Internet]*; Anaya, J. M., Shoenfeld, Y., Rojas-Villarraga, A., Levy, R. A., Cervera, R., Eds.; El Rosario University Press: Bogota, Colombia, **2013**.
- (69) Liu, T.; Zhang, L.; Joo, D.; Sun, S. C. NF- $\kappa$ B signaling in inflammation. *Signal Transduct. Target. Ther.* **2017**, *2*, 17023.
- (70) Smith, N. C.; Rise, M. L.; Christian, S. L. A comparison of the innate and adaptive immune systems in cartilaginous fish, ray-finned fish, and lobe-finned fish. *Front. Immunol.* **2019**, *10*, 2292.
- (71) Kunkl, M.; Frasca, S.; Amormino, C.; Volpe, E.; Tuosto, L. T helper cells: the modulators of inflammation in multiple sclerosis. *Cells* **2020**, *9*, 482.
- (72) Sewell, H. F.; Agius, R. M.; Stewart, M.; Kendrick, D. Cellular immune responses to covid-19. *BMJ* **2020**, *370*, m3018.
- (73) Janeway Jr., C. A.; Travers, P.; Walport, M.; Shlomchik, M. J.: *Immunobiology: the immune system in health and disease. 5<sup>th</sup> edition.*; Garland Science/Taylor & Francis: New York, USA, **2001**. pp. 1-732.
- (74) Jongsmá, M. L. M.; Guarda, G.; Spaapen, R. M. The regulatory network behind MHC class I expression. *Mol. Immunol.* **2019**, *113*, 16-21.
- (75) Tunland, B.: Chapter 4 – Role of gut microbiota in immune homeostasis. In *Human microbiota in health and disease*; Tunland, B., Ed.; Academic Press/Elsevier: New York, USA, **2018**; pp 135-154.

- (76) Chen, L.; Deng, H.; Cui, H.; Fang, J.; Zuo, Z.; Deng, J.; Li, Y.; Wang, X.; Zhao, L. Inflammatory responses and inflammation-associated diseases in organs. *Oncotarget* **2018**, *9*, 7204-7218.
- (77) Yang, Z.; Kang, L.; Wang, Y.; Xiang, J.; Wu, Q.; Xu, C.; Zhou, Y.; Chen, S.; Fang, H.; Liu, J.; Dong, M. Role of IL-37 in cardiovascular disease inflammation. *Can. J. Cardiol.* **2019**, *35*, 923-930.
- (78) Jang, J.; Kim, W.; Kim, K.; Chung, S. I.; Shim, Y. J.; Kim, S. M.; Yoon, Y. Lipoteichoic acid upregulates NF- $\kappa$ B and proinflammatory cytokines by modulating  $\beta$ -catenin in bronchial epithelial cells. *Mol. Med. Rep.* **2015**, *12*, 4720-4726.
- (79) Lively, S.; Schlichter, L. C. Microglia responses to pro-inflammatory stimuli (LPS, IFN $\gamma$  + TNF $\alpha$ ) and reprogramming by resolving cytokines (IL-4, IL-10). *Front. Cell. Neurosci.* **2018**, *12*, 215.
- (80) Park, M. H.; Hong, J. T. Roles of NF- $\kappa$ B in cancer and inflammatory diseases and their therapeutic approaches. *Cells* **2016**, *5*, 15.
- (81) Mitchell, J. P.; Carmody, R. J.: Chapter 2 – NF- $\kappa$ B and the transcriptional control of inflammation. In *Transcriptional gene regulation in health and disease*; Loos, F., Ed.; International Review of Cell and Molecular Biology; Academic Press/Elsevier: New York, USA, **2018**; pp 41-84.
- (82) Sun, S. C. Non-canonical NF- $\kappa$ B signaling pathway. *Cell Res.* **2011**, *21*, 71-85.
- (83) Ajibade, A. A.; Wang, Q.; Cui, J.; Zou, J.; Xia, X.; Wang, M.; Tong, Y.; Hui, W.; Liu, D.; Su, B.; Wang, H. Y.; Wang, R. F. TAK1 negatively regulates NF- $\kappa$ B and p38 MAP kinase activation in Gr-1+CD11b+ neutrophils. *Immunity* **2012**, *36*, 43-54.
- (84) Espín-Palazón, R.; Traver, D. The NF- $\kappa$ B family: key players during embryonic development and HSC emergence. *Exp. Hematol.* **2016**, *44*, 519-527.
- (85) Gorman, C. E.; Hulsey, C. D. Non-trophic functional ecology of vertebrate teeth: a review. *Integr. Comp. Biol.* **2020**, *60*, 665-675.
- (86) Teaford, M. F.; Smith, M. M.; Ferguson, M. W. J.: *Development, function and evolution of teeth*; Cambridge University Press: Cambridge, United Kingdom, **2000**. pp. 1-314.
- (87) Boushell, L. W.; Sturdevant, J. R.: Chapter 1 – Clinical significance of dental anatomy, histology, physiology and occlusion. In *Sturdevant's art and science of operative dentistry*; Ritter, A. V., Boushell, L. W., Walter, R., Eds.; Mosby/Elsevier: St. Louis, USA, **2019**; pp 1-39.

- 
- (88) Jin, S. S.; He, D. Q.; Wang, Y.; Zhang, T.; Yu, H. J.; Li, Z. X.; Zhu, L. S.; Zhou, Y. H.; Liu, Y. Mechanical force modulates periodontal ligament stem cell characteristics during bone remodelling via TRPV4. *Cell Prolif.* **2020**, *53*, e12912.
- (89) Dorozhkin, S. V.; Epple, M. Biological and medical significance of calcium phosphates. *Angew. Chem. Int. Ed. Engl.* **2002**, *41*, 3130-3146.
- (90) Berkovitz, B.; Shellis, P.: Chapter 2 – Mammalian tooth structure and function. In *The teeth of mammalian vertebrates*; Berkovitz, B., Shellis, P., Eds.; Academic Press/Elsevier: New York, USA, **2018**; pp 25-46.
- (91) White, S. N.; Luo, W.; Paine, M. L.; Fong, H.; Sarikaya, M.; Snead, M. L. Biological organization of hydroxyapatite crystallites into a fibrous continuum toughens and controls anisotropy in human enamel. *J. Dent. Res.* **2001**, *80*, 321-326.
- (92) LeGeros, R. Z.; Trautz, O. R.; Klein, E.; LeGeros, J. P. Two types of carbonate substitution in the apatite structure. *Experientia* **1969**, *25*, 5-7.
- (93) Daculsi, G.; Kerebel, L. M. Ultrastructural study and comparative analysis of fluoride content of enameloid in sea-water and fresh-water sharks. *Arch. Oral Biol.* **1980**, *25*, 145-151.
- (94) LeGeros, R. Z. Apatites in biological systems. *Prog. Cryst. Growth Charact. Mater.* **1981**, *4*, 1-45.
- (95) LeGeros, R. Z.; Suga, S. Crystallographic nature of fluoride in enameloids of fish. *Calcif. Tissue Int.* **1980**, *32*, 169-174.
- (96) Enax, J.; Prymak, O.; Raabe, D.; Epple, M. Structure, composition and mechanical properties of shark teeth. *J. Struct. Biol.* **2012**, *178*, 290-299.
- (97) Lübke, A.; Enax, J.; Loza, K.; Prymak, O.; Gaengler, P.; Fabritius, H. O.; Raabe, D.; Epple, M. Dental lessons from past to present: ultrastructure and composition of teeth from plesiosaurs, dinosaurs, extinct and recent sharks. *RSC Adv.* **2015**, *5*, 61612-61622.
- (98) Lübke, A.; Loza, K.; Patnaik, R.; Enax, J.; Raabe, D.; Prymak, O.; Fabritius, H. O.; Gaengler, P.; Epple, M. Reply to the ‘Comments on “Dental lessons from past to present: ultrastructure and composition of teeth from plesiosaurs, dinosaurs, extinct and recent sharks”’ by H. Botella *et al.*, RSC Adv., 2016, 6, 74384–74388. *RSC Adv.* **2017**, *7*, 6215-6222.
- (99) Kohn, M. J.; Schoeninger, M. J.; Barker, W. W. Altered states: effects of diagenesis on fossil tooth chemistry. *Geochim. Cosmochim. Acta* **1999**, *63*, 2737-2747.

- (100) Sakaguchi, R. L.; Powers, J. M.: Chapter 2 – The oral environment. In *Craig's restorative dental materials. 13<sup>th</sup> edition*; Sakaguchi, R. L., Powers, J. M., Eds.; Mosby/Elsevier: St. Louis, USA, **2012**; pp 5-23.
- (101) Wittwer-Backofen, U.; Gampe, J.; Vaupel, J. W. Tooth cementum annulation for age estimation: results from a large known-age validation study. *Am. J. Phys. Anthropol.* **2004**, *123*, 119-129.
- (102) Tabuce, R.; Delmer, C.; Gheerbrant, E. Evolution of the tooth enamel microstructure in the earliest proboscideans (*Mammalia*). *Zool. J. Linn. Soc.* **2007**, *149*, 611-628.
- (103) Roca, A. L.; Georgiadis, N.; Pecon-Slattery, J.; O'Brien, S. J. Genetic evidence for two species of elephant in Africa. *Science* **2001**, *293*, 1473-1477.
- (104) Landolfi, J. A.; Terrell, S. P.: Chapter 16 – *Proboscidea*. In *Pathology of wildlife and zoo animals*; Terio, K. A., McAloose, D., Leger, J. S., Eds.; Academic Press/Elsevier: New York, USA, **2018**; pp 413-431.
- (105) Marchant, G. H.; Shoshani, J. Head muscles of *Loxodonta africana* and *Elephas maximus* with comments on *Mammuthus primigenius* muscles. *Quat. Int.* **2007**, *169-170*, 186-191.
- (106) Todd, N. E. Qualitative comparison of the cranio-dental osteology of the extant elephants, *Elephas maximus* (Asian elephant) and *Loxodonta africana* (African elephant). *Anat. Rec.* **2010**, *293*, 62-73.
- (107) Pasenko, M. R. Quantitative and qualitative data of footprints produced by Asian (*Elephas maximus*) and African (*Loxodonta africana*) elephants and with a discussion of significance towards fossilized proboscidean footprints. *Quat. Int.* **2017**, *443*, 221-227.
- (108) Maglio, V. J. Origin and evolution of the *Elephantidae*. *Trans. Am. Philos. Soc.* **1973**, *63*, 1-149.
- (109) Wiedner, E.: Chapter 53 – *Proboscidea*. In *Fowler's zoo and wild animal medicine*; Miller, R. E., Fowler, M. E., Eds.; Saunders/Elsevier: Philadelphia, USA, **2015**; pp 517-532.
- (110) Gheerbrant, E. Paleocene emergence of elephant relatives and the rapid radiation of African ungulates. *Proc. Natl. Acad. Sci. USA* **2009**, *106*, 10717-10721.
- (111) Gheerbrant, E.; Sudre, J.; Cappetta, H.; Bignon, G. *Phosphatherium escuilliei*, from the Thancetian of the Ouled Abdoun Basin (Morocco), oldest known proboscidean (*Mammalia*) from Africa. *Geobios (Lyon)* **1998**, *31*, 247-269.

- (112) Gheerbrant, E.; Bouya, B.; Amaghzaz, M. Dental and cranial anatomy of *Eritherium azzouzororum* from the Paleocene of Morocco, earliest known proboscidean mammal. *Palaeontogr. Abt. A* **2012**, *297*, 151-183.
- (113) Shoshani, J.: *Proboscidea* (elephants). In *Encyclopedia of life sciences*; John Wiley & Sons: Hoboken, USA, **2001**; pp 1-16.
- (114) Liu, A. G. S. C.; Seiffert, E. R.; Simons, E. L. Stable isotope evidence for an amphibious phase in early proboscidean evolution. *Proc. Natl. Acad. Sci. USA* **2008**, *105*, 5786-5791.
- (115) van der Made, J.: The evolution of the elephants and their relatives in the context of changing climate and geography. In *Elefantentreich – eine Fossilwelt in Europa*; Höhne, D., Schwarz, W., Eds.; Landesamt für Denkmalpflege und Archäologie Sachsen-Anhalt & Landesmuseum für Vorgeschichte: Halle, Germany, **2010**; pp 340-360.
- (116) Wu, Y.; Deng, T.; Hu, Y.; Ma, J.; Zhou, X.; Mao, L.; Zhang, H.; Ye, J.; Wang, S. Q. A grazing *Gomphotherium* in Middle Miocene Central Asia, 10 million years prior to the origin of the *Elephantidae*. *Sci. Rep.* **2018**, *8*, 7640.
- (117) Rögl, F. Palaeogeographic considerations for mediterranean and paratethys seaways (Oligocene to Miocene). *Ann. Naturhist. Mus. Wien* **1998**, *99A*, 279-310.
- (118) Patnaik, R. Neogene-Quaternary mammalian paleobiogeography of the Indian subcontinent: an appraisal. *C. R. Palevol* **2016**, *15*, 889-902.
- (119) Tassy, P.: Chapter 16 – The “Proboscidean Datum Event”: how many proboscideans and how many events? In *European Neogene mammal chronology*; Lindsay, E. H., Fahlbusch, V., Mein, P., Eds.; Springer: Boston, USA, **1990**; pp 237-252.
- (120) Liscaljet, N. *Napakaliit trompa*: new pygmy proboscidean remains from the Cagayan Valley (Philippines). *Quat. Int.* **2012**, *276-277*, 278-286.
- (121) Fowler, M. E.; Mikota, S. K.: *Biology, medicine and surgery of elephants*; Blackwell Publishing/John Wiley & Sons: Hoboken, USA, **2006**. pp. 1-565.
- (122) Ginsberg, J. R.: Mammals, biodiversity of. In *Encyclopedia of biodiversity. 2<sup>nd</sup> edition. Life sciences.*; Scheiner, S. M., Ed.; Academic Press/Elsevier: New York, USA, **2013**.
- (123) Lister, A. M. The role of behaviour in adaptive morphological evolution of African proboscideans. *Nature* **2013**, *500*, 331-334.
- (124) Codron, J.; Lee-Thorp, J. A.; Sponheimer, M.; Codron, D.; Grant, R. C.; de Ruiter, D. J. Elephant (*Loxodonta africana*) diets in Kruger National Park, South Africa: spatial and landscape differences. *J. Mammal.* **2006**, *87*, 27-34.

- (125) Skarpe, C.; Moe, S. R.; Wallgren, M.; Stokke, S.: Chapter 13 – Elephants and the grazing and browsing guilds. In *Elephants and savanna woodland ecosystems: a study from Chobe National Park, Botswana*; Skarpe, C., du Toit, J. T., Moe, S. R., Eds.; John Wiley & Sons: Hoboken, USA, **2014**; pp 207-228.
- (126) Todd, N. E.; Falco, N.; Silva, N.; Sanchez, C. Dental microwear variation in complete molars of *Loxodonta africana* and *Elephas maximus*. *Quat. Int.* **2007**, *169-170*, 192-202.
- (127) Sander, P. M.: Chapter 7 – Prismless enamel in amniotes: terminology, function and evolution. In *Development, function and evolution of teeth*; Teaford, M. F., Smith, M. M., Ferguson, M. W. J., Eds.; Cambridge University Press: Cambridge, United Kingdom, **2000**; pp 92-106.
- (128) Yilmaz, E. D.; Bechtle, S.; Özcoban, H.; Kieser, J. A.; Swain, M. V.; Schneider, G. A. Micromechanical characterization of prismless enamel in the tuatara, *Sphenodon punctatus*. *J. Mech. Behav. Biomed. Mater.* **2014**, *39*, 210-217.
- (129) LeBlanc, A. R. H.; Apestequía, S.; Larsson, H. C. E.; Caldwell, M. W. Unique tooth morphology and prismatic enamel in Late Cretaceous sphenodontians from Argentina. *Curr. Biol.* **2020**, *30*, 1755-1761.e1752.
- (130) Ferretti, M. P. Structure and evolution of mammoth molar enamel. *Acta Palaeontol. Pol.* **2003**, *48*, 383–396.
- (131) von Koenigswald, W.; Sander, P. M.: Chapter 15 – Glossary of terms used for enamel microstructures. In *Tooth enamel microstructure*; von Koenigswald, W., Sander, P. M., Eds.; CRC Press/Balkema/Taylor & Francis Group: London, United Kingdom, **1997**; pp 267-281.
- (132) Boyde, A. The development of enamel structure. *Proc. R. Soc. Med.* **1967**, *60*, 923-928.
- (133) Dumont, E. R. Mammalian enamel prism patterns and enamel deposition rates. *Scanning Microscopy* **1995**, *9*, 429-442.
- (134) Vrba, E. S.; Grine, F. E. *Australopithecine* enamel prism patterns. *Science* **1978**, *202*, 890-892.
- (135) Enax, J.; Fabritius, H. O.; Rack, A.; Prymak, O.; Raabe, D.; Epple, M. Characterization of crocodile teeth: correlation of composition, microstructure and hardness. *J. Struct. Biol.* **2013**, *184*, 155-163.
- (136) Eder, M.; Amini, S.; Fratzl, P. Biological composites – complex structures for functional diversity. *Science* **2018**, *362*, 543-547.

- (137) Vollrath, F.; Mi, R.; Shah, D. U. Ivory as an important model bio-composite. *Curator* **2018**, *61*, 95-110.
- (138) Ben-Zvi, Y.; Maria, R.; Pierantoni, M.; Brumfeld, V.; Shahar, R.; Weiner, S. Response of the tooth-periodontal ligament-bone complex to load: a microCT study of the minipig molar. *J. Struct. Biol.* **2019**, *205*, 155-162.
- (139) Ferretti, M. P. Enamel structure of *Cuvieronius hyodon* (*Proboscidea*, *Gomphotheriidae*) with a discussion on enamel evolution in elephantoids. *J. Mammal. Evol.* **2008**, *15*, 37-58.
- (140) Shoshani, J. Understanding proboscidean evolution: a formidable task. *Trends Ecol. Evol.* **1998**, *13*, 480-487.
- (141) Manthi, F. K.; Sanders, W. J.; Plavcan, J. M.; Cerling, T. E.; Brown, F. H. Late Middle Pleistocene elephants from Natodomeri, Kenya and the disappearance of *Elephas* (*Proboscidea*, *Mammalia*) in Africa. *J. Mammal. Evol.* **2020**, *27*, 483-495.
- (142) Kozawa, Y. Evolution of proboscidean enamel structure. *J. Fossil Res.* **1985**, *2*, 45-50.
- (143) Bertrand, P.: Évolution de la structure de l'émail chez les *Proboscidea* primitifs: aspects phylogénétique et fonctionnel. In *Teeth revisited: proceedings of the 7<sup>th</sup> international symposium on dental morphology*; Russell, D. E., Santoro, J. P., Sigogneau-Russell, D., Eds.; Editions du Muséum in Paris: Paris, France, **1988**; pp 109-124.
- (144) von Koenigswald, W.; Martin, T.; Pfretzschner, H. U.: Chapter 21 – Phylogenetic interpretation of enamel structures in mammalian teeth: possibilities and problems. In *Mammal phylogeny – placentals*; Szalay, F. S., Novacek, M. J., McKenna, M. C., Eds.; Springer: New York, USA, **1993**; pp 303-314.
- (145) Pfretzschner, H. U. Biomechanics of the enamel microstructure of large mammals. *Palaeontogr. Abt. A* **1994**, *234*, 1-88.
- (146) Patnaik, R.; Premjit Singh, N.; Paul, D.; Sukumar, R. Dietary and habitat shifts in relation to climate of Neogene-Quaternary proboscideans and associated mammals of the Indian subcontinent. *Quat. Sci. Rev.* **2019**, *224*, 105968.
- (147) Khan, M. A.; Iliopoulos, G.; Akhtar, M.; Ghaffar, A.; Zubaid-ul-Haq. The longest tusk of cf. *Anancus sivalensis* (*Proboscidea*, *Mammalia*) from the Tatrot Formation of the Siwaliks, Pakistan. *Curr. Sci.* **2011**, *100*, 249-255.
- (148) Mothé, D.; Ferretti, M. P.; Avilla, L. S. The dance of tusks: rediscovery of lower incisors in the Pan-American proboscidean *Cuvieronius hyodon* revises incisor evolution in *Elephantimorpha*. *PLoS One* **2016**, *11*, e0147009.

- (149) Trapani, J.; Fisher, D. C. Discriminating proboscidean taxa using features of the Schreger pattern in tusk dentin. *J. Archaeol. Sci.* **2003**, *30*, 429-438.
- (150) Albéric, M.; Gourrier, A.; Wagermaier, W.; Fratzl, P.; Reiche, I. The three-dimensional arrangement of the mineralized collagen fibers in elephant ivory and its relation to mechanical and optical properties. *Acta Biomater.* **2018**, *72*, 342-351.
- (151) Le Page, M. Unnatural selection: hunting down elephants' tusks. *New Sci.* **2011**, *210*, 33.
- (152) Chiyo, P. I.; Obanda, V.; Korir, D. K. Illegal tusk harvest and the decline of tusk size in the African elephant. *Ecol. Evol.* **2015**, *5*, 5216-5229.
- (153) Huang, X.; El-Sayed, M. A. Gold nanoparticles: optical properties and implementations in cancer diagnosis and photothermal therapy. *J. Adv. Res.* **2010**, *1*, 13-28.
- (154) Tang, M.; Zhang, J.; Yang, C.; Zheng, Y.; Jiang, H. Gold nanoclusters for bacterial detection and infection therapy. *Front. Chem.* **2020**, *8*, 181.
- (155) Botteon, C. E. A.; Silva, L. B.; Ccana-Ccapatinta, G. V.; Silva, T. S.; Ambrosio, S. R.; Veneziani, R. C. S.; Bastos, J. K.; Marcato, P. D. Biosynthesis and characterization of gold nanoparticles using Brazilian red propolis and evaluation of its antimicrobial and anticancer activities. *Sci. Rep.* **2021**, *11*, 1974.
- (156) Nguyen, D. T.; Kim, D. J.; So, M. G.; Kim, K. S. Experimental measurements of gold nanoparticle nucleation and growth by citrate reduction of HAuCl<sub>4</sub>. *Adv. Powder Technol.* **2010**, *21*, 111-118.
- (157) Liu, G.; Yang, X.; Li, Y.; Yang, Z.; Hong, W.; Liu, J. Continuous flow controlled synthesis of gold nanoparticles using pulsed mixing microfluidic system. *Adv. Mater. Sci. Eng.* **2015**, *2015*.
- (158) Gerosa, C.; Crisponi, G.; Nurchi, V. M.; Saba, L.; Cappai, R.; Cau, F.; Faa, G.; Van Eyken, P.; Scartozzi, M.; Floris, G.; Fanni, D. Gold nanoparticles: a new golden era in oncology? *Pharmaceuticals (Basel)* **2020**, *13*, 192.
- (159) Zhou, Y.; Kong, Y.; Kundu, S.; Cirillo, J. D.; Liang, H. Antibacterial activities of gold and silver nanoparticles against *Escherichia coli* and bacillus Calmette-Guérin. *J. Nanobiotechnology* **2012**, *10*, 19.
- (160) Shah, M.; Badwaik, V.; Kherde, Y.; Waghwani, H. K.; Modi, T.; Aguilar, Z. P.; Rodgers, H.; Hamilton, W.; Marutharaj, T.; Webb, C.; Lawrenz, M. B.; Dakshinamurthy, R. Gold nanoparticles: various methods of synthesis and antibacterial applications. *Front. Biosci. (Landmark Ed.)* **2014**, *19*, 1320-1344.

- (161) Jassal, M.; Junka, R.; Laurencin, C. T.; Yu, X.: Chapter 52 – Introduction to regenerative engineering. In *Encyclopedia of biomedical engineering*; Narayan, R., Ed.; Elsevier: Amsterdam, The Netherlands, **2019**; pp 624-630.
- (162) Bai, X.; Wang, Y.; Song, Z.; Feng, Y.; Chen, Y.; Zhang, D.; Feng, L. The basic properties of gold nanoparticles and their applications in tumor diagnosis and treatment. *Int. J. Mol. Sci.* **2020**, *21*, 2480.
- (163) Ghosh, P.; Han, G.; De, M.; Kim, C. K.; Rotello, V. M. Gold nanoparticles in delivery applications. *Adv. Drug Deliv. Rev.* **2008**, *60*, 1307-1315.
- (164) Cabuzu, D.; Cirja, A.; Puiu, R.; Grumezescu, A. M. Biomedical applications of gold nanoparticles. *Curr. Top. Med. Chem.* **2015**, *15*, 1605-1613.
- (165) Zheng, K.; Setyawati, M. I.; Leong, D. T.; Xie, J. Overcoming bacterial physical defenses with molecule-like ultrasmall antimicrobial gold nanoclusters. *Bioact. Mater.* **2020**, *6*, 941-950.
- (166) Woźniak, A.; Malankowska, A.; Nowaczyk, G.; Grześkowiak, B. F.; Tuśnio, K.; Słomski, R.; Zaleska-Medynska, A.; Jurga, S. Size and shape-dependent cytotoxicity profile of gold nanoparticles for biomedical applications. *J. Mater. Sci. Mater. Med.* **2017**, *28*, 92.
- (167) Favi, P. M.; Gao, M.; Johana Sepúlveda Arango, L.; Ospina, S. P.; Morales, M.; Pavon, J. J.; Webster, T. J. Shape and surface effects on the cytotoxicity of nanoparticles: gold nanospheres versus gold nanostars. *J. Biomed. Mater. Res. A* **2015**, *103*, 3449-3462.
- (168) Fuerst, J. A.: Beyond prokaryotes and eukaryotes: *Planctomycetes* and cell organization. In *Cell origins and metabolism*; Coté, G., De Tullio, M., Eds.; Nature Publishing Group: London, United Kingdom, **2010**; online.
- (169) Wiese, M.; Bannister, A. J. Two genomes, one cell: mitochondrial-nuclear coordination via epigenetic pathways. *Mol. Metab.* **2020**, *38*, 100942.
- (170) Silhavy, T. J.; Kahne, D.; Walker, S. The bacterial cell envelope. *Cold Spring Harb. Perspect. Biol.* **2010**, *2*, a000414.
- (171) Cole, L. A.: Chapter 13 – Evolution of chemical, prokaryotic and eukaryotic life. In *Biology of life: biochemistry, physiology and philosophy*; Cole, L. A., Ed.; Academic Press/Elsevier: New York, USA, **2016**; pp 93-99.
- (172) Maleki, S. S.; Mohammadi, K.; Ji, K. S. Characterization of cellulose synthesis in plant cells. *Sci. World J.* **2016**, *2016*, 8641373.
- (173) Brown, H. E.; Esher, S. K.; Alspaugh, J. A.: Chapter 5 – Chitin: a “hidden figure” in the fungal cell wall. In *The fungal cell wall*; Latgé, J. P., Ed.; Current Topics in

- Microbiology and Immunology; Springer International Publishing: Basel, Switzerland, **2020**; pp 83-111.
- (174) Coico, R. Gram staining. *Curr. Protoc. Microbiol.* **2006**, A.3C.1-C.2.
- (175) Ginsburg, I. Role of lipoteichoic acid in infection and inflammation. *Lancet Infect. Dis.* **2002**, 2, 171-179.
- (176) Slavin, Y. N.; Asnis, J.; Häfeli, U. O.; Bach, H. Metal nanoparticles: understanding the mechanisms behind antibacterial activity. *J. Nanobiotechnology* **2017**, 15, 65.
- (177) Liao, C.; Li, Y.; Tjong, S. C. Bactericidal and cytotoxic properties of silver nanoparticles. *Int. J. Mol. Sci.* **2019**, 20, 449.
- (178) Niño-Martínez, N.; Salas Orozco, M. F.; Martínez-Castañón, G. A.; Torres Méndez, F.; Ruiz, F. Molecular mechanisms of bacterial resistance to metal and metal oxide nanoparticles. *Int. J. Mol. Sci.* **2019**, 20, 2808.
- (179) Mitchell, G. J.; Wiesenfeld, K.; Nelson, D. C.; Weitz, J. S. Critical cell wall hole size for lysis in Gram-positive bacteria. *J. R. Soc. Interface* **2013**, 10, 20120892.
- (180) Mai-Prochnow, A.; Clauson, M.; Hong, J.; Murphy, A. B. Gram-positive and Gram-negative bacteria differ in their sensitivity to cold plasma. *Sci. Rep.* **2016**, 6, 38610.
- (181) Swift, B. J. F.; Baneyx, F. Microbial uptake, toxicity and fate of biofabricated ZnS:Mn nanocrystals. *PLoS One* **2015**, 10, e0124916.
- (182) Białas, N.; Kasperkiewicz, K.; Radziejewska-Lebrecht, J.; Skurnik, M. Bacterial cell surface structures in *Yersinia enterocolitica*. *Arch. Immunol. Ther. Exp. (Warsz.)* **2012**, 60, 199-209.
- (183) Mitchell, A. M.; Srikumar, T.; Silhavy, T. J. Cyclic enterobacterial common antigen maintains the outer membrane permeability barrier of *Escherichia coli* in a manner controlled by YhdP. *mBio* **2018**, 9, e01321-01318.
- (184) Alexander, C.; Rietschel, E. T. Invited review: bacterial lipopolysaccharides and innate immunity. *J. Endotoxin Res.* **2001**, 7, 167-202.
- (185) Fung, F. M.; Su, M.; Feng, H. T.; Li, S. F. Y. Extraction, separation and characterization of endotoxins in water samples using solid phase extraction and capillary electrophoresis-laser induced fluorescence. *Sci. Rep.* **2017**, 7, 10774.
- (186) Maciejewska, A.; Kaszowska, M.; Jachymek, W.; Ługowski, C.; Łukasiewicz, J. Lipopolysaccharide-linked enterobacterial common antigen (ECA<sub>LPS</sub>) occurs in rough strains of *Escherichia coli* R1, R2 and R4. *Int. J. Mol. Sci.* **2020**, 21, 6038.
- (187) Feng, Z. V.; Gunsolus, I. L.; Qiu, T. A.; Hurley, K. R.; Nyberg, L. H.; Frew, H.; Johnson, K. P.; Vartanian, A. M.; Jacob, L. M.; Lohse, S. E.; Torelli, M. D.; Hamers, R. J.;

- Murphy, C. J.; Haynes, C. L. Impacts of gold nanoparticle charge and ligand type on surface binding and toxicity to Gram-negative and Gram-positive bacteria. *Chem. Sci.* **2015**, *6*, 5186-5196.
- (188) Miller, S. I. Antibiotic resistance and regulation of the Gram-negative bacterial outer membrane barrier by host innate immune molecules. *mBio* **2016**, *7*, e01541-01516.
- (189) Miller, K. P.; Wang, L.; Benicewicz, B. C.; Decho, A. W. Inorganic nanoparticles engineered to attack bacteria. *Chem. Soc. Rev.* **2015**, *44*, 7787-7807.
- (190) Vergalli, J.; Bodrenko, I. V.; Masi, M.; Moynié, L.; Acosta-Gutiérrez, S.; Naismith, J. H.; Davin-Regli, A.; Ceccarelli, M.; van den Berg, B.; Winterhalter, M.; Pagès, J. M. Porins and small-molecule translocation across the outer membrane of Gram-negative bacteria. *Nat. Rev. Microbiol.* **2020**, *18*, 164-176.
- (191) Coltharp, C.; Xiao, J. Super resolution microscopy for microbiology. *Cell. Microbiol.* **2012**, *14*, 1808-1818.
- (192) Mei, L.; Lu, Z.; Zhang, W.; Wu, Z.; Zhang, X.; Wang, Y.; Luo, Y.; Li, C.; Jia, Y. Bioconjugated nanoparticles for attachment and penetration into pathogenic bacteria. *Biomaterials* **2013**, *34*, 10328-10337.
- (193) Butler, K. S.; Peeler, D. J.; Casey, B. J.; Dair, B. J.; Elespuru, R. K. Silver nanoparticles: correlating nanoparticle size and cellular uptake with genotoxicity. *Mutagenesis* **2015**, *30*, 577-591.
- (194) Kloepfer, J. A.; Mielke, R. E.; Nadeau, J. L. Uptake of CdSe and CdSe/ZnS quantum dots into bacteria via purine-dependent mechanisms. *Appl. Environ. Microbiol.* **2005**, *71*, 2548-2557.
- (195) Demchick, P.; Koch, A. L. The permeability of the wall fabric of *Escherichia coli* and *Bacillus subtilis*. *J. Bacteriol.* **1996**, *178*, 768-773.
- (196) Novikova, O. D.; Solovyeva, T. F. Nonspecific porins of the outer membrane of Gram-negative bacteria: structure and functions. *Biochem. Moscow Suppl. Ser. A* **2009**, *3*, 3-15.
- (197) Morones, J. R.; Elechiguerra, J. L.; Camacho, A.; Holt, K.; Kouri, J. B.; Ramirez, J. T.; Yacaman, M. J. The bactericidal effect of silver nanoparticles. *Nanotechnology* **2005**, *16*, 2346-2353.
- (198) Kumar, M.; Tegge, W.; Wangoo, N.; Jain, R.; Sharma, R. K. Insights into cell penetrating peptide conjugated gold nanoparticles for internalization into bacterial cells. *Biophys. Chem.* **2018**, *237*, 38-46.

- (199) Lonhienne, T. G. A.; Sagulenko, E.; Webb, R. I.; Lee, K. C.; Franke, J.; Devos, D. P.; Nouwens, A.; Carroll, B. J.; Fuerst, J. A. Endocytosis-like protein uptake in the bacterium *Gemmata obscuriglobus*. *Proc. Natl. Acad. Sci. USA* **2010**, *107*, 12883-12888.
- (200) Wang, S.; Lawson, R.; Ray, P. C.; Yu, H. Toxic effects of gold nanoparticles on *Salmonella typhimurium* bacteria. *Toxicol. Ind. Health* **2011**, *27*, 547-554.
- (201) Butler, K. S.; Casey, B. J.; Garborcauskas, G. V. M.; Dair, B. J.; Elespuru, R. K. Assessment of titanium dioxide nanoparticle effects in bacteria: association, uptake, mutagenicity, co-mutagenicity and DNA repair inhibition. *Mutat. Res. Genet. Toxicol. Environ. Mutagen.* **2014**, *768*, 14-22.
- (202) Pajerski, W.; Ochońska, D.; Brzywczy-Włoch, M.; Indyka, P.; Jarosz, M.; Golda-Cepa, M.; Sojka, Z.; Kotarba, A. Attachment efficiency of gold nanoparticles by Gram-positive and Gram-negative bacterial strains governed by surface charges. *J. Nanopart. Res.* **2019**, *21*, 186.
- (203) Weiss, G.: Chapter 9 – Impact of metals on immune response and tolerance, and modulation of metal metabolism during infection. In *Trace metals and infectious diseases [Internet]*; Nriagu, J. O., Skaar, E. P., Eds.; MIT Press: Cambridge, USA, **2015**; pp 147-160.
- (204) Locatelli, F. M.; Goo, K. S.; Ulanova, D. Effects of trace metal ions on secondary metabolism and the morphological development of *Streptomyces*. *Metallomics* **2016**, *8*, 469-480.
- (205) Argudín, M. A.; Hofer, A.; Butaye, P. Heavy metal resistance in bacteria from animals. *Res. Vet. Sci.* **2019**, *122*, 132-147.
- (206) De, J.; Ramaiah, N.; Vardanyan, L. Detoxification of toxic heavy metals by marine bacteria highly resistant to mercury. *Mar. Biotechnol. (N.Y.)* **2008**, *10*, 471-477.
- (207) Ali, H.; Khan, E.; Ilahi, I. Environmental chemistry and ecotoxicology of hazardous heavy metals: environmental persistence, toxicity, and bioaccumulation. *J. Chem.* **2019**, *4*, 1-14.
- (208) Stanić, V.; Tanasković, S. B.: Chapter 11 – Antibacterial activity of metal oxide nanoparticles. In *Nanotoxicity. Prevention and antibacterial applications of nanomaterials. Micro and nano technologies*; Rajendran, S., Nguyen, T. A., Shukla, R. K., Mukherjee, A., Godugu, C., Eds.; Elsevier: Amsterdam, The Netherlands, **2020**; pp 241-274.

- 
- (209) Tchounwou, P. B.; Yedjou, C. G.; Patlolla, A. K.; Sutton, D. J.: Chapter 6 – Heavy metal toxicity and the environment. In *Molecular, clinical and environmental toxicology. Experientia supplementum*; Luch, A., Ed.; Experientia Supplementum; Springer: Basel, Switzerland, **2012**; pp 133-164.
- (210) Tumanyan, A. F.; Seliverstova, A. P.; Zaitseva, N. A. Effect of heavy metals on ecosystems. *Chem. Technol. Fuels Oils* **2020**, *56*, 390-394.
- (211) Bruins, M. R.; Kapil, S.; Oehme, F. W. Microbial resistance to metals in the environment. *Ecotoxicol. Environ. Saf.* **2000**, *45*, 198-207.
- (212) Altimira, F.; Yáñez, C.; Bravo, G.; González, M.; Rojas, L. A.; Seeger, M. Characterization of copper-resistant bacteria and bacterial communities from copper-polluted agricultural soils of central Chile. *BMC Microbiol.* **2012**, *12*, 193.
- (213) Lu, M.; Li, Z.; Liang, J.; Wei, Y.; Rensing, C.; Wei, G. Zinc resistance mechanisms of P1B-type ATPases in *Sinorhizobium meliloti* CCNWSX0020. *Sci. Rep.* **2016**, *6*, 29355.
- (214) Cai, Y.; Li, X.; Liu, D.; Xu, C.; Ai, Y.; Sun, X.; Zhang, M.; Gao, Y.; Zhang, Y.; Yang, T.; Wang, J.; Wang, L.; Li, X.; Yu, H. A novel Pb-resistant *Bacillus subtilis* bacterium isolate for co-biosorption of hazardous Sb(III) and Pb(II): thermodynamics and application strategy. *Int. J. Environ. Res. Public Health* **2018**, *15*, 702.
- (215) Lusi, E. A.; Patrissi, T.; Guarascio, P. Nickel-resistant bacteria isolated in human microbiome. *New Microbes New Infect.* **2017**, *19*, 67-70.
- (216) Francisco, R.; Alpoim, M. C.; Morais, P. V. Diversity of chromium-resistant and -reducing bacteria in a chromium-contaminated activated sludge. *J. Appl. Microbiol.* **2002**, *92*, 837-843.
- (217) Norton, R.; Finley, P. J. Clinically-isolated bacteria resistance to silver-based wound dressings. *J. Wound Care* **2021**, *30*, 238-247.
- (218) Checa, S. K.; Soncini, F. C. Bacterial gold sensing and resistance. *Biometals* **2011**, *24*, 419-427.
- (219) Choudhary, S.; Sar, P. Uranium biomineralization by a metal resistant *Pseudomonas aeruginosa* strain isolated from contaminated mine waste. *J. Hazard. Mater.* **2011**, *186*, 336-343.
- (220) Wheaton, G.; Counts, J.; Mukherjee, A.; Kruh, J.; Kelly, R. The confluence of heavy metal biooxidation and heavy metal resistance: implications for bioleaching by extreme thermoacidophiles. *Minerals* **2015**, *5*, 397-451.

- (221) Dong, Q.; Springeal, D.; Schoeters, J.; Nuyts, G.; Mergeay, M.; Diels, L. Horizontal transfer of bacterial heavy metal resistance genes and its applications in activated sludge systems. *Water Sci. Technol.* **1998**, *37*, 465-468.
- (222) Lermينياux, N. A.; Cameron, A. D. S. Horizontal transfer of antibiotic resistance genes in clinical environments. *Can. J. Microbiol.* **2019**, *65*, 34-44.
- (223) Li, L. G.; Xia, Y.; Zhang, T. Co-occurrence of antibiotic and metal resistance genes revealed in complete genome collection. *ISME J.* **2017**, *11*, 651-662.
- (224) Bankier, C.; Matharu, R. K.; Cheong, Y. K.; Ren, G. G.; Cloutman-Green, E.; Ciric, L. Synergistic antibacterial effects of metallic nanoparticle combinations. *Sci. Rep.* **2019**, *9*, 16074.
- (225) Zucca, M.; Savoia, D. The post-antibiotic era: promising developments in the therapy of infectious diseases. *Int. J. Biomed. Sci.* **2010**, *6*, 77-86.
- (226) Ramteke, L.; Gawali, P.; Jadhav, B. L.; Chopade, B. A. Comparative study on antibacterial activity of metal ions, monometallic and alloy noble metal nanoparticles against nosocomial pathogens. *BioNanoSci.* **2020**, *10*, 1018-1036.
- (227) Mohammadi, G.; Nokhodchi, A.; Barzegar-Jalali, M.; Lotfipour, F.; Adibkia, K.; Ehyaei, N.; Valizadeh, H. Physicochemical and anti-bacterial performance characterization of clarithromycin nanoparticles as colloidal drug delivery system. *Colloids Surf. B Biointerfaces* **2011**, *88*, 39-44.
- (228) Shaker, M. A.; Shaaban, M. I. Formulation of carbapenems loaded gold nanoparticles to combat multi-antibiotic bacterial resistance: *in vitro* antibacterial study. *Int. J. Pharm.* **2017**, *525*, 71-84.
- (229) Fuller, M.; Whiley, H.; Köper, I. Antibiotic delivery using gold nanoparticles. *SN Appl. Sci. (online)* **2020**, *2*, 1022.
- (230) Farooq, M. U.; Novosad, V.; Rozhkova, E. A.; Wali, H.; Ali, A.; Fateh, A. A.; Neogi, P. B.; Neogi, A.; Wang, Z. Gold nanoparticles-enabled efficient dual delivery of anticancer therapeutics to HeLa cells. *Sci. Rep.* **2018**, *8*, 2907.
- (231) Gupta, A.; Mumtaz, S.; Li, C. H.; Hussain, I.; Rotello, V. M. Combatting antibiotic-resistant bacteria using nanomaterials. *Chem. Soc. Rev.* **2019**, *48*, 415-427.
- (232) Jelinkova, P.; Mazumdar, A.; Sur, V. P.; Kociova, S.; Dolezelikova, K.; Jimenez, A. M. J.; Koudelkova, Z.; Mishra, P. K.; Smerkova, K.; Heger, Z.; Vaculovicova, M.; Moulick, A.; Adam, V. Nanoparticle-drug conjugates treating bacterial infections. *J. Control. Release* **2019**, *307*, 166-185.

- (233) Ranjan, A.; Pothayee, N.; Seleem, M. N.; Tyler Jr, R. D.; Brenseke, B.; Sriranganathan, N.; Riffle, J. S.; Kasimanickam, R. Antibacterial efficacy of core-shell nanostructures encapsulating gentamicin against an *in vivo* intracellular *Salmonella* model. *Int. J. Nanomedicine* **2009**, *4*, 289-297.
- (234) Mohammadi, G.; Valizadeh, H.; Barzegar-Jalali, M.; Lotfipour, F.; Adibkia, K.; Milani, M.; Azhdarzadeh, M.; Kiafar, F.; Nokhodchi, A. Development of azithromycin-PLGA nanoparticles: physicochemical characterization and antibacterial effect against *Salmonella typhi*. *Colloids Surf. B Biointerfaces* **2010**, *80*, 34-39.
- (235) Umamaheshwari, R. B.; Jain, N. K. Receptor mediated targeting of lectin conjugated gliadin nanoparticles in the treatment of *Helicobacter pylori*. *J. Drug Target.* **2003**, *11*, 415-423.
- (236) Demurtas, M.; Perry, C. C. Facile one-pot synthesis of amoxicillin-coated gold nanoparticles and their antimicrobial activity. *Gold Bull.* **2014**, *47*, 103-107.
- (237) Payne, J. N.; Waghvani, H. K.; Connor, M. G.; Hamilton, W.; Tockstein, S.; Moolani, H.; Chavda, F.; Badwaik, V.; Lawrenz, M. B.; Dakshinamurthy, R. Novel synthesis of kanamycin conjugated gold nanoparticles with potent antibacterial activity. *Front. Microbiol.* **2016**, *7*, 607.
- (238) Sidhu, P. K.; Nehra, K. Bacteriocin-nanoconjugates as emerging compounds for enhancing antimicrobial activity of bacteriocins. *J. King Saud Univ. Sci.* **2019**, *31*, 758-767.
- (239) Solleti, V. S.; Alhariri, M.; Halwani, M.; Omri, A. Antimicrobial properties of liposomal azithromycin for *Pseudomonas* infections in cystic fibrosis patients. *J. Antimicrob. Chemother.* **2015**, *70*, 784-796.
- (240) Rukavina, Z.; Vanić, Ž. Current trends in development of liposomes for targeting bacterial biofilms. *Pharmaceutics* **2016**, *8*, 18.
- (241) Kozlova, D.; Chernousova, S.; Knuschke, T.; Buer, J.; Westendorf, A. M.; Epple, M. Cell targeting by antibody-functionalized calcium phosphate nanoparticles. *J. Mater. Chem.* **2012**, *22*, 396-404.
- (242) Białas, N.; Müller, E. K.; Epple, M.; Hilger, I. Silica-coated calcium phosphate nanoparticles for gene silencing of NF- $\kappa$ B p65 by siRNA and their impact on cellular players of inflammation. *Biomaterials* **2021**, *276*, 121013.
- (243) Martín, I.; Teixidó, M.; Giralt, E. Design, synthesis and characterization of a new anionic cell-penetrating peptide: SAP(E). *Chembiochem* **2011**, *12*, 896-903.

- (244) Li, S. S.; Zhang, M.; Wang, J. H.; Yang, F.; Kang, B.; Xu, J. J.; Chen, H. Y. Monitoring the changes of pH in lysosomes during autophagy and apoptosis by plasmon enhanced Raman imaging. *Anal. Chem.* **2019**, *91*, 8398-8405.
- (245) Henderson, R. G.; Verougstraete, V.; Anderson, K.; Arbildua, J. J.; Brock, T. O.; Brouwers, T.; Cappellini, D.; Delbeke, K.; Herting, G.; Hixon, G.; Odnevall Wallinder, I.; Rodriguez, P. H.; Van Assche, F.; Wilrich, P.; Oller, A. R. Inter-laboratory validation of bioaccessibility testing for metals. *Regul. Toxicol. Pharmacol.* **2014**, *70*, 170-181.
- (246) Kollenda, S.; Kopp, M.; Wens, J.; Koch, J.; Schulze, N.; Papadopoulos, C.; Pöhler, R.; Meyer, H.; Epple, M. A pH-sensitive fluorescent protein sensor to follow the pathway of calcium phosphate nanoparticles into cells. *Acta Biomater.* **2020**, *111*, 406-417.
- (247) Laroui, H.; Ingersoll, S. A.; Liu, H. C.; Baker, M. T.; Ayyadurai, S.; Charania, M. A.; Laroui, F.; Yan, Y.; Sitaraman, S. V.; Merlin, D. Dextran sodium sulfate (DSS) induces colitis in mice by forming nano-lipocomplexes with medium-chain-length fatty acids in the colon. *PLoS One* **2012**, *7*, e32084.
- (248) Białas, N.; Prymak, O.; Singh, N. P.; Paul, D.; Patnaik, R.; Epple, M. Teeth of past and present elephants: microstructure and composition of enamel in fossilized proboscidean molars and implications for diagenesis. *Geochemistry, Geophys. Geosystems* **2021**, *22*, e2020GC009557.
- (249) Kundal, S. N.; Bhadar, G.; Kumar, S. A Late Pliocene baby *Stegodon* cf. *Stegodon insignis* (*Proboscidea*) from Upper Siwalik of Samba District, Jammu and Kashmir, India. *Earth Sci. India* **2017**, *10*, 82-93.
- (250) Patnaik, R.; Singh Kotla, S.; Premjit Singh, N.; Singla, A.; Kaur, J. A new murid rodent assemblage from the Upper Siwaliks, Himachal Pradesh, India: biostratigraphic, phylogenetic and palaeobiogeographic implications. *J. Asian Earth Sci.* **2018**, *162*, 93-106.
- (251) Abbas, S. G.; Khan, M. A.; Babar, M. A.; Hanif, M.; Akhtar, M. New materials of *Choerolophodon* (*Proboscidea*) from Dhok Pathan Formation of Siwaliks, Pakistan. *Vertebrata Palasiatica* **2018**, *56*, 295–305.
- (252) Abbas, S. G.; Khan, M. A.; Babar, M. A.; Akhtar, M. New remains of *Elephantidae* from the Upper Siwalik subgroup (Plio-Pleistocene) of Pakistan. *Quat. Sci. Rev.* **2019**, *224*, 105967.
- (253) Wey, K.; Epple, M. Ultrasmall gold and silver/gold nanoparticles (2 nm) as autofluorescent labels for poly(D,L-lactide-co-glycolide) nanoparticles (140 nm). *J. Mater. Sci. Mater. Med.* **2020**, *31*, 117.

- (254) Hein, J. E.; Fokin, V. V. Copper-catalyzed azide–alkyne cycloaddition (CuAAC) and beyond: new reactivity of copper(I) acetylides. *Chem. Soc. Rev.* **2010**, *39*, 1302-1315.
- (255) Castro, V.; Rodríguez, H.; Albericio, F. CuAAC: an efficient click chemistry reaction on solid phase. *ACS Comb. Sci.* **2016**, *18*, 1-14.
- (256) van der Meer, S. B.; Loza, K.; Wey, K.; Heggen, M.; Beuck, C.; Bayer, P.; Epple, M. Click chemistry on the surface of ultrasmall gold nanoparticles (2 nm) for covalent ligand attachment followed by NMR spectroscopy. *Langmuir* **2019**, *35*, 7191-7204.
- (257) Mao, X.; Li, Z. P.; Tang, Z. Y. One pot synthesis of monodispersed L-glutathione stabilized gold nanoparticles for the detection of Pb<sup>2+</sup> ions. *Front. Mater. Sci.* **2011**, *5*, 322-328.
- (258) Schütze, B.; Mayer, C.; Loza, K.; Gocyla, M.; Heggen, M.; Epple, M. Conjugation of thiol-terminated molecules to ultrasmall 2 nm-gold nanoparticles leads to remarkably complex 1H-NMR spectra. *J. Mater. Chem. B* **2016**, *4*, 2179-2189.
- (259) Angius, F.; Ilioaia, O.; Amrani, A.; Suisse, A.; Rosset, L.; Legrand, A.; Abou-Hamdan, A.; Uzan, M.; Zito, F.; Miroux, B. A novel regulation mechanism of the T7 RNA polymerase based expression system improves overproduction and folding of membrane proteins. *Sci. Rep.* **2018**, *8*, 8572.
- (260) Rosenberg, M.; Azevedo, N. F.; Ivask, A. Propidium iodide staining underestimates viability of adherent bacterial cells. *Sci. Rep.* **2019**, *9*, 6483.
- (261) Ji, Y.; Jones, C.; Baek, Y.; Park, G. K.; Kashiwagi, S.; Choi, H. S. Near-infrared fluorescence imaging in immunotherapy. *Adv. Drug Deliv. Rev.* **2020**, *167*, 121-134.
- (262) Aneja, A.; Mathur, N.; Bhatnagar, P. K.; Mathur, P. C. Triple-FRET technique for energy transfer between conjugated polymer and TAMRA dye with possible applications in medical diagnostics. *J. Biol. Phys.* **2008**, *34*, 487-493.
- (263) Lauzurica, P.; Sancho, D.; Torres, M.; Albella, B.; Marazuela, M.; Merino, T.; Bueren, J. A.; Martínez-A, C.; Sánchez-Madrid, F. Phenotypic and functional characteristics of hematopoietic cell lineages in CD69-deficient mice. *Blood* **2000**, *95*, 2312-2320.
- (264) Park, K. Y.; Kim, J. Cyclic pentapeptide cRGDfK enhances the inhibitory effect of sunitinib on TGF-β1-induced epithelial-to-mesenchymal transition in human non-small cell lung cancer cells. *PLoS One* **2020**, *15*, e0232917.
- (265) Han, P.; Hanlon, D.; Sobolev, O.; Chaudhury, R.; Edelson, R. L. *Ex vivo* dendritic cell generation – a critical comparison of current approaches. *Int. Rev. Cell Mol. Biol.* **2019**, *349*, 251-307.

- (266) Kocsis, L.; Gheerbrant, E.; Mouflih, M.; Cappetta, H.; Yans, J.; Amaghzaz, M. Comprehensive stable isotope investigation of marine biogenic apatite from the Late Cretaceous-Early Eocene phosphate series of Morocco. *Palaeogeogr. Palaeoclimatol. Palaeoecol.* **2014**, *394*, 74-88.
- (267) Sakae, T.; Mishima, H.; Kozawa, Y.: Chapter 4.23 – *Proboscidea* fossil teeth suggest the evolution of enamel crystals. In *Mechanisms and phylogeny of mineralization in biological systems*; Suga, S., Nakahara, H., Eds.; Springer: Tokyo, Japan, **1991**; pp 477-481.
- (268) Roche, D.; Ségalen, L.; Balan, E.; Delattre, S. Preservation assessment of Miocene-Pliocene tooth enamel from Tugen Hills (Kenyan Rift Valley) through FTIR, chemical and stable-isotope analyses. *J. Archaeol. Sci.* **2010**, *37*, 1690-1699.
- (269) Puech, P. F.; Dhamelincourt, P.; Taieb, M.; Serratrice, C. Laser Raman microanalysis of fossil tooth enamel. *J. Hum. Evol.* **1986**, *15*, 13-19.
- (270) Wilmers, J.; Bargmann, S. Nature's design solutions in dental enamel: uniting high strength and extreme damage resistance. *Acta Biomater.* **2020**, *107*, 1-24.
- (271) Nakagaki, H.; Koyama, Y.; Sakakibara, Y.; Weatherell, J. A.; Robinson, C. Distribution of fluoride across human dental enamel, dentine and cementum. *Arch. Oral Biol.* **1987**, *32*, 651-654.
- (272) Dauphin, Y.; Williams, C. T. The chemical compositions of dentine and enamel from recent reptile and mammal teeth – variability in the diagenetic changes of fossil teeth. *CrystEngComm* **2007**, *9*, 1252-1261.
- (273) Dauphin, Y.; Williams, C. T. Chemical composition of enamel and dentine in modern reptile teeth. *Mineral. Mag.* **2008**, *72*, 247-250.
- (274) Peters, F.; Schwarz, K.; Epple, M. The structure of bone studied with synchrotron X-ray diffraction, X-ray absorption spectroscopy and thermal analysis. *Thermochim. Acta* **2000**, *361*, 131-138.
- (275) Elliott, J. C. Calcium phosphate biominerals. *Rev. Mineral. Geochem.* **2002**, *48*, 427-453.
- (276) Nowicki, D. A.; Skakle, J. M. S.; Gibson, I. R. Nano-scale hydroxyapatite compositions for the utilization of CO<sub>2</sub> recovered using post-combustion carbon capture. *J. Mater. Chem. A* **2018**, *6*, 5367-5377.
- (277) Fleet, M. E.; Liu, X.; King, P. L. Accommodation of the carbonate ion in apatite: an FTIR and X-ray structure study of crystals synthesized at 2-4 GPa. *Am. Mineral.* **2004**, *89*, 1422-1432.

- (278) Fleet, M. E. Infrared spectra of carbonate apatites: evidence for a connection between bone mineral and body fluids. *Am. Mineral.* **2017**, *102*, 149-157.
- (279) Garskaite, E.; Gross, K. A.; Yang, S. W.; Yang, T. C. K.; Yang, J. C.; Kareiva, A. Effect of processing conditions on the crystallinity and structure of carbonated calcium hydroxyapatite (CHAp). *CrystEngComm* **2014**, *16*, 3950-3959.
- (280) Klug, H. P.; Alexander, L. E.: *X-ray diffraction procedures: for polycrystalline and amorphous materials. 2<sup>nd</sup> edition*; John Wiley & Sons: Hoboken, USA, **1974**. pp. 1-992.
- (281) Lee-Thorp, J. A.; van der Merwe, N. J. Aspects of the chemistry of modern and fossil biological apatites. *J. Archaeol. Sci.* **1991**, *18*, 343-354.
- (282) Zazzo, A.; Lécuyer, C.; Sheppard, S. M. F.; Grandjean, P.; Mariotti, A. Diagenesis and the reconstruction of paleoenvironments: a method to restore original  $\delta^{18}\text{O}$  values of carbonate and phosphate from fossil tooth enamel. *Geochim. Cosmochim. Acta* **2004**, *68*, 2245-2258.
- (283) Martin, C.; Bentaleb, I.; Kaandorp, R.; Iacumin, P.; Chatri, K. Intra-tooth study of modern rhinoceros enamel  $\delta^{18}\text{O}$ : is the difference between phosphate and carbonate  $\delta^{18}\text{O}$  a sound diagenetic test? *Palaeogeogr. Palaeoclimatol. Palaeoecol.* **2008**, *266*, 183-189.
- (284) Linglin, M.; Amiot, R.; Richardin, P.; Porcier, S.; Antheaume, I.; Berthet, D.; Grossi, V.; Fourel, F.; Flandrois, J. P.; Louchart, A.; Martin, J. E.; Lécuyer, C. Isotopic systematics point to wild origin of mummified birds in ancient Egypt. *Sci. Rep.* **2020**, *10*, 15463.
- (285) Owocki, K.; Kremer, B.; Cotte, M.; Bocherens, H. Diet preferences and climate inferred from oxygen and carbon isotopes of tooth enamel of *Tarbosaurus bataar* (Nemegt Formation, Upper Cretaceous, Mongolia). *Palaeogeogr. Palaeoclimatol. Palaeoecol.* **2020**, *537*, 109190.
- (286) Uno, K. T.; Fisher, D. C.; Wittemyer, G.; Douglas-Hamilton, I.; Carpenter, N.; Omondi, P.; Cerling, T. E. Forward and inverse methods for extracting climate and diet information from stable isotope profiles in proboscidean molars. *Quat. Int.* **2020**, *557*, 92-109.
- (287) Patnaik, R.; Sharma, K. M.; Mohan, L.; Williams, B. A.; Kay, R.; Chatrath, P. Additional vertebrate remains from the Early Miocene of Kutch, Gujarat *Special publication of the Palaeontological Society of India* **2014**, *5*, 335-351.
- (288) Hobot, J. A.: Chapter 2 – Bacterial ultrastructure. In *Molecular medical microbiology*; Sussman, M., Ed.; Academic Press/Elsevier: New York, USA, **2002**; pp 7-32.

- (289) Shukla, R.; Bansal, V.; Chaudhary, M.; Basu, A.; Bhonde, R. R.; Sastry, M. Biocompatibility of gold nanoparticles and their endocytotic fate inside the cellular compartment: a microscopic overview. *Langmuir* **2005**, *21*, 10644-10654.
- (290) Rizvi, S. M. D.; Hussain, T.; Ahmed, A. B. F.; Alshammari, T. M.; Moin, A.; Ahmed, M. Q.; Barreto, G. E.; Kamal, M. A.; Ashraf, G. M. Gold nanoparticles: a plausible tool to combat neurological bacterial infections in humans. *Biomed. Pharmacother.* **2018**, *107*, 7-18.
- (291) Zhang, H.; Liu, H.; Tian, Z.; Lu, D.; Yu, Y.; Cestellos-Blanco, S.; Sakimoto, K. K.; Yang, P. Bacteria photosensitized by intracellular gold nanoclusters for solar fuel production. *Nature Nanotech.* **2018**, *13*, 900-905.
- (292) Sanyal, S. K.; Brugger, J.; Etschmann, B.; Pederson, S. M.; Delport, P. W. J.; Dixon, R.; Tearle, R.; Ludington, A.; Reith, F.; Shuster, J. Metal resistant bacteria on gold particles: implications of how anthropogenic contaminants could affect natural gold biogeochemical cycling. *Sci. Total Environ.* **2020**, *727*, 138698.
- (293) Hayden, S. C.; Zhao, G.; Saha, K.; Phillips, R. L.; Li, X.; Miranda, O. R.; Rotello, V. M.; El-Sayed, M. A.; Schmidt-Krey, I.; Bunz, U. H. F. Aggregation and interaction of cationic nanoparticles on bacterial surfaces. *J. Am. Chem. Soc.* **2012**, *134*, 6920-6923.
- (294) Boda, S. K.; Broda, J.; Schiefer, F.; Weber-Heynemann, J.; Hoss, M.; Simon, U.; Basu, B.; Jahnen-Dechent, W. Cytotoxicity of ultrasmall gold nanoparticles on planktonic and biofilm encapsulated Gram-positive staphylococci. *Small* **2015**, *11*, 3183-3193.
- (295) Bayal, M.; Janardhanan, P.; Tom, E.; Chandran, N.; Devadathan, S.; Ranjeet, D.; Unniyampurath, U.; Pilankatta, R.; Nair, S. S. Cytotoxicity of nanoparticles – are the size and shape only matters? or the media parameters too?: a study on band engineered ZnS nanoparticles and calculations based on equivolume stress model. *Nanotoxicology* **2019**, *13*, 1005-1020.
- (296) Bachmann, M.; Fiederling, F.; Bastmeyer, M. Practical limitations of super resolution imaging due to conventional sample preparation revealed by a direct comparison of CLSM, SIM and dSTORM. *J. Microsc.* **2016**, *262*, 306-315.
- (297) Štumpf, S.; Hostnik, G.; Primožič, M.; Leitgeb, M.; Bren, U. Generation times of *E. coli* prolong with increasing tannin concentration while the lag phase extends exponentially. *Plants (Basel)* **2020**, *9*, 1680.
- (298) Turner, L.; Ryu, W. S.; Berg, H. C. Real-time imaging of fluorescent flagellar filaments. *J. Bacteriol.* **2000**, *182*, 2793-2801.

- (299) Wirth, R.; Bellack, A.; Bertl, M.; Bilek, Y.; Heimerl, T.; Herzog, B.; Leisner, M.; Probst, A.; Rachel, R.; Sarbu, C.; Schopf, S.; Wanner, G. The mode of cell wall growth in selected *Archaea* is similar to the general mode of cell wall growth in bacteria as revealed by fluorescent dye analysis. *Appl. Environ. Microbiol.* **2011**, *77*, 1556-1562.
- (300) Zhang, H.; Sun, S. C. NF- $\kappa$ B in inflammation and renal diseases. *Cell Biosci.* **2015**, *5*, 63.
- (301) Buso Junior, A. A.; Pessenda, L. C. R.; Mayle, F. E.; Lorente, F. L.; Volkmer-Ribeiro, C.; Schiavo, J. A.; Pereira, M. G.; Bendassolli, J. A.; Macario, K. C. D.; Siqueira, G. S. Paleovegetation and paleoclimate dynamics during the last 7000 years in the Atlantic forest of Southeastern Brazil based on palynology of a waterlogged sandy soil. *Rev. Palaeobot. Palynol.* **2019**, *264*, 1-10.

## 11. List of publications

- ❖ Müller, E. K.; Białas, N., *et al.* Gene silencing of NF- $\kappa$ B p65 in DSS-induced colitis in mice with calcium phosphate nanoparticles carrying siRNA (manuscript submitted).
- ❖ Białas, N., *et al.* Uptake of fluorescently-labelled ultrasmall gold nanoparticles (2 nm) by bacteria (manuscript in preparation).
- ❖ Müller, E. K.; Białas, N., *et al.* Surface-decorated silica-coated calcium phosphate nanoparticles for siRNA-based gene silencing of NF- $\kappa$ B p65 in inflammatory cells (manuscript submitted).
- ❖ Białas, N., *et al.* Silica-coated calcium phosphate nanoparticles for gene silencing of NF- $\kappa$ B p65 by siRNA and their impact on cellular players of inflammation. *Biomaterials* **2021**, 276, 121013.
- ❖ Białas, N., *et al.* Teeth of past and present elephants: microstructure and composition of enamel in fossilized proboscidean molars and implications for diagenesis. *Geochemistry, Geophys. Geosystems* **2021**, 22, e2020GC009557.
- ❖ Sokolova, V.; Rojas-Sánchez, L.; Białas, N., *et al.* Calcium phosphate nanoparticle-mediated transfection in 2D and 3D mono- and co-culture cell models. *Acta Biomater.* **2019**, 84, 391-401.
- ❖ Białas, N.; Radziejewska-Lebrecht, J. Bacterial exopolysaccharides as factors supplementing the bioremediation of heavy metal-polluted terrains. In *Innovative solutions for revitalization of degraded areas*; Skowronek, J., Ed.; Institute for Ecology of Industrial Areas Publishing House: Katowice, Poland, **2013**; pp 289-296 (ISBN: 978-83-930319-9-3).
- ❖ Białas, N., *et al.* Bacterial cell surface structures in *Yersinia enterocolitica*. *Arch. Immunol. Ther. Exp. (Warsz.)* **2012**, 60, 199-209.
- ❖ Białas, N. Microbial exopolysaccharides and their application in environmental protection. In *Interdisciplinary issues in engineering and environmental protection 2*; Traczewska, T., Ed.; Wrocław University of Technology Publishing House: Wrocław, Poland, **2012**; pp 73-80 (ISBN: 978-83-7493-671-2).
- ❖ Białas, N., *et al.* Production of an exopolysaccharide by a wild type strain of *Yersinia enterocolitica* O:3. *Sepsis* **2011**, 4, 95.

## 12. List of conference presentations

- ❖ Białas, N., *et al.* Silica-coated calcium phosphate nanoparticles for gene silencing of NF- $\kappa$ B p65 siRNA and their impact on cells of the blood compartment. 9<sup>th</sup> NRW Nano Conference: *Innovations in materials and applications* (online), Münster, Germany, April 21-23, **2021**; poster presentation. Poster awarded with a prize.
- ❖ Białas, N., *et al.* Crystallographic studies on fossilized elephant teeth. Joint Polish-German Crystallographic Meeting of the Polish Crystallographic Society (within the 62<sup>th</sup> annual meeting) and the German Crystallographic Society (within the 27<sup>th</sup> annual meeting), Wrocław, Poland, February 24-27, **2020**; oral presentation.
- ❖ Białas, N., *et al.* Calcium phosphate nanoparticles as carriers of therapeutic biomolecules into cells – an *in vitro* study. 30<sup>th</sup> Annual Conference of the European Society for Biomaterials together with the 26<sup>th</sup> Annual Meeting of the German Society for Biomaterials, Dresden, Germany, September 9-13, **2019**; poster presentation.
- ❖ Müller, E. K.; Białas, N., *et al.* Cellular uptake and cytotoxicity of CaP nanoparticles in immunological relevant cells. Conference of the University Hospital Jena: *The day of young scientists*, Jena, Germany, May 9, **2019**; poster presentation.
- ❖ Białas, N., *et al.* Nanoparticle-mediated transfection of eukaryotic cells in 2D and 3D cell culture models. 25<sup>th</sup> Annual Meeting of the German Society for Biomaterials, Braunschweig, Germany, November 8-10, **2018**; poster presentation. Poster awarded with a prize.
- ❖ Sokolova, V.; Białas, N., *et al.* Three-dimensional *in vitro* co-culture model for nanoparticle-mediated transfection. 3D Cell Culture Conference of the German Society for Chemical Engineering and Biotechnology: *How close to in vivo can we get? Models, applications and translation*, Freiburg, Germany, June 5-7, **2018**; poster presentation.
- ❖ Białas, N., *et al.* Calcium phosphate nanoparticles as tools for nucleic acid delivery in cells – 2D and 3D cell culture studies. 12<sup>th</sup> Winter Seminar of the University Hospital Essen, Pichl, Austria, March 4-7, **2018**; oral presentation.
- ❖ Białas, N., *et al.* The interaction of ultrasmall gold nanoparticles with bacteria – an imaging study. 24<sup>th</sup> Annual Meeting of the German Society for Biomaterials, Würzburg, Germany, November 9-11, **2017**; poster presentation.
- ❖ Białas, N., *et al.* Calcium phosphate nanoparticles for gene transfer and silencing – a 2D and 3D cell culture model study. 26<sup>th</sup> Annual Conference: *Biomaterials in medicine and veterinary medicine*, Ryty, Poland, October 12-15, **2017**; oral presentation.

- ❖ Białas, N., *et al.* Fluorescence imaging of the interactions between ultrasmall gold nanoparticles and bacteria. International Fall Meeting of the German Society for Biochemistry and Molecular Biology: *Molecular basis of life*, Bochum, Germany, September 24-27, **2017**; poster presentation.
- ❖ Białas, N. The influence of aging on the human microbiota. 10<sup>th</sup> International Congress of Societas Humboldtiana Polonorum: *Longevity – a blessing or a curse?*, Łódź, Poland, June 30 - July 2, **2016**; poster presentation.
- ❖ Białas, N., *et al.* Studies on *Rhizobium etli* strain ZD13 and its exopolysaccharide. The International Workshop (Humboldt-Kolleg): *Progress in biomedicine and neuromedicine* with participation of Prof. Dr. Erwin Neher, the Nobel Prize winner, Kraków, Poland, June 21-23, **2015**; poster presentation. Poster awarded with a prize.
- ❖ Białas, N., *et al.* Exopolysaccharide production by *Rhizobium etli* strain ZD13, a heavy metal-resistant soil isolate. 6<sup>th</sup> Congress of the Federation of European Microbiological Societies, Maastricht, The Netherlands, June 7-11, **2015**; poster presentation.
- ❖ Białas, N., *et al.* The exopolysaccharide of *Rhizobium etli* strain ZD13 – a potential biotechnological tool? 8<sup>th</sup> International Conference: *Innovative solutions for revitalization of degraded areas*, Ustroń, Poland, October 6-8, **2014**; oral presentation.
- ❖ Białas, N., *et al.* The exopolysaccharide produced by *Yersinia enterocolitica* O:3 strain 6471/76. 6<sup>th</sup> Baltic Meeting on Microbial Carbohydrates, Gdańsk, Poland, September 7-10, **2014**; oral presentation.
- ❖ Kasperkiewicz, K.; Białas, N., *et al.* Biofilm formation and exopolysaccharide production by *Yersinia enterocolitica* O:3. 13<sup>th</sup> Bratislava Symposium on Saccharides: *Recent advances in glycomics*, Smolenice, Slovakia, June 22-26, **2014**; poster presentation.
- ❖ Białas, N., *et al.* Screening for exopolysaccharide-producing bacterial strains in soils of the Upper Silesian Industrial Region. Isolation of *Rhizobium etli* strain ZD13 and studies on its exopolysaccharide. 13<sup>th</sup> Bratislava Symposium on Saccharides: *Recent advances in glycomics*, Smolenice, Slovakia, June 22-26, **2014**; oral presentation.
- ❖ Białas, N., *et al.* Screening for exopolysaccharide-producing bacterial strains in soils of the Upper Silesian Industrial Region and isolation of a *Rhizobium etli* strain. 7<sup>th</sup> International Conference: *Innovative solutions for revitalization of degraded areas*, Ustroń, Poland, October 2-4, **2013**; oral presentation.

- ❖ Białas, N., *et al.* Exopolysaccharide production and biofilm formation by a wild type strain of *Yersinia enterocolitica* O:3. 5<sup>th</sup> Congress of the Federation of European Microbiological Societies, Leipzig, Germany, July 21-25, **2013**; poster presentation.
- ❖ Fogt, M.; Białas, N., *et al.* Exopolysaccharides – sticky shields of bacteria. 2<sup>nd</sup> Polish Meeting of Young Biotechnologists – ATRINBIOTECH, Katowice, Poland, March 16-17, **2013**; poster presentation.
- ❖ Białas, N.; Radziejewska-Lebrecht, J. Bacterial exopolysaccharides as factors supplementing the bioremediation of heavy metal-polluted terrains. 6<sup>th</sup> International Conference: *Innovative solutions for revitalization of degraded areas*, Ustroń, Poland, October 2-4, **2012**; oral presentation.
- ❖ Białas, N. Microbial exopolysaccharides and their application in environmental protection. 4<sup>th</sup> Polish Conference: *Interdisciplinary problems in environmental protection and engineering – EKO-DOK*, Szklarska Poręba, Poland, April 15-18, **2012**; oral presentation.
- ❖ Białas, N., *et al.* Production of an exopolysaccharide by a wild type strain of *Yersinia enterocolitica* O:3. 4<sup>th</sup> Polish-Ukrainian Weigl Conference: *From microbiology to synthetic biology*, Czeszów, Poland, May 18-21, **2011**; oral presentation.

**13. Curriculum Vitae** (not included in the online version of the thesis for privacy reasons)

*Curriculum Vitae*

*Curriculum Vitae*

*Curriculum Vitae*

## **14. Acknowledgements**

First of all, I would like to express my deepest gratitude to Professor Dr. Matthias Epple for enabling me to work in his research group and under his supervision. I am thankful to Prof. Epple for the opportunity to work in very interesting interdisciplinary research projects described in this doctoral thesis. I truly appreciate the kindness and openness of Prof. Epple, which I experienced while working together. I am also grateful to him for his support and giving me many excellent opportunities to develop scientifically.

Next, I would like to thank Ms. Elena K. Müller and Professor Dr. Ingrid Hilger from University Hospital Jena for a fruitful collaboration within the DFG research project.

I am grateful to Professor Rajeev Patnaik and his research group (Panjab University, India) for a good collaboration within the DAAD research project and wonderful hospitality during my research stay in India.

Professor Ryan Roeder and his research group (University of Notre Dame, United States of America) I would like to thank for fruitful discussions and great hospitality during my research stay in the United States.

I am also grateful to the scientific workers from the group of Prof. Epple: Dr. Kateryna Loza, Dr. Viktoriya Sokolova, Dr. Tatjana Ruks, Dr. Selina van der Meer, Dr. Oleg Prymak and Mr. Kai Klein, as well as to Dr. Torben Knuschke (University Hospital Essen) and Professor Debayoti Paul (Indian Institute of Technology) for successful collaborative research work.

I would like to thank the technical staff from the group of Prof. Epple: Ms. Ursula Giebel, Mr. Tobias Bochmann and Mr. Smail Boukercha for SEM imaging, as well as Ms. Kerstin Brauner, Ms. Beate Römer and Mr. Robin Meya for AAS analyses.

I am grateful to Ms. Sabine Kiefer, Ms. Sabine Bollmann and Ms. Carola Fischer for their cordiality, advice and help in organizational and technical matters.

I would like to express my sincere thanks to all members of the group of Prof. Epple, whom I had pleasure to meet during these years. I truly appreciate the friendly atmosphere and the time we spent together.

## Acknowledgements

---

I am grateful to Professor Dr. Rainer Meckenstock and his research group (Environmental Microbiology and Biotechnology, University of Duisburg-Essen) for providing me access to the equipment of the laboratories of Aquatic Microbiology, as well as for technical assistance.

Furthermore, I would like to thank Ms. Alexandra Brenzel and Dr. Anthony Squire (Imaging Center Essen, University Hospital Essen) for technical support in super resolution microscopy imaging.

I am also grateful to Professor Dr. Wiebke Hansen and Dr. Sebastian Kollenda for providing me the strain *E. coli* TOP10 and the plasmid pGEX-6P-1-eGFP, respectively.

I am thankful to Professor Dr. Bettina Siebers (Environmental Microbiology and Biotechnology, University of Duisburg-Essen) for the agreement to be second reviewer of my doctoral thesis and to Professor Dr. Maik Walpuski (Chemistry Education, University of Duisburg-Essen) for being chairman of my doctoral commission.

I would also like to thank the German grant institutions: the DFG (Deutsche Forschungsgemeinschaft) and the DAAD (Deutscher Akademischer Austauschdienst) for funding the research projects in which I had pleasure to work.

Finally, I would like to express my sincere gratitude to my lovely daughter Basia, my wife Małgorzata and my parents for their constant support in my life.

## **15. Eidesstattliche Erklärung**

Hiermit versichere ich, die vorliegende Arbeit mit dem Titel:

*Medical application and biological occurrence of inorganic nanoparticles and nanostructures*

selbst verfasst und keine außer den angegebenen Hilfsmitteln und Quellen verwendet zu haben. Zudem erkläre ich, dass ich die Arbeit in dieser oder einer ähnlichen Form bei keiner anderen Fakultät eingereicht habe.

Essen, den 05.11.2021

---

(Nataniel Białas)